

Ph.D. thesis

Synthesis, characterization, and
testing of catalytic nanomaterials
– greener route to synthetic methods

Alcina Johnson Sudagar



Ph.D. thesis

Synthesis, characterization, and testing
of catalytic nanomaterials
– greener route to synthetic methods

Alcina Johnson Sudagar

Supervisor: Prof. Włodzimierz Kutner, Ph.D., D.Sc.

Auxiliary supervisor: Dr. Krzysztof Noworyta, Ph.D.

The thesis was prepared within the International Doctoral Studies in Chemistry
at the Institute of Physical Chemistry, Polish Academy of Sciences in Warsaw, Poland
in the Molecular Films Research group, in collaboration with the Prof. Francis D'Souza group
at the University of North Texas in Denton, TX, USA.

Warsaw, August 2022

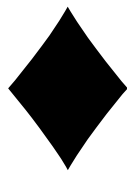


There is light at the end of the tunnel,
the tunnel though, as long as the mind conceived

The soul caught in the forest maze
as Alice in some wonderland

When a light flashed into the abyss
it saw perpetual darkness

The quest found that the end was naught
continuum was all it saw



Declaration of originality

I declare that the research included within the present Ph.D. thesis was carried out by myself or with the support of others included in the acknowledgments.

I state that I have exercised care to ensure that the work is original and contains no previously published material or written by another person, except where citations have been made in the text. The content provided here does not violate any copyrights to the best of my knowledge.

I accept that the Polish Academy of Sciences has the right to use plagiarism detection software to ensure the legitimacy of the thesis.

I certify that the thesis has not been submitted previously for obtaining a degree or diploma by the Institute of Physical Chemistry, Polish Academy of Science, or any other educational institution.

This thesis's copyright rests with the author, and no information derived from it may be published without the author's consent.

Warsaw, 1st August 2022



.....
Signature



Acknowledgments

The present Ph.D. work has been an inspiring journey and a learning curve that will, hopefully, take me higher. I thank God for this blessing to experience life through this path. Indeed, it has been a long and arduous path that has taught me the way of life through highs and lows. My ever-supporting family has made this journey so far from home possible. My mom (Henrita), grandma (Kancy), and mama (Arulraj) have been the pillars of my life and have believed in me and supported me no matter the situation. Thanks to these beautiful people, I have always felt like I could be limitless in life. I also am grateful to have my athai (Menaha Mary) and brothers (Aldrin Samuel and Aldrich), who have brought more warmth to my life. Today, I also remember my dad (Johnson Sudagar) and grandpa (Jeyadason), who were integral parts of my life, inspiring me to go beyond the horizons. I miss them more than ever, and I hope they will be happy to see me here. This journey would not have been possible without my friends, that have almost traveled with me through all the highs and lows. There was always someone to offer moral support, a caring shoulder, wisdom, or even comforting food. Life has been colorful and memorable because of these beautiful people around me. Jeni for being my 'gyan guru' and gourmet chef, Neha for being the shadow that kept me company even through the night and the cake boss, Vicky for being the 'tsunami buddha' and amazing fusion chef, Jyoti for being my partner in crime and the spontaneous chef, Swaraj for being the warmth in our lives and the tiramisu queen, and Tanvi for being the cool inspiration and exotic food chef. There are also quite a few more people who have been a part of this journey, making it memorable, that are not mentioned.

I would take this opportunity to acknowledge my supervisors, Prof. dr hab. Włodzimierz Kutner and Dr. Krzysztof R. Noworyta, for their never-ending support and guidance. I truly feel blessed to have been able to work under some knowledgeable minds. Throughout this journey, I have been inspired by the way they approach science and research, and I hope to be able to be a scientist like them someday. Professor Kutner has been a teacher and a guide, and his dedication is awe-inspiring. Dr. Noworyta has been my support system throughout this period and someone that always had answers or found ways whenever I came across a boulder, which is quite admirable. I have learned a lot from both of them, which has been a gratifying experience. They have always given constructive reviews that have helped me polish my skills. Moreover, I acknowledge Dr. K. Noworyta for atomic force microscopy (AFM), Fourier-transform infrared (FT-IR) spectroscopy, and mass spectroscopy (MS) analyses. He has also taught me different techniques and operations of instruments related to electrochemistry, plasma cleaning, and UV-vis spectroscopy.

Several colleagues from our group and institute have supported me through different parts of this Ph.D. work. I would like to thank **Dr. Piyush Sindhu Sharma** for enabling me to be a part of his Functional Polymers Research group, supporting the faster progress of the projects, and all group members for their purposeful insights. **Dr. Maciej Cieplak** has been a major support for high-performance liquid chromatography (HPLC) and silica column preparation and was always kind and helpful whenever I required something of him. I would also like to acknowledge **M.Sc. Valerii Malyshev** for helping me with electrode preparations and technical issues in the laboratory. **Dr. Paweł Borowicz** from the Laboratory of Molecular Film Investigation is thanked for the FT-IR spectra collection and revision of the FT-IR spectroscopy parts of the thesis. I would also like to acknowledge **Dr. Monika Asztemborska** from the laboratory of Chromatography Analysis for optimizing the HPLC protocol for molecularly imprinted polymer (MIP) mediated electrosynthesis products' analysis. The MS data were collected in the Mass Spectrometry Laboratory Institute of Organic Chemistry, Polish Academy of Sciences, Warsaw, Poland. For the project dealing with nanoparticles (NPs), primarily **Dr. hab. Beata Lesiak-Orłowska** has been an immense support for funding, establishing collaborations, and publications. Her support was crucial for developing this project. **Dr. B. Lesiak-Orłowska** also played a significant role in data collection and X-ray diffraction and electron spin resonance (ESR) spectroscopy analyses. **Dr. Martin Jonsson-Niedziółka** has been very kind and helpful in teaching me and granting access to the scanning electron microscopy facility and equipment for NP coating. I would like to acknowledge **M.Sc. Iliia Smirnov** from the Dynamics of Nanocrystal Structure Induced by Surface Chemistry group for always being ready to help me with the X-ray fluorescence and X-ray diffraction experiments. **Dr. Magdalena Bonarowska** from the group of Modern Heterogeneous Catalysis is acknowledged for being so helpful in teaching me and granting access to the Brunauer-Emmett-Teller instrument. **Dr. Agnieszka Wiśniewska** from the Laboratory for Soft Matter Research is acknowledged for thermogravimetry data collection. **Dr. Michał Leszczyński** from the Coordination Metal Complexes and Functional Materials group is acknowledged for teaching and granting access to the dynamic light scattering instrument and accessories. **Dr. Piotr Bernatowicz** from the Laboratory for NMR Spectroscopy is acknowledged for nuclear magnetic resonance spectroscopy analyses of the MIP pre-polymerization complexes. Moreover, I would like to mention **Dr. Wojciech Nogala**, **Prof. dr hab. Zbigniew Kaszukur**, **M.Sc. Artur Ruszczak** and **Dr. Marcin Hołdyński** for being available for queries and help with equipment and data analysis. I would also like to acknowledge **Prof. dr hab. Adam Kubas** for the computer graphics in chemistry course that paved way to interesting scientific illustrations during my Ph.D including the thesis. It has to be mentioned that a joint effort with **M.Sc. Neha Rangam** led to the fruitful development of the NPs project.

Moreover, I would like to acknowledge our collaborators from outside the institute who have played major roles in supporting the projects. For the MIP project, **M.Sc. Shuai Shao** and **Prof. Francis D'Souza**

from the University of North Texas in Denton, TX, USA, are acknowledged for providing the *p*-bis(2,2',5',2''-terthien-5'-yl)methylbenzoic acid functional monomer. Dr. Tiziana Benincori from the University of Insubria, Como, Italy, is acknowledged for providing the 2,4,5,2',4',5'-hexa(thiophen-2-yl)-3,3'-bithiophene and 2,2'-bis(2,2'-bithiophene-5-yl)-3,3'-bithianaphthene cross-linking monomers. I acknowledge Dr. Teresa Iwona Żołek and Prof Dr. hab. Dorota Maciejewska from the Medical University of Warsaw, Warsaw, Poland, for performing extensive theoretical simulations on MIP cavities to elucidate the superiority of MIPs toward selective electrosynthesis. In the NPs project, I would like to acknowledge Dr. Katarzyna Jakubów-Piotrowska from the Centre of New Technologies, the University of Warsaw, Warsaw, Poland, for being so kind and always promptly available to setup and guide me through photoelectrochemical measurements. I thank Dr. Jarosław Grzegorz Sadło for being so kind in teaching me ESR spectroscopy and helping with instrumentation and data analysis. Dr. Sadło also performed the γ -irradiation on the nanocomposites. I thank Dr. Dorota Michałowska and Prof. Marek Ł. Roszko from the Institute of Agriculture and Food Biotechnology - State Research Institute, Warsaw, Poland, for performing the brewery wastes analysis. The total organic content analysis was performed at the Central Research Laboratory of the University of Life Sciences, Lublin, Poland. Prof. László Kövér and Dr. József Tóth from the Institute for Nuclear Research, Debrecen, Hungary, are thanked for supporting the NPs project in terms of funding, characterization experiments, and publications. It has been a gratifying experience crossing paths with several exceptional researchers, and I thank everyone for contributing to the growth of my project and myself as a researcher.

Funding

The following funding organizations financed the present research.

The European Union Horizon 2020 Research and Innovation Programme under the Marie Skłodowska-Curie grant agreement no. 711859 and the Polish Ministry of Science and Higher Education for implementing an international co-financed NaMeS project in the years 2017 – 2021.



Funded by the Horizon 2020
Framework Programme of the
European Union



Ministry of Science
and Higher Education

Republic of Poland

Erasmus+ to Alcina Johnson Sudagar.



Erasmus+

List of scientific accomplishments

A. Publications included in the thesis

1. **Sudagar, A. J.**; Rangam, N.V.; Ruszczak, A.; Borowicz, P.; Tóth, J.; Kövér, L.; Michałowska, D.; Roszko, M.Ł.; Noworyta, K.R.; Lesiak, B. "Valorization of brewery wastes for the synthesis of silver nanocomposites containing orthophosphate." *Nanomaterials* 2021, 11, 2659. <https://doi.org/10.3390/nano11102659>.
2. Rangam, N.V.; **Sudagar, A. J.**; Ruszczak, A.; Borowicz, P.; Tóth, J.; Kövér, L.; Michałowska, D.; Roszko, M.Ł.; Noworyta, K.R.; Lesiak, B. "Valorizing the unexplored filtration waste of brewing industry for green silver nanocomposite synthesis." *Nanomaterials* 2022, 12, 442. <https://doi.org/10.3390/nano12030442>.
3. **Sudagar, A. J.**; Shao, S.; Żołek, T.; Maciejewska, D.; Benincori, T.; Borowicz, P.; Asztemborska, M.; Sharma, P. S.; D'Souza, F.; Kutner, W.; Noworyta, K.R. "Molecularly imprinted polymer selectively electrosynthesizes the C-C coupled product: an enhanced route from phenol to biphenol," in preparation.
4. **Sudagar, A. J.**; Rangam, N.V.; Bonarowska, M.; Wiśniewska, A.; Sadło, J.; Tóth, J.; Kövér, L.; Lesiak, B.; Kutner, W.; Noworyta, K.R.; "Green silver nanocomposites – thermal and γ -irradiation stability, and electrocatalytic properties," in preparation.

B. Other publications

1. **Sudagar, A. J.**; Andrejkovičová, S.; Patinha, C.; Velosa, A.L.; McAdam, A.; Silva, E.F.d.; Rocha, F. "A novel study on the influence of cork waste residue on metakaolin-zeolite based geopolymers." *Applied Clay Science* 2018, 152, 196-210. <https://doi.org/10.1016/j.clay.2017.11.013>.
2. **Sudagar, A. J.**; Andrejkovičová, S.; Rocha, F.; Patinha, C.; Soares, M.R.; Velosa, A.L.; Silva, E. F. d. "Combined influence of low-grade metakaolins and natural zeolite on compressive strength and heavy metal adsorption of geopolymers." *Minerals* 2021, 11, 486. <https://doi.org/10.3390/min11050486>.
3. Rangam, N.V.; **Sudagar, A. J.**; Pilz, M.; Kwapiszewska K.; Lesiak B. "Cytotoxic effects of nanocomposites synthesized using brewery wastes against human cell lines," in preparation.
4. Rangam, N.V.; **Sudagar, A. J.**; Koronkiewicz, R.; Pawlak, K.; Borowicz, P.; Wiśniewska, A.; Tóth, J.; Kövér, L.; Michałowska, D.; Roszko, M.; Pilz, M.; Kwapiszewska, K.; Lesiak, B. "Surface and bulk composition effects on the biphasic cytotoxicity of nanocomposites synthesized using leaf extracts," in preparation.
5. Malyshev, V.; Kidakova, A.; **Sudagar, A. J.**; Jyoti; Rybakiewicz-Sekita, R.; Borowicz, P.; Kutner, W.; Syritski, V.; Noworyta, K. R., "Selective sarcosine determination using molecular imprinting in combination with impedimetric and electrochemical generation-collection transductions," in preparation.

C. Patent

1. **Sudagar, A. J.**, Rangam, N. V., Borowicz, P., Tóth, J., Lesiak, B., Kövér, L. Sposób otrzymania nanocząstek metalu oraz nanocząstki metalu (Method of obtaining metal nanoparticles and metal nanoparticles). Patent no P.435084 (2020).

D. Conference active participations

1. **Sudagar, A. J.**, Rangam, N. V., Borowicz, P., Tóth, J., Lesiak, B., Kövér, L. "Industrial by-product mediated synthesis of nanoparticles containing orthophosphate." International Conference on Nano Science and Technology (ICONSAT), 5 – 7 March 2020, Kolkata, India (Poster presentation).
2. **Sudagar, A. J.**, Borowicz, P., Asztemborska, M., Kutner, W., Noworyta, K.R. "Molecularly imprinted polymer for selective electrosynthesis of biphenols." PRIME 2020, 4 – 9 October 2020, Honolulu, USA. <https://doi.org/10.1149/MA2020-02161462mtgabs> (Oral presentation).
3. **Sudagar, A. J.**, Rangam, N. V., Borowicz, P., Tóth, J., Lesiak, B., Kövér, L. "Industrial by-product mediated synthesis of silver nanocomposites." Microsymposium organized at IPC PAS, 19 – 20 January 2021, Warsaw, Poland (Poster presentation).

E. Research visits and schools

1. Smart Materials for and from Electrochemistry, Castellammare del Golfo, Sicily, Italy, 19 – 26 May 2019 (Summer school).
2. Electrochemically initiated silica-based structures on Indium Tin Oxide, CNRS Laboratoire de Chimie Physique et Microbiologie pour les Matériaux et l'Environnement, Nancy, France, 13 – 29 July 2019 (Research visit).
3. European School on Nanosciences and Nanotechnologies (ESONN'21), Grenoble, France, 23 August – 10 September 2021 (School).

List of abbreviations

A

ACN – Acetonitrile
AFM – Atomic force microscopy
Ag_{met} – Ag metal
AO – Atomic orbital
APCI – Atmospheric pressure chemical ionization
ATR – Attenuated total reflectance (spectroscopy)
ATRP – Atom transfer radical polymerization

B

B3 – Becke's 3 parameter
BET – Brunauer-Emmett-Teller (isotherm)
BP – 2,2'-Biphenol
BSG – Brewer's spent grains
BSY – Brewer's spent yeast
BW3 – Brewery waste from stage 3 of the brewing process
BW5 – Brewery waste from stage 5 of the brewing process
BW7 – Brewery waste from stage 7 of the brewing process
BW9 – Brewery waste from stage 9 of the brewing process

C

C – Chemical reaction step
CM – Cross-linking monomer
CM-1 – 2,4,5,2',4',5'-Hexa(thiophen-2-yl)-3,3'-bithiophene
CM-2 – 2,2'-Bis(2,2'-bithiophene-5-yl)-3,3'-bithianaphthene
CO₂RR – Carbon dioxide reduction reaction
COD – Crystallography open database
CV – Cyclic voltammetry

D

DACA – Dipethylamine-2-carboxylic acid (**FM-1**)
DCM – Dichloromethane
DFT – Density functional theory
DMF – *N,N*-Dimethylformamide
DLS – Dynamic light scattering
DMPH – 2,4-Dimethylphenol
DPV – Differential pulse voltammetry
DSC – Differential scanning calorimetry
DTGS – Deuterated triglycine sulfate

E

E – Electrode reaction step
EDL – Electric double layer
EDXRF – Energy-dispersive X-ray fluorescence (spectroscopy)
EDXS – Energy-dispersive X-ray spectroscopy
E_m – Thiophene electroactive monomer
ESR – Electron spin resonance (spectroscopy)

F

FM – Functional monomer
FM-1 – Diphenylamine-2-carboxylic acid (DACA)
FM-2 – *p*-Bis(2,2';5',2''-terthien-5'-yl)methylbenzoic acid
FT-IR – Fourier-transform infrared (spectroscopy)
FTO – Fluorine doped tin-oxide (electrode)

G

GA-FTIR – Grazing angle-reflectance Fourier-transform infrared (spectroscopy)
GC – Glassy carbon (electrode)
GGA – Generalized gradient approximation

H

HEC – Hydrogen evolution catalyst
HER – Hydrogen evolution reaction
HOMO – Highest occupied molecular orbital
HPLC – High-performance liquid chromatography
HPLC-CD – HPLC with conductometric detection
HPLC-RID – HPLC with refractometric index detection

I

ICDD – International Center for Diffraction Data
IR – Infrared (spectroscopy)
IRRAS – Infrared reflection-absorption spectroscopy
IUPAC – International Union of Pure and Applied Chemistry

K

KS-DFT – Kohn-Sham density functional theory

L

LC – Liquid chromatography
LDA – Local density approximation
LYP – Lee, Yang, and Parr correlation functional
LSV – Linear sweep voltammetry
LUMO – Lowest unoccupied molecular orbital

M

MD – Molecular dynamics
MEP – Molecular electrostatic potential
MIP – Molecularly imprinted polymer
MM – Molecular mechanics
MO – Molecular orbital
MS – Mass spectrometry

N

NIP – Non-imprinted polymer
NMP – Nitroxide-mediated polymerization
NMR – Nuclear magnetic resonance (spectroscopy)
NP – Nanoparticle
NRR – Nitrogen reduction reaction

O

Ox – Oxidized species
OEC – Oxygen evolution catalyst
OER – Oxygen evolution reaction
ORR – Oxygen reduction reaction

P

PANI – Polyaniline
PEDOT – Polyethylenedioxythiophene
PEM – Photoelastic modulator
PM-IRRAS – Polarization-modulated infrared reflection-absorption spectroscopy
PQNM™ – PeakForce quantitative nanomechanics
PXRD – Powder X-ray diffraction

Q

QM – Quantum mechanics

R

Rd – Reduced species

RAFT – Reversible addition-fragmentation chain-transfer

RF – Radiofrequency

RHE – Reversible hydrogen electrode

RID – Refractometric detection

RIR – Reference intensity ratio

rpm – Revolutions per minute

RRDE – Rotating ring-disk electrode

S

SEM – Scanning electron microscopy

SHE – Standard hydrogen electrode

SPR – Surface plasmon resonance

STO – Slater-type orbital

T

(TBA)ClO₄ – Tetrabutylammonium perchlorate

TEA – Triethylamine

TEOS – Ethyl orthosilicate

TGA – Thermogravimetric analysis

TMBh – 3,3',5,5'-Tetramethyl-2,2'-biphenol

TMOS – Methyl orthosilicate

TOC – Total organic carbon

TOF – Time-of-flight

TPR – Temperature-programmed reaction

U

UV-vis – Ultraviolet-visible (spectroscopy)

V

vs. – versus

W

WDXS – Wavelength-dispersive X-ray spectroscopy

X

XRD – X-ray diffraction

XRF – X-ray fluorescence

List of symbols

A

- A – Absorbance
- A_1 – Intensity of positive ESR peak
- A_2 – Intensity of negative ESR peak
- A_{ESR} – ESR peak amplitude
- a_s – Shielding constant

B

- B_0 – Magnetic field of resonant absorption of radiation
- B_{ext} – External magnetic field
- b_s – Shielding constant
- b_x – Line broadening
- ΔB – Magnetic field change produced by the nuclei

C

- c – Speed of light
- C – BET constant
- C_{O}^0 – Bulk concentration of the oxidized species
- c_s – Sample molar concentration

D

- D – Diffusion coefficient
- d_{H} – Hydrodynamic particle diameter
- D_{O} – Diffusion coefficient of oxidized species
- d_x – Lattice d-spacing

E

- e^- – Electron
- E_{anode} – Equilibrium potential for the oxygen evolution reaction
- E_{cathode} – Equilibrium potential for the hydrogen evolution reaction
- E_e – Energy of unpaired electron in the external magnetic field
- E_g – Bandgap energy
- E_1 – Initial potential
- E_2 – Final potential
- ΔE – Energy separation of spin states
- E^{eq} – Equilibrium electrode potential of redox reaction
- E_{pa} – Anodic peak potential
- E_{pc} – Cathodic peak potential
- E_v – Energy of the permissible vibration mode

E_v – Electrode potential

E_λ – Energy of radiation

F

F – Faraday's constant

G

g – g -factor

G – Gibbs free energy

ΔG – Gibbs free energy change

$g_2(t)$ – Intensity correlation function

ΔG_{bind} – Gibbs free energy change accompanying complex formation

ΔG_{bind}^0 – Standard Gibbs free energy change accompanying complex formation

ΔG_{conf} – Gibbs free energy change related to adverse conformational changes

g_e – g -value of a free electron

ΔG_h – Gibbs free energy change due to hydrophobic interactions

ΔG_{pr} – Gibbs free energy change due to polar interactions

ΔG_p^0 – Standard Gibbs free energy change accompanying product formation

ΔG_r – Gibbs free energy change due to complexation restriction on rotors

$\Delta G_{\text{reaction}}$ – Gibbs free energy change of reaction

$\Delta G_{\text{reaction}}^0$ – Standard Gibbs free energy change of reaction

ΔG_s^0 – Standard Gibbs free energy change accompanying substrate formation

$\Delta G_{\text{t\&r}}$ – Gibbs free energy change due to translational and rotational motion

ΔG_{vib} – Gibbs free energy change due to residual vibrational modes

ΔG_{vdW} – Gibbs free energy of unfavorable van der Waals interactions

H

h – Planck's constant

H_1 – Magnetic field of the maximum of the ESR peak

H_2 – Magnetic field of the minimum of the ESR peak

ΔH_{pp} – Peak linewidth

$\Delta H_{\text{reaction}}$ – Enthalpy change of the reaction

$\Delta H_{\text{reaction}}^0$ – Standard enthalpy change of the reaction

\hbar – Reduced Planck's constant

I

I – Light intensity exiting the sample

I_0 – Light intensity hitting the sample

I_1 – Current just before the pulse is applied

I_2 – Current just before the end of the pulse

I_{disk} – Current at the disk of rotating ring disk electrode

I_{pa} – Anodic peak current

I_{pc} – Cathodic peak current
 I_{ring} – Current at the ring of rotating ring disk electrode
 I_v – Current

J

$j_{d,o}$ – Diffusion-convection rate-limited current density of the reduction reaction
 $j_{k,o}$ – Electron-transfer-rate limited current density of the reduction reaction
 j^0 – Exchange current density of electrode reaction

K

k – Boltzmann constant
 K_α – L → K electron transition
 K_β – M → K electron transition
 K_x – Scherrer constant

L

l – Optical path length
 L_α – M → L electron transition

M

m – mass
 M_s – Electron energy state

N

n – Number of electrons
 N – Number of atoms in a molecule
 n_o – Non-bonding molecular orbital
 n_x – Diffraction order

P

p – Gas pressure
 p_0 – Saturation pressure of the gas
 p_x – Crystallite size

R

ΔR – Difference in the reflectivity between s- and p-polarized light
 ΣR – Sum of the reflectivity of s- and p-polarized light
 R_a – Roughness measured as the average of profile height deviations from the mean line
 R_g – Universal gas constant
 R_p – p-polarized light reflectivity
 R_s – s-polarized light reflectivity
 R_T – Reflectance

S

$\Delta S_{\text{reaction}}$ – Entropy change of the reaction

T

t – Time

T_K – Absolute temperature

T_s – Temperature of the system

X

X – Adsorbed weight of the gas

x_c – Unknown exchange-correlation functional

X_m – Amount of gas adsorbed at standard temperature and pressure

Z

z – charge

Z – Atomic number

Special characters

α – Electron-transfer coefficient in the rate-determining step

α_L – Langmuir constant

β – Bohr magneton

γ – Gyromagnetic ratio

ε – Electric permittivity

ε_s – Molar absorption coefficient

η – Dynamic solution viscosity

θ – Fraction of surface coverage

θ_p – Angle of incidence

θ_x – Diffraction angle

λ – Wavelength of fluorescence emission

λ_x – Wavelength of electromagnetic radiation

ν – Frequency of electromagnetic radiation

ν_k – Kinematic solution viscosity

ν_Q – Vibrational quantum number

π – Pi-bonding molecular orbital

π^* – Pi-antibonding molecular orbital

$\rho(\mathbf{r})$ – Electron density of the system

σ – Sigma bonding molecular orbital

σ^* – Sigma antibonding molecular orbital

ν_0 – Fundamental vibrational frequency of the bond

ω – Angular rotation rate of a rotating electrode

Abstract

The present dissertation involves the development of nanomaterials for catalytic applications. Toward that, molecularly imprinted polymer (MIP) films were devised, fabricated, and tested for selective electrosynthesis of an industrially important chemical. Moreover, silver nanocomposites were synthesized using green chemistry methods for photo- and electrocatalytic applications.

2,2'-Biphenols are widespread motifs in natural products, forming the backbones of highly potent ligand systems in catalysts and pharmaceuticals. For that, 3,3',5,5'-tetramethyl-2,2'-biphenol (**TMBh**), a 2,2'-biphenol derivative, was chosen as the target of selective electrosyntheses. The industrial synthesis of biphenols leads to several different products. Obtaining high selectivity for this synthesis is challenging. Therefore, our research focused on improving the selectivity and yield of the **TMBh** electrosynthesis. Accordingly, the successful MIPs were prepared using the **TMBh** product as the electropolymerization synthesis template and the carboxylate form of *p*-bis(2,2';5',2"-terthien-5'-yl)methylbenzoic acid functional monomer **2 (FM-2)** to provide non-covalent interactions. The resulting MIP films were characterized, and then the MIP film-coated electrodes were used for electro-oxidation of the 2,4-dimethylphenol (**DMPH**) substrate. The MIP film-coated electrode provided selectivity of ~39% for synthesizing the desired **TMBh** product. The effectiveness of the imprinting in electrosynthesis was confirmed using the non-imprinted polymer (NIP) film-coated electrode and bare electrode as the controls.

Nanosilver is an attractive material due to its interesting electronic and optical properties. Therefore, the "green" synthesis of silver nanomaterials for application in catalysis is gaining popularity. Herein, we developed a method of synthesis of silver nanocomposites by valorizing the brewing industry wastes. These wastes are a growing concern because of difficulties with their disposal. Therefore, there is a high demand for these wastes to be reused or recycled for alternate applications. Our project focused on understanding the potential of the wastes to synthesize nanoparticle (NP) composites. We prepared the nanocomposites by a "one-pot" eco-friendly and cheap process. The nanocomposites were then characterized in depth using several techniques to determine their chemical compositions and structural properties. In the final step, the nanocomposites containing silver, silver phosphate, and/or silver chloride were tested for photo- and electrocatalytic applications. Some of the nanocomposites fabricated did exhibit photoactivity and promising photocurrents. However, the nanocomposite films' preparation method needs further optimization to remove difficulties with charge recombination and hindered charge transport. Moreover, these green nanomaterials revealed appealing electrocatalytic activity for the oxygen reduction reaction (ORR) by positively shifting its reduction potential by ~100 mV.

Streszczenie

Niniejsza praca doktorska obejmuje opracowanie nanomateriałów do zastosowań katalitycznych. W tym celu zaprojektowaliśmy i wytworzyliśmy polimery wdrukowane molekularnie (ang. molecularly imprinted polymers, MIPs) umożliwiające selektywną elektrosyntezę przemysłowo istotnego związku chemicznego. Ponadto, za pomocą metod „zielonej chemii” przygotowaliśmy nanokompozyty związków srebra i zastosowaliśmy je jako foto- i elektrokatalizatory.

2,2'-Bifenol to strukturalny motyw często występujący w naturalnych produktach chemicznych. Tworzy one szkielet wielu ligandów spotykanych w katalizatorach i farmaceutykach. Dlatego jako cel naszej selektywnej elektrosyntezy wybraliśmy pochodną 2,2'-bifenolu, 3,3',5,5'-tetrametyl-2,2'-bifenol (**TMBh**). Przemysłowa synteza bifenoli prowadzi do wielu produktów. Opracowanie wysoce selektywnej syntezy tych związków to duże wyzwanie. Nasze badania skupiły się na podwyższeniu zarówno selektywności jak i wydajności syntezy **TMBh**. W tym celu przygotowaliśmy MIP z zastosowaniem produktu reakcji (**TMBh**) jako szablonu i zdeprotonowanego kwasu *p-bis*(2,2';5',2"-tertien-5'-yl)metylobenzoowego jako monomeru funkcyjnego (**FM-2**). W ten sposób zapewnione zostały oddziaływania niekowalencyjne. Otrzymane warstwy MIP-u scharakteryzowaliśmy a następnie elektrody pokryte tym polimerem zastosowaliśmy do elektrotleniania substratu, 2,4-dimetylofenolu (**DMPH**). Elektrody pokryte warstwami MIP-u zapewniały selektywność ~39% względem pożądanego produktu, **TMBh**. Efektywność wdrukowania w elektrosyntezie potwierdziliśmy za pomocą elektrosyntez kontrolnych z zastosowaniem elektrody pokrytej warstwą polimeru niewdrukowanego (ang. non-imprinted polymer, NIP) i elektrody niepokrytej.

Nanosrebro to materiał atrakcyjny ze względu na interesujące właściwości elektryczne i optyczne. Równocześnie, „zielona” synteza nanomateriałów zawierających srebro do zastosowań w katalizie zdobywa coraz większą popularność. W niniejszej pracy opracowaliśmy metodę syntezy nanokompozytów na bazie srebra wykorzystując materiały odpadowe przemysłu piwowarskiego. Odpady te coraz trudniej utylizować. Dlatego poszukuje się sposobów ich wykorzystania.

W ramach niniejszego projektu oceniliśmy możliwości zastosowania odpadów przemysłu piwowarskiego do syntezy kompozytów nanocząsteczkowych. Nanokompozyty te przygotowaliśmy za pomocą przyjaznej ekologicznie, taniej syntezy „jednego garnka”. Następnie, z wykorzystaniem szeregu technik doświadczalnych, określiliśmy skład chemiczny i wyznaczyliśmy strukturę nanokompozytów. Po czym nanokompozyty zawierające srebro, fosforan srebra i/lub chlorek srebra sprawdziliśmy pod względem ich przydatności do foto- i elektrokatalizy. Niektóre z badanych związków wykazały obiecującą fotoaktywność. Jednakże sposób przygotowania warstw nanokompozytów wymaga dalszej optymalizacji w celu wyeliminowania nadmiernej liczby defektów i problemów z rekombinacją nośników ładunku oraz utrudnionym transportem ładunku. Te „zielone” nanomateriały wykazały również interesujące właściwości elektrokatalityczne względem reakcji redukcji tlenu (ang. oxygen reduction reaction, ORR). Potencjał redukcji tlenu dodatnio przesunął się o ~100 mV.

Table of contents

Declaration of originality	v
Acknowledgments	vii
Funding	x
List of scientific accomplishments	xi
List of abbreviations	xiii
List of symbols	xvii
Abstract	xxi
Streszczenie (Abstract in Polish)	xxii
1 Introduction	2
1.1 Selectivity	2
1.2 Catalysis.....	3
1.3 Molecularly imprinted polymers (MIPs) for selective electrosynthesis.....	10
1.4 Green nanomaterials for catalysis.....	28
1.5 Thesis aims and scope.....	42
2 Experimental techniques and methods	44
2.1 Theoretical background	44
2.1.1 Experimental techniques.....	44
2.1.2 Characterization techniques.....	56
2.2 Experimental part.....	80
2.2.1 Molecularly imprinted polymers (MIPs).....	80
2.2.2 Silver nanocomposites.....	93

3	Molecularly imprinted polymers (MIPs) for selective electrosyntheses	101
3.1	Synopsis	102
3.2	Density functional theory simulations to prescreen functional monomers (FMs)	103
3.3	TMBh template and functional monomers (FMs) binding.....	107
3.4	Preparation of molecularly imprinted polymer (MIP) and control non-imprinted polymer (NIP) films	113
3.5	Solution aging	120
3.6	Characterizing optimized MIP-2 and NIP-2 films	126
3.7	Selective TMBh electrosynthesis	132
3.8	Conclusions.....	146
4	Green silver nanocomposites for catalytic applications	149
4.1	Synopsis	150
4.2	Analysis of the brewery wastes composition.....	150
4.3	Characterization of nanocomposites	153
4.4	Discussion and conclusions	192
5	Overview, summary, and future prospective	196
	Annex	200
	References	206



1

Introduction

1.1 Selectivity

Selectivity is derived from the Latin word '*selectus*,' the past participle of '*seligere*' wherein '*se*' stands for 'apart,' and '*legere*' means 'to gather or select.' Selectivity is a crucial attribute that results in effective and efficient processes. There are several fields in which this attribute plays a decisive role in successful process development. Studies have revealed that our brain encodes and retains significant memories selectively that strongly affect the life quality of the individuals by prioritizing some valuable information at the cost of several other trivial pieces of information¹. This value-directed remembering framework has facilitated efficient memory systems as humans age through their lifespan². Moreover, drug selectivity in pharmacology is a critical attribute that defines the drug's ability to affect a particular population of a cell, gene, protein, or signaling pathway discriminately to others to produce a targeted effect³. In analytical chemistry, selectivity enables more discriminating and sensitive methods to identify and quantify the desired analytes with less interference from similar or dissimilar components⁴. Furthermore, reaction selectivity enables one reaction channel to become energetically favorable. Research has focused on enhancing this selectivity by modulating the systems' chemical, compositional, electronic, kinetic, energy, and structural factors⁵. There is a perpetual search for the most selective process that could yield unprecedented efficiencies, resulting in cost-effective and resource-efficient technologies.

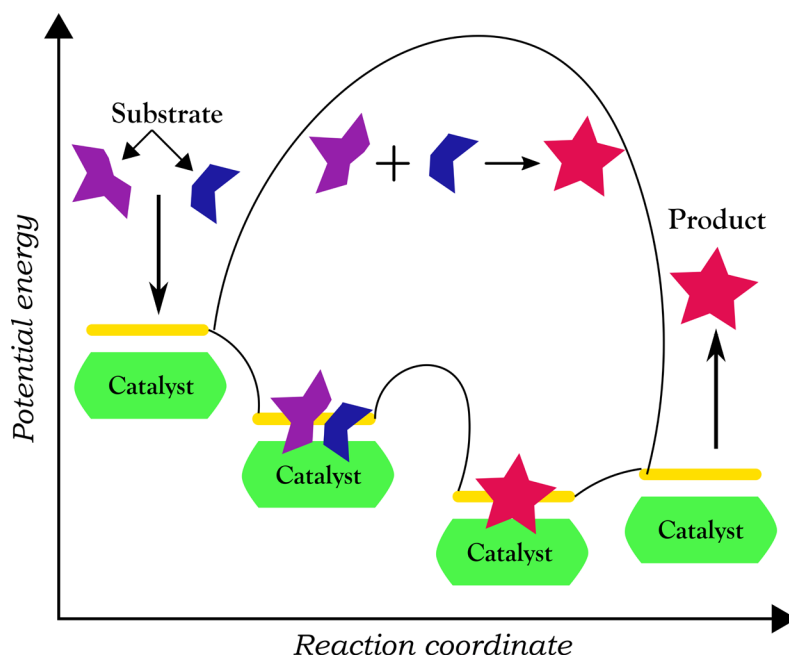
1.2 Catalysis

1.2.1 Understanding catalysis

The word 'catalysis' has Greek origins derived by Berzelius in 1835 from the words 'kata' meaning go down and 'lysis' or 'lyein' meaning letting⁶. Catalysts form the backbone of several chemical reactions in the chemical industry. Catalysis involves ~90% of processes in this industry⁷. Moreover, catalysts are essential in environmental protection technologies. Although the "catalysis" term was not coined or understood for a long time, catalytic reactions have been a part of human evolutionary technologies from ancient times. For centuries, enzymes have catalyzed the sugar fermentation to ethanol and ethanol conversion to acetic acid. The earliest evidence of fermentation of sugars in fruits, honey, and rice to alcohol dates back to 7000 – 6600 BCE in Neolithic China⁸.

Moreover, the art of wine-making can be traced back to ~6000 BCE in Georgia in the Caucasus region of Eurasia. However, the systematic study and development of the catalytic process were not before two centuries. Afterward, there has been an exponential increase in the discovery and application of catalysts in several monumental technological processes. Berzelius used the "catalysis" term to explain several transformation reactions. According to Berzelius, catalysts possessed special powers that affected the affinity of chemical substances⁶. In 1895, Ostwald defined a catalyst within the laws of physical chemistry as a substance that "accelerates a chemical reaction without affecting the equilibrium position"⁹. An alternative path for the reaction, which might be more complex but energetically favorable, is pursued in catalysis. That means the catalytic reaction's activation energy is significantly lower than the uncatalyzed reaction, resulting in an increased catalytic reaction rate. However, the overall free energy change is the same for catalyzed and noncatalyzed reactions. Hence, the reaction equilibrium is not affected by a catalyst. Ergo, a thermodynamically unfavorable reaction cannot be activated by a catalyst. Notably, a catalyst can only change the reaction kinetics, not its thermodynamics.

Catalysis is defined as a cyclic process wherein one form of catalyst binds to the substrate, and the product is released from another catalyst form, thereby regenerating the initial state (Scheme 1.1)⁶⁻⁷. Although a catalyst should not be consumed under ideal conditions during the reaction, competing reactions can induce chemical changes in the catalyst, which may lead to its deactivation⁷. Therefore, catalysts need to be regenerated or replaced after some cycles. Moreover, catalysts influence the selectivity of chemical reactions and accelerate the reactions indicating that different products can be obtained using different catalysts.



Scheme 1.1. The potential energy difference between a non-catalyzed reaction and a reaction catalyzed by a heterogeneous catalyst (adapted from ⁷).

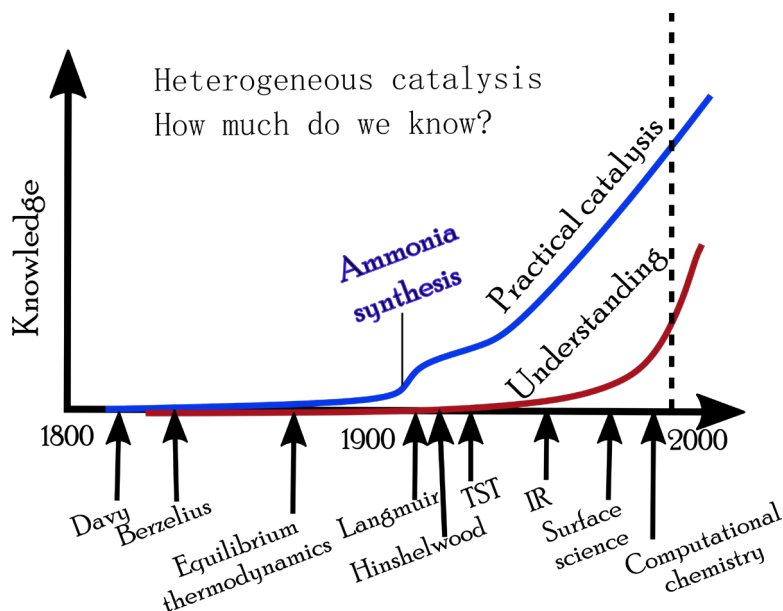
Catalysts can be gases, liquids, or solids, wherein solids interact only through their surface. Catalysts are indispensable in preparing organic intermediate products essential for producing globally significant materials like dyes, pharmaceuticals, plastics, pigments, resins, and synthetic fibers ¹⁰. Catalysis can be heterogeneous when the catalyst has a different physical state than the substrate or homogeneous when the catalyst and substrate are in the same physical state ⁹.

1.2.2 Heterogeneous catalysis

Heterogeneous catalysis occurs on the catalyst surface in a gaseous or liquid environment ¹¹. Therefore, the design of material surfaces is the most crucial aspect of achieving high selectivity and efficiency in heterogeneous catalytic processes. Heterogeneous catalysis has played a central role in science in enabling carbon-neutral, sustainable technologies with minimum waste because the catalyst can be easily separated after the reaction. Breslow, Bard, and Fox pursued rational designing of catalysts in 1995 ¹².

The soaring global demand for food, chemicals, and energy has led to increased CO₂ emissions, raising the alarm to develop catalysts for driving monumental processes, including biomass conversion, CO₂ reduction, chemical syntheses, and water splitting. Approximately 25% of industrial energy is used in catalytic processes; therefore, these processes' energy consumption and environmental impact can be decreased by increasing catalytic efficiency ¹³.

The catalytic ammonia synthesis, developed in the early 1900s, is a powerful example of heterogeneous catalysis's huge potential impact on the world (Scheme 1.2)¹⁴. This process led to a historic increase in agricultural production enabled by synthetic ammonia fertilizers.

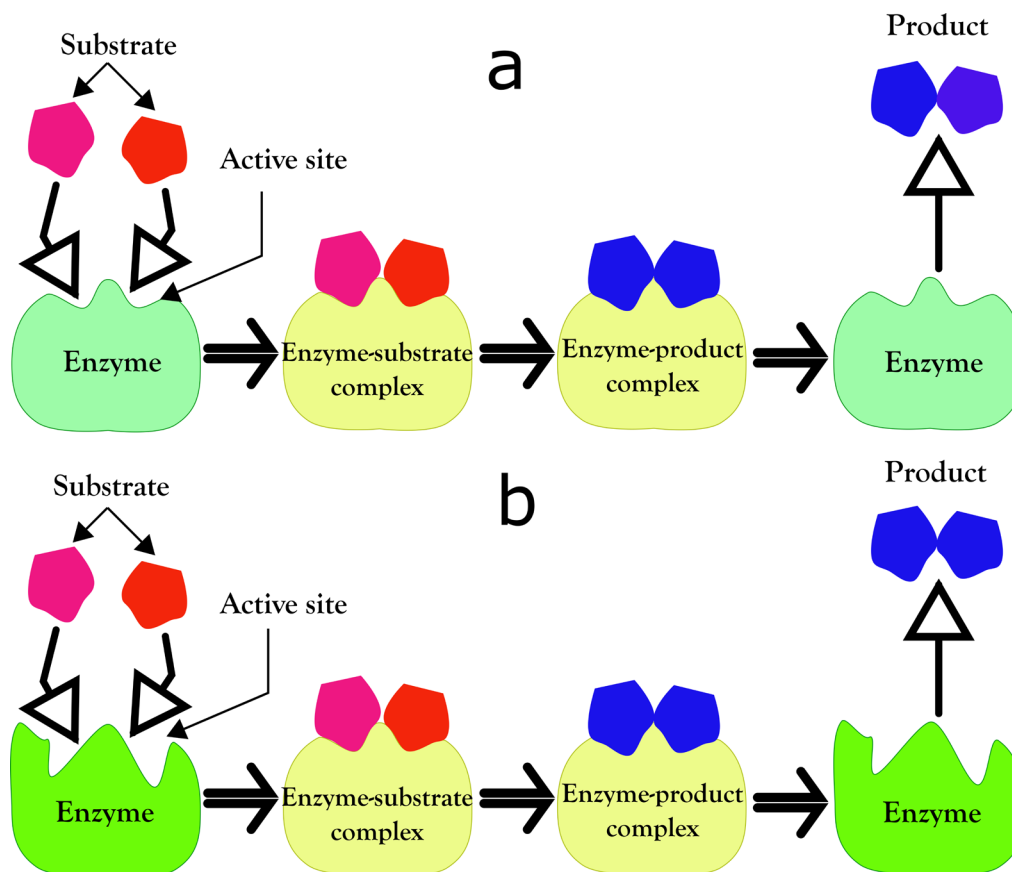


Scheme 1.2. Overview of the growth in the field of heterogeneous catalysis (adapted from¹⁴).

A fundamental understanding of catalytic processes and surface reactions has led to pronounced advances in experimental and theoretical methods of heterogeneous catalyst preparation. Moreover, innumerable novel materials, including size-controlled nanoparticles (NPs), and hierarchical and hybrid materials, are now available in the library of catalysts¹⁵. Furthermore, theoretical modeling has extensively been studied in designing efficient catalysts. The optimization of a catalytic process is initiated by studying detailed reaction mechanisms on pre-defined model systems under the catalytic conditions, which aids in predicting new reactions. In this approach, the conditions in the model studies mimic those under operative catalytic conditions.

In nature, enzymes selectively, and in some instances specifically (i.e., 100% selectively), catalyze numerous biochemical reactions. The enzyme active site binds the substrate. Functional groups precisely arranged in this site are involved in intermolecular interactions with the substrate. Hydrogen bonding, van der Waals, and electrostatic intermolecular interactions are responsible for substrate molecular recognition¹⁶. Other functional groups in the enzyme body activate the substrate, stabilize the transition state, and minimize the activation energy of the reaction. These interactions drive the reaction in a specific pathway, and the desired product formed has a low affinity for the active site. Therefore, it dissociates

or changes the enzyme's structural orientation, leading to the product being expelled. When the product is released, the enzyme restores to its original state and is ready for the subsequent turnover of the catalytic cycle.



Scheme 1.3. (a) The "lock-and-key" and (b) "induced fit" mechanism in enzyme catalysis for selective substrate transformation to a product (adapted from ¹³).

One of the models explaining this enzyme-substrate interaction is the Lock and Key model (Scheme 1.3a) postulated by Emil Fischer in 1894. In this model, the enzyme and substrate molecules' shapes should be complementary, fitting perfectly, like a lock and its key ¹⁷⁻¹⁸. The enzyme will bind to the substrate and catalyze the reaction if their shapes are complementary. But, enzymes also exhibit conformational flexibility. Therefore, a modification to the 'lock and key' model was postulated by Daniel Koshland. This modification, called the 'induced fit' model, states that the enzyme's active sites can change their conformation during interactions with the substrate (Scheme 1.3b). In this case, the 'lock' (enzyme) is considered a dynamic entity, and the 'key' (substrate) modulates the 'key hole' conformation. When the correct substrate interacts with the enzyme active site, it induces the required conformational changes for the desired outcome. The 'induced fit' model is more widely accepted for enzyme catalysis

as it accounts for substrate specificity for an enzyme as not all substrates can be catalyzed even though their molecular shape requirements to bind to the active site are satisfied. Research has focused on replicating this intricate enzymatic catalytic design because of the finesse of this catalysis to obtain high selectivity. This shape-selective catalysis is mimicked in molecularly imprinted polymers (MIPs).

However, a major part of heterogeneous catalysis occurs at the surface of metals, insulators, and semiconductors, pure or composite materials that involve the adsorption of the substrate onto the surface through chemisorption¹⁹⁻²⁰. Herein, the catalysis is structure-sensitive wherein the edges, fissures, kinks, peaks, and steps of crystal structures are considered active sites that selectively catalyze reactions²¹. The chemisorption results in the bond formation between the catalyst and the substrate, lowering the activation energy for the desired product formation. However, depending on the heterogeneity of these active sites, several different reactions could occur, as in oxidations where both the substrate and gaseous oxygen have to be activated²⁰.

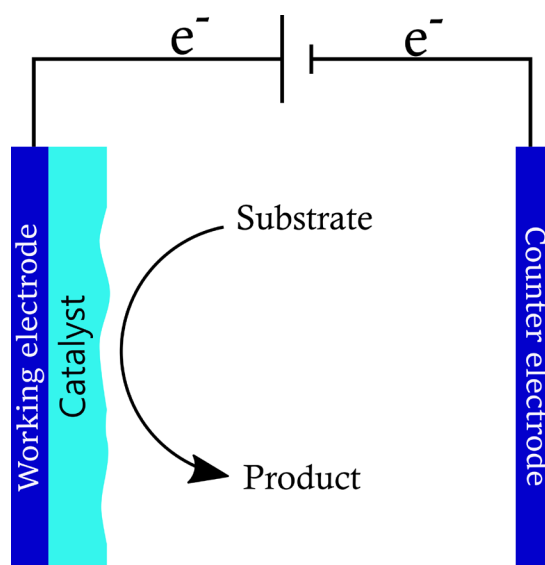
1.2.3 Electrocatalysis and selective electrosynthesis

The exponential rise in energy demands and environmental pollution has stimulated research into more sustainable energy production, including solar, hydropower, and wind energy production as a replacement for fossil fuels energy production²². In this regard, the direct application of electricity produced using sustainable sources has become a challenge as these energy sources are sporadic in space and time. Therefore, electrochemical processes have come to the rescue, allowing renewable energy storage and conversion.

The electrochemical part of electrochemistry is defined as a surface science that involves physicochemical phenomena at the electrode-electrolyte interface, resulting in the interconversion of chemical and electrical energy²³. Electron transfer between two species interacting via a chemical reaction results in the conversion of the chemical reaction energy into the electrical energy related to electron transfer between the two species. The oxidation and reduction involved in every electron transfer must be separated to utilize the electrical energy for technological applications. Therefore, the electrochemical system contains an electron-conducting phase, which can be a metal conductor or a semiconductor, an ion-conducting phase, i.e., the electrolyte that enables the chemical separation, and the interface between the electrolyte and electrode where the oxidation-reduction reactions occur²⁴. Fundamental electrochemical system features include (i) electric potentials difference across

the phases and interfaces, (ii) charge transport across the ion-conducting and electron-conducting or electron-semiconducting phases, and (iii) chemical redox reactions at the interfaces²³.

There is a significant difference between electrochemical reactions and non-electrochemical heterogeneous reactions. The chemical changes in the former result from the potential or current applied to the electrified interface of the ion-conducting electrolyte and the electrode surface, whereas in the latter, the chemical changes involve bond making or breaking without potential or current application²⁵. In addition to parameters, such as reactant concentration and temperature, the surface, nature, and morphology of the electrode, which acts as the catalyst, is a significant factor affecting the electrocatalytic reactions. Electrocatalysis occurs on this active surface site, paving the pathway for electron transfer (Scheme 1.4). Electrocatalysis aims to accelerate electrochemical reactions occurring at the electrode surface²⁶. However, the overpotential, i.e., the difference between the thermodynamic redox potential of a half-reaction of the redox reaction and the experimentally determined potential of the redox event, arises because of kinetic potential losses at the electrodes, and transport potential losses in the electrolyte must be minimized at high currents²⁷. Contrastingly, selective electrosynthesis is a surface process that selectively produces desired chemicals. However, the materials used do not necessarily exhibit catalytic properties. The selectivity can result from blocking side reaction pathways, e.g., by the electrode surface coating.



Scheme 1.4. Catalyzed reaction leading to product formation at the catalyst-coated electrode surface.

In 1928, Bowden and Rideal observed different currents for a reaction at different electrode surfaces under the same electrode potential conditions and termed this phenomenon as catalytic electrode reactions ²⁸. Interesting electrocatalytic applications, such as hydrocarbon electro-oxidation and oxygen electro-reduction, have been developed since the 1800s that could be applied for driving fuel cells ²⁹⁻³⁰. Electrocatalysis has thus become a crucial green technology for energy conversion and storage through reactions like carbon fuels oxidation reaction, CO₂ reduction reaction (CO₂RR), hydrogen evolution reaction (HER), oxygen evolution reaction (OER), oxygen reduction reaction (ORR), and nitrogen reduction reaction (NRR) ³¹. One of the most successful organic electrosynthesis is the C–C bond-forming in carboxylic acids, olefins, organic halides, and different aromatic compounds ³². Organic electrosynthesis has become one of the most efficient and powerful routes to oxidant- and reductant-free chemical transformations through anodic oxidation and cathodic reduction. Stoichiometric amounts of oxidants or reductants are not required, and the waste generation is consequently minimized, thereby labeling the organic electrosynthesis process as a greener synthetic strategy than traditional methods ³³.

However, large-scale electrocatalysis has been limited as researchers have struggled with developing suitable catalysts combining high activity and stability, durability, and low cost. The past decade has witnessed great strides toward developing such efficient electrocatalysts. The factors crucial for improving the electrocatalyst performance are the constitution, size, surface, and support of the electrocatalyst. Catalysts prepared using two or more metals have yielded higher electrocatalytic activity owing to the electronic interaction and synergistic effect between the different components ³⁴. Moreover, nanostructures reveal a higher density of active centers, which significantly enhances the catalytic efficiency of the materials ³⁵. The surface design of the catalyst plays a major role as the reaction occurs at the surface. Therefore, the surface must be carefully engineered to achieve high surface-active centers to improve electrocatalyst activity. Moreover, the catalyst support affects the catalytic efficiency of the active material depending on the porosity and surface area of the support, which can affect the uniform dispersion of the catalyst ³¹.

1.3 Molecularly imprinted polymers (MIPs) for selective electrosynthesis

Molecularly imprinted polymers (MIPs) are attractive enzyme mimics with immense potential for selective catalysis³⁶. However, these MIP materials have not been widely explored yet for metal-free catalysis/selective synthesis. Therefore, developing and understanding the mechanistic aspects of these MIPs and their catalytic activity is significant to enable extensive advancement in this field. Herein, we will discuss the preparation and application of these MIPs in catalysis/ selective synthesis to understand the current scenario and future prospective of these imprinted materials.

1.3.1 A historical outlook on molecular imprinting

In 1931, Polyakov discovered that silica particles exhibited higher selectivity for the adsorption of the additives used in the preparation of silica gel materials than other structurally related ligands³⁷. His student Dickey further developed the imprinting concept. He used methyl orange as the template during silica gel preparation, which proved the shape-selective affinity of the inorganic silica materials towards the template dye over other dyes³⁸. Then, K. Mosbach and B. Sellergren reported pioneering works with organic imprinted polymers in the 1980s³⁹⁻⁴¹ and, separately, G. Wulff in a series entitled "Enzyme-Analog Built Polymers" since 1973⁴² and the term "imprinting" was defined during this period. Mosbach and Sellergren developed separation and sensing materials⁴³, whereas Wulff extensively applied MIPs for catalytic reactions⁴⁴. While the Mosbach group focused on non-covalent interactions between the template and host, the Wulff group applied covalent binding to prepare imprinted polymers⁴⁵. The major difference between the two methods is the required template removal techniques. Furthermore, the covalent synthesis yields more homogeneous binding cavities because the covalent bond stability results in higher target selectivity. However, covalent imprinting is less flexible as the requirement of reversible covalent interactions limits the templates and functional monomers (**FMs**) suitable for covalent imprinting applications. In contrast, these restrictions in non-covalent imprinting are relatively fewer. Mosbach and co-workers proposed the "self-assembly" approach in which non-covalent adducts between a template and **FMs** resulted in cavity formation⁴⁶. The non-covalent interactions between templates and **FMs** usually rely on hydrogen bonding, which has favorable interaction energy in nonpolar solvents. The template molecules usually contain polar functional groups or sites, including heteroatoms like oxygen and nitrogen, the primary target points of molecular

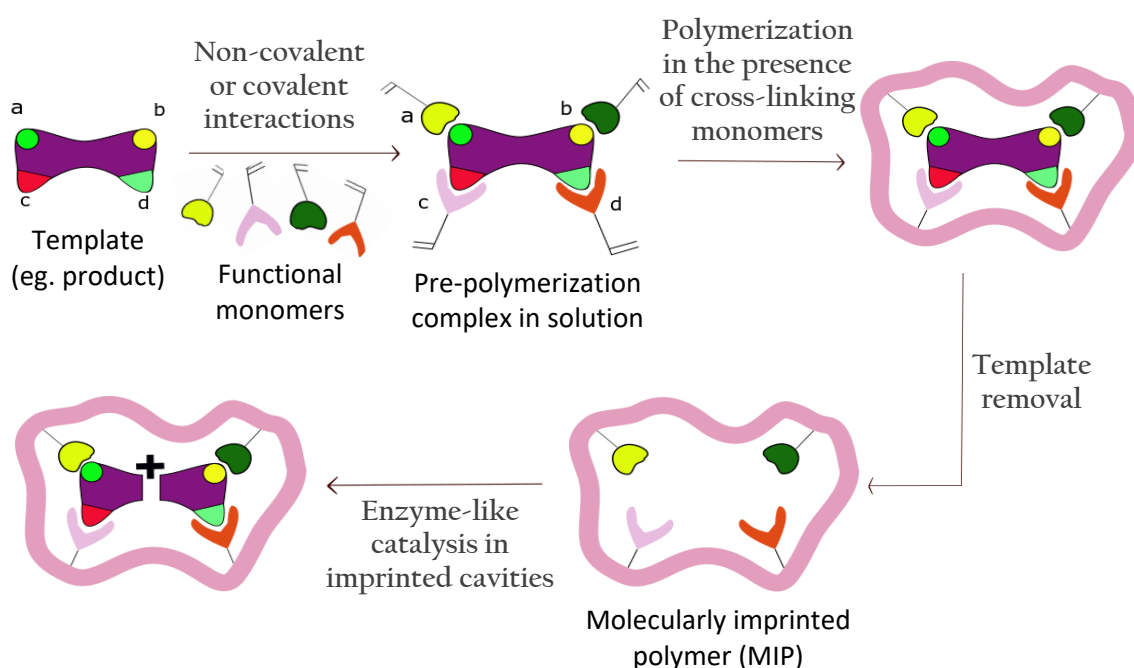
imprinting. Strong interactions with the few heteroatom-based functional moieties are responsible for binding the template to the MIP in nonpolar organic solvents and determining the effectiveness of the interactions. The analyte binding to the MIP also occurs through the same non-covalent interactions. Facile MIP synthesis and the availability of many **FMs** suitable for non-covalent interactions are the reasons why non-covalent molecular imprinting is more widely explored. For catalytic applications, desired functional groups can readily be introduced in cavity design in non-covalent imprinting to enhance catalytic activity. Nonetheless, the imprinted cavities are not uniformly distributed over the polymer matrix, which decreases the selectivity of the interactions over the polymer surface. Some reports also describe semi-covalent imprinting pioneered by Whitcome and coworkers⁴⁷. In this approach, the covalent bonding forms the template-monomer complex during MIP preparation, and non-covalent interaction is used for analyte binding to the MIP.

MIPs can be prepared using both organic and inorganic materials. Early examples of molecular imprinting used silica to bind organic dye templates, and the silica was cross-linked using sol-gel condensation⁴⁸. Although inorganic imprinted materials using silica⁴⁹ or metal oxide networks⁵⁰ are still being explored, there has been a paradigm shift to MIPs prepared using organic compounds primarily because free radical polymerization is more compatible with several template structures⁵¹. MIPs are highly selective and sensitive to the target analyte. Several **FMs** have been used to enhance molecular recognition. MIPs are mechanically stable, resistant to high temperatures and pressures, and inert to chemically aggressive media like acids, bases, and organic solvents, in contrast to biological catalysts like enzymes. Moreover, MIPs are cheap, and their storage life is long, with recognition capacity unaffected for several years under room temperature. Large-scale MIPs' preparation in any desired form, including beads⁵², gels⁵³, membranes⁵⁴, microcapsules⁵⁵, monoliths⁵⁶, NPs⁵⁷, and thin films⁵⁸, is now readily possible.

1.3.2 Principles of molecular imprinting

The progress in synthetic chemistry and engineering primarily depends on the catalysts' efficiency. Utilizing the principles of enzyme catalysis to develop new catalytic materials provides a promising pathway. Therefore, research has focused on preparing enzyme analogs artificially with high catalytic activity and selectivity at par with enzymes. These enzyme mimics have the advantage of higher accessibility and stability and the ability to catalyze various reactions. Moreover, they can help understand the characteristics of enzyme catalysis

in greater detail by methodically simplifying and varying the functional groups forming parts of the active site ⁵⁹. Molecular recognition forms an intrinsic part of several biologically essential systems like enzymes with their substrates, antibodies with their antigens, and hormone receptors with their hormones, wherein the two parts are complementary and fit exclusively ⁶⁰. This recognition of biomacromolecules is now widely applied in affinity technology in biomedical and analytical chemistry ⁶¹. However, the biomacromolecules are unstable outside their native environment, so integrating them into industrial fabrication is a big challenge ^{44,62}. Moreover, their low abundance and unavailability of a natural receptor for a target molecule of interest limit their extensive use. Ergo, the way forward is to build the macromolecules artificially and incorporate receptors capable of recognizing and binding the desired target with a high affinity and selectivity. Molecular imprinting of synthetic polymers is one of the notably facile ways to achieve artificial macromolecular receptors ⁶³. Molecular imprinting applies the above-discussed lock-and-key model to recognize the imprinted species, called template ⁶⁴. It has been extensively developed in the past decades to recognize biological and chemical molecules, including amino acids and proteins ⁶⁵⁻⁶⁸, drugs ⁶⁹⁻⁷⁰, explosives ⁷¹⁻⁷², food ⁷³⁻⁷⁴, pollutants ⁷⁵, and even whole bacteria ⁷⁶ and viruses ⁷⁷. Moreover, molecular imprinting has been used for separating and purifying ⁷⁸, chemical sensing ⁷⁹, catalyzing and synthesizing ³⁶, and biological applying, including drug delivering, imaging, and tissue engineering ⁸⁰⁻⁸¹.



Scheme 1.5. The principle mechanism of molecular imprinting exhibiting the enzyme-mimicking activity.

The underlying principle of molecular imprinting is as follows (Scheme 1.5).

1. A complex is formed between the target molecule used here as the template and an **FM** or several **FMs** in solution. The intermolecular interactions between the **FMs** and the template that drive the complex formation can either be non-covalent like hydrogen bonds, dipole-dipole, van der Waals, electrostatic interactions, or covalent^{64, 82}.
2. A three-dimensional polymer network is formed in excess of cross-linking monomer (**CM**) presence. This network is rigid and forms the imprint of the target molecule in the polymer.
3. After polymerization, the template is removed from the polymer structure resulting in molecular recognition cavities that are complementary in chemical functionality, shape, and size to the template molecule. Therefore, the resulting MIP recognizes and selectively binds the template molecules.

The MIP preparation begins with the dissolution of the template, **FM**, and **CM** in a solution. The **FMs** are selected based on their interaction with the template molecule to enable the formation of a stable template-monomer complex which is fundamental for successful molecular recognition. Often, theoretical simulations have been applied to screen **FMs** by studying complex formation "in silico"⁸³. Experimental studies of monomer-template interaction can also be used to find appropriate functional monomers capable of strong interactions with the selected template⁸⁴⁻⁸⁵. The study of molecular interactions will be discussed later in this chapter. Worth mentioning, however, that the monomer cost, solubility, structural stability, and reactivity are also significant in the selection process⁸⁵.

The complex consisting of monomers positioned around the template is fixed by copolymerization with **CMs**. The template molecules' removal from the polymer by washing with solvents or acid/base solutions vacates the cavities resulting in binding sites complementary to the template molecule. Thus, the MIP is a macroporous matrix containing cavities complementary to the template. Consequently, the resultant polymer is capable of selectively binding the template molecules. The binding sites possess unique characteristics emanating from the intermolecular interactions, as in the case of enzyme active sites. Control non-imprinted polymers (NIPs) are also prepared similarly to MIPs but without the template molecule. Therefore, the NIPs would be void of the cavities that act as recognition units. Only non-specific interactions between NIP and the target molecule are expected.

1.3.3 Understanding molecular interactions

Molecular interactions between templates and **FMs** significantly affect the recognition properties of the MIPs, as discussed previously. Excessive amounts of **FMs** lead to high nonspecific interactions because of binding sites' overabundance randomly distributed in the polymer matrix. On the other hand, too low amounts of **FMs** result in fewer cavities due to insufficient extent of molecular self-assembly, thereby adversely affecting the selectivity of the MIP system⁸⁶. Ergo, stoichiometric interactions between monomers and templates are crucial for yielding the highest selectivity. Spectroscopic studies like Fourier transform infrared (FT-IR)⁸⁷⁻⁸⁸, nuclear magnetic resonance (NMR)^{39, 89}, and ultraviolet-visible (UV-vis)⁹⁰ spectroscopy, as well as theoretical simulations^{86, 91-92} of the pre-polymerization complex have been developed to aid monomer selection and gain a deeper understanding of the imprinting process. In spectroscopic studies, titrating the **FMs** to the template should shift the overall spectral bands. The stoichiometric ratio is attained when the shift is maximal, and no further shift in the spectrum is observed with a further increase in the monomer amount. The thermodynamic analysis application to molecular recognition for identifying the individual molecular characteristics contributions to the binding free energy, discussed by Nicholls, can be used for studying the pre-polymerization complex formation⁹³.

$$\Delta G_{\text{bind}} = \Delta G_{\text{t+r}} + \Delta G_{\text{r}} + \Delta G_{\text{h}} + \Delta G_{\text{vib}} + \sum \Delta G_{\text{pr}} + \Delta G_{\text{conf}} + \Delta G_{\text{vdW}} \quad \text{Equation 1.1}$$

ΔG_{bind} is the Gibbs free energy of complex formation, $\Delta G_{\text{t+r}}$ is the translational and rotational free energy, ΔG_{r} is the complexation restriction on rotors, ΔG_{h} is the energy of hydrophobic interactions, ΔG_{vib} is the energy of residual vibrational modes, ΔG_{pr} is the energy of polar interactions, ΔG_{conf} is the energy related to the adverse conformational changes and ΔG_{vdW} represents the Gibbs free energy change due to unfavorable van der Waals interactions.

Several successful examples of molecular studies can be seen in literature⁸⁵. UV-vis analysis indicated complex formation between a template L-2-chloromandelic acid and functional monomer acrylamide. Accordingly, HyperChem simulations showed a higher binding capacity of the MIP to L-2-chloromandelic acid than other analogs with a chiral separation factor of 1.76, yielding a highly selective separation by the MIP⁹⁴. The FTIR band shifts representing the strength of non-covalent interaction between the template 2-aminopyridine and the functional monomer were compared to those of the template isomers 3- and 4-aminopyridine yielding a clear correlation between the template pKa and the degree

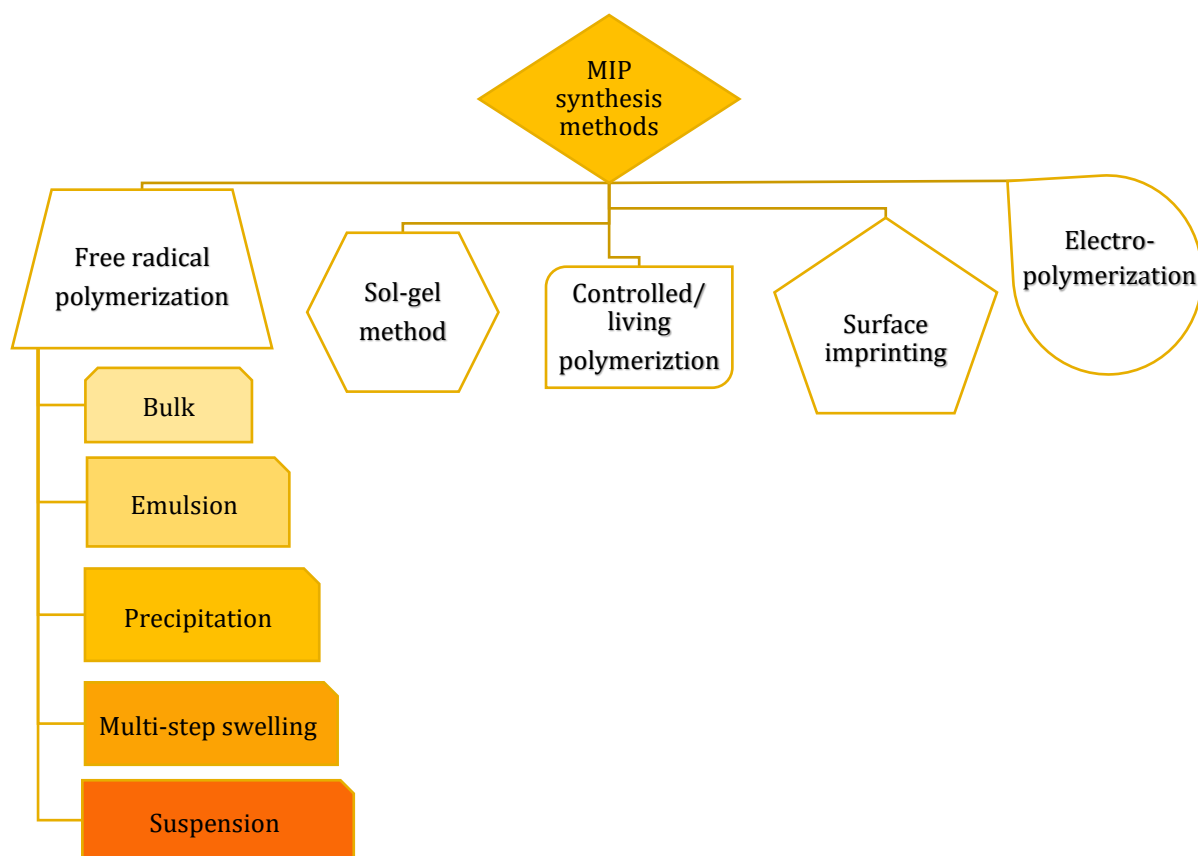
of molecular interactions⁸⁸. Moreover, NMR shifts due to molecular interactions have been used to calculate dissociation constants, consequently enabling the prediction of binding selectivity of MIP⁹⁵. However, there have still been issues in observing several systems' molecular interactions. For example, the complex of 2,4-dichlorophenoxyacetic acid and 4-vinylpyridine occurs involving several different interactions, including van der Waals interactions such as the π - π stacking between aromatic rings of the template and monomers, hydrophobic interactions, and the strong electrostatic interaction between the template acid group and the pyridine molecule of the basic monomers⁸⁹. All these interactions were visible clearly in the NMR spectra. Contrastingly, the norephedrine template–methacrylic acid monomer complex exhibited only one of the electrostatic interactions between the acid carboxylate functional group of methacrylic acid monomer and the norephedrine hydroxyl and amino groups in NMR analysis because of the intramolecular bonding between the hydroxyl group and amino groups of the template molecule⁸⁹. This pre-polymerization complex consequently led to the formation of MIP with low selectivity. As several interaction points are essential for a successful MIP formation⁴⁴, observing and studying all possible interactions is crucial.

1.3.4 Preparation methods for molecularly imprinted polymers (MIPs)

As the MIP morphology is determined by the synthesis method, it is essential to analyze the technique suitable for obtaining MIPs for a specified application. Several different MIP preparation methods (Scheme 1.6) have been developed, i.e., the sol-gel method, free-radical and controlled/living polymerization, nanoscale and surface imprinting, and electropolymerization. Here, typical MIP preparation techniques are briefly described before moving to the major technique for this project, electropolymerization.

In **free radical polymerization**, three major steps are involved⁹⁶.

1. Free radicals are generated by decomposing an initiator, which attacks the double bond of a monomer, leading to intermediate radical formation. That is the rate-limiting step of the polymerization reaction.
2. The next step is propagation, wherein the polymeric chain is formed by successive monomer additions to the growing macroradical.
3. The final step is termination which can occur either by macroradical recombination or by disproportionation yielding a double bond.



Scheme 1.6. Molecularly imprinted polymer (MIP) preparation methods.

There are several types of free radical polymerization. The first is the **bulk polymerization** technique, in which a rapid reaction occurs in a bulk solution at atmospheric pressure under mild conditions. Generally, an initiator is thermally or photothermally decomposed to obtain free radicals that react with monomers in the solution, thereby starting the polymerization process. The bulk polymerization method is inexpensive, rapid, and straightforward that does not require heavy instrumentation. Generally, MIP blocks are crushed and passed through sieves to get specific particle sizes, typically in micrometers⁹⁷. However, this technique suffers from a long processing time and low affinity due to the irregular shape of particles that contain heterogeneously distributed cavities. Advanced free radical polymerization techniques like emulsion, precipitation, multi-step swelling, and suspension polymerizations have been developed to overcome the shortcomings of the bulk polymerization technique.

Emulsion polymerization involves polymerization occurring in the presence of two immiscible media, e.g., oil in water. The surfactants are dissolved in the continuous phase (water), and the initiators, template, functional and cross-linking monomers are in the dispersed phase (oil). When the solution is vigorously ultrasonicated or stirred, emulsification occurs, leading to stable monomer micelles that are then polymerized to form MIP⁷⁹. The

homogeneous distribution of cavities on monodispersed particles can be obtained simply using this technique. However, sometimes the surfactants can contaminate the MIP particles. In **multi-step swelling polymerization**, seeds of materials such as polystyrene or titanium dioxide are used to grow uniform polymer layers. Firstly, the seeds are swollen in a free radical initiator micro-emulsion. Then these swollen particles are dispersed in another solution containing the polymerization complex, which adsorbs onto the seed surface, after which polymerization gets initiated. These steps can be repeated multiple times to obtain polymers of different thicknesses. It is possible to control the polymer formation by varying parameters such as initiator concentration and dispersion solution phases. Although this technique yields monodispersed MIP particles, the process is quite extensive, and using water as the solvent can adversely affect intermolecular interactions between the template and functional monomers that are significant for efficient MIP formation ⁹⁷.

The **precipitation polymerization** involves bulk polymerization in the presence of an excess solvent. When initiator, template, and monomers are added to the excess solvent, polymerization leads to the growth of chains that will precipitate when they grow long enough to become insoluble in the solvent and can be centrifuged ⁹⁸. This technique is quite promising as it does not require surfactants yet exhibits high homogeneity and control over polymerization extent that can be altered by modulating the porogen, stirring conditions, and polymerization temperature ⁷⁹. In **suspension polymerization**, droplets containing the pre-polymerization complex are suspended into a surfactant-containing continuous liquid phase resulting in mini-bulk reactions in each droplet yielding polydispersed MIP particles ⁷⁴. The template extraction process is easier in this technique than bulk polymerization, however the use of surfactant is still a disadvantage as stated above and moreover, when water is used as the continuous phase it can affect non-covalent hydrogen bonding interactions significantly.

The one-step **sol-gel synthesis method** offering some advantages over free radical polymerization starts with using a catalyst like acid, base, or ions such as F^- to dissolve a metal oxide precursor ($M(OR)_n$). The next stage is hydrolysis, followed by polycondensation, which yields a highly stable crosslinked inorganic polymer gel. Ethyl orthosilicate (TEOS) and methyl orthosilicate (TMOS) are the most commonly used precursors for introducing the imprinting template into the inorganic network, resulting in cavity imprinting during the formation of the gel ⁷⁴. This method has several advantages like simplicity and cost-effectiveness of preparation. Large-scale synthesis of highly porous and chemically, mechanically, and thermally stable MIP particles with a high surface area can be achieved. High-temperature template extraction is performed, resulting in efficient template removal.

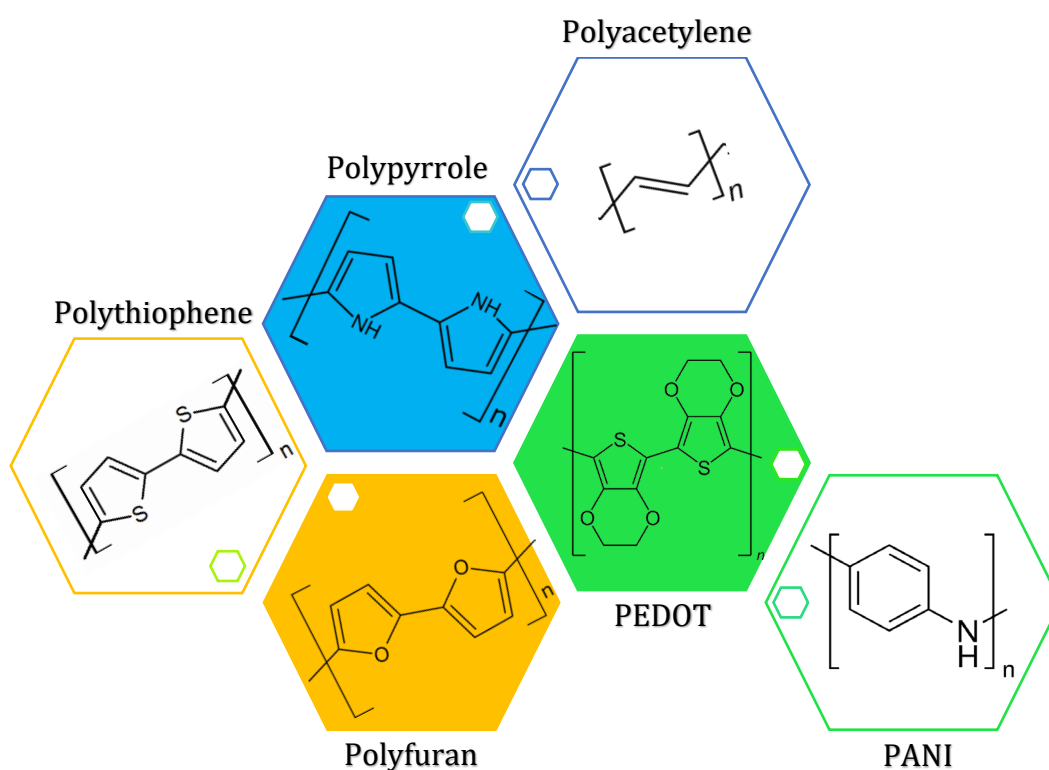
Moreover, the cavity lifetime is longer as these silica-based materials yield strong, stable structures resistant to harsh template extraction conditions⁹⁹. This method produces highly homogeneous materials at the molecular level without using expensive chemicals like initiators and surfactants. However, the sol-gel MIPs have to be studied using complex analytical techniques like HPLC, and they have suffered from delayed response time and low sensitivity⁹⁹⁻¹⁰⁰.

The **controlled / living polymerization** can be of different types, namely, atom transfer radical polymerization (ATRP), nitroxide mediated polymerization (NMP), and reversible addition-fragmentation chain transfer (RAFT) polymerization method. This technique also offers advantages over the free-radical polymerization method. In contrast to free radical polymerization, this technique uses a transition metal catalyst in RAFT and a chain-transfer reagent in ATRP to grow polymers in a controlled fashion, yielding highly selective materials⁹⁶. The NMP technique involves a thermally reversible termination reaction in which an alkyl radical is formed as an active species and nitroxyl radical as a dormant species by the homolytic cleavage of the C–ON bond of alkoxyamine that control the reaction¹⁰¹. These techniques are majorly applied for preparing the core-shell type of MIP NPs. The central issue in these techniques is that oxygen, polar functional groups, and protic solvents need to be used, which can lead to unwanted side reactions. Another issue is that as cross-linking in MIP is required to maintain the structural integrity of the binding cavities, cross-linking monomers have to be used, resulting in partial or total loss of control over the polymer molecule sizes. Moreover, the template molecules can interfere with polymerization. However, this process can still help improve the matrix's structural stability and allows for highly controlled polymer structure formation.

Generally, conventional MIP preparation methods result in deeply embedded cavities that suffer from incomplete template extraction and sluggish mass transfer⁶⁹. Therefore, the **surface imprinting** approach is applied wherein, as the name suggests, most of the binding sites are concentrated on the surface of MIPs, which enhances template extraction efficiency and the mass transfer rate⁷⁴. Carriers, such as carbon nanomaterials, metal NPs, metal-organic frameworks, and quantum dots, are popular structures over which the imprinted material is present¹⁰². These processes are quite extensive, which also adds to the preparation costs. Therefore, it can be seen that simpler methods are necessary that would still yield uniform MIP systems.

Electropolymerization is predominantly used if films must be deposited on conducting or semiconducting substrates. Electropolymerization enables high control of the polymer

nucleation and growth rates and thereby the film thickness by adjusting the charge passed during film deposition ¹⁰³. Moreover, the film morphology can be modulated by varying the supporting electrolyte and solvent used. Electropolymerization can be performed under galvanostatic, potentiostatic, or potentiodynamic conditions. Moreover, this technique is simple and is considered greener as fewer chemicals are required. Therefore, this technique is one of the popular methods of MIP preparation. The polymer film formed could be charged or neutral as solvated counter ions enter and leave the film during its growth. This counter ion transport through the polymer film in the oxidation-reduction cycles can result in periodic film swelling and shrinking, generating defects ¹⁰³. Notably, the template should be electroinactive in the region where the polymerization occurs, which can limit the targeted molecules pool.



Scheme 1.7. Structural formulae of some common conducting polymers.

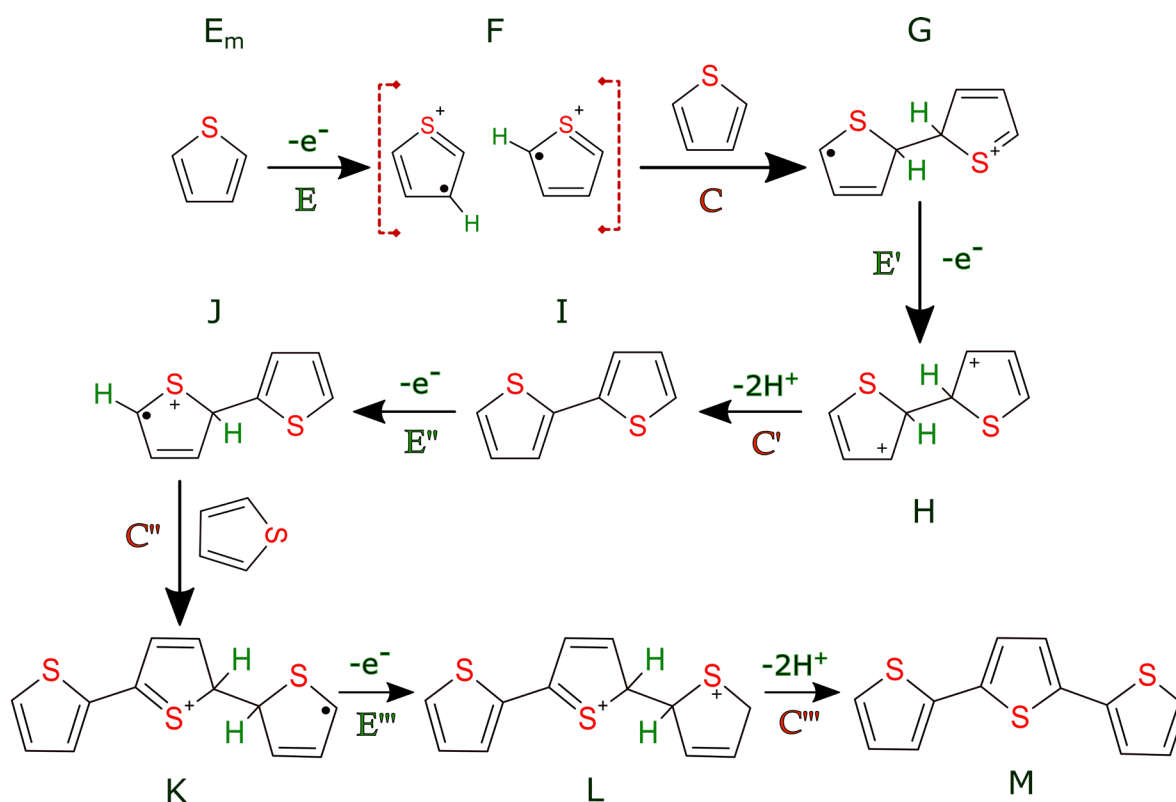
Electroactive monomers are a class of compounds that can polymerize to form either conducting or non-conducting polymers. A major group of conducting polymers contains electrically conducting polymers. These polymers' electronic properties, including magnetic, conducting, and optical features, can be comparable to those of metals ¹⁰⁴⁻¹⁰⁶. However, they are fabricated like and exhibit properties of traditional organic polymers. Several stable conducting polymers, like polythiophene ¹⁰⁷, polyacetylene ¹⁰⁸, polyfuran ¹⁰⁹, polypyrrole ¹¹⁰, polyaniline (PANI) ¹¹¹, and polyethylene dioxythiophene (PEDOT) ¹¹², have been successfully synthesized for numerous applications (Scheme 1.7). Notably, these polymers have found

application in commercial display modules ¹¹³, batteries ¹¹⁴, electrophosphorescent light-emitting devices ¹¹⁵, supercapacitors ¹¹⁶, and superconductors ¹¹⁷. These conducting polymers can be prepared chemically using an external reactant or electrochemically by electropolymerization.

The early MIPs prepared for applications like chemosensing were nonconducting. They were synthesized using free-radical polymerization in the presence of an initiator and light or heat to induce this polymerization ¹¹⁸⁻¹²⁰. In the chemical synthesis of MIPs, the template and a vinylic or acrylic **FM** are non-covalently preassembled in solution followed by bulk polymerization. Gravimetric or optical transduction methods must be used for MIPs with insulating acrylic or vinyl polymers. They lack a direct path for electron conduction from the recognition units to the electrode ¹²⁰. Redox probes with the so-called "gate effect" or conductivity measurements can be used with such non-conducting polymers if used in electrochemical sensors ¹²¹. MIP films with acrylic or vinyl polymers suffer from incomplete template removal. Several procedures have been developed to deposit MIP films directly on transducer surfaces, including depositing composite membranes ¹²², coating a polymer solution ¹²³, and electropolymerizing an electroactive monomer ¹²⁴. Notably, the MIP films obtained using electropolymerization firmly adhere to the transducer surface and are readily and quickly prepared ¹⁰³. Moreover, easy control of film thickness and morphology, high reproducibility, and the possibility of using aqueous solutions make electropolymerization an attractive MIP synthesis route ¹²⁵. With the evolution of the MIP technology, molecular imprinting has used conducting polymers like those discussed above to avoid undesirable effects such as irreproducibility in film thickness. The electrochemically fabricated MIP films can be prepared as compact films or grains with sizes ranging from a few tens to a few hundreds of nanometers. Therefore, such MIPs can be considered nanomaterials. The film thickness can also be precisely controlled by fixing the charge passed through the system. Furthermore, these polymers are sparingly soluble and highly structurally rigid, which helps preserve the imprinted cavity's integrity after template removal ⁷². For the current project, MIPs were prepared by anodic electropolymerization because the ultimate goal was to obtain MIP films deposited on electrode surfaces that could be applied for selective electrosynthesis.

Anodic oxidation ^{124, 126} is the most common electrochemical method used to prepare MIPs using conducting polymers, although some examples of cathodic deposition ¹²⁷⁻¹²⁸ have also been shown. The formation of a polymer film and counter ions doping in the film through oxidation coincide. The monomer oxidation potential leading to polymerization is generally higher than the potential of oxidation of oligomeric intermediates or the polymer. In this

method, the template, as well as functional and cross-linking monomers, are dissolved in an electrolyte solution, and the film is formed by potentiodynamic or potentiostatic electrodeposition. The technique is quite facile and does not require additional chemicals as initiators, surfactants, or terminators.



Scheme 1.8. Thiophene electropolymerization mechanism (adapted from ¹²⁹).

A simplified mechanism postulated for the electropolymerization of a thiophene electroactive monomer (E_m) involves alternate electrode (E) and chemical (C) reaction steps ^{107, 129}. During the potentiodynamic electropolymerization of E_m (Scheme 1.8), a radical cation (**F**) is formed in the first electrode step, E of thiophene electro-oxidation indicated by an anodic peak at ~ 1.60 V vs. Ag/AgCl. The second step is a chemical step, C, in which F reacts with E_m forming a protonated dimer form of radical cation **G**. Subsequently, G is electro-oxidized to the doubly charged σ -dimer **H** at the electrode. When the two protons are eliminated from H, a neutral dimer **I** is formed, which is then oxidized in the next electrode step resulting in the formation of the radical cation **J**. Afterward, J reacts with E_m in the chemical step. The steps follow the ECE'C'E''C''' mechanism to form the trimer, **M**. The dimer I has a lower oxidation potential of ~ 1.10 V vs. Ag/AgCl than the monomer E_m , which results in a more efficient and faster polymerization at lower potentials. The oxidation potential

of the trimer is even lower. Therefore, thiophene dimers and trimers are generally more preferred than monomers. Polythiophenes are highly chemically and mechanically stable, thereby maintaining the structural integrity of the imprinted cavities even if the template is extracted under harsh conditions.

1.3.5 Crucial factors affecting electrochemical MIP preparation

The MIP preparation depends on the target compound and its application. The functional monomer, cross-linking monomer, and solvent must be carefully chosen to obtain successful MIPs. Additionally, electrolyte choice is essential for successful electropolymerization.

As a stable template-functional monomer complex is crucial for preparing MIPs, the interaction between the template and the **functional monomers** is a vital factor determining the MIP systems' efficiency. So, it is essential to screen functional monomers, study their interactions with the template using simulations or experimental titrations, and determine the stoichiometric ratio of the template to functional monomers that will result in the strongest interactions^{85,130}. Moreover, the interactions should be dependent on the nature of the template and monomers to yield selectivity to these molecular interactions. Furthermore, the functional monomer should be soluble and stable in the electrolyte solution. Multi-point interaction between the template and functional monomers is vital to achieving superior MIPs⁸⁵. The monomers are also chosen based on their application, as for large-scale synthetic applications, cheap monomers are preferred to maintain the cost of the system low.

The second essential component is the **cross-linking monomers**. The cross-linking monomer defines the durability, morphology, and rigidity of the MIP⁹⁷. The morphological features are important for MIPs as they directly affect MIPs' binding capacities. The rigidity of the MIP is crucial for maintaining the integrity of the cavities after template extraction. Several cross-linking monomers are used if porous materials are desired⁸². Moreover, the binding capacity of a MIP is observed to increase with the increase of the cross-linking monomer amount to a certain value, after which no further effect or adverse effect on binding capacity is observed¹³⁰. However, too low cross-linking monomer amount can result in inhomogeneous MIPs with an excess of binding sites, consequently leading to unsuccessful template removal and non-specific interactions. Therefore, it is important to optimize the cross-linking monomer amount. Additionally, the functional monomer and the solvent used will affect the cross-linking monomer selection.

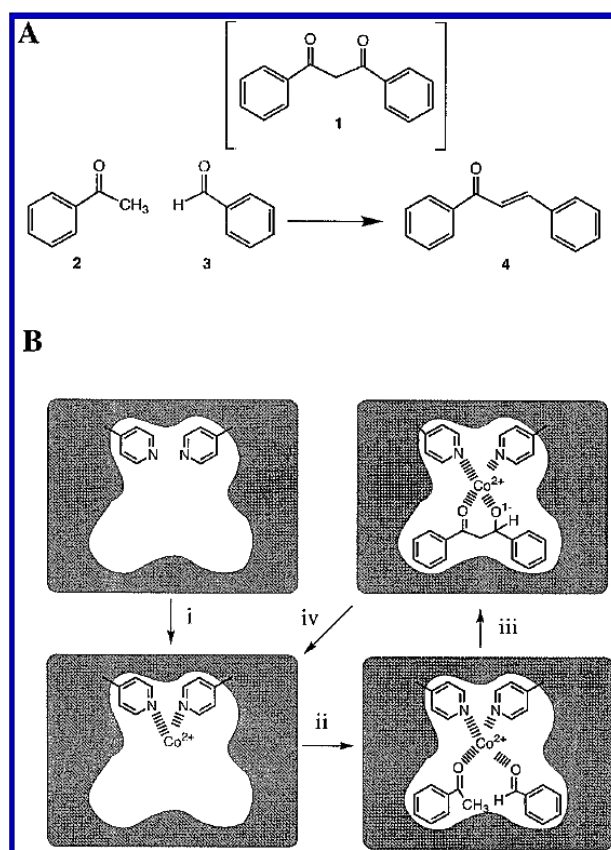
Another critical factor is the **solvent** used for the polymerization, as it acts as the medium where the template and the monomer molecular interact. The solvent must be able to dissolve the template and monomers and stay inert during the polymerization. Moreover, if the solvent has a high solvation value, it would protect the cavities and prevent strong interactions with the template, thereby decreasing the recognition capacity of the MIPs ¹³⁰. The water presence can also affect the hydrogen-bonding interactions; therefore, organic solvents are preferred ¹³¹. The solvent polarity plays a significant role in the MIP system. Solvents of low polarity are better as they do not interfere much with the molecular interactions between the template and the monomer. However, the low solubility of polymers in low polar solvents can result in fast precipitation of MIPs ¹³². Additionally, the **electrolyte** is a significant factor. The size of the electrolyte ions, conductivity, and stability in the potential range of electropolymerization is to be accounted for when selecting the electrolyte. The electrolyte ions affect the morphological homogeneity of MIPs ¹³³. Electrochemical potential control is a significant parameter affecting the MIP films' morphology.

1.3.6 Catalysis and selective electrosynthesis by molecularly imprinted polymers (MIPs)

Although molecular imprinting affords molecular recognition ability, it does not automatically lead to the catalytic ability of the resulting MIP ⁶⁸. Therefore, research has primarily focused on understanding the underlying mechanism in enzyme catalysis to achieve selective catalytic activity. Selective catalysis requires a specified arrangement of functional groups around the template to yield suitable binding sites complementary to the substrate's chemical structure. A successful example of substrate binding provides the hydrolysis of L-phenylalaninamide by chymotrypsin enzymes ¹³⁴⁻¹³⁶. Such binding of the substrate and enzyme induces significant changes in the three-dimensional orientation of the amino acid residues and the peptide chain present in the active sites. When the **FMs** are correctly oriented around the substrate, catalysis in such a cavity results in a firmly bound reaction's transition state as the active sites more precisely accommodate this state. This preferential binding of the transition state in the cavities lowers the reaction activation energy, thereby increasing the reaction rate and demonstrating high catalytic ability. Therefore, the active sites' shape and the functional groups' arrangement in the MIP cavities should complement the transition state's chemical structure. The transition state should precisely fit the MIP cavity to yield a catalytic ability similar to enzymes. MIPs have been used as catalytic microreactors to obtain regioselectivity and stereoselectivity ⁵³. In that case, the MIP is imprinted with one of the

products of the reaction. The similarity between the product and the imprinted site decreases the free energy change accompanying that reaction pathway, resulting in the desired product formation. Enantioselective C–C bond formation inside a chiral cavity using optically active amino acids¹³⁷ and regioselective 1,3-dipolar cycloaddition¹³⁸ has been achieved using the product templating approach. Imprinting the intermediate transition state may also yield enzyme-like properties, decreasing the reaction activation energy¹³⁹. However, as the transition states of a reaction are usually unstable, stable template analogs have been explored for catalytic applications of MIPs. Selective MIP catalysts with transition state analog imprinting have been developed for the ester and carbonates hydrolysis and several other synthetic transformations¹⁴⁰⁻¹⁴¹.

One of the earliest works on catalytic carbon-carbon bond formation using the MIPs reports cobalt(II) containing artificial class II aldolase MIP particles, successfully applied for aldol condensation of benzaldehyde and acetophenone to produce chalcone with an eight times higher product formation under harsh conditions using dimethyl fluoride at 100 °C for several weeks (Scheme 1.9)¹⁴².



Scheme 1.9. (A) Aldol condensation of acetophenone (2) with benzaldehyde (3) to produce chalcone (4) and the reactive intermediate analog dibenzoyl methane (1) used for MIP preparation. (B) MIP-mediated catalytic aldol condensation of acetophenone (2) and benzaldehyde (3) to produce chalcone (4)¹⁴².

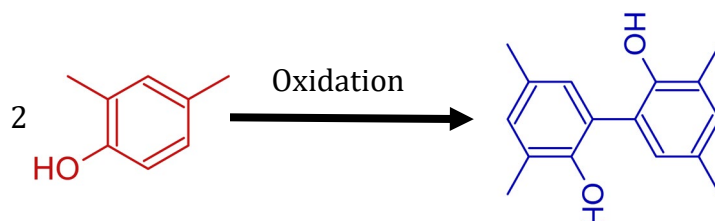
Enantioselective MIPs mimicking class II aldolase for the catalysis of C–C bond formation resulted in a 55-fold enhancement in the reaction rate of camphor with benzaldehyde than the homogeneous uncatalyzed reaction ¹⁴³. Catechol imprinted catalysts derived from palladium (II)–phosphine complexes exhibited performance superior to those prepared using conventional polymeric ligands owing to their semi-rigid ligand geometry in the carbon-carbon coupling reaction ¹⁴⁴. After several catalytic cycles, the imprinted metalloenzyme effectively retained the palladium and catalyst efficiency. Moreover, a polymer imprinted with a palladium complex functionalized with a crown ether receptor near the metallic site has been successfully used to enhance the catalytic activity of the reactive site in the Suzuki coupling reaction ¹⁴⁵. Defined imprinting assemblies lead to higher synergism between the recognition unit and the metal. A recent account of imprinted catalysts for coupling reactions reports high selectivity towards the C–C bond formation in the Suzuki cross-coupling reaction. However, the product yield significantly varied based on the substrate steric volume and shape ¹⁴⁶. Notably, metal-free shape-selective catalyst materials have not been widely studied for catalytic C–C bond formation using MIPs.

Organic MIP catalysts are mostly insoluble. Therefore, they can be filtered off after a reaction and placed in a flow reactor. However, the MIP catalysts prepared so far largely depend on understanding enzyme catalysis ^{62,147}. There are several demerits in this technology, one of which is selectivity. The MIPs cannot outperform even catalytic antibodies, let alone enzymes. The lack of a generic protocol for preparing MIP catalysts has resulted in limited growth in this field. Ergo, significant strides are required to advance the MIP catalyst technology to a practically viable scale. A strong focus on improving the stability and selectivity of the imprinted catalysts is essential to create possibilities for practical applications of these enzyme mimics.

1.3.7 Biphenols as candidates for selective electrosynthesis using molecularly imprinted polymers (MIPs)

The 2,2'-biphenols are widespread structural motifs in natural products and pharmaceutical compounds ¹⁴⁸⁻¹⁴⁹. They also form the backbones of some highly potent ligand systems in transition metal-based catalysis ¹⁵⁰⁻¹⁵³. A particularly representative compound of this group is the **TMBh**. Some examples of applying the 2,2'-biphenol motifs used as ligand backbones include phosphite or phosphoramidite ligands containing copper ¹⁵⁴ or rhodium ¹⁵⁵ that catalyze the asymmetric addition of alkyl radicals resulting in the formation of double bonds. Moreover, these motifs are found in the ligands containing palladium applied for catalyzing the Heck

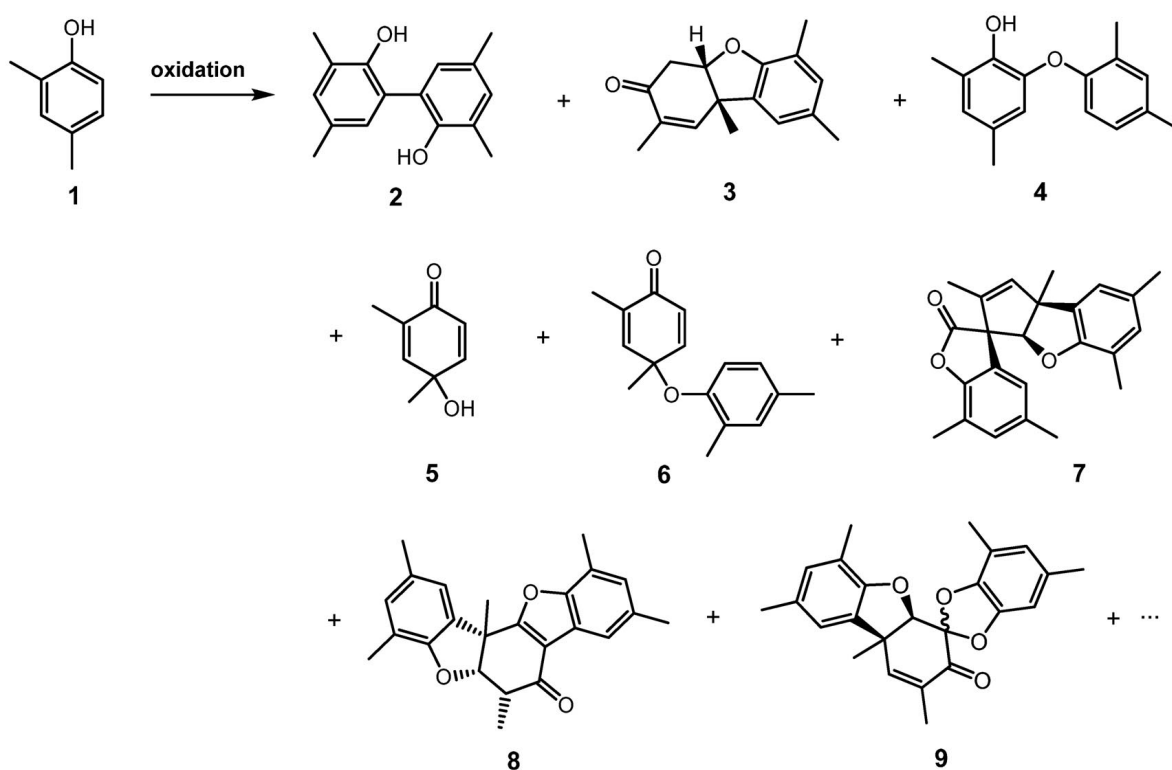
alkylation¹⁵⁶ and the allylic alkylation¹⁵⁷. **TMBh** is a significant ligand building block for the catalysts used in hydroformylation¹⁵⁸⁻¹⁵⁹, one of the largest fields in homogeneous industrial catalysis. Therefore, **TMBh** can be considered a crucial chemical for industrial catalysis. **TMBh** is primarily synthesized through the oxidative homocoupling of **DMPH** (Scheme 1.10). Conventionally, chemical methods using stoichiometric or over-stoichiometric amounts of oxidants are applied for this homocoupling¹⁶⁰⁻¹⁶¹. Several transition metal catalysts, including cobalt, iron, rhodium, and ruthenium, have also been tested¹⁶²⁻¹⁶⁴. However, the yield and selectivity of these methods toward **TMBh** are low, extensive preparation methods are applied, and they also produce large quantities of waste. Moreover, the catalysts or oxidants used for this homocoupling are generally expensive and toxic. Therefore, the conventional chemical methods developed for **TMBh** synthesis are inefficient and require hazardous chemicals. Hence, developing alternative synthesis routes for the oxidative homocoupling reaction is crucial.



Scheme 1.10. A general oxidation route of **DMPH** homocoupling leading to **TMBh**.

Electrosynthesis can be a prospective alternative pathway of **TMBh** synthesis, as it well aligns with the green chemistry strategy¹⁶⁵. As electric current activates electrosynthesis, toxic oxidants and catalysts are not required, and consequently, waste generation can be minimized. Moreover, electrosynthesis is considered more atom-economical as the number of synthetic steps is decreased³². The electrochemical reactions often occur under mild conditions, and there is a possibility to stop the reaction by simply switching off the power supply in case of an emergency. Furthermore, renewable sources can be used to run electrochemical processes, which can make electrosynthesis eco-friendlier. All these advantages make electrochemistry an attractive, sustainable alternative for organic chemical syntheses¹⁶⁶. Nilsson et al. in 1973¹⁶⁷, first proposed the **TMBh** electrosynthesis by direct electro-oxidative homocoupling of **DMPH**, wherein a lead oxide anode and aqueous sulfuric acid solution were used to reach a yield of ~30%. Electrosynthetic homocoupling of **DMPH** was much advanced in the past few decades, particularly by the Waldvogel group¹⁶⁸⁻¹⁷⁰. **DMPH** is prone to side reactions that yield structurally diverse polycyclic products under most conditions (Scheme 1.11)¹⁷¹.

Moreover, the phenols' oxidation leads to over-oxidation as the reaction products undergo further oxidation resulting in electrode passivation³². A boron-templated anodic process was developed, resulting in a high yield of **TMBh** even in a large-scale synthesis¹⁷². This process, however, was multi-step, generating wastewater containing borate. Several other approaches of direct **TMBh** electrosynthesis with moderate yields have also been reported¹⁷³⁻¹⁷⁴. The **TMBh** yield was increased up to 60% using a graphite anode and a 1,1,1,3,3,3-hexafluoropropan-2-ol-based solution. The increase in the local concentration of the substrate at the electrode surface facilitated electron transfer from the substrate to the electrode, thereby increasing the process efficiency¹⁷⁵.



Scheme 1.11. Structural formulae of some possible products of the **DMPb** anodic oxidation occurring under different synthesis conditions. **1** - **DMPb**, **2** - **TMBh**, **3** - Pummerer's ketone, **4** - phenolic ethers, **5** - quinols, **6** - quinol ethers, **7-9** - polycyclic structures¹⁷¹.

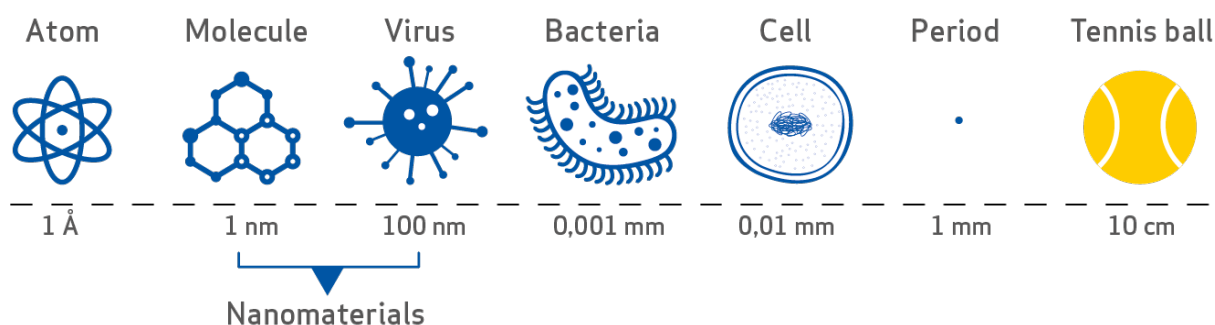
Furthermore, the solution's low viscosity positively affected mass transfer during the electrosynthesis resulting in a dynamic process¹⁷⁶. The main challenge in synthesizing **TMBh** is side reactions producing several side products, depending on the reaction conditions. The **TMBh** overoxidation also leads to the formation of oligomers and polymers¹⁷¹. Moreover, it is crucial to establish large-scale setups for **TMBh** synthesis for industrial applicability. Therefore, it is essential to advance the **TMBh** synthesis method further to yield the desired

product selectively without using toxic solvents, excess electrolytes, or additional chemicals. Ergo, developing a MIP-based catalyst for greener electrosynthesis could be a prospective route for oxidative homocoupling reactions.

1.4 Green nanomaterials for catalysis

Green nanochemistry has become popular in the past decades. It refers to both green syntheses of nanocatalysts and applying nanomaterials as green catalysts enabling eco-friendlier conditions of catalysis of industrially important reactions¹⁷⁷. Green synthesis of nanocatalysts involves the preparation of nanocatalysts under green conditions like low synthesis temperature, green solvents, and natural reducing/capping agents. Alternatively, green nanocatalysis involves performing the catalytic reaction in green solvents, preferably using green synthesized nanocatalysts. We will now explore these nanomaterials and their synthesis and catalytic applications.

1.4.1 What are nanomaterials?



Scheme 1.12. A brief outlook of the nanoscale¹⁷⁸.

Nanoscience involves the study of structures with at least one dimension in the nanometer (nm) range that is a billionth of a meter (1 nanometer is 10^{-9} meter) (Scheme 1.12). Although the "nanotechnology" and "nanoscience" terms have gained popularity in the past decades, nanostructures have been known for a long time¹⁷⁹. In 1959, Richard Feynman brought the concept of nanotechnology into the limelight in his lecture, wherein he is quoted saying, "There's plenty of room at the bottom"¹⁸⁰. After that, research on miniaturization opened a new area and has found numerous applications in every field of science and technology. Miniaturization of materials has increased their surface-to-volume ratio, transforming their chemical and physical properties enormously¹⁸¹, yielding higher reactivity and efficiency of

nanomaterials than their bulk counterparts. Nanomaterials' properties are size-dependent. Hence, these properties can be tuned depending on the requirements. Nanotechnology has made great strides in disease-targeting fluorescent labels, high-resolution displays, optoelectronic devices, sensors, and solar cells ¹⁸². Nanostructured materials have also been promising candidates in catalysis ³⁵, cosmetics ¹⁸³, medicine ¹⁸⁴, and photonics ¹⁸⁵. Metal-based NPs of different sizes have been fabricated using biological and chemical methods depending on the application.

1.4.2 Synthetic approaches to nanomaterials

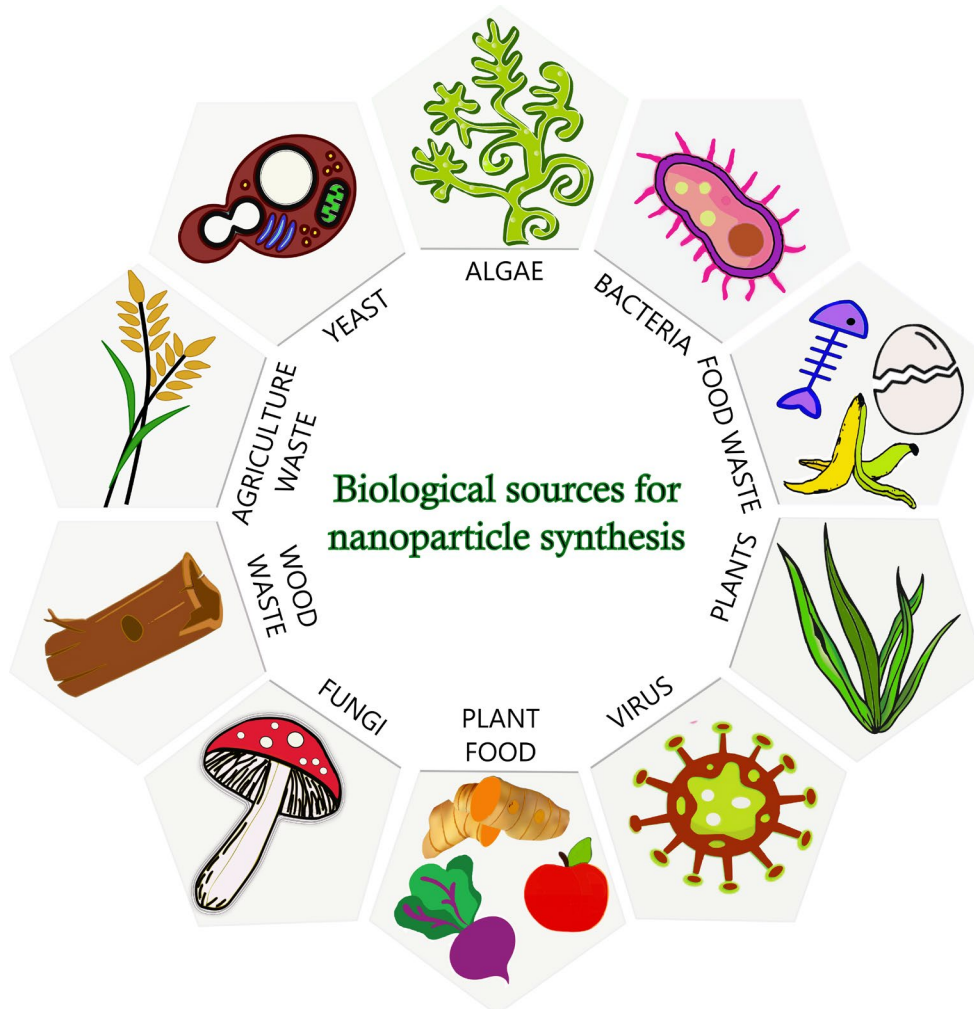
Nanomaterial synthesis is generally classified into two categories, namely, top-down and bottom-up. Nanoscale structures are engraved onto a substrate in a top-down approach using electron beams followed by etching and deposition ¹⁸⁶. Physical methods like evaporation-condensation and laser ablation are also commonly used top-down approaches. The evaporation-condensation method involving evaporating the bulk source metals in an inert environment and then cooling the evaporated vapor rapidly using a steep temperature gradient near the heater surface yielded high concentrations of stable NPs ¹⁸⁷. Laser ablation involves striking a metallic source kept in a solution using a laser to prepare structures like silver nanospheroids ¹⁸⁸. The inability to accurately control the surface structure in a top-down approach adversely affects metallic NPs' physical properties and surface chemistry because their high aspect ratio cannot be properly maintained.

Nanomaterial components are formed using their precursors' building blocks by chemical or physical methods in the bottom-up approach ¹⁸⁹. Chemical reduction using organic and inorganic reducing agents is more extensively developed because of its ease of preparation. Reducing agents, including elemental hydrogen, sodium borohydride (NaBH₄), and sodium citrate, have been applied for reducing metal ions in solutions, followed by aggregation of metallic colloidal particles ¹⁹⁰. In this chemical approach, stabilizers, like surfactants and polymers with acid, alcohol, amine, and thiol functional groups, have to be used to terminate the NPs' agglomeration and protect their surface properties.

1.4.3 Green synthesis of nanomaterials

The green route for synthesizing NPs is a bottom-up approach that has gained attention in the past decade as a sustainable alternative. This method can minimize the use of hazardous chemicals and solvents, lower energy inputs, and lower the amount of waste produced ¹⁹¹.

When biological sources are used to synthesize nanomaterials, the approach is termed green synthesis ¹⁹². The biological sources that are interesting for green synthesis applications include microbes (like algae, bacteria, or fungi), plant extracts, food, agriculture, and wood industry wastes (Scheme 1.13) ¹⁹³. These biological sources contain chemicals like amino acids, carbohydrates, flavonoids, polyphenols, and proteins or enzymes that can effectively reduce metal ions and stabilize the NPs ^{192, 194}. However, this method often leads to non-uniform distribution of particles and nanocomposites, which require additional agents to improve the materials' uniformity.



Scheme 1.13. Biological substrates utilized for nanomaterial syntheses.

Several metal-based NPs, including Ag, Au, Cu, Fe, and Zn NPs, have been prepared using wastes ^{193, 195}. Platinum and palladium NPs have been synthesized using lignin, banana peel, tea, and coffee extracts ¹⁹⁶. NPs of metal oxides, such as copper oxide synthesized using brown alga extract, have also been reported ¹⁹⁷. Banana peel extract constituents like cellulose,

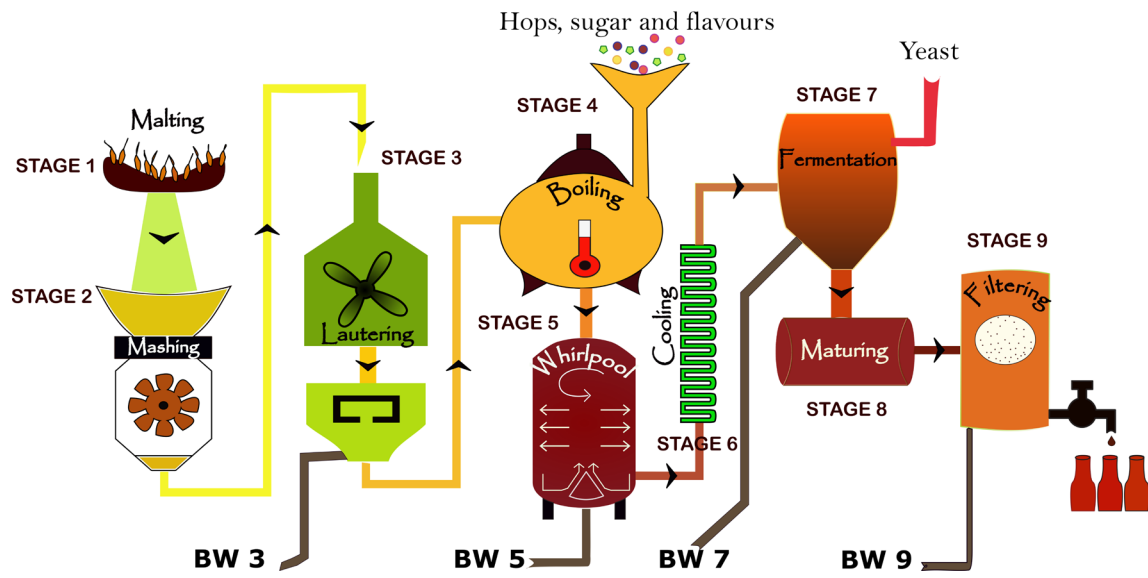
hemicellulose, lignin, and pectin synthesized and stabilized Mn₃O₄ NPs with super-capacitive properties¹⁹⁸. Polyphenols in the *Terminalia arjuna* fruit¹⁹⁹ and *S*-allyl-cysteine in the *Allium sativum* extract²⁰⁰ were responsible for tuning the size of gold NPs. The size and shape of the Ag NPs prepared using a seed extract of cashew apple fruit were tuned using a temperature-dependent method. The chicken eggshell membrane contains glycoproteins like collagen and amino acids like alanine, glycine, and uronic acid that are effective NP synthesis agents²⁰¹. Another interesting example is the synthesis of Ag NPs using the peel of the tropical fruit *Annona squamosa*, commonly called custard apple, in which the water-soluble ketone and hydroxyl groups were proposed to be involved in the reduction and stabilization of the NPs²⁰²⁻²⁰³. Grape stalk waste extract has been used to produce Ag NPs with application in screen-printed electrode²⁰⁴. The silver ions reduction to obtain Ag NPs has been explored using wastes such as orange peel, mango peel, and pineapple extract¹⁹⁶. Furthermore, tansy fruit extracts have been used to produce gold and silver nanospheres²⁰⁵. The orange peel aqueous extract of *Citrus Clementina* was successfully used in the one-pot green synthesis of stable, highly antimicrobial, and anti-cancerous Ag NPs¹⁹⁵. Moreover, chicken feathers, cotton fibers, milk, rice bran, and watermelon rind are efficient chemical sources of metal NP synthesis²⁰⁶. Green synthesis is an easier method to obtain bioactive and eco-friendly NPs.

1.4.4 Brewery wastes as prospective precursors for green synthesis of silver-containing nanomaterials

Globally, the brewing industry is a significant source of waste effluents. This waste management is increasingly problematic because of the increased annual production rate²⁰⁷. Brewery industry wastes have not been widely explored as materials for synthesis and particularly not in terms of NP synthesis. However, brewery waste analysis has been performed to determine its constituents. Amino acids, phosphates, polyphenols, proteins, and sugars have been determined and quantified²⁰⁸. Brewery waste remediation and valorization research have shown potential in different application fields. Brewery waste has been used as the carbon source for the *Bacillus subtilis* N3-1P bacterium to synthesize biosurfactants²⁰⁹. Brewery waste has been extracted to obtain bioactive compounds in food, pharmaceutical, agricultural, cosmetic, and chemical industries²¹⁰⁻²¹¹. Nevertheless, there is still much potential in brewery waste valorization.

The malt beer is produced in a 10-step process, leading to brewery wastes at various production stages (Scheme 1.14)²¹². Malt is a sprouted and dried cereal grain, in this case, barley. Malting comes down to steeping the cleaned grain and maintaining its moisture for a

sufficiently long time. Steeping, which lasts from three to four days, aims to wake the embryos from sleep and initiate germination. This process is accompanied by the secretion of enzymes in the grain that break down excess protein and sugars. Amylase helps break down barley starch into simple sugars and disaccharides (primarily maltose). Breaking down as many spare materials into simple sugars and amino acids in malting is vital. The malt is then milled, mixed with water, and mashed to dissolve the starch and protein, releasing sugar and tannin.



Scheme 1.14. Schematic of the brewing process indicating the nine stages and the wastes produced during those stages.

The sweet malt extract, wort, is separated from the solid substances called Brewer's spent grains (BSG) at the third stage and is the first type of waste, **BW3**. In the following stage, the wort is boiled after adding the bitter, aromatic hops and sometimes sugar. The tannin and part of proteins are separated during boiling. The wort is clarified in a whirlpool, tapping out the clear wort. The undissolved hop particles and proteins are collected at the whirlpool center, forming the second type of waste, **BW5**, called wort precipitate. The clear wort is then cooled and fermented by adding yeast. Absorbed nutrients not used by the embryo are the substrate of the alcoholic fermentation carried out by yeast in the brewery while brewing beer. The yeast filtered out after fermentation, called Brewer's spent yeast (BSY), at the seventh stage forms the third type of waste, **BW7**. After maturing, the fermented beer is filtered using diatomaceous earth before going into the production line and yielding the final product, beer. The waste, including diatomaceous earth, separated at this ninth stage, forms the fourth type of waste, **BW9**.

Roughly 15% of the hops constituents are retrieved in the beer, and the rest (85%) becomes spent hop material (BW5)²¹³. The BW5 waste obtained after the wort boiling includes majorly insoluble hop materials, condensation products of hop polyphenols, wort proteins, and isomerized hop acids adsorbed on the solid surface²¹⁴⁻²¹⁵. The spent hops cannot be used as feed supplements as they contain 2-methyl-3-buten-2-ol, the product of bitter acid degradation with hypnotic–sedative properties. Therefore, spent hops have been used as fertilizers and soil conditioners, as their nitrogen content is high. Moreover, spent hops are mixed with spent grain and used as animal fodder²¹³. However, several valuable compounds can be recovered from spent hops, such as flavors, saccharides, and organic hop acids.

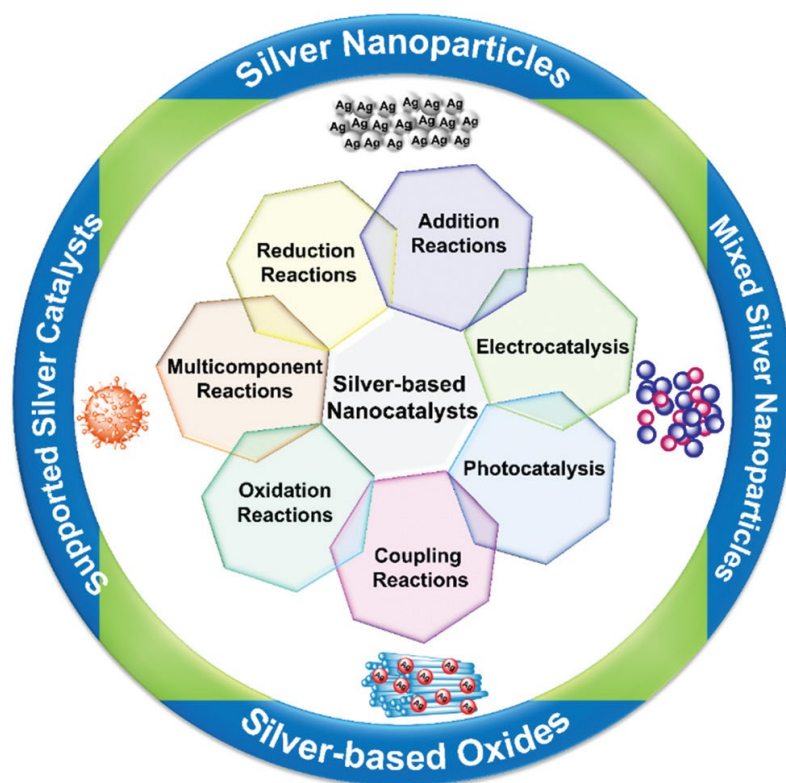
BSY (BW7) is the second major by-product of the brewing industry that has a significant environmental impact as this waste contains a large amount of biomass (1 hl of beer generates ~2 – 4 kg of BSY)²¹⁶ and water, which makes their management quite difficult for the brewing industry. The BW7 waste is rich in carbohydrates, proteins, amino acids, ash, and vitamins. BSY is also rich in minerals such as calcium, chromium, copper, iron, magnesium, manganese, phosphorus, potassium, selenium, and zinc²¹³. Yeast's mineral content is approximately 5–10% of the cell dry weight²¹⁴. Therefore, these brewery industry wastes are rich sources of several essential compounds that can be recycled efficiently for various applications. However, they are usually mixed with spent grains and supplied as animal fodder or used for laboratory alcohol synthesis.

The third by-product, BW9, has not previously been explored in the literature as it is a filtration waste; therefore, its recycling potential is unknown. Presumably, this waste contains similar compounds as BW7 and the product beer as it is the brewing process's final stage waste. The diatomaceous earth used for filtration can also be expected in this BW9 waste. BW9 contains ~8 tons of dense sludge, including the diatomaceous earth and sediments, and ~40 - 56 tons of wastewater are generated monthly in the medium-sized brewing industry. The sludge is recycled as soil fertilizers, but a huge amount of wastewater is discarded into sewage. Although a limited number of recent research has reported the synthesis of Ag NPs using beer yeast²¹⁷, the unprocessed brewery wastes still have remained unexplored in recycling applications despite being so rich in several valuable compounds.

1.4.5 Silver-containing nanomaterials for catalytic application

Advantageously, nanomaterials have large surface areas. Therefore, nano-sized catalysts are popular because the elevated surface area significantly increases the number of available active

sites for the catalytic activity compared to bulk catalysts, thereby increasing the catalysis efficiency and yield ²¹⁸. Moreover, these catalysts are generally insoluble, facilitating easy separation and reuse of catalysts. As seen in Section 1.4.3, these nanomaterials can be prepared by cost-effective methods that are easily scalable.



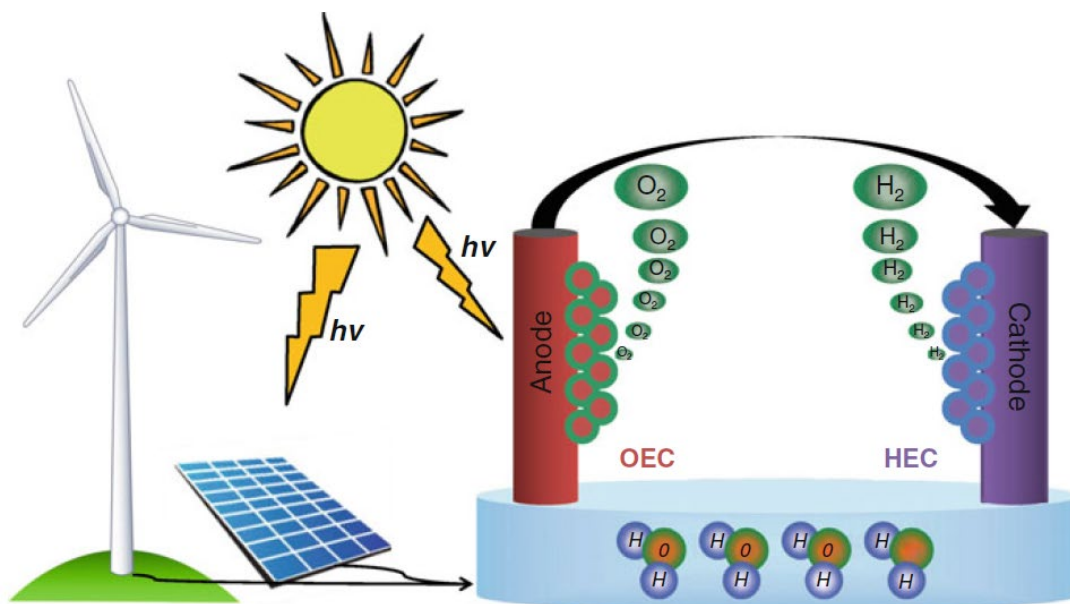
Scheme 1.15. Different types of silver nanomaterials and their potential applications in catalysis ²¹⁸.

In the case of Ag-based nanomaterials, their chemical, electric, and optical properties are size- and shape-dependent. Therefore, research has focused on altering their structure to suit the application. Several catalytic applications such as CO₂RR ²¹⁹⁻²²¹, electrocatalysis ²²²⁻²²⁵, HER ²²⁶⁻²²⁷, OER ²²⁸⁻²²⁹, organic pollutants degradation ²³⁰⁻²³⁵, and ORR ²³⁶⁻²³⁷ have successfully used Ag-based nanomaterials including silver metal, silver oxides, silver halides, multi-metallic composites, and supported silver materials (Scheme 1.15). Mainly, nanosilver is interesting for catalytic applications because of its unique electronic and optical properties ²³⁸⁻²³⁹. Therefore, it has found application in several organic transformations for synthesizing fine chemicals ²⁴⁰. Silver (Ag) NPs have been widely studied for reducing functional molecules like carbonyl compounds and nitroaromatics ²⁴⁰⁻²⁴¹. Several powerful heterogeneous catalysts made of nanosilver have been applied to oxidize alcohols, silanes, and related oxidative

transformations ²⁴⁰. Silver has been used for centuries for its outstanding properties, including antimicrobial activity and environmental friendliness ²⁴². Moreover, Ag is attractive for heterogeneous industrial catalysis as it is relatively cheaper than highly catalytic metals like gold (Au), platinum (Pt), and palladium (Pd). The current project was focused on OER and ORR by silver composite nanomaterials. Therefore, these two reactions have been discussed further in detail.

1.4.5.a Oxygen evolution reaction (OER)

Progress in renewable energy storage systems is a significant step toward the practical utilization of sustainable energies, including solar and wind. Therefore, processes such as water electrolysis for hydrogen production are crucial for successfully developing these energy storage technologies. The origin of the electrochemical splitting of water can be traced back to the 19th century, wherein it was discovered that water could be decomposed into hydrogen and oxygen using electricity ²⁴³. However, the OER which occurs at the anode is still an enigmatic topic. There are challenges in developing the ideal highly active and stable yet inexpensive catalyst ²⁴⁴. Understanding the electrochemical mechanism is the key to developing efficient catalysts.



Scheme 1.16. Pictorial drawing of water electrolysis represented by using electricity from renewable sources like wind and solar or photoelectrolysis. OEC- oxygen evolution catalyst, HEC- hydrogen evolution catalyst ²⁴⁵.

The overall water splitting process involves the formation of molecular hydrogen and oxygen at the cathode and anode, respectively. Various energy sources can be used for this

water-splitting reaction, making it highly attractive for energy conversion technology (Scheme 1.16). The electrochemical water splitting devices, called water electrolyzers, can be coupled with wind turbines or photovoltaics in renewable energy grids, in which the electrolyzer can act as a local storage system ²⁴⁶⁻²⁴⁷. Alternatively, solar energy can be harvested through light-driven water splitting wherein semiconductors incorporated as electrode materials harvest the solar energy directly ²⁴⁸. However, regardless of the application, these technologies' viability depends on oxygen's electrochemistry, as hydrogen production is sustainable. Molecular oxygen generation at the anode is very energy-intensive ²⁴⁹.

The conventional OER and HER mechanisms in alkaline solution are described as follows.



The OER and HER mechanisms in acidic solution are described as follows.

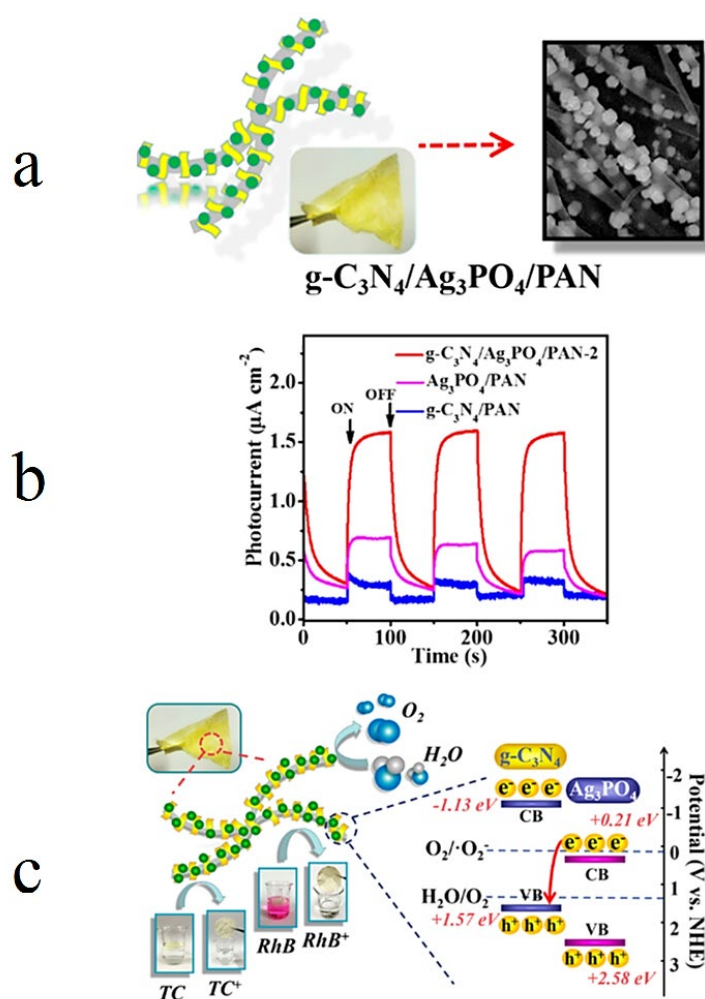


E_{anode} - equilibrium potential for the OER, E_{cathode} - equilibrium potential for the HER, RHE - reversible hydrogen electrode.

The HER occurs at potentials comparable to the equilibrium potential, but the OER requires a significant overpotential. Therefore, no electrolysis device has been able to approach the minimum operating voltage of 1.23 V vs. RHE ²⁵⁰. Moreover, the slow OER kinetics adversely affects the photoelectrolysis devices. In light-driven water splitting, the semiconductor band-gap must be sufficiently large to overcome the OER overpotential for obtaining reasonable efficiencies ²⁵¹. Therefore, over the past decades, devising the oxygen-evolution anode materials has focused on efficient OER ²⁴⁹ with the lowest possible overpotentials. Pure metal catalysts suffer from instabilities and oxide formations on surfaces ²⁵²⁻²⁵³. Metal oxides have evolved as popular OER catalysts as they are quite stable under the oxygen evolution conditions ²⁵⁴⁻²⁵⁵. The RuO₂- and IrO₂-based anodes reveal the lowest OER overpotentials at reasonable current densities. However, these materials are not abundant and consequently quite expensive, which limits their commercialization ²⁵⁴. Therefore, various transition metal oxides are studied as their corrosion resistance in alkaline media is long, and these oxides are relatively less expensive ²⁵⁶. The metal oxide composition and surface morphology significantly influence their catalytic activities. Moreover, several OER

mechanisms at metal catalytic sites have been proposed yet the process has to be fully understood. Therefore, there is still much scope for developing the OER process.

Ag_3PO_4 exhibits a bandgap of about 2.43 eV, and the valence band maximum of this compound is ~ 2.67 V vs. standard hydrogen electrode (SHE), which is more positive than that of the $\text{O}_2/\text{H}_2\text{O}$ couple (~ 1.23 V vs. SHE)²⁵⁷. Therefore, the Ag_3PO_4 energy band structure is favorable for photocatalytic OER. However, charge recombination and photocorrosion of Ag_3PO_4 have been a significant challenge, and composite structures of Ag_3PO_4 have been researched to overcome this corrosion problem and mediate charge transfer efficiently²⁵⁸⁻²⁵⁹.



Scheme 1.17. (a) Structure of the $\text{g-C}_3\text{N}_4/\text{Ag}_3\text{PO}_4/\text{polyacrylonitrile}$ composite, (b) photocurrents for OER, and (c) photocatalytic mechanism for $\text{g-C}_3\text{N}_4/\text{Ag}_3\text{PO}_4/\text{polyacrylonitrile}$ ²⁶⁰.

Several interesting composite structures with Ag_3PO_4 exhibiting high photocatalytic activity have been reported, including $\text{MoS}_2/\text{Ag dots}/\text{Ag}_3\text{PO}_4$ ²²⁸, graphene-supported $\text{Ag}_3\text{PO}_4/\text{Ag}/\text{AgBr}$ ²⁶¹, and $\text{g-C}_3\text{N}_4/\text{Ag}_3\text{PO}_4/\text{polyacrylonitrile}$ (Scheme 1.17)²⁶⁰. Hence, a

composite structure containing different silver forms could be interesting for catalytic applications by overcoming these challenges of Ag₃PO₄.

1.4.5.b Oxygen reduction reaction (ORR)

The ORR is one of the most crucial reactions in life processes, like biological respiration, and in energy conversion systems, like fuel cells ²⁶². In an aqueous solution, the ORR mainly occurs via two routes. One involves a direct 4-electron reduction pathway from oxygen (O₂) directly to water (H₂O), and the other is a 2-electron reduction pathway from O₂ via the hydrogen peroxide (H₂O₂) intermediate and then to water. Alkaline and aprotic solvent solutions can also give rise to the one-electron reduction pathway from O₂ to superoxide (O₂⁻) ²⁶³⁻²⁶⁴. The electrochemical ORR mechanism is very complex. It involves several intermediates formed, depending on the catalyst, electrode material, and electrolyte nature.

The following reaction equations describe the direct four-electron pathway.



The following reaction equations present the two-electron pathway with an intermediate formation.



The unstable peroxide formed in acidic media is either reduced to water or disproportionates to water and oxygen.



The ORR is the slowest reaction in fuel cell operations because the bond energy of the oxygen molecule is very high ²⁶⁵. Therefore, a higher current density is required to overcome the activation barrier at the cathode. As the entropy change accompanying the O₂ molecule dissociation ($\Delta S_{\text{reaction}}$) is positive due to the increased randomness of this system, the dissociation should be more favorable according to the Gibbs free energy change equation.

$$\Delta G_{\text{reaction}} = \Delta H_{\text{reaction}} - T_s \Delta S_{\text{reaction}} \quad \text{Equation 1.12}$$

wherein $\Delta G_{\text{reaction}}$ is the Gibbs free energy change of the reaction that is a measure of the spontaneity of the reaction, $\Delta H_{\text{reaction}}$ is the enthalpy change, and T_s is the system temperature.

However, the overall $\Delta S_{\text{reaction}}$ of the reaction is negative as the reactant oxygen molecule is in gaseous form, and the reaction results in the formation of the H₂O molecules in the liquid state. Therefore, increasing the temperature will only decrease the efficiency of the overall reaction. Ergo, at room temperature, the cathode potential can be lowered, or an electrocatalyst can be used to lower the activation energy barrier of the ORR²⁶⁶. Several mechanisms can govern the electrocatalytic ORR. Below, two major mechanisms are outlined. The complete reduction can occur on the catalyst surface without intermediates desorbing from the surface²⁶⁷.



The ads subscript indicates that the species is adsorbed on the catalyst surface and the sol subscript indicates that the species is in the solution.

The electron acceptance can also occur in two distinct steps wherein H₂O₂ is the intermediate formed. This reaction route is called the peroxide pathway^{265, 267}. The peroxide is either desorbed into the solution or is further reduced to water.

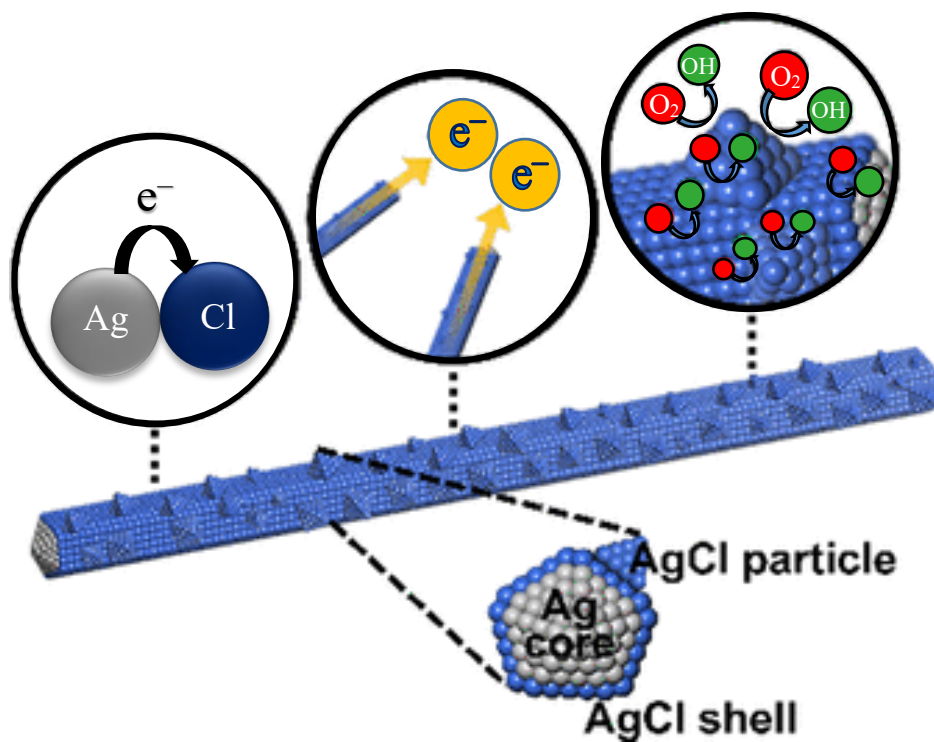


As catalyzed ORR is a multi-step reaction, the rate-determining step plays a significant role in determining the reaction efficiency. According to the Sabatier principle²⁶⁸, the interactions between the catalyst and substrate significantly determine the reaction flow. If the interactions are too strong, dissociating the substrate, intermediates, and products from the catalyst surface is very slow, thus limiting the catalyst availability for the reaction. Conversely, if the interactions are too weak, no bond will be formed between the catalyst and the substrate, and consequently, no reaction will occur. Therefore, the choice of the catalyst is very significant.

Very large overpotentials must be applied in both directions to oxidize H₂O to O₂ and reduce O₂ to H₂O²⁶⁸. Optimal catalysis of the ORR depends on the intermediate's compromise

in the adsorption energy. Therefore, no electrode catalyst can drive the ORR reaction reversibly at ambient conditions. The ORR catalysts should be highly catalytically active toward ORR, highly chemically and electrochemically stable, and reveal high electrical conductivity, insolubility in acidic and basic aqueous solutions or methanolic solutions, optimum structural composition and morphology, high specific surface area, high porosity, uniform distribution of catalyst particles over the support and strong interaction between the catalyst and support which will affect the catalytic stability of the system²⁶⁹. In recent years, the preparation of various metal-based NPs for catalytic applications has gained much attention. Platinum has been the most common inert metal for cathodes and anodes in fuel cells as it exceptionally well adsorbs and aids the dissociation of gasses²⁷⁰. Platinum is one of the best ORR catalysts. However, platinum is rare and, hence, costly. Moreover, its methanol tolerance is low, and it suffers from carbon monoxide poisoning²⁷¹. Therefore, research has been focused on finding alternative materials for ORR. Although several successful alternatives for anodes have been developed for commercial applications, commercially viable alternative material design for the cathode is still a challenge as still considerable improvements are required.

The Ag nanomaterials are popular electrocatalysts for ORR in fuel cells as they are thermodynamically and electrochemically stable even in strong acid solutions and are appreciably catalytically active toward ORR in alkaline media²³⁷. The Ag nanoalloys with Au, cobalt (Co), copper (Cu), and Pd have been demonstrated to enhance the catalytic performance of Ag for obtaining a highly efficient four-electron pathway of ORR²⁷². Moreover, silver compounds, including silver chloride (AgCl) and silver orthophosphate (Ag₃PO₄), are catalytically active toward ORR in composite structures²⁷³. AgCl effectively catalyzes the ORR photocatalytically and electrocatalytically, but its electrical conductivity is low²⁷⁴⁻²⁷⁵. Therefore, a composite Ag structure could be beneficial for ORR, as shown in the research on AgCl-Ag@AgCl nanowires, containing a structure that reveals appreciable electrical conductivity because of the Ag core and high ORR catalytic activity because of AgCl (Scheme 1.18)²⁷⁴.



Scheme 1.18. Structure and catalytic activity mechanism of AgCl-Ag@AgCl nanowires (adapted from ²⁷⁴).

1.5 Thesis aims and scope

The project goal was to enable greener routes in catalysis. For this, MIPs were prepared electrochemically using conducting organic polymers. The electro-oxidation of **DMPH** was chosen as the model reaction candidate to test the efficiency of MIPs in comparison with NIP-coated and bare electrodes for the selective electrosynthesis of **TMBh**. Electrosynthesis is a relatively greener process that was used for the preparation of MIPs via electro-oxidation. Therefore, we aimed to develop greener catalysts that mimic the shape-selective catalytic activity of enzymes to catalyze the C–C coupling reaction selectively. Furthermore, valorizing the brewing industry wastes developed a greener method for catalytic Ag NPs synthesis. These nanomaterials were characterized for applications in catalysis.

The experimental section in **Chapter 2** describes the experimental procedure of the project in two sub-parts. The first includes the theoretical background of major techniques and instruments used in this project. The second part reports on the chemicals, synthesis, and characterization techniques applied to develop and apply the catalytic materials. Further, two chapters discuss the results obtained for MIPs and Ag nanomaterials verbosely. **Chapter 3** reports on the synthesis and characterization of MIP films and their application in selective electrosynthesis of the **TMBh** chemical compound. Moreover, this chapter unravels the aging mechanism of the pre-polymerization MIP solution and provides routes to control the aging process. **Chapter 4** focuses on the characterization of the biological precursor, brewery waste used for nanomaterial synthesis, and the preparation and extensive characterization of the nanocomposites. Subsequently, the nanomaterials have been characterized toward their possible application in catalysis. Finally, **Chapter 5** provides a grasp of the overall work and some of its future prospects.



2

Experimental techniques and methods

2.1 Theoretical background

This section gives a brief outlook of the theoretical basis of the techniques and methods used in this work.

2.1.1 Experimental techniques

2.1.1.a Theoretical simulations

Non-covalent interactions, including hydrogen bonds, ion-pair interactions, and London dispersion forces, are significant for molecules binding, thus yielding complexes with unique properties. Therefore, understanding and controlling these non-covalent interactions play a significant role in supramolecular chemistry involving host-guest interactions and molecular recognition in a defined environment²⁷⁶.

In computational chemistry, attempts are being made to solve the non-relativistic Schrödinger equation using relativistic corrections for atoms and nuclei in molecules. It should be possible to solve the time-dependent or time-independent form of the Schrödinger equation in principle for every system. But in practice, it is only possible for very small molecular systems²⁷⁷. Therefore, approximate methods have been extensively developed to optimize computational techniques that balance computational accuracy and costs. Ab-initio, semi-empirical, and molecular mechanics (MM) are now superior computational techniques.

Ab-initio is a Latin word for "from scratch," which includes calculations of molecular structures using only the atomic numbers, physical constants, and the Schrödinger equation²⁷⁷. This computationally expensive technique based on quantum physics includes extensive approximations for calculating molecules' transition and excited states in small systems of a few tens of atoms. Semi-empirical techniques are also based on quantum physics and use experimental (empirical) data-based approximations as inputs for mathematical models²⁷⁸. These methods also apply several approximations but are less computationally demanding than ab-initio methods and, therefore, can be applied for a system with a few hundred atoms. Contrastingly, molecular mechanics is based on classical physics, which utilizes empirical or semi-empirical force fields to compute the behavior of atoms or molecules²⁷⁹. It is computationally least demanding and can be applied for very large systems of thousands of atoms; however, it cannot provide information on the electronic properties of the systems.

It has been demonstrated that a state's energy depends on electron density distribution. The information about the correlation of electron movement can be derived from the electron distribution. This proof gave rise to density functional methods, wherein only electron density was considered to determine the system's energy instead of electron movement, resulting in lower computing requirements^{277,279}. Hohenberg and Kohn were the first to establish the exact energy functional of the electron density. Density functional theory (DFT) describes orbitals and electron states less accurately than an ab-initio method. Nevertheless, it is an exact theory based on the concept that calculates the total electronic energy of a system and all other components using electron density as the fundamental quantity being quite precise for most applications at a low computational cost. Subsequently, Kohn and Sham expanded the basis set to circumvent the difficulties in calculating the kinetic energy of the electrons as a function of electron density. Their KS-DFT framework described a fictitious system of noninteracting electrons with the same density as the real, interacting counterparts using orbitals²⁸⁰. All the differences between the two systems are combined into the unknown exchange-correlation (xc) functional. The KS-DFT is based on the mathematical object exact exchange-correlation functional returning a number (xc energy) when the electron density of the system [$\rho(r)$ three-dimensional function] is given as input²⁸⁰. The exact exchange enforces the Pauli principle, stating that two electrons with the same spin cannot occupy the same quantum state.

However, the primary issue is that the exact method of deriving energy of a system of electrons from their density distribution is unknown. Therefore, the functionals that split the system's energy into several parts were created. Some functionals, such as the electron-nucleus interaction energy, can precisely be defined. Disparately, some functionals, such as the energy

of electron-electron interaction, cannot be determined precisely. Therefore, local density approximation (LDA) using the functional for electron gas has been applied for approximating these functionals. However, the density functionals do not accurately predict the long-range dispersion interactions.

The hybrid B3LYP functional has been derived and applied to understand a broad range of systems in chemistry to study the structures and energies of interacting molecules²⁸¹. The B3LYP functional incorporates the exact exchange and generalized gradient approximation (GGA) of the electron gradient in the LDA electron-electron and electron-nuclei energy. B3 is Becke's three-parameter exchange-correlation functional. It uses three parameters to account for the exact Hartree-Fock exchange correlation, and LYP is the Lee, Yang, and Parr correlation functional that recovers DFT dynamic electron correlation. The B3LYP is popular as it was used in one of the first DFT methods, significantly improving the Hartree-Fock method. Moreover, the B3LYP is generally faster than most wave-function theory-based Post-Hartree-Fock methods yielding comparable results. Furthermore, it is quite robust for a DFT method. However, B3LYP can only capture short-range interactions as it fails to define long-range interactions accurately. The basis set is an approximate representation of the atomic orbitals (AOs). Numerous basis sets have been developed for various purposes, e.g., the split valence 6-31G(d) basis set. DFT has been a popular choice among chemists and physicists. It reasonably compromises the accuracy and computing costs, allowing the routine treatment of molecules containing several hundred atoms²⁸¹.

2.1.1.b Linear sweep voltammetry (LSV) and cyclic voltammetry (CV)

Cyclic voltammetry (CV) is one of the most widespread electroanalytical techniques for easy determination of the energy levels of the electroactive species, the thermodynamics of heterogeneous redox processes, and the electron-transfer reactions kinetics²⁸². In CV, the current response of a redox-active compound in solution is measured versus a linearly swept potential, cycled between set values. The potential is linearly scanned forward from E_1 to E_2 , then backward from E_2 to E_1 , yielding a potential triangular cycle (Figure 2.1a)²⁸². During this cycle, the electroactive compounds either lose an electron (oxidation) or gain an electron (reduction) depending on the potential ramping direction. In linear sweep voltammetry (LSV), the potential is scanned only from E_1 to E_2 ; no backward scan is performed (Figure 2.1a). The scan rate is the change in potential with time.

The current generated through electron transfer between the redox species and the electrode is passed through the solution primarily by diffusion of ions because ion migration is suppressed by excess supporting electrolyte added. That forms an electric double layer (EDL) at the electrode-solution interface. The EDL (Figure 2.1b) consists of ions and orientated solvent electric dipoles that counterbalance the charge on the electrode surface.

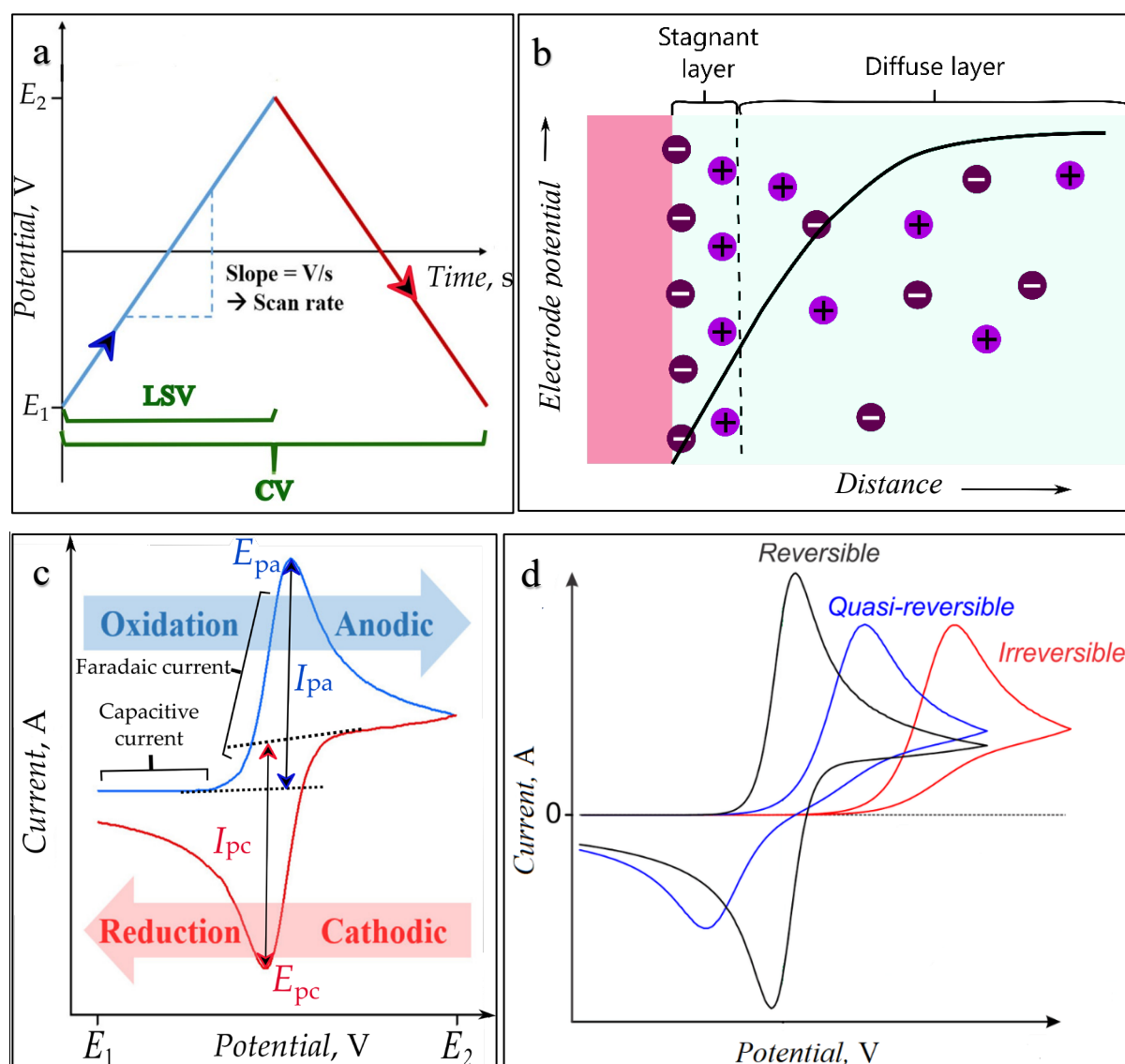


Figure 2.1. (a) The linear sweep voltammetry (LSV) and cyclic voltammetry (CV) potential waveforms obtained by switching the potential from the initial E_1 to the final E_2 value (adapted from ²⁸³), (b) schematic view of the electric double layer (EDL) at the electrode-solution interface, and (c) cyclic voltammogram. E_{pc} and E_{pa} - cathodic and anodic peak potential, respectively; I_{pc} and I_{pa} - cathodic and anodic peak current, respectively (adapted from ²⁸³). (d) Cyclic voltammograms for reversible, quasi-reversible, and irreversible electron transfers (adapted from ²⁸⁴).

A current measured against the potential scanned is the 'voltammogram.' The voltammogram is produced if a redox reaction occurs, as shown in Figure 2.1c for a CV reversible redox reaction. When the onset of oxidation is reached, the current exponentially increases as the electroactive species is oxidized at the working electrode surface. Then the anodic current reaches a maximum (I_{pa}) at the anodic peak potential (E_{pa}). For reversible processes, the current is limited by the rate of the mass transport of the electroactive species from the solution bulk to the electrode surface at all potentials. That is, this transport rate is lower than the charge transfer rate at all potentials. As the diffusion layer thickness increases with the scanning time, the current decreases proportionally to the reciprocal square root of time ($I_v \propto t^{-1/2}$) at potentials exceeding the E_{pa} value. Then a steady-state capacity background current is reached. Further potential increase beyond this point no longer affects the current. The electroactive species thus oxidized is reduced during the backward scan to negative potentials (reductive scan) until the cathodic (reduction) peak potential (E_{pc}) and the cathodic peak current (I_{pc}) is reached. For irreversible processes, the mass transport rate limits the current at potentials exceeding the peak potential²⁸⁵. Before the E_p is reached, the current is limited by the charge transfer rate for this process. The electrode process reversibility depends on the voltammetric experiment timescale (Figure 2.1d). The diffusional transport at a high potential scan rate is faster than the charge transfer. So, the rate of the latter limits the whole process, i.e., the process is irreversible. The process is quasi-reversible if the transport rate is comparable to the charge transfer rate.

The shape and position of the voltammogram are sensitive to factors including but not limited to electrode material and geometry, potential scan rate, the electrolyte nature, and the presence of other chemical species in solution. Therefore, several interesting details regarding the electrochemically active surface area, electron transfer mechanism and kinetics, mass transport, and system reversibility can be determined using LSV and CV. It is crucial to choose chemically and electrochemically stable electrolytes in the potential range of analysis. Both techniques use three-electrode systems with the working, counter, and reference electrode. The LSV technique is beneficial for irreversible systems to calculate voltammogram parameters that readily yield practical information.

2.1.1.c Differential pulse voltammetry (DPV)

Differential pulse voltammetry (DPV) is a sensitive voltammetric technique capable of achieving detection limits of redox species of the order of 10^{-7} M²⁸⁶. In DPV, the potential waveform comprises pulses superimposed on a staircase potential transient (Figure 2.2a). The current I_1 just before the pulse is applied (i.e., at point 1 in Figure 2.2a) and the current I_2 just before the end of the pulse (i.e., at point 2 in Figure 2.2a) are measured. Then, the current difference, $\Delta I_v = I_2 - I_1$, is plotted against the staircase potential applied, yielding the peak-shaped profile (Figure 2.2b). Faradaic processes are the electron transfers at the electrode-electrolyte interface between the electrode and target chemical species in the electrolyte solution. Non-Faradaic processes include adsorption and desorption at the electrode surface, charging current produced due to electrode polarization, and electrode-electrolyte interactions, which can cause significant background current. DPV markedly decreases the contribution of these non-Faradaic processes, mainly capacitive current contributions, to the recorded signal²⁸⁶. These unwanted contributions are canceled out by subtracting I_1 from I_2 .

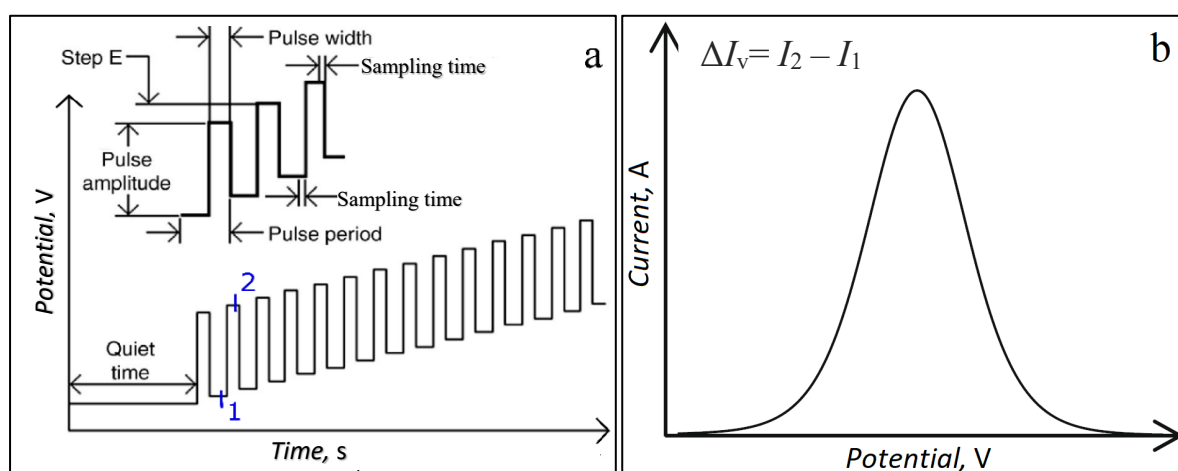


Figure 2.2. Differential pulse voltammetry (DPV) (a) potential waveform (adapted from²⁸⁷) and (b) output signal (adapted from²⁸⁸).

DPV can be applied to monitor the "gate effect" in MIPs¹²¹ before and after template extraction (Figure 2.3). Initially, unrestricted diffusion of the redox probe from solution bulk to the electrode surface is recorded, giving rise to high current intensity. If the electrode is coated with a MIP or control NIP film, this diffusion is severely restricted, and therefore DPV currents are negligible. Following template extraction from the MIP film, the signal of the redox probe increases as the empty cavities allow for some redox probe diffusion through the film. This increase in current after template extraction is not observed at the control NIP film-

coated electrode as cavities are not formed in NIP films. Therefore, DPV serves as an indirect proof of template extraction from the MIP film.

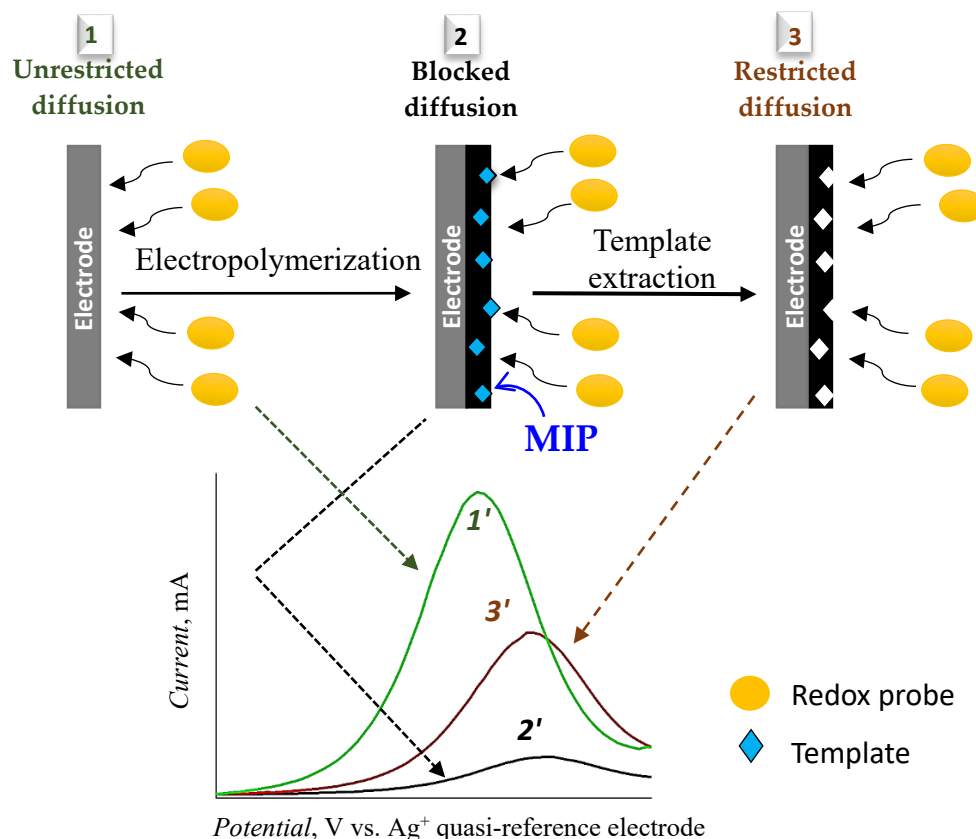


Figure 2.3. The "gate effect" monitoring of molecularly imprinted polymers (MIPs) operation using differential pulse voltammetry (DPV).

2.1.1.d Bulk electrolysis

Different types of bulk electrolysis methods can be defined by the parameter controlled in the experiment and by the process carried out or quantities measured. Potentiostatic experiments are based on the controlled potential (E_v) of the working electrode, and galvanostatic experiments involve a controlled current (I_v) (Figure 2.4). The potential is instantaneously stepped from E_1 to E_2 in potentiostatic electrolysis, and a large current decaying over time with the depletion of the reactant species in the electrode vicinity is obtained as output (Figure 2.4a and 2.4b). The working electrode potential is maintained constant against a reference electrode in controlled-potential techniques. In galvanostatic electrolysis with a constant current I_v applied, the output potential change depends on the reactant concentration close to the electrode surface (Figure 2.4c and 2.4d). Initially, the potential increases reaching a plateau where the reactant is continuously oxidized. Further rise in potential occurs when all the reactant species near the electrode are depleted.

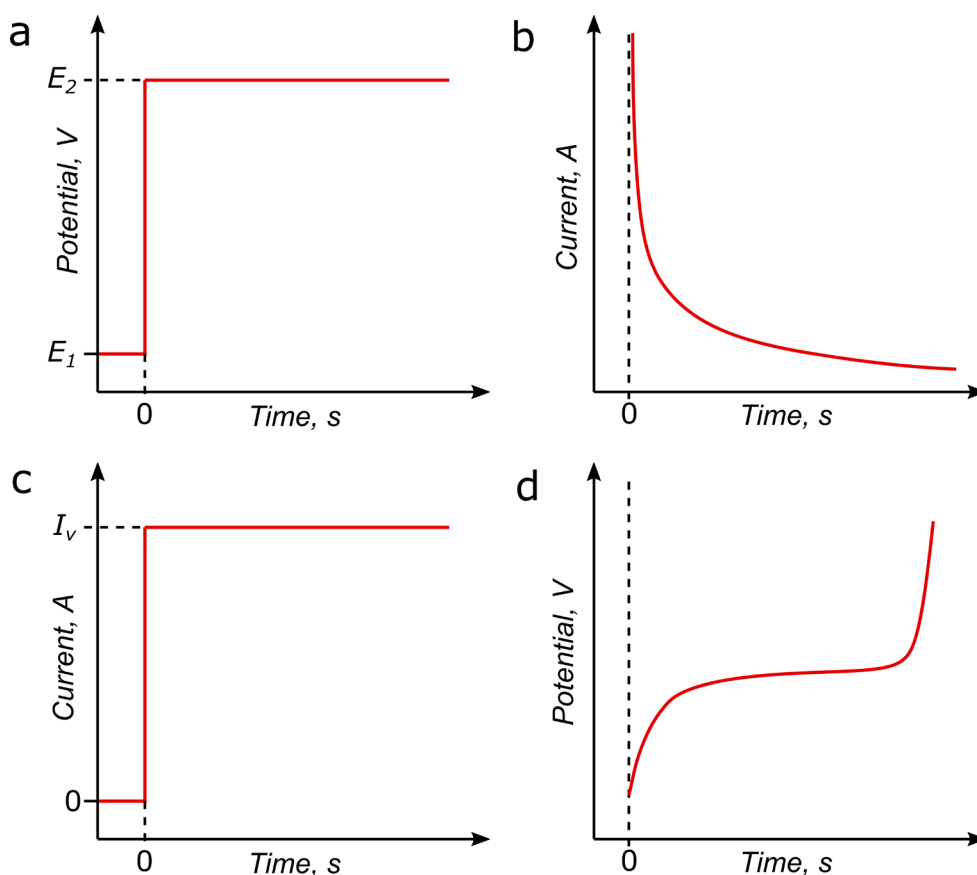


Figure 2.4. The potentiostatic electrolysis (a) potential waveform generated by switching the potential from the initial E_1 to the final E_2 value and (b) output current transient. The galvanostatic electrolysis (c) current waveform generated by applying constant current I_v and (d) output potential transient.

As, generally, the working electrode potential precisely controls the degree of completion of an electrode process, the controlled-potential techniques are the most desirable for bulk electrolysis. However, the equipment necessary for constant current electrolysis is simpler than that needed for constant potential electrolysis. Significantly, when performing preparative electrosynthesis with constant current techniques, the working electrode's potential should not shift into a region where undesirable side reactions, e.g., electrolyte oxidation, occur^{282, 289}.

2.1.1.e Photoelectrochemistry

Photoelectrochemistry deals with studying the light irradiation influence on electrochemical systems. The photoeffect involves photoexciting either the electrode material or molecular species in the electrolyte in these systems. The electrode material will be affected differently depending on whether it is made of a metal or semiconductor. If a metal is used as the working electrode material, the electrons ejected from the metal will travel into the electrolyte to form

species that can interact with electron scavengers. When irradiated, the semiconductor electrode material can absorb photons if the incident energy of the photons matches the semiconductor bandgap energy (E_g) or exceeds this value. Semiconductors contain valence and conduction bands that are analogous to molecules' energy levels. The highest occupied molecular orbital (HOMO) correlates to the valence band, and the lowest unoccupied molecular orbital (LUMO) to the conduction band. Therefore, E_g is analogous to the HOMO-LUMO energy gap. These bands are partially filled in metals, making them conductive when the electric field is applied. In semiconductors, the valence and conduction bands are separated by E_g , in the 0.1 eV to 3.5 eV range²⁹⁰.

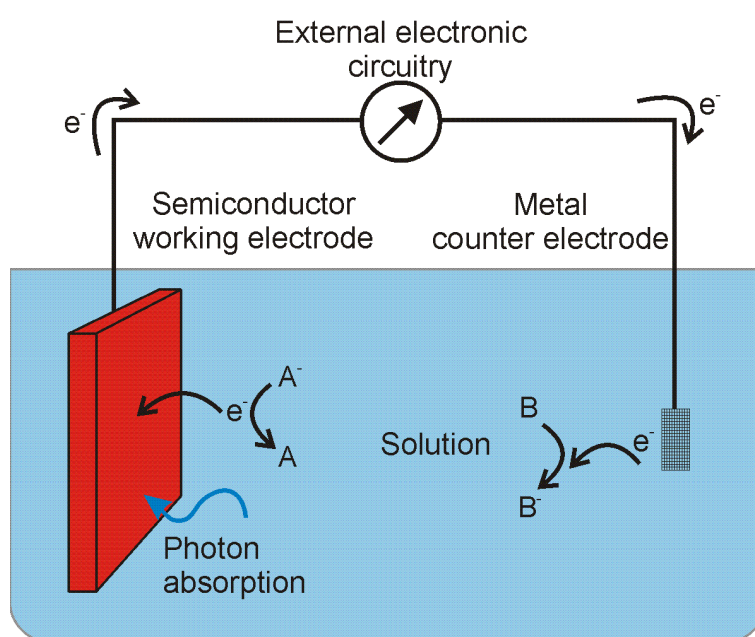


Figure 2.5. The working principle of the photoelectrochemical setup for an n-type semiconductor material used as the working electrode²⁹¹.

Electron-hole pairs are created in semiconductors when the incoming radiation energy, $h\nu$, becomes equal to E_g . The minority carriers (electrons for p-type and holes for n-type semiconductors) reach the semiconductor and the electrolyte interface, resulting in respective photo-oxidation and photo-reduction reactions. A general photoelectrochemistry working principle involving an n-type semiconductor can be seen in Figure 2.5. In aqueous systems, photo-oxidation of adsorbed water molecules or hydroxide ions by an n-type semiconductor generates dioxygen²⁹⁰. The electrons reduce the protons in the electrolyte at the counter electrode. This process is called the water photosplitting into dioxygen and dihydrogen. Photoelectrochemistry is a prospective route to convert and store solar energy in chemical bonds.

2.1.1.f Rotating ring-disk electrode system for electrocatalytic oxygen reduction reaction (ORR) studies

Ion migration can be neglected in solutions with the supporting electrolyte excess. Therefore, diffusion and convection are the only two major processes to be accounted for in the electroactive species mass transport to the electrode surface. In the convection absence, the thickness of the diffusion layer near the electrode surface increases with increasing the electrode reaction time, resulting in transient currents that do not reach a steady state. However, if there is strong solution convection, such as solution agitation or electrode rotation, this layer thickness will be fixed, and the current will reach its steady-state limiting value. Therefore, by including convection in the system, the thickness of the diffusion layer can be controlled precisely, and then the diffusion rate controls the transport rate of the reactants through the diffusion layer. By accurately controlling the rotation rate of the electrode using the rotating ring-disk electrode (RRDE) device, quantitative control of the thickness of the diffusion layer is possible, enabling quantitative analysis of the electrode reaction rate kinetics. The reactants in the solution are transported by convection at the same transport rate. The LSV at the RRDE is a powerful technique for detecting electrode reaction intermediates, e.g., peroxides produced during the ORR. The RRDE comprises two working electrodes, i.e., the disk and ring electrode (Figure 2.6). The disk electrode is located axially, and the ring electrode surrounds the disk electrode. There is a thin insulating gap between the two electrodes. The disk and ring electrodes rotate at the same rate. Consequently, the rotating RRDE draws the electrolyte to its surface, and then centrifugal force expels the solution radially outward from the center. A solution laminar flow perpendicular to the RRDE surface replenishes the reactant ²⁹².

The solution's convective speed increases as the electrode's rotation rate increases; consequently, the diffusion layer becomes thinner. The diffusion and convection rate of the reactant can be regulated by controlling the electrode rotation rate. Due to the defined hydrodynamic conditions, the diffusion and convection near the ring/disk electrode surface can be calculated using the data measured. That would yield information on the electrode reaction kinetics as a function of the applied potential even with the mass transport limitation. The hydrodynamic equations of an RRDE system can be solved for steady-state conditions. Therefore, this hydrodynamic electrode system provides a controllable, reproducible, and uniform mass transport of the electrochemically active species to or from the electrode surface that can be quantified. Moreover, the steady-state conditions can be attained quickly for such systems, and thus measurements can be made with high precision.

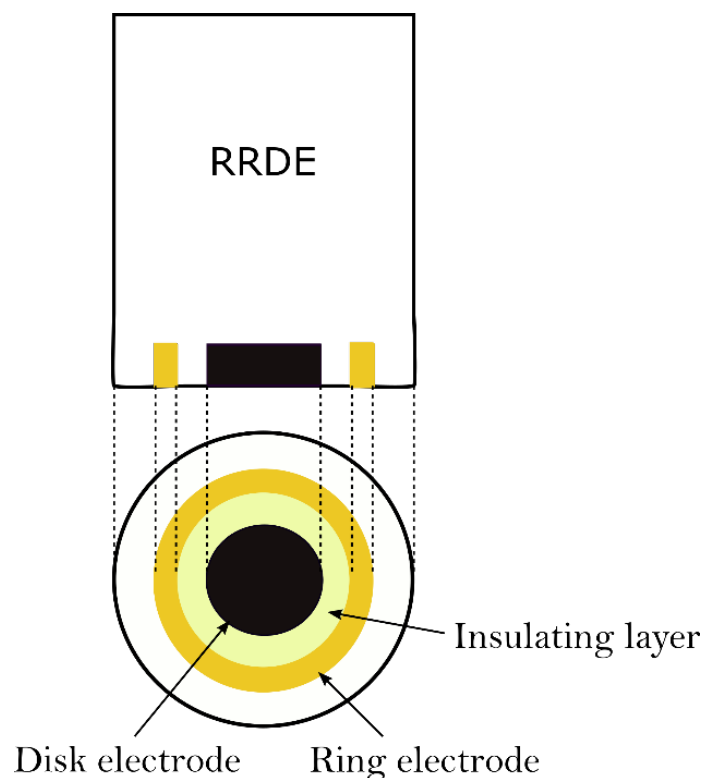
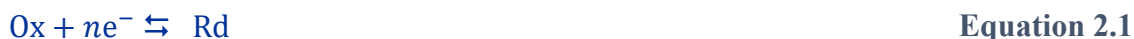


Figure 2.6. Schematic of a rotating ring-disk electrode (RRDE) comprising the glassy carbon (GC) disk and platinum (Pt) ring electrodes (adapted from ²⁹²).

Suppose we consider the following electrode reaction:



where Ox is the oxidized species, Rd is the reduced species, and n is the number of electrons transferred during the reaction. Under laminar flow conditions, the diffusion-convection limited current density at the disk electrode of the RRDE induced by the forward direction of the above reaction can be described by the Levich equation ²⁹²

$$j_{d,O} = 0.201nFD_0^{2/3}\nu_k^{-1/6}\omega^{1/2}C_0^0 \quad \text{Equation 2.2}$$

where $j_{d,O}$ is the diffusion-convection limited current density of the reduction reaction (A cm^{-2}). D_0 is the diffusion coefficient of the oxidized species ($\text{cm}^2 \text{s}^{-1}$), F is the Faraday's constant ($96,487 \text{ C mol}^{-1}$), ν_k is the kinematic solution viscosity ($\text{cm}^2 \text{s}^{-1}$), ω is the angular rotation rate of the RRDE (rad s^{-1}), and C_0^0 is the oxidized species bulk concentration (mol cm^{-3}). Suppose the electron transfer kinetics of the reduction in the reaction described by Equation 2.1 is fast, and the reaction becomes diffusion-convection rate limited. In that case, the surface concentration of the oxidized species reaches zero quite quickly, and the Levich

plot of $j_{d,o}$ against $\omega^{1/2}$ will be a straight line according to Equation 2.2. The slope of the straight line can yield values of one of the n , D_O , ν_k , or C_O^0 parameters if the other parameters are known. However, if the reduction is electron transfer rate limited, the concentration of the oxidized species is not wholly exhausted near the electrode surface unless a very large overpotential is reached. Under these conditions, the Levich plot is not a straight line as it gradually tapers with the $\omega^{1/2}$ value increase. In these cases, for a smooth planar disk electrode, the Koutecký-Levich equation holds ²⁹²:

$$\frac{1}{j_{d,o}} = \frac{1}{j^0} \exp\left(\frac{(1-\alpha)nF(E_V - E^{eq})}{R_g T_K}\right) + \frac{\omega^{-1/2}}{0.201nFD_O^{2/3}\nu_k^{-1/6}C_O^0} \quad \text{Equation 2.3}$$

where j^0 stands for the exchange current density of the reaction in Equation 2.1 ($A\text{ cm}^{-2}$), E_V is the electrode potential (V), E^{eq} is the equilibrium electrode potential, α is the charge transfer coefficient in the rate-determining step, R_g represents the universal gas constant ($8.314\text{ J mol}^{-1}\text{ K}^{-1}$), and T_K stands for absolute temperature (K). The $j^0 \exp\left(-\frac{(1-\alpha)nF(E_V - E^{eq})}{R_g T_K}\right)$ term is called the electron transfer rate limited current density, $j_{k,o}$. If the Koutecký-Levich plots of $1/j_{d,o}$ against $\omega^{-1/2}$ are constructed for different electrode potentials (Figure 2.7), the slope and intercepts can be used to calculate n and $j_{k,o}$, respectively ²⁹².

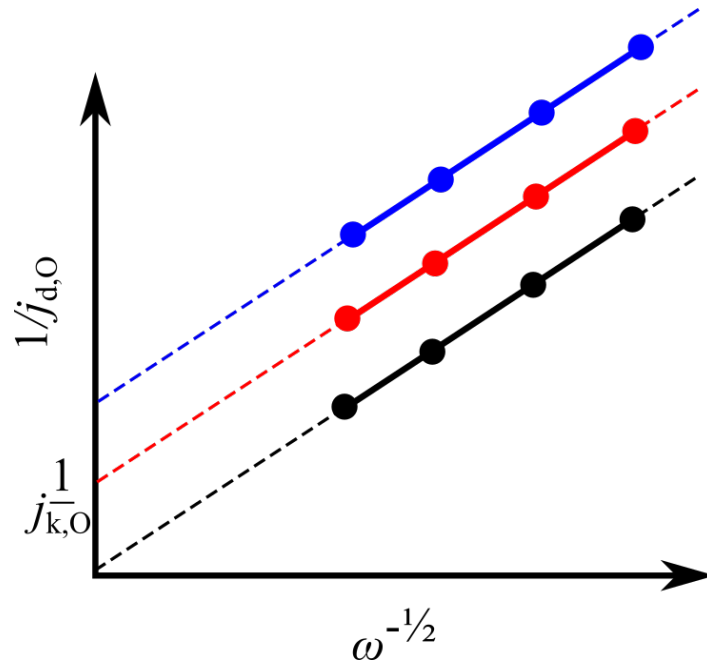


Figure 2.7. The current density inverse ($1/j_{d,o}$) against the square root of rotation rate inverse ($\omega^{-1/2}$) plotted to obtain the Koutecký-Levich lines (adapted from ²⁹³).

2.1.2 Characterization techniques

2.1.2.a Nuclear magnetic resonance (NMR) spectroscopy

Magnetic resonance monitors the energy transition between the spin states of nuclei and electrons in a molecule. Nuclear magnetic resonance (NMR) spectroscopy focuses on nuclear spin transitions. It is a widely used spectroscopic technique for studying molecular structure and dynamics. Nuclei "spin" is its fixed intrinsic property²⁹⁴. This spin creates a magnetic moment in the nucleus, behaving like a small bar magnet. For nuclei spin $\frac{1}{2}$, there are two spin states, $+\frac{1}{2}$ and $-\frac{1}{2}$, in the external magnetic field of the B_{ext} intensity (Figure 2.8a). The low-energy $+\frac{1}{2}$ -state magnetic moment aligns with the external magnetic field, while the high-energy $-\frac{1}{2}$ -spin magnetic moment is opposite to the external magnetic field²⁹⁵. The difference in the energies between the two spin states depends on the strength of the external magnetic field. These two spin states' energies are the same if the external field is zero but diverge as the field increases.

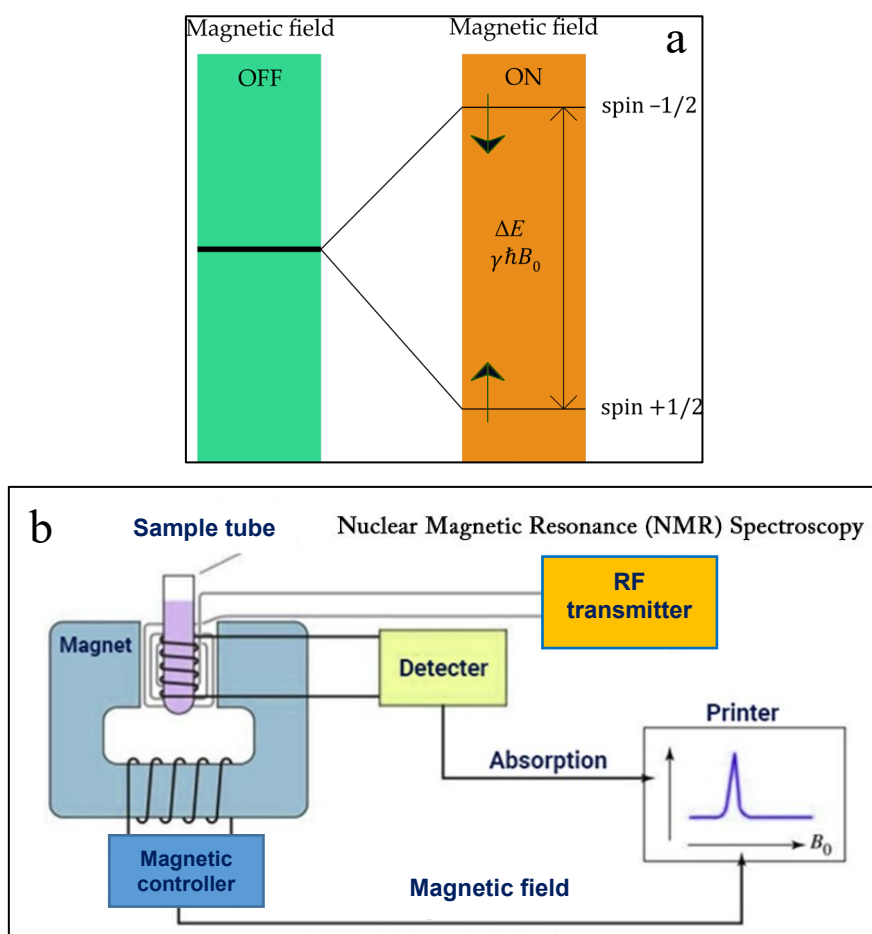


Figure 2.8. (a) Principle of operation and (b) instrumentation for nuclear magnetic resonance (NMR) spectroscopy (adapted from²⁹⁶).

At the B_0 field intensity, resonant radiation absorption occurs if the energy separation of the levels matches the energy of the photons.

$$\Delta E = \gamma \hbar B_0 \quad \text{Equation 2.4}$$

where γ is the gyromagnetic ratio (its value depends on the identity of the nucleus, which is determined empirically); \hbar is the reduced Planck's constant; B_0 is the intensity of the magnetic field applied²⁹⁴. The corresponding electromagnetic radiation frequency required for transition between the spin states is given by the Bohr frequency condition, $\Delta E = h\nu$

$$h\nu = \gamma \hbar B_0 \text{ or } \nu = \frac{\gamma B_0}{2\pi} \quad \text{Equation 2.5}$$

where h is the Planck's constant.

NMR spectroscopy measures transitions between nuclear spin energy levels based on resonance phenomena. Resonance is the strong coupling of oscillators of the same frequency. The most common nuclei in NMR spectroscopic studies are ^1H and ^{13}C . The increase in the magnetic field results in the excitation of the nucleus from the lower to the higher energy level. This excitation is recorded as the induced voltage resulting from energy absorption from the high-frequency magnetic field. Free induction decay in the time domain results in an equivalent frequency domain signal in the Fourier transform²⁹⁵. The peak area is proportional to the number of excited nuclei, and the molecule's structure can be postulated by measuring the strength of the field where protons absorb energy.

The heart of the NMR spectrometer (Figure 2.8b) is the magnet into which the sample is inserted. Modern NMR spectrometers use superconducting magnets to generate magnetic fields exceeding 12 T²⁹⁷. These magnets produce stable magnetic fields over time and do not require electrical energy to maintain these fields. With currently available magnets, all NMR frequencies are in the radiofrequency range. The data output is given as a function of chemical shifts, which indicates the resonance frequency of a nucleus relative to a standard (typically tetramethylsilane)²⁹⁵.

2.1.2.b UV-vis spectroscopy

The UV-vis absorption spectroscopy utilizes the 190 to 800 nm electromagnetic radiation region divided into the ultraviolet (190 – 400 nm) and visible (400 – 800 nm) sub-regions²⁹⁸. Valence electrons of organic molecules and polyatomic ions (e.g., CO_3^{2-}) occupy quantized sigma, pi, and unbound n_0 MOs. The unoccupied sigma antibonding (σ^*) and pi-antibonding

(π^*) MOs energies are slightly higher²⁹⁹. The electron energy difference between the occupied MO with the highest energy and the unoccupied MO with the lowest energy corresponds to ultraviolet and visible light radiations; therefore, photons can be absorbed. The excitation of electrons from low-energy AOs to high-energy orbitals occurs after the absorption of photons. Most of the UV-vis spectra of molecules are made up of four types of transitions between quantized energy levels (Table 2.1).

Table 2.1. Common electron transitions in UV-vis spectroscopy²⁹⁹.

Transition	Wavelength range, nm	Bond examples
$\sigma \rightarrow \sigma^*$	< 200	C–C, C–H
$n_o \rightarrow \sigma^*$	160 – 260	H ₂ O, CH ₃ OH, CH ₃ Cl
$\pi \rightarrow \pi^*$	200 – 500	C=C, C=O, C=N, C≡C
$n_o \rightarrow \pi^*$	250 – 600	C=O, C=N, N=N, N=O

The most important transitions that occur at accessible wavelengths are $n \rightarrow \pi^*$ and $\pi \rightarrow \pi^*$ as they represent functional groups critical to many molecules. This spectroscopy follows the principles of Beer-Lambert's law, which states that the radiation absorption by a sample material is directly proportional to the sample concentration and the optical path length²⁹⁸. This proportionality is expressed by Equation 2.6.

$$A = \log\left(\frac{I_0}{I}\right) = \epsilon_s c_s l \quad \text{Equation 2.6}$$

where A is the absorbance, I_0 is the incident light intensity, I is the transmitted light intensity, c_s is the sample molar concentration, l is optical path length (cm), and ϵ_s is the molar absorption coefficient.

The major components of the UV-vis spectrometer include the radiation source, monochromator, beam chopper, mirrors, sample and reference cells, detector, and recorder (Figure 2.9). The UV-vis absorption spectroscopy can also be applied for studies of nanomaterials yielding information about bandgap, defects, as well as size and shape of the NPs. In the case of metallic NPs (e.g., silver)^{298, 300}, the strong interaction of metallic NPs with radiation of specific wavelengths occurs because the conduction electrons on the metal undergo collective oscillations³⁰¹. Those are surface plasmon resonances (SPRs).

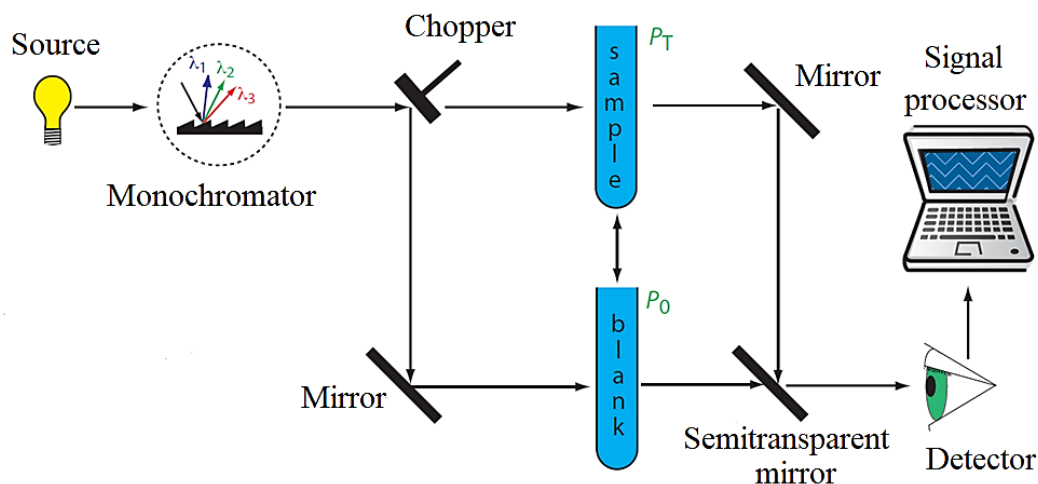


Figure 2.9. A block diagram of the UV-vis spectroscopy setup (adapted from ²⁹⁹).

2.1.2.c Infrared spectroscopy

Infrared radiation causes changes in the vibrational energy of molecules or polyatomic ions, but it is not sufficiently strong to cause changes in their electronic energy (Figure 2.10) ²⁹⁹.

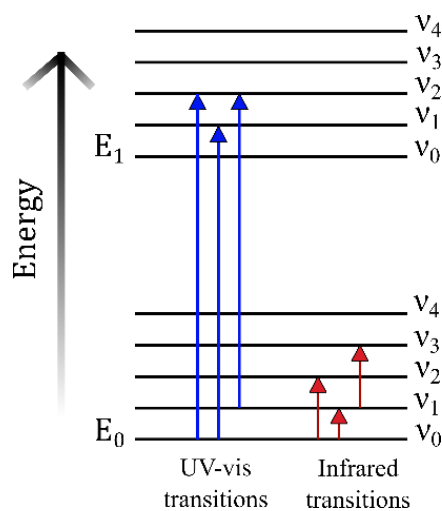


Figure 2.10. Possible electronic and vibrational transitions in the UV-vis and IR spectroscopy, respectively.

The vibration energy level is quantized; therefore, a molecule can only have specific discrete vibrational energies. The following equation describes the energy of the permissible vibration mode, E_v ,

$$E_v = (v_Q + \frac{1}{2})v_0 \quad \text{Equation 2.7}$$

where ν_Q is the vibrational quantum number with values of 0, 1, 2, ..., ν_0 is the fundamental vibrational frequency of the bond ²⁹⁹. That is the harmonic approximation. The ν_0 value is determined by the strength of the bond and the mass at both ends of the bond. For example, a carbon-carbon single bond (C–C) absorbs infrared light with less energy than a carbon-carbon double bond (C=C) ²⁹⁹. That is because single bonds are weaker than double bonds. Generally, molecules are at room temperature in the vibrational ground state ($\nu = 0$). The transition from the ground state to the first excited vibrational state ($\nu = 1$) requires the absorption of photons with an energy of $h\nu_0$. The transition where $\Delta\nu_Q$ is ± 1 leads to the fundamental line of absorption. Weak absorption lines result from transitions where $\Delta\nu_Q$ is ± 2 or ± 3 , called overtones. Generally, the potential curve is inharmonic. Therefore, the distance between the IR levels is not equal for real systems. This anharmonicity leads to the possibility of observing the overtones. The number of possible normal vibration modes for linear molecules is $3N - 5$, and for those non-linear, it is $3N - 6$; N is the number of atoms in the molecule ²⁹⁹. Therefore, the IR spectrum often has a significant number of absorption bands. The main parts of the IR spectrometer include the radiation source, sample cells, monochromators, detectors, and readout system.

Fourier-transform infrared (FT-IR) spectroscopy

FT-IR spectroscopy has been developed to overcome the limitation of low scanning rates in dispersive instruments. An interferometer was invented to measure all IR frequencies simultaneously. In an FT-IR spectrophotometer, the monochromator is replaced by an interferometer (Figure 2.11) ²⁹⁹.

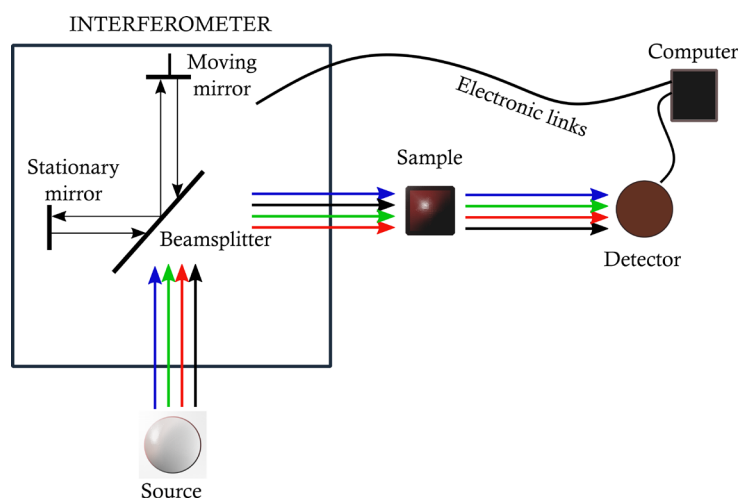


Figure 2.11. Instrumentation for Fourier-transform infrared (FT-IR) spectroscopy (adapted from ³⁰²).

The interferometer produces a unique signal in which all IR frequencies are "encoded." The signal is measured within seconds, decreasing the time factor per sample. Most interferometers use a beam splitter that receives an incoming IR beam and splits it into two. Either of the beams is reflected by a flat mirror that is fixed. The other beam is reflected by a flat mirror with a mechanism that allows this mirror to move a very short distance (usually a few millimeters) from the beam splitter. The signal exiting the interferometer results from an "interference" between these two beams as one beam travels a fixed length and the path length of the other beam constantly changes with the moving mirror. The signal resulting from interference of the two split beams is called an interferogram ³⁰².

Attenuated total reflectance Fourier-transform infrared (ATR-FTIR) spectroscopy

One approach to obtaining the infrared spectrum from a small amount of material is using attenuated total reflectance rather than transmission (Figure 2.12). Attenuated total reflectance (ATR) cells are made of high refractive index materials such as diamond, germanium, or ZnSe sandwiched between a low index substrate and an even lower index sample. IR radiation from the source enters the ATR crystal, where it undergoes a series of total internal reflections before leaving the crystal as the incidence angle at the interface between the crystal and the sample is greater than the critical angle ²⁹⁹. Each time it reflects, the radiation penetrates the sample to a few micrometers creating evanescent waves ³⁰³. As a result, radiation at the wavelengths absorbed by the sample is selectively attenuated.

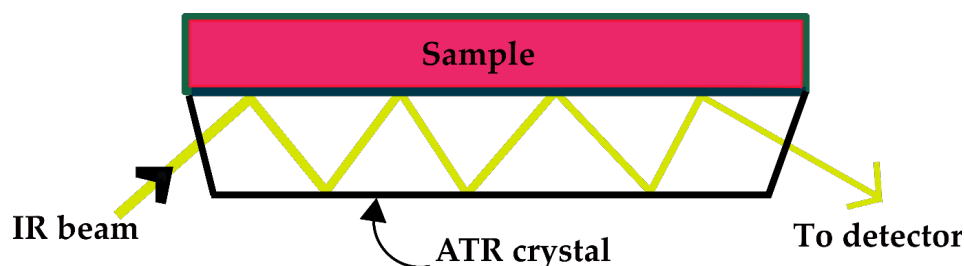


Figure 2.12. The operation principle of multiple-reflection attenuated total reflectance Fourier-transform infrared (ATR-FTIR) spectroscopy.

Grazing-angle FTIR (GA-FTIR) spectroscopy

The FT-IR analysis sensitivity is greatly improved using the grazing angle of incidence ($\sim 65^\circ$). The large incidence angle increases the pathway of the IR radiation in the layer. In particular, spectra of samples of a few nanometers' thicknesses can reliably be measured. Thus, this

technique allows for examining thin films of organic or inorganic materials deposited on flat surfaces of conducting substrates (e.g., metals)³⁰⁴.

Polarization-modulated infrared reflection-absorption (PM-IRRAS) spectroscopy

The IRRAS technique provides sensitive IR spectra of thin films on metal substrates using p-polarized light parallel to the plane of incidence. Parallel polarized radiation means that the electric vector of the electromagnetic field is in the plane of incidence. The electric vector of s-polarized light is perpendicular to the plane of incidence. The phase shift of the perpendicular 's' component shows no significant dependence on changes in the angle of incidence (Figure 2.13). The phase shift of this 's' component is approximately 180° at all angles of incidence, so the net amplitude of IR radiation in the direction parallel to the surface of the substrate is zero. In contrast, the parallel 'p' component phase shift strongly depends on the incidence angle. The p-polarized light creates an electric field with steady vibration leading to increased sensitivity of the measurements³⁰⁵. That makes it possible to measure layers with thickness at the angstrom level. The intensities of IRRAS absorption bands are usually very low, so often, the bands require a long acquisition time. Therefore, the H₂O and CO₂ absorption from the atmosphere can significantly affect the spectrum. Moreover, the reference and sample bands need to be measured.

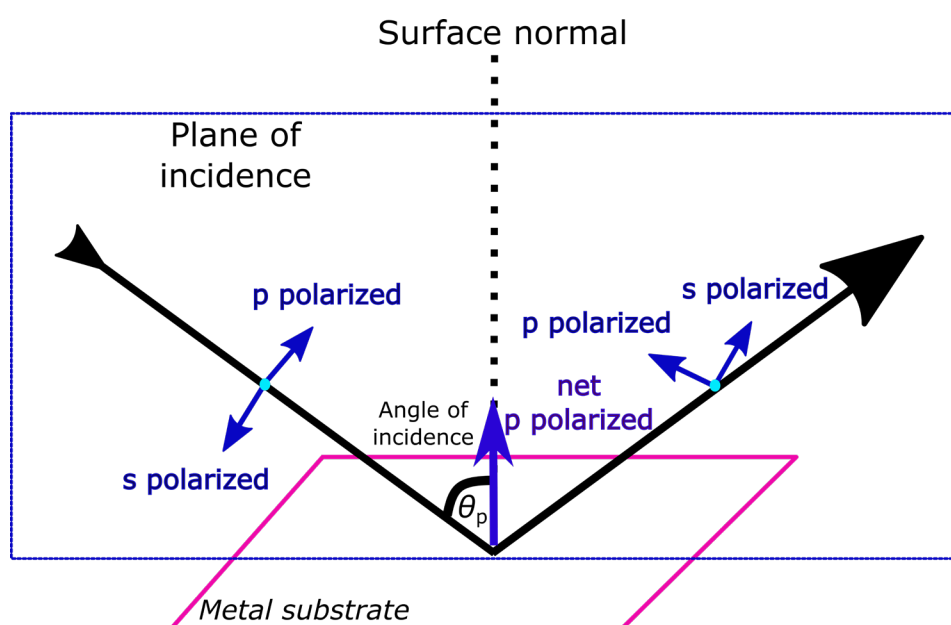


Figure 2.13. Light polarization in infrared reflection-absorption spectroscopy (IRRAS) (adapted from³⁰⁶).

PM-IRRAS provides a solution to the above deficiencies. It uses a photoelastic modulator (PEM) to determine the difference in the reflectivity between the s-polarized and p-polarized light perpendicular or parallel to the plane of incidence ($\Delta R = R_p - R_s$)³⁰⁷. The s-polarized light does not generate an electric field with a stable vibration. Hence, it is absorbed much less than p-polarized light. Furthermore, the sum of the 's' and 'p' polarized signals ($\Sigma R = R_p + R_s$) is used as the reference for PM-IRRAS, thereby eliminating the need for reference. Therefore, the effects of atmospheric H₂O and CO₂ absorption are diminished significantly. Consequently, the PM-IRRAS detects very small changes in absorption signals, yielding higher sensitivity using an FT-IR interferometer and PEM double modulation spectroscopy.

PM-IRRAS depends on the optical constants of the thin film and the substrate, the angle of incidence, and the polarization of the incident IR radiation. The PEMs alternate between linear states of polarized light. The incident and reflected electrical vectors of the p and s components of radiation can be seen in Figure 2.13. The p-polarized light component passes the maximum value at $\sim 88^\circ$ ³⁰⁵. The net amplitude of the total p-polarized radiation is approximately twice that of the incident radiation at this grazing incidence angle. This feature is applied for obtaining the differential reflectance spectra of the adsorbed surface species expressed by Equation 2.8.

$$\frac{\Delta R}{R_T} = \frac{R_p - R_s}{R_p + R_s} \quad \text{Equation 2.8}$$

R_p and R_s are the reflectivities of the p- and s-polarized radiation components, respectively, and R_T is the total reflectance^{305, 307}.

Only the p- component of the radiation interacts with the sample surface. Therefore, the active vibration that PM-IRRAS can detect requires a component of a polarized dynamic dipole perpendicular to the sample surface, which is one of the surface selection rules of PM-IRRAS. These rules determine the molecular orientation of thin films deposited on dielectric or metal substrates. In the instrument, IR light from an FT-IR spectrometer passes through the polarizer that selects the p-polarized component and focuses the sample at a grazing incidence angle of 80° (Figure 2.14). The IR beam reflected by the sample is focused on the detector. The PEM is placed at an angle of 45° to the incident p-polarized light in the incident optical path just before the sample cell window³⁰⁸. That allows the incident light to be modulated between p- and s-polarized light.

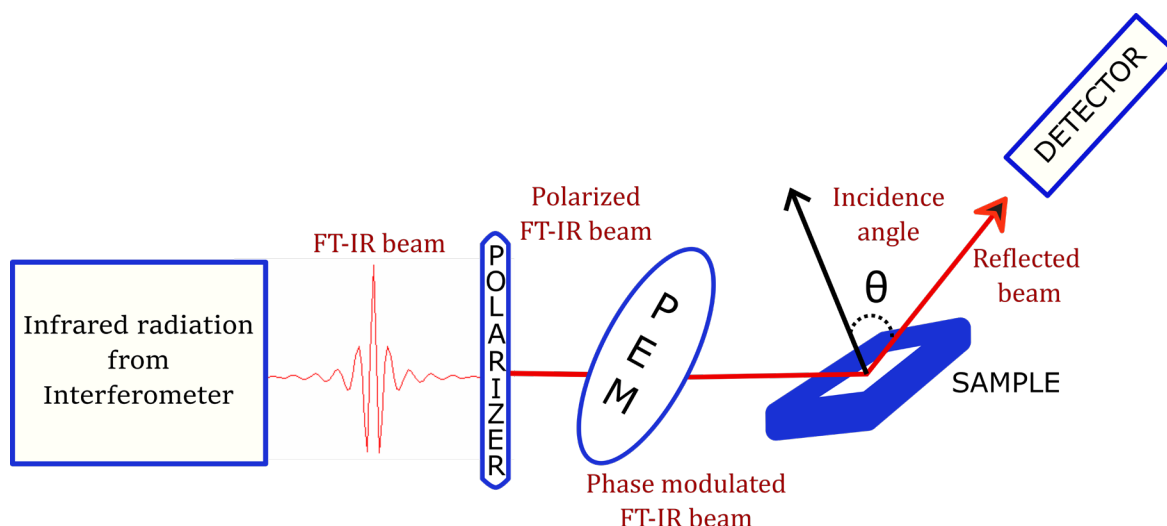


Figure 2.14. A block diagram of the polarization-modulation infrared reflection-absorption spectrometer (PM-IRRAS).

2.1.2.d Dynamic light scattering (DLS) analysis

When a monochromatic light beam hits a solution containing macromolecules, the light is scattered in all directions. Light scattering depends upon particles' size and shape. The static light scattering analyzer records the intensity of scattered light as a function of time. This scattering provides useful information about molecular weights and gyration radii of macromolecules. The analysis of variation of the intensity of scattered light caused by the Brownian motion of particles in solution provides the diffusion coefficient (D) associated with the hydrodynamic size of the particles. Dynamic light scattering (DLS) primarily measures the Brownian motion of particles in a solution caused by the bombardment of the particles with solvent molecules and correlates this motion with the particle size. This movement of macromolecules depends on the size of the macromolecule, the temperature, and the viscosity of the solvent³⁰⁹. Therefore, knowing the exact temperature and solvent viscosity is essential for DLS measurements. Suppose the movement of the particles is monitored for some time. In that case, the larger particles will diffuse slowly and occupy similar positions at different times, unlike smaller particles, giving information about the particles' size. Smaller particles will diffuse faster and therefore do not occupy a specific position.

When the laser light hits the particles in a DLS device, the incident light is scattered in all directions, and the detector records the scattering intensity. Monochromatic incident light is affected by a phenomenon known as Doppler broadening due to the continuous movement of particles in solution³⁰⁹. Light scattering can lead to mutually destructive phases that cancel out or mutually constructive phases that combine to produce a detectable signal. The digital

autocorrelator then correlates the intensity variation of the scattered light over time to determine how fast the intensity associated with the diffusion of the particles fluctuates. DLS measures the velocity of particles subjected to Brownian motion. The rate of Brownian motion is affected by the particle size, sample viscosity, and temperature, of which viscosity is a critical parameter. The temperature should be constant during the measurement. Experimentally, the intensity fluctuations are characterized by computing the intensity correlation function, $g_2(t)$, and the analysis of this function provides the value of D . This value can be converted to the particle size using the Stokes-Einstein equation ³¹⁰.

$$d_H = \frac{kT_K}{3\eta\pi_d D} \quad \text{Equation 2.9}$$

d_H is the hydrodynamic particle diameter (m), k is the Boltzmann constant (1.38×10^{-23} N m K⁻¹), T_K is the absolute temperature (K), η is the solution dynamic viscosity (N s m⁻²), and D is the diffusion coefficient (m² s⁻¹). The value of π_d is 3.14159. Three factors primarily control the diffusion of the molecules:

1. Temperature – the temperature elevation increases particle motion.
2. Solvent viscosity – the particles move slower in more viscous solvents.
3. Particle size – the motion of the particles is inversely related to particle size.

The block diagram of the DLS instrumentation is shown in Figure 2.15. It is possible to conduct experiments with a wide range of buffers, concentrations, and temperatures. DLS is a non-invasive technique that requires a relatively small sample amount and provides a reliable particle size assessment in a short time.

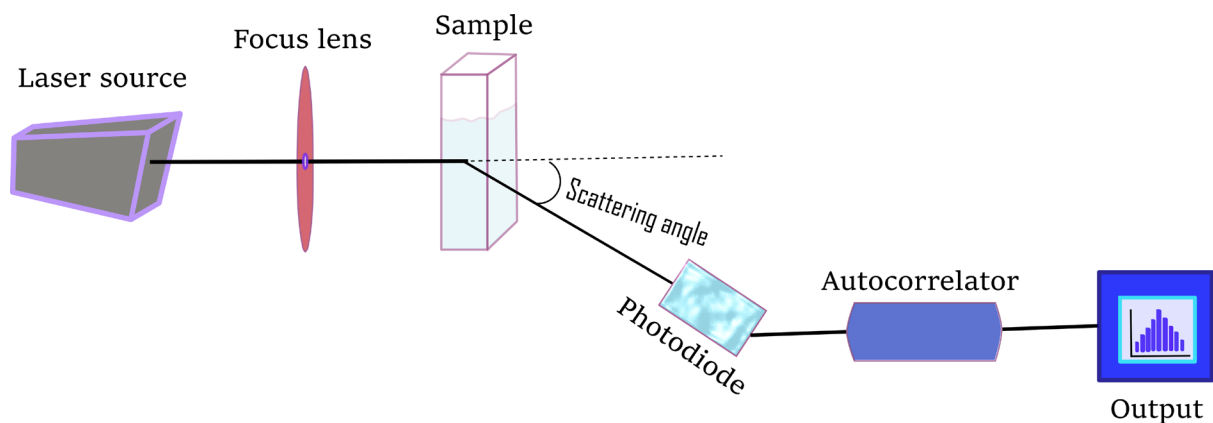


Figure 2.15. A block diagram of dynamic light scattering (DLS) instrument setup.

2.1.2.e Atomic force microscopy (AFM)

In atomic force microscopy (AFM), a sharp tip attached to a cantilever scans the sample's surface. The force exerted by the surface and all the molecules attached to it pulls and pushes the AFM tip, thereby deflecting the cantilever (Figure 2.16a). A laser beam monitors this deflection. The AFM can measure ultra-small forces (< 1 nN) between the AFM tip and the sample surface³¹¹. As no current flows between the sample and the AFM probe, this technique can be used on non-conductive surfaces or to investigate solid-liquid interfaces. Two modes of operation of AFM have commonly been used: the contact and non-contact mode. The force between the chip and the surface is kept constant in the contact mode or constant force mode, and the AFM probe comes into contact with the sample surface. This operation mode can damage fragile structures on the sample's surface. In the non-contact mode, the tip bounces over the surface at a specific frequency without touching it²⁹⁴. The tip vibration amplitude changes depending on the morphological features on the surface. The material and force constants of the AFM tip play an essential role in AFM imaging and analysis. A schematic of the commercial AFM components can be seen in Figure 2.16b.

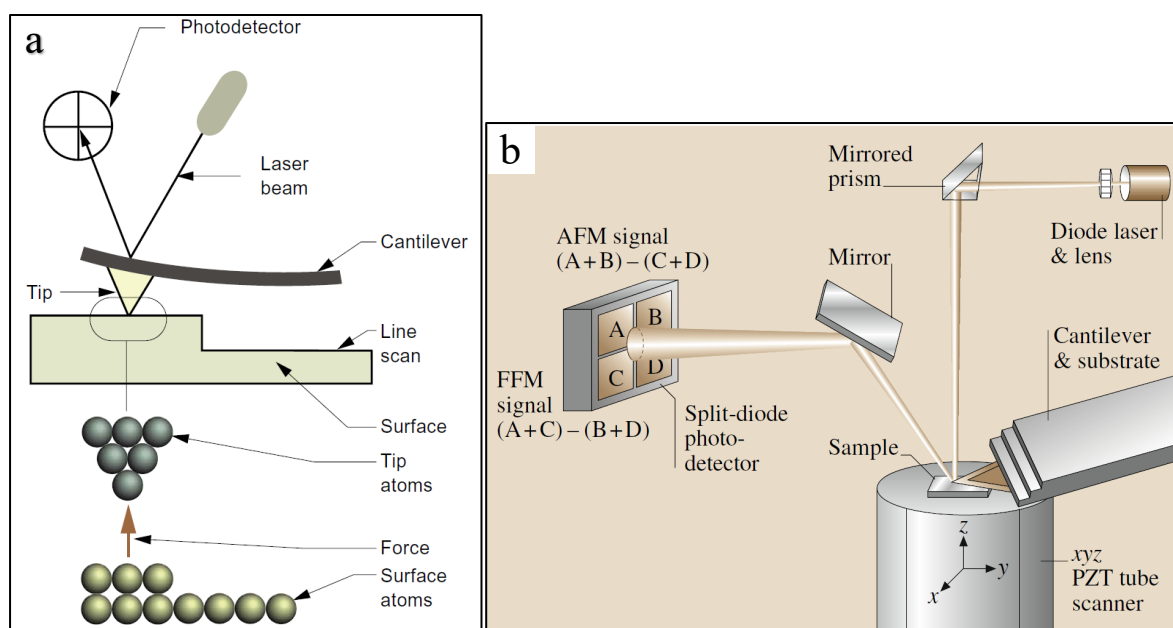


Figure 2.16. (a) Operation principle³¹² and (b) instrumentation³¹¹ of atomic force microscopy (AFM).

2.1.2.f High-performance liquid chromatography (HPLC)

The HPLC separation principle is based on the sample distribution between the mobile phase (eluent) and the stationary phase (column filler). Depending on the chemical structure of the sample components, the molecules get retained as they travel through the stationary phase. Intramolecular interactions between sample molecules and fillers define their retention time in column ³¹³. Therefore, different sample components are eluted at different times, thereby separating the sample components. The detection unit analyzes the sample component after it leaves the column. The signal is converted and processed by a data management system and represented as a chromatogram (i.e., the detector signal vs. time or an eluent volume). After passing through the detector, the mobile phase can be fed to other systems like the fraction collection unit. Generally, HPLC systems include modules for solvent reservoirs, pumps, injection valves, columns, detectors, and data processing units (Figure 2.17) ³¹⁴. The eluent is pumped into the system at high pressure and at a constant rate. A constant, pulseless flow is vital to minimize the detector signal noise and drift. The sample is added to the eluent via an infusion valve. An HPLC system is an isocratic elution system if the mobile phase composition remains constant during the separation. If the mobile phase composition changes during separation, the HPLC system is called a gradient elution system ³¹⁴. The column is crucial for all HPLC systems, responsible for properly separating sample components. Separation performance correlates with column inner diameter, length, filler type, and particle size.

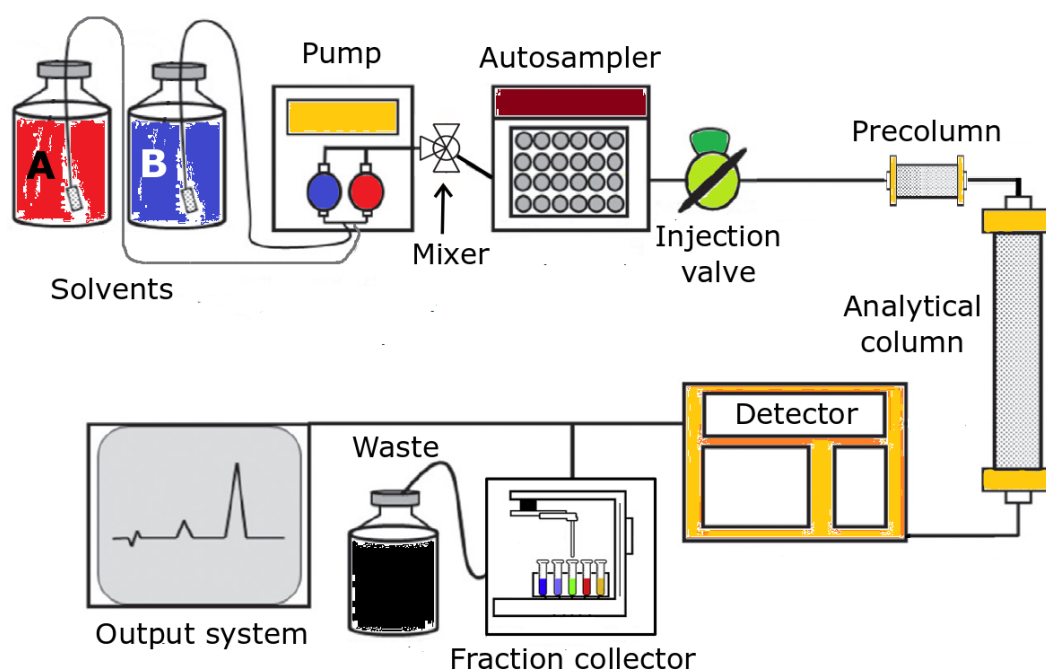


Figure 2.17. A block diagram of high-performance liquid chromatography (HPLC) instrumental setup (adapted from ³¹⁵).

2.1.2.g X-ray diffraction (XRD)

X-ray diffraction (XRD) is valuable for studying crystal structures and interatomic plane distances. It is based on constructive interference between monochromatic X-rays and crystalline samples ³¹⁶. These X-rays are generated in the cathode ray tube by heating the filament to generate electrons. The electrons are then accelerated towards a target by applying high voltage and bombarding the target. If the generated electrons have sufficient energy, they displace the electrons in the target material's atom's inner shell; consequently, a characteristic X-ray spectrum is generated when an electron from an outer shell fills this vacancy. These spectra are composed of several components, the most common of which are K_{α} and K_{β} . The wavelengths are characteristic of the target material (Cu, Fe, Mo). The resulting X-rays are filtered to give monochromatic radiation collimated, concentrated, and directed to the sample. The interaction between the incident ray and sample causes constructive interference if the interference condition satisfies Bragg's law:

$$n_x \lambda_x = 2d_x \sin \theta_x \quad \text{Equation 2.10}$$

This law associates the wavelength of electromagnetic radiation (λ_x) with the diffraction angle (θ_x) and lattice spacing (d_x) of a crystal sample ³¹⁷. The diffraction order, which correlates the path length difference between X-rays diffracted from two different atomic layers to the number of wavelengths, is given by n_x and is an integer ³¹⁸. The diffracted X-rays are then detected and processed. By scanning the sample in the entire 2θ angle range, all possible diffraction directions of the grating can be achieved for randomly oriented powder materials. The construction of the X-ray diffractometer in the θ - θ configuration is such that the sample is stationary in the horizontal position, whereas the X-ray tube and the detector move simultaneously over the angular range theta (Figure 2.18). The device used to maintain the angle and rotate the sample is called a goniometer ³¹⁶. Converting the diffraction peak to d-spacing allows for identifying the materials as each mineral has its own set of d-spacing values. The material is identified by comparing the d-spacing obtained with standard reference patterns in XRD databases, such as the Crystallography Open Database (COD) and International Center for Diffraction Data (ICDD).

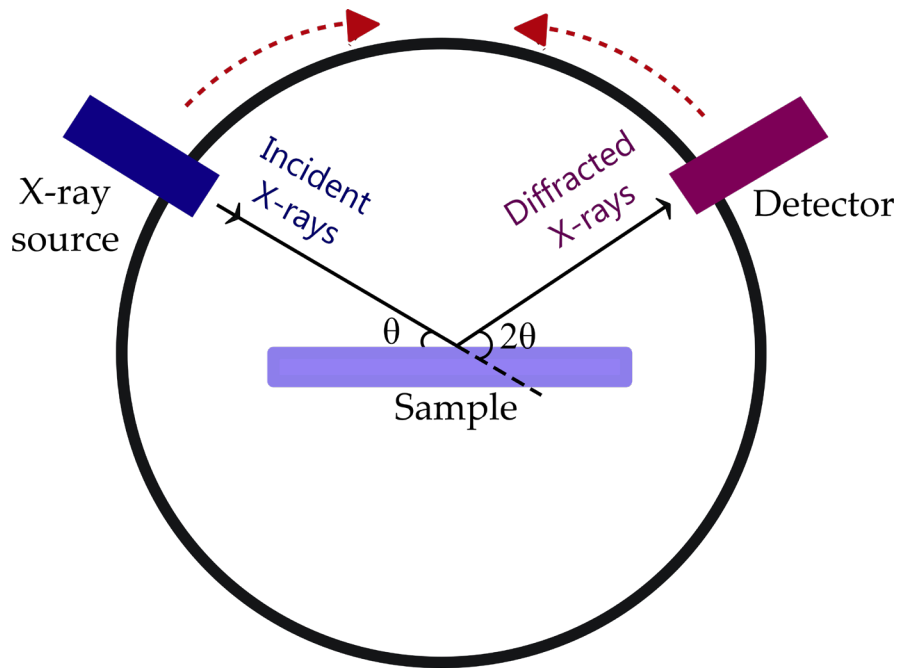


Figure 2.18. Principle of operation of the X-ray diffractometer (adapted from ³¹⁹).

The diffraction pattern maxima of sufficiently small crystallites in a powdered sample are broadened. This broadening amount is inversely proportional to the crystallite size. Therefore, the following formula can be used to calculate the crystallite size:

$$p_x = \frac{K_x \lambda_x}{b_x \cos \theta_x} \quad \text{Equation 2.11}$$

where p_x is the crystallite size, b_x is the line broadening (in radians) given by the full width at half maximum, and K_x is the Scherrer constant defined as the shape factor with its value dependent on the shape of the crystallites ³²⁰.

2.1.2.h Energy-dispersive X-ray fluorescence spectroscopy (EDXRF)

X-ray fluorescence (XRF) spectroscopy is useful for determining the elemental composition of materials in a non-destructive method. The primary X-rays produced by the X-ray tube hit the atom's inner shell electrons (usually K and L) and eject electrons from this shell. The vacancy is then filled with electrons from the outer shell, and subsequently, characteristic secondary fluorescence is emitted to compensate for the decrease in the binding energy of the inner electron orbital compared to the outer electron orbital ³²¹. The emitted fluorescence energy is equal to the energy difference between the two orbitals. Therefore, this radiation energy is characteristic of the atoms and indicates atoms of which elements are present in the

sample. The sample contains several different atoms, so it emits X-rays with different energies. There are two types of XRF measurements, namely, energy-dispersive and wavelength-dispersive. In the energy-dispersive XRF (EDXRF) instrument, fluorescent radiation is collected by a semiconductor detector equipped with a multi-channel analyzer to sort the energies of the photons ³²¹. In practical applications, most commercial instruments cannot accurately measure the abundance of elements with atomic number $Z < 11$. The main transitions observed in EDXRF are the $L \rightarrow K$ transition (K_α), the $M \rightarrow K$ transition (K_β), and the $M \rightarrow L$ transition (L_α) (Figure 2.19) ³²². These transitions result in a fluorescent photon with characteristic energy equal to the energy difference between the initial and final orbitals.

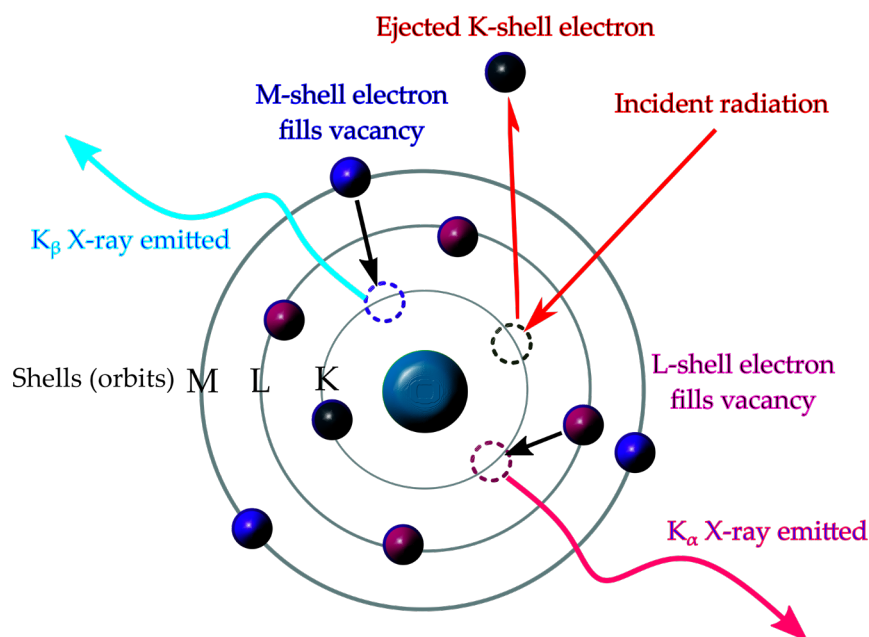


Figure 2.19. Principle of operation of energy dispersive X-ray fluorescence (EDXRF) (adapted from ³²³).

This fluorescence emission's wavelength (λ) can be calculated from Planck's law (Equation 2.12) ³²⁴.

$$\lambda = \frac{hc}{E_\lambda} \quad \text{Equation 2.12}$$

hc represents the product of the Planck constant (h) and speed of light (c), and E_λ is the radiation energy.

The essential components of all EDXRF spectrometers include an X-ray source, sample cell, and detector (Figure 2.20).

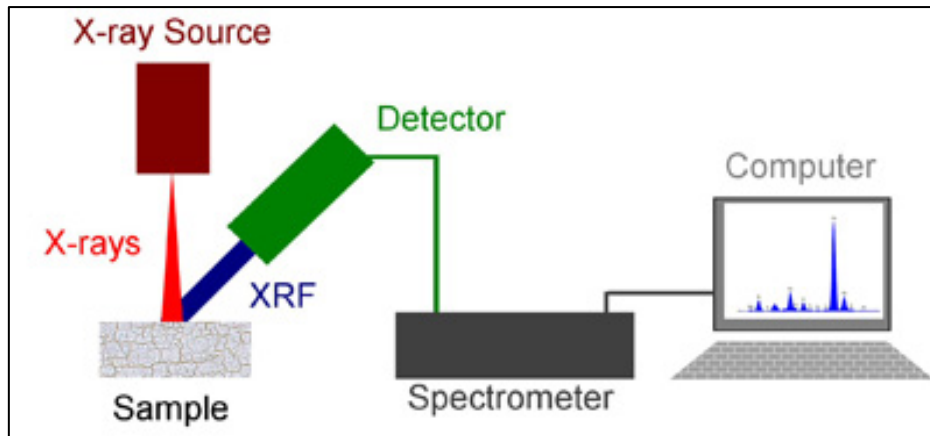


Figure 2.20. A block diagram of the instrument setup for measuring energy dispersive X-ray fluorescence (EDXRF) ³²².

2.1.2.i Scanning electron microscopy (SEM) and energy-dispersive X-ray spectroscopy (EDXS)

Scanning electron microscopy (SEM) is high-magnification microscopy that uses a focused electron beam to yield sample topography images. The effective SEM resolution is ~ 1 nm. The primary electron beam interacts with the sample's surface in several ways (Figure 2.21) ³²⁵⁻³²⁶.

- (i) Primary electrons generate secondary electrons with low energy that emphasize the sample's topography. The interaction between the primary electrons from the incident electron beam and the loosely bound electrons in the sample's atoms under observation results in the formation of secondary electrons. The energy of secondary electrons generated near the sample surface is 10 to 50 eV.
- (ii) Primary electrons may also be backscattered, producing images with a high degree of atomic number (Z) contrast. Backscattered electrons can be produced either by single large-angle or multiple small-angle scattering, and their proportion depends on the atomic numbers of the elements. The backscattered electrons originate from layers below the surface up to $0.1 - 1 \mu\text{m}$. Phases and particles with a higher average atomic number appear brighter as more primary electrons are backscattered. Therefore, backscattered electron imaging can differentiate between phases and particles having different atomic numbers.

- (iii) Relaxation of ionized atoms results in electron shell-to-shell transitions, which can cause X-ray emission and Auger electron ejection. The EDXS detector measures the emitted X-rays that are characteristic of the elements in the top few layers of the sample.

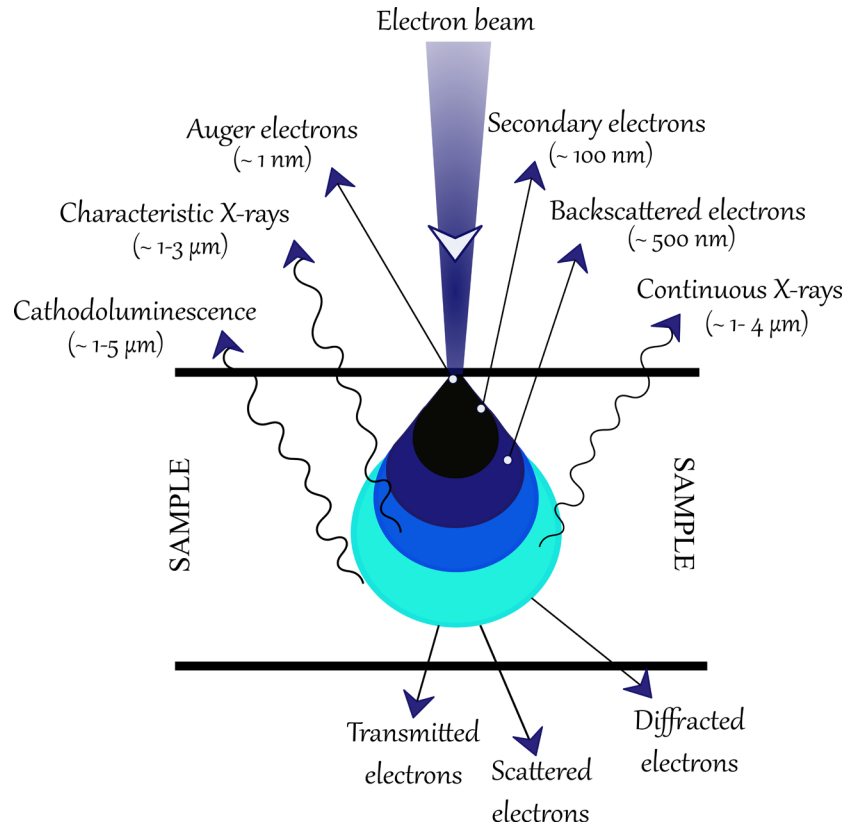


Figure 2.21. Possible scanning electron microscopy (SEM) incident electron beam interactions with the sample surface at various depths (adapted from ³²⁷).

The operating principle of EDXS is based on a high-energy electron beam's ability to eject an atom's core electrons. This principle, known as Moseley's law, determines the direct correlation between the frequency of electromagnetic radiation (ν) released and the atomic number (Z) of the atom, as follows ³²⁸.

$$\sqrt{\nu} = a_s(Z - b_s) \quad \text{Equation 2.13}$$

where a_s and b_s are the shielding constants. The primary electron beam has energy sufficient to knock out electrons from atoms and produce characteristic X-rays. The X-rays generated from the sample can be used for (i) determining the sample chemistry using either EDXS or wavelength dispersive spectroscopy (WDXS), (ii) creating an X-ray dot image or elemental map that exhibits the elemental distribution in the sample, or (iii) generating line scans across

the samples to determine elemental variations along with the interfaces and phase boundaries³²⁹.

In SEM, an electron beam is generated by heating a tungsten filament, a lanthanum hexaboride (LaB₆) crystal, or a field-emission source, and electromagnetic lenses focus this beam to form the image³²⁶. A typical SEM instrument consists of the electron column, including the e-beam gun and condenser lenses to focus and collimate the beam, sample chamber, vacuum system, EDXS detector, imaging system, electronics console, and visual display monitors (Figure 2.22).

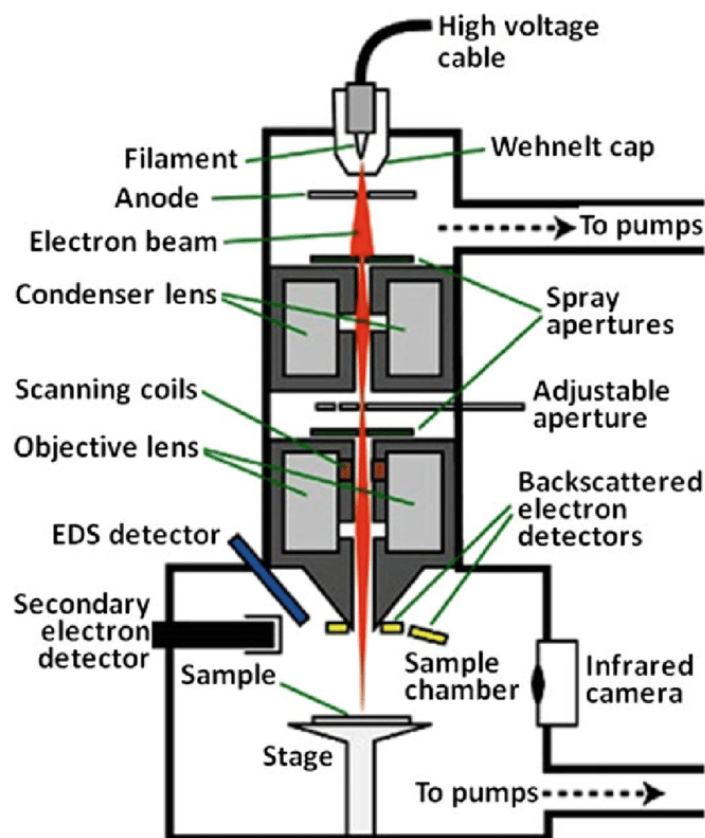


Figure 2.22. A sketch of the scanning electron microscopy (SEM) instrument with the energy-dispersive X-ray spectroscopy (EDXS) detector attached³²⁵.

2.1.2.j Brunauer-Emmett-Teller (BET) analysis

Adsorption can be described as the adhesion of an atom or molecule to a solid surface. The amount of gas adsorbed depends on not only the exposed surface but also the temperature, pressure, and strength of the interaction of the gas with the surface³³⁰. The Brunauer-Emmett-Teller (BET) theory behind the surface area determination extends the Langmuir theory (Figure 2.23). Langmuir's theory correlates the monolayer adsorption of gas molecules on a solid surface to the gas pressure of the medium above the surface at a fixed temperature.

$$\theta = \frac{\alpha_L p}{1 + \alpha_L p}$$

Equation 2.14

where θ is the fraction of surface coverage, p is the gas pressure, and α_L is the surface association/binding constant.

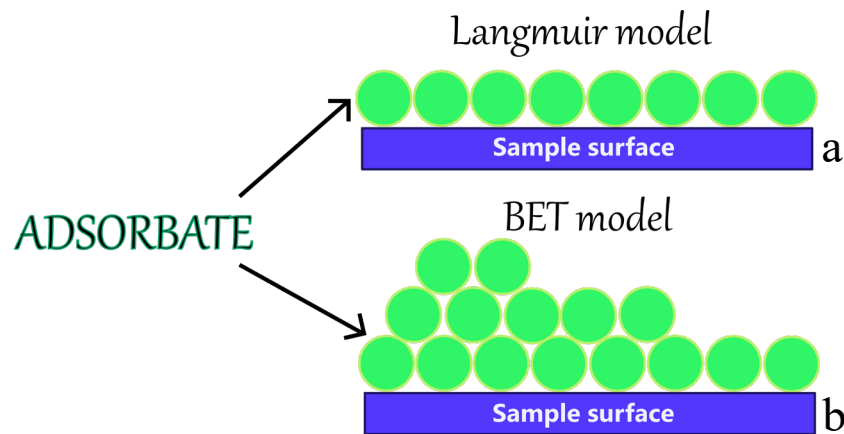


Figure 2.23. Models of gas atoms or molecules adsorption on a solid sample surface assumed in the approach of (a) Langmuir (monolayer adsorption) and (b) BET (multilayer adsorption).

Langmuir's theory assumes the following simplifications³³¹.

- (i) The area on the sample where the molecule can be adsorbed is called the surface site. Each surface site interacts with the adsorbate atom or molecule with the same energy. The gas adsorbate is usually argon, krypton, or, more frequently, nitrogen.
- (ii) Adsorption at one site is independent of adsorption at adjacent sites.
- (iii) The adsorbate activity is directly proportional to its concentration.
- (iv) The adsorbate forms a monolayer.
- (v) Each surface site can be occupied by only one atom or molecule.
- (vi) Atoms or molecules adsorbed do not move on the surface and do not interact with each other.

Langmuir's theory has drawbacks that the BET theory addresses. The BET theory extends Langmuir's theory to include multi-layer adsorption (Figure 2.23) with three additional assumptions³³¹.

- (i) Gas molecules are physically and infinitely adsorbed in layers over the solid surface.
- (ii) The various adsorption layers do not interact.
- (iii) The BET theory can be applied to any layer.

The setup of the BET instrument can be seen in Figure 2.24a. Liquid nitrogen in a Dewar is used to cool the sample and keep its temperature constant. The gas (usually nitrogen, krypton, or argon) is then physically adsorbed on the sample's surface at cryogenic temperatures so that the gas molecule or atom's interaction with the surface is sufficiently strong to generate measurable adsorption (Figure 2.24b). After the adsorption layer is formed, the sample is removed from the nitrogen atmosphere and heated to release and quantify the nitrogen adsorbed on the sample.

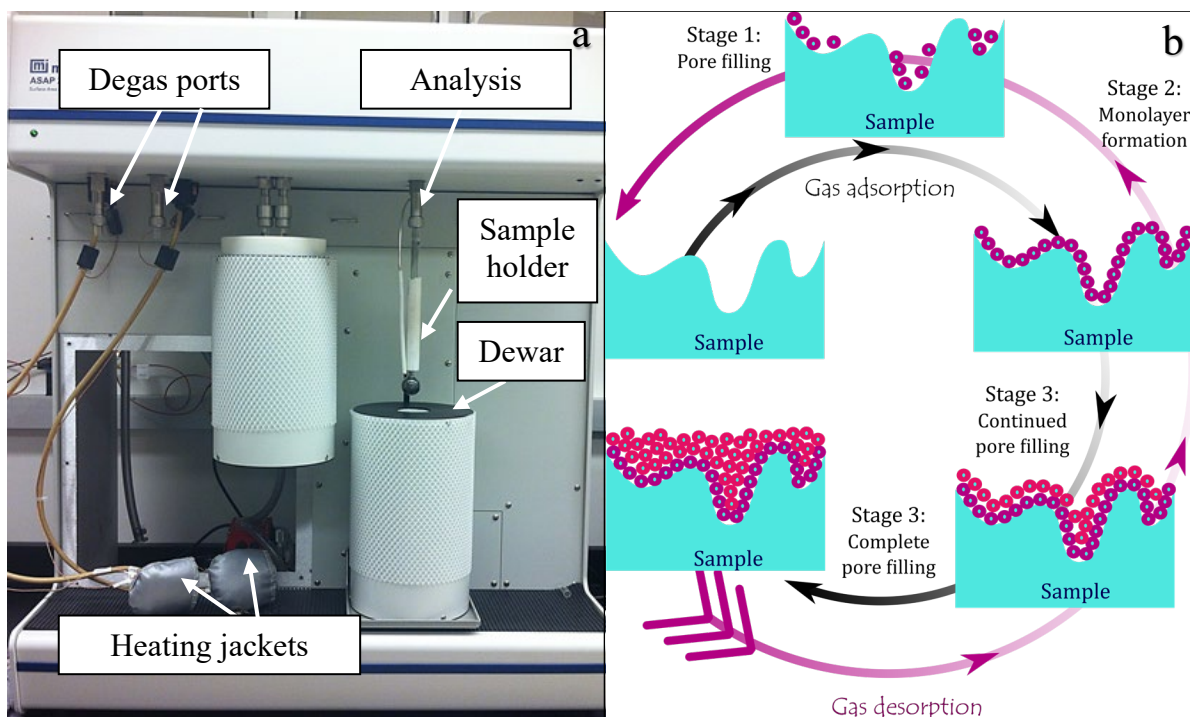


Figure 2.24. (a) The instrument set up and (b) principle of the Brunauer-Emmett-Teller (BET) adsorption model (adapted from ³³²).

The data collected is displayed as a BET isotherm, i.e., the amount of gas adsorbed as a function of relative pressure ³³³. The International Union of Pure and Applied Chemistry (IUPAC) describes six types of adsorption isotherms depending on the type of adsorbent and pores (Figure 2.25) ^{330, 334}. The BET equation uses information from the isotherms' linear low relative pressure regions to determine the sample's specific surface area.

$$\frac{1}{X\left[\left(\frac{p_0}{p}\right)-1\right]} = \frac{1}{X_m C} + \frac{C-1}{X_m C} \left(\frac{p_0}{p}\right) \quad \text{Equation 2.15}$$

Symbol X stands for the adsorbed gas weight at a specific relative pressure (p/p_0), and X_m is the adsorption capacity or volume of the gas adsorbed at standard temperature and pressure STP

(273 K and 1 bar). The C symbol is the BET constant, which can be calculated from the intercept and slope of the graph. It is related to the adsorption energy in the first adsorbed layer 331, 333.

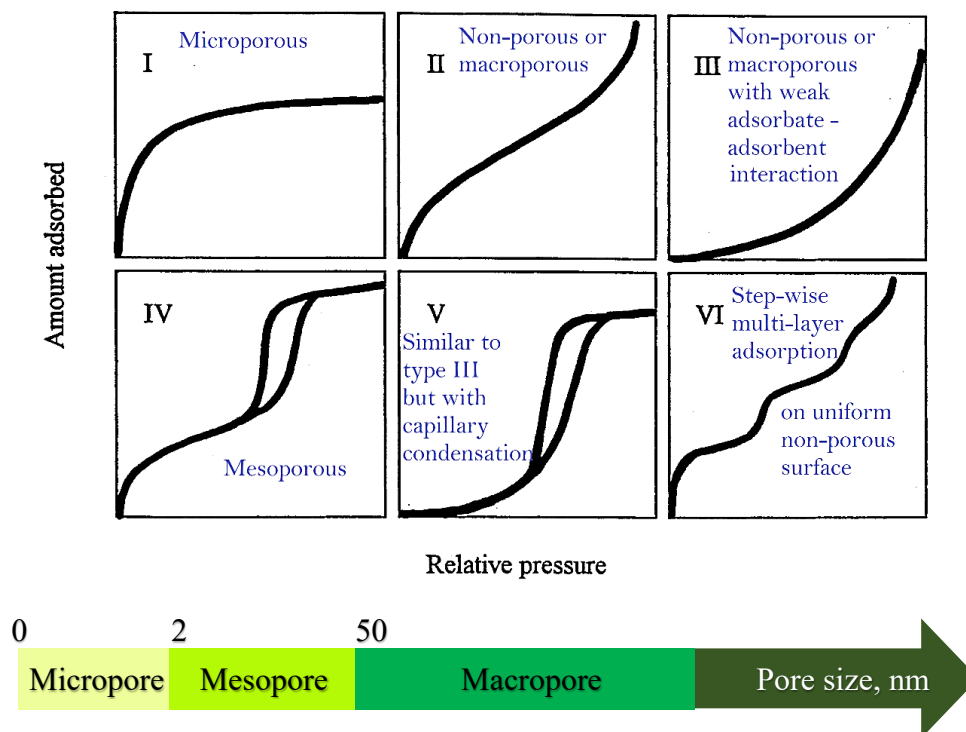


Figure 2.25. The different isotherms described by IUPAC based on the adsorbent type and pores (adapted from ³³⁴⁻³³⁵).

2.1.2.k Thermogravimetric analysis (TGA)

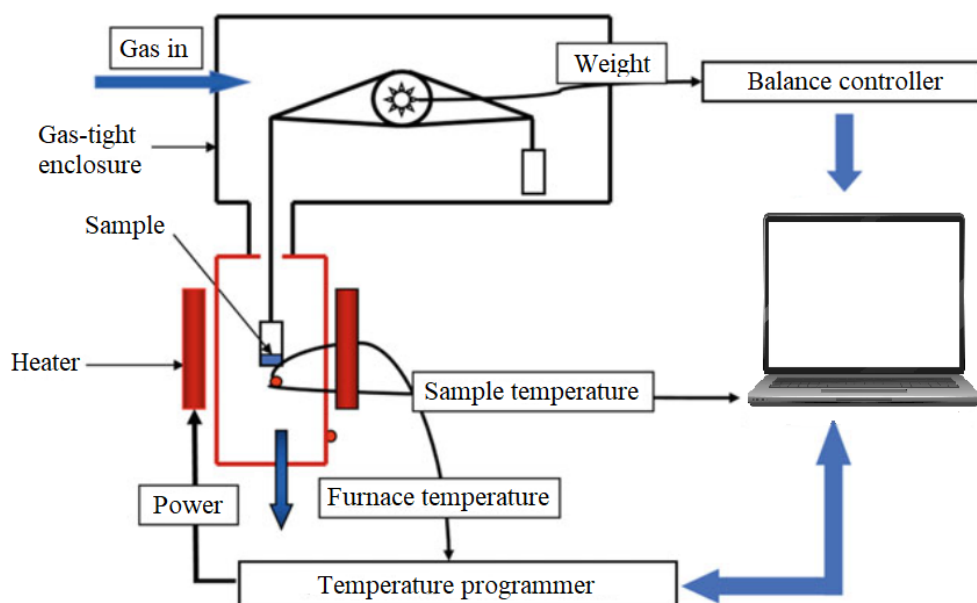


Figure 2.26. A block diagram of the instrument setup for thermogravimetric analysis (TGA) (adapted from ³³⁶).

Thermogravimetric analysis (TGA) measures material weight changes with temperature in a controlled atmosphere, yielding information about the material's thermal stability, moisture and/or solvent contents, sample components, and polymer filler levels for polymer analysis³³⁶. The autosampler loads the sample into the microbalance (Figure 2.26). The thermocouple is placed directly above the sample and measures changes in temperature. TGA analysis is performed by gradually increasing the temperature of the sample in the oven and simultaneously weighing the sample by finding the deflection of the beam with an analytical balance placed outside the oven. In TGA, mass is lost when the loss of volatile components accompanies the thermal event. Chemical reactions like combustion are associated with mass loss, but no physical changes like melting. The sample weight is plotted against temperature or time to show the thermal transition of the material and material decomposition³³⁷.

2.1.2.1 Electron spin resonance (ESR) spectroscopy

Electron spin resonance (ESR) spectroscopy is based on the characteristic magnetic properties of atoms, ions, molecules, or molecular fragments with an odd number of electrons. The electron's spin is its intrinsic property, and there is a magnetic moment due to this spin. When the sample is placed in an external magnetic field of the B_{ext} intensity, the electrons with unpaired spins absorb electromagnetic radiation, and a transition from low to high energy levels is recorded (Figure 2.27a).

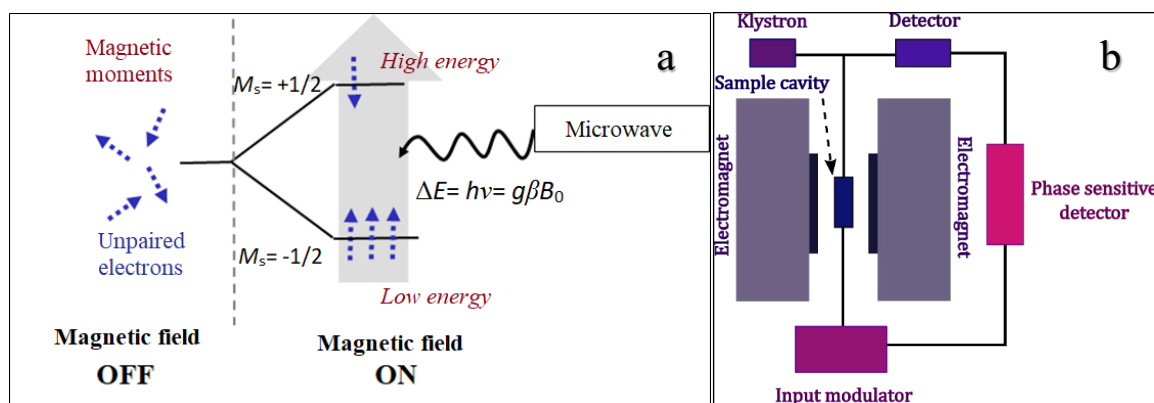


Figure 2.27. (a) Principle of operation (adapted from¹⁸²) and (b) a block diagram of an electron spin resonance (ESR) X-band spectrometer setup (adapted from³³⁸).

In principle, ESR spectroscopy is similar to NMR spectroscopy, where nucleus energy transitions between two energy levels are observed. In ESR spectroscopy, these energies differ mainly due to electron magnetic moment interacting with the external magnetic field. The

unpaired electrons act like tiny bar magnets due to the magnetic moment in the presence of this field. The electrons have the lowest energy if their magnetic moment is aligned with the external magnetic field vector and the highest if aligned opposite this vector. This phenomenon is commonly known as the Zeeman effect²⁹⁴. Since the electrons are spin $\frac{1}{2}$ particles, the low- and high-energy states can be called $M_s = -\frac{1}{2}$ and $M_s = +\frac{1}{2}$, respectively. The energy of the unpaired electron, E_e , in the external magnetic field is defined as follows³³⁹:

$$E_e = g\beta M_s B_{\text{ext}} = \pm \frac{1}{2} g\beta B_{\text{ext}} \quad \text{Equation 2.16}$$

$$\Delta E = g\beta B_{\text{ext}} = \hbar\gamma B_{\text{ext}} \quad \text{Equation 2.17}$$

where ΔE is the energy difference between the two states, dimensionless parameter g is called a g -factor or g -value, β is Bohr magneton being a unit of magnetic moment, $\gamma = g\beta/\hbar$ is the gyromagnetic ratio, and \hbar is the reduced Planck's constant. When B_0 is the external magnetic field intensity, ΔE becomes equivalent to the radiation energy $h\nu$ and can be written as

$$h\nu = g\beta B_0 \quad \text{Equation 2.18}$$

where ν is the frequency of electromagnetic excitation in hertz, usually in the radiofrequency (RF) range. The splitting of energy states linearly depends on B_{ext} ³³⁹. The energy levels degenerate at $B_{\text{ext}} = 0$, implying that the two states have the same energy without an external magnetic field. Electromagnetic radiation is absorbed when Equation 2.18 is satisfied in the presence of an external magnetic field. To fulfill this condition, the radiation frequency, ν , or the external magnetic field, must be adjusted by keeping the other constant. The unpaired electron absorbs RF radiation at a low energy level, thus jumping to a high level if resonating. These excited electrons relax to a lower energy state by emitting excess energy. The ESR spectroscopy records the transition between low and high energy levels. Since the unpaired electrons are exposed to the surroundings, a nucleus with a magnetic moment near the unpaired electrons can affect the local magnetic field of the unpaired electrons, and further splitting of the spectrum, called hyperfine splitting, can occur. The schematic of the ESR spectrometer is shown in Figure 2.27b. The radiation source (Klystron) is made of vacuum tubes containing stable high-power microwave sources with low-noise characteristics, yielding high sensitivity to the instrument. The microwaves enter the sample resonant cavity through an iris. The sample cavity is positioned at the center of the electromagnet to amplify the weak signals from the sample. Furthermore, several components, including an attenuator, field modulator, and amplifier, enhance the instrument performance³⁴⁰.

The g -factor of an ESR sample determines the position in the magnetic field (at a given microwave frequency) where an ESR transition will occur. Therefore, it is a characteristic of an electron in a specific environment. With Equation 2.19, the g -value can be calculated after applying the values of h and β , thereby giving the following equation:

$$g = \frac{71.4484 \nu(\text{GHz})}{B_0(\text{mT})} \quad \text{Equation 2.19}$$

Although the g -value (g_e) of a free-electron equals 2.00232 in a vacuum, when the electron is in a complex chemical environment, e.g., of a transition metal ion complex, a second magnetic field is produced by the nuclei, thereby changing the effective field by ΔB , which strongly influences the electron. The g -factor value is affected not only by the electronic environment but also by its anisotropy³⁴⁰. Due to the spin-orbit coupling, the g -value deviates from 2 for electrons in atoms. When these atoms are placed in an electrostatic field from other atoms, their orbital energy level will change, and the g -factor will become anisotropic. This anisotropy leads to line broadening in otherwise isotropic ESR spectra. Anisotropy is an essential parameter for free electrons in non-symmetric p and d orbitals³⁴¹.

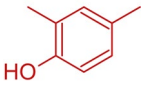
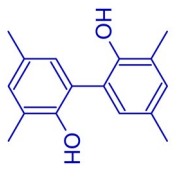
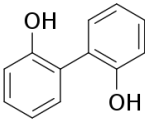
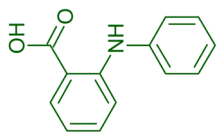
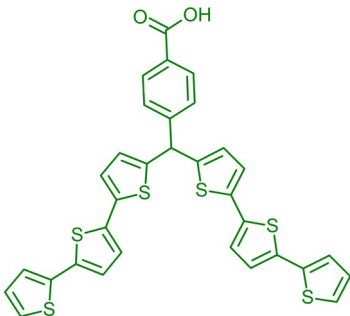
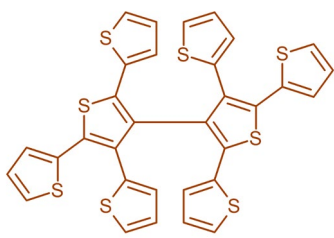
2.2 Experimental part

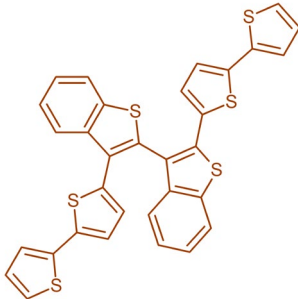
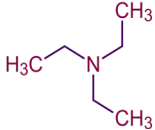
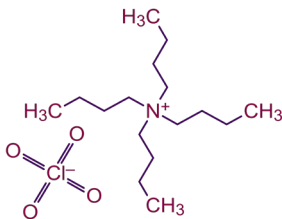
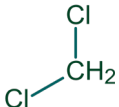
This section includes the materials and methods used in this work and is divided into two sub-sections: Section 2.2.1 for MIPs and Section 2.2.2 for silver nanocomposites.

2.2.1 Molecularly imprinted polymers (MIPs)

2.2.1.a Materials and chemicals

Table 2.2. List of chemicals.

Name	Acronym	Structural formula	Application	Source
2,4-Dimethylphenol	DMPH		Reactant for electro-oxidation	Merck KGaA
3,3',5,5'-Tetramethyl-2,2'-biphenol	TMBh		The desired product of electro-oxidation. Template for MIPs	Strem Chemicals
2,2'-Biphenol	BP		TMBh analog	Sigma-Aldrich
Diphenylamine-2-carboxylic acid	DACA FM-1		Functional monomer for MIP-1	Sigma-Aldrich
<i>p</i> -Bis(2,2';5',2''-terthien-5'-yl)methylbenzoic acid	FM-2		Functional monomer for MIP-2	Synthesized at the University of North Texas, TX, USA
2,4,5,2',4',5'-Hexa(thiophen-2-yl)-3,3'-bithiophene	CM-1		Cross-linking monomer for MIP-1	Synthesized at the University of Insubria, Como, Italy

Name	Acronym	Structural formula	Application	Source
2,2'-Bis(2,2'-bithiophene-5-yl)-3,3'-bithianaphthene	CM-2		Cross-linking monomer for MIP-2	Synthesized at the University of Insubria, Como, Italy ³⁴³
Triethylamine, purity > 99.5%	TEA		Deprotonating agent for FMs in MIPs	Sigma-Aldrich
Tetrabutylammonium perchlorate, for electrochemistry, purity >99.0%	TBA(ClO ₄)		Electrolyte	Sigma-Aldrich
Ferrocene, p.a.			Redox probe	Sigma-Aldrich
Acetonitrile, anhydrous	ACN	$\text{H}_3\text{C}-\text{C}\equiv\text{N}$	Solvent	Sigma-Aldrich
Dichloromethane	DCM		Solvent	Sigma-Aldrich

Other chemicals used.

1. Acetic acid, p.a. (POCH S.A.).
2. Acetone (Linegal Chemicals, Sp. z o.o.).
3. Acetonitrile HPLC grade (Carl Roth).
4. Doubly distilled deionized water (resistivity 15 MΩ.cm).
5. Methanol, purity 99.8% (Linegal Chemicals, Sp. o.o.).
6. Millipore water with a resistivity of 18.2 MΩ cm (at 25 °C) and a total organic carbon (TOC) value below 5 ppb.

2.2.1.b Experimental techniques and methods

2.2.1.b1 Theoretical simulations

The simulation workstation containing four Intel dual-core processors was used for molecular structure optimization, energy changes, and bond vibrations calculations with Gaussian 09 software (Gaussian, Inc., CT, USA) ³⁴⁴. The B3LYP functional and the 6-31G(d) basis set were applied to simulate the structure of the pre-polymerization complex of the **TMBh** template and **FM**. Calculations were performed for molecules in a vacuum at room temperature (298.15 K). Avogadro software helped prepare input files ³⁴⁵⁻³⁴⁶. The optimized three-dimensional molecules' structures were used to calculate the standard Gibbs free energy change values due to complex formation, ΔG_{bind}^0 .

For illustrating the selective electrosynthesis by MIPs, preliminary quantum chemistry calculations were performed to optimize structures of the molecular components and to determine the changes of standard Gibbs free energy joined with the formation of the pre-polymerization complexes using hybrid-DFT with B3LYP functional, and the split-valence 6-31G(d) basis set implemented in Gaussian 09 software ³⁴⁴. All calculations were estimated using the data computed in a vacuum at room temperature (298.15 K) and 1 atm. Input files were prepared by using GaussView v.5 software ³⁴⁷.

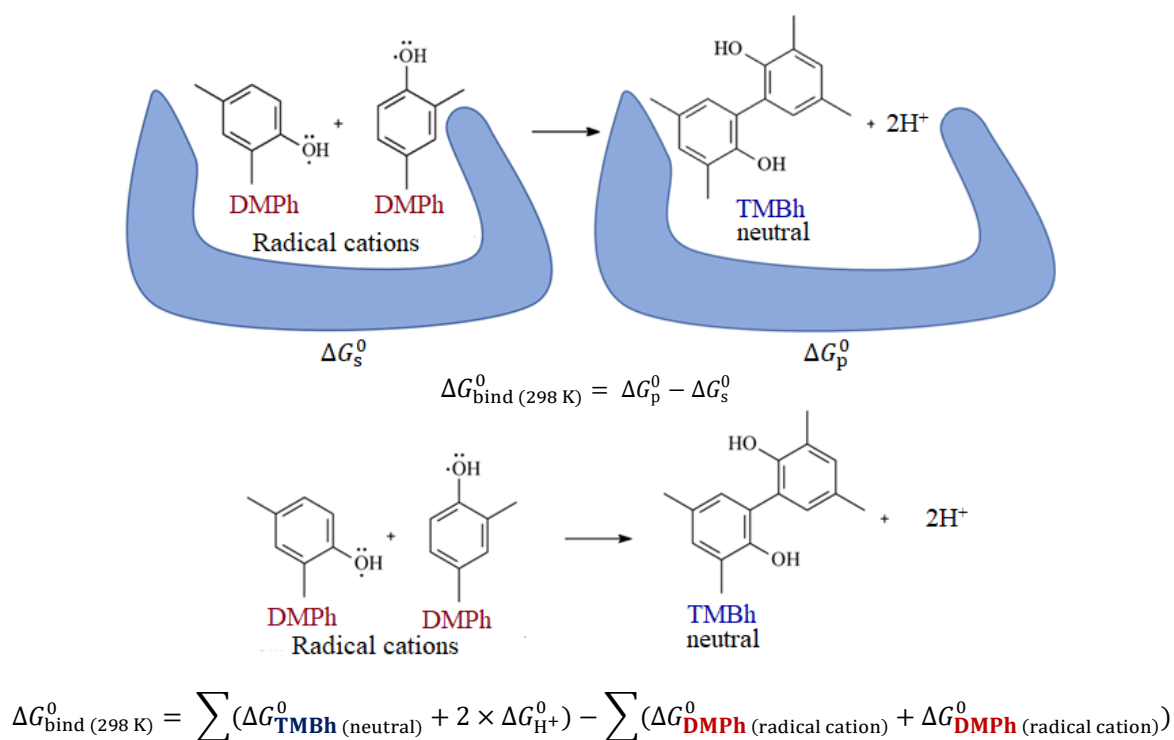
In the next step, the cavity in the MIP film was simulated. Initially, three-dimensional molecular structures of **TMBh** acting as the template, the **DMPH** substrate, the deprotonated form of functional monomer (**FM-2**), and the cross-linking monomer (**CM-2**) were constructed using Discovery Studio 2020 visual interface BIOVIA ³⁴⁸. All structures were optimized using the DFT method with the B3LYP/6-311G (d,p) hybrid functional implemented in Gaussian 16 software ³⁴⁹. All computations were accounted for by the electric permittivity (ϵ) value of the ACN : DCM (9 : 1, v/v) mixed solvents at 298.15 K ($\epsilon = 34.64 r_{ij}$) ³⁵⁰, in agreement with the experimental procedure. The ϵ value was calculated using the ratios of the solvents used. Charges were set as 0 on **TMBh**, **DMPH**, and **CM-2**, whereas as -1 on monomer **FM-2**. The electrostatic potentials, derived for atomic partial charges on the atoms, were computed using the Breneman model ³⁵¹, reproducing the molecular electrostatic potential. These components were used to construct the cavity in the MIP film. The optimizations of created systems were run one by one using the CHARMM force field ³⁵² implemented in the Discovery Studio 2020 module. In the beginning, the system was relaxed through energy minimization (steepest descend algorithm followed by the conjugate gradient algorithm introducing 3000 steps each). The design of the cavity in the MIP was accomplished in two steps to get a closer insight into

the synthetic steps of biphenols. The structure of the pre-polymerization complex was constructed with the molar ratio of template **TMBh** to monomer **FM-2** of 1 : 2 based on the molar ratio used in the synthesis. Preliminary, eight molecules of **FM-2** surrounded one molecule of **TMBh**. The **FM-2** molecules were placed randomly around **TMBh**, and energy was minimized. Next, the 1 : 2 pre-polymerization complex was generated by removing six monomers. The main criteria of the monomer selection were the strong hydrogen bond and π - π interactions of **TMBh** with **FM-2**. Then, the structure of the 1 : 2 complex was optimized once more. For the behavior of the internal geometry, an auxiliary potential restraining was applied to the **FM-2** molecules. A force constant of $83.74 \text{ kJ mol}^{-1} \text{ \AA}^2$ was sufficient for the calculations. Then, ten molecules of cross-linking monomer **CM-2** were added to the system at random positions.

After optimization, five molecules of **CM-2** were chosen in the same way as above to complete the formation of the pre-polymerization complex system. The structure of the generated 1 : 2 : 5 complex was optimized again. Finally, a theoretical model of the recognizing cavity was generated by simulating the electropolymerization. Based on previous observations in simulating molecular electropolymerization for similar systems³⁵³, it can be said that the C2 positions in thiophene rings of neighboring molecules of **FM-2** and cross-linking **CM-2** monomers have been joined by covalent bonds. The resulting structure of the cavity was optimized, and then molecular dynamics (MD) was used to get the final structure. The systems in MD computations were heated from 0 K to 298.15 K within 50 ps (1 fs per step) before equilibrating thermally for 100 ps (1 fs per step) to reach the equilibration state. The equilibrated system was taken as the starting structure for 5 ns production runs with the canonical ensemble (NVT, 298.15 K) using a Berendsen thermostat³⁵⁴. The leapfrog Verlet algorithm and Langevin temperature coupling method were applied during the simulation. The constraints were set on heavy atoms with a force constant of $418.68 \text{ kJ mol}^{-1} \text{ \AA}^2$ to immobilize the 3D structure of the cavity during MD calculations. In the end, the template was removed from the system, and the obtained cavity was considered the theoretical model of the site where the synthesis of biphenols takes place.

In the next step, the combined quantum mechanical/molecular mechanical (QM/MM) methods were used in the simulations of the electro-oxidation of **DMPH** to the C-C coupled product **TMBh** in the molecular cavity and outside the cavity. QM/MM calculations were performed *via* a two-layer ONIOM scheme in the Gaussian 16 software package. The ONIOM method is a hybrid quantum chemical approach developed by Morokuma and his co-workers³⁵⁵⁻³⁵⁶, where different levels of theory are applied to different parts of molecular systems. The

most crucial elements of the systems are computed on a high-level method (e.g., QM), which can describe chemical bond breaking and formation, whereas the rest of the system is computed on a low-layer computational method (often MM). The environmental effects of the molecular surroundings on the tested system are well described using this methodology. In this study, the high-level method was the functional B3LYP³⁵⁷⁻³⁵⁹, and the low-level method adopted the Amber force field³⁶⁰. The feasibility of the ONIOM (B3LYP : Amber) method has previously been demonstrated for several enzymatic systems³⁶¹. The QM regions comprised the product (**TMBh**) and radical cation substrates (**DMPH**^{•+}). Two hydrogen ions were employed to saturate the reaction. The 6-311G basis set was used for geometries optimizations. The rest of the system, i.e., the molecular cavity (MM region), was treated by the Amber force field. For the QM cluster calculations, calculations adopting the SCRF-SMD solvation model with a dielectric constant $\epsilon = 34.64$, simulating the reaction environment, were used. During the ONIOM calculations, the electrostatic embedding method, implemented in Gaussian 16, was employed to evaluate the Coulomb interactions between MM and QM regions in all calculations³⁶².



Scheme 2.1. The electro-oxidation of **DMPH** to the C–C coupled product **TMBh** in the molecular cavity and outside the cavity, and the equation describing the standard Gibbs free energy change associated with these reactions.

Two molecules of **DMPH** and their radical cations **DMPH^{•+}**, the molecule of product **TMBh** together with 2H^+ were consecutively inserted into the cavity again and, after MD treatment, were selected as starting systems for QM/MM simulations. The standard Gibbs free energy changes due to complexation in the polymer matrix were accounted for and used in the calculations of the standard Gibbs free energy associated with these reactions (Scheme 2.1).

2.2.1.b2 Preparation of Pt and Au electrodes

Platinum electrodes of different sizes were used. Soft glass shrouded Pt disk electrodes (diameter of 0.75 mm and area of 0.44 mm^2) were used for preliminary optimization of MIP preparation and electrosynthesis. The $22 \times 5\text{ mm}^2$ Pt plates (2.74 cm^2 area) were used for large-scale electrosyntheses. The active surface area in electrosynthesis was 1.90 cm^2 . Before depositing MIP films, the Pt electrodes were roughened with sandpaper (PP 2500) and then cleaned with acetone under ultrasonication in an ultrasonic bath (Power 160 W, model IS-3R of InterSonic, Olsztyn, Poland) for 15 min. The electrodes were roughened to enable stronger adhesion of films to their surface. The $22 \times 7\text{ mm}^2$ glass slides with a 100-nm thick gold layer evaporated over a 10-nm thick titanium underlayer (Institute of Electronic Materials Technology, Warsaw, Poland) were used to characterize the MIP and NIP films using AFM and PM-IRRAS techniques. These slides were rinsed with deionized water followed by acetone under ultrasonication for 15 min before polymer film coating.

2.2.1.b3 Electrochemical setup

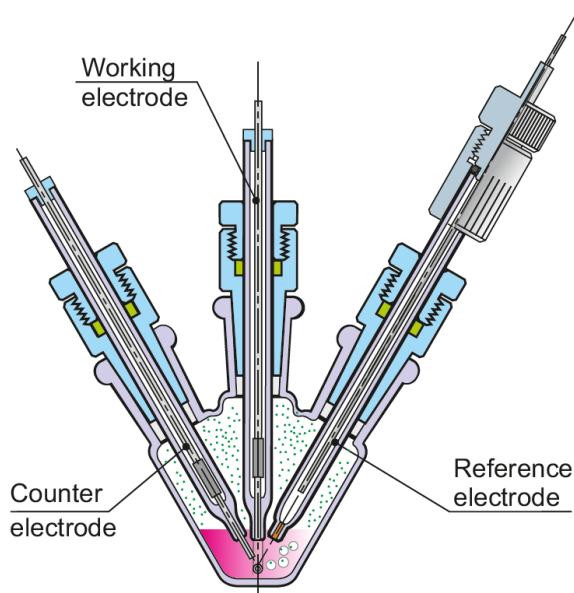


Figure 2.28. The cross-sectional view of the three-electrode V-shaped electrochemical glass minicell designed at the Institute of Physical Chemistry, PAS (Warsaw, Poland) and custom-manufactured by Labit Sp. z o.o. (Stare Babice, Poland).

Although electrochemical techniques require only two electrodes in principle, a three-electrode potentiostat-aided system (Figure 2.28) is often used. Then, a separate reference electrode controlling the potential applied to the working electrode is added, and the ohmic potential loss in the solution is eliminated²⁸⁹. Our setup included a three-electrode system containing the working, counter, and reference electrode. The Pt disk or plate and Au-layered glass slides were used as working electrodes. The working electrode potential is varied, while the reference electrode potential is kept constant. The generally used Ag/AgCl reference electrode contains each electrode reaction component, i.e., a saturated solution of silver and chloride ions at a constant concentration in saturated sodium chloride solution and a silver chloride film-coated silver wire to keep the potential constant.

In our case, a quasi-reference electrode as the silver wire was used, and ferrocene was used as an internal reference of potentials to calibrate the silver wire potential. The current passing through the working electrode is equal but opposite in sign to the current passing through the counter electrode, whose surface area is much larger. No current flows through the reference electrode. We used a Pt wire or a 4-mm diameter graphite rod with 45-mm length as the counter electrodes depending on the working electrode surface area. An excess (TBA)ClO₄ electroinactive salt was added to the test solution to maintain high ionic strength for minimizing electroactive ions migration. This high ionic strength makes the EDL thin, and, consequently, the applied potential abruptly decreases to a negligible level within nanometers from the working electrode surface. That results in a well-defined current response at the electrode surface. This setup was used for all electrochemical experiments related to MIPs.

2.2.1.b4 Preparation of films of molecularly imprinted polymer (MIP) and non-imprinted polymer (NIP) control

Two different MIP films were prepared for the **TMBh** template. Moreover, control NIP films were prepared to understand the effect of imprinting on electrosynthesis.

(a) MIP-1 with commercial functional monomer **FM-1**

Several **TMBh** : **FM-1** : **CM-1** molar ratios and TEA concentrations were tested to optimize the MIP film preparation. For MIP-1 film electrosynthesis, the exemplary solution of a pre-polymerization complex was 100 μM **TMBh** (template), 200 μM DACA (**FM-1**), 500 μM 2,4,5,2',4',5'-hexa(thiophen-2-yl)-3,3'-bithiophene (**CM-1**), 1000 μM TEA, and 100 mM (TBA)ClO₄ (supporting electrolyte) in ACN. Next, electrodes were immersed in the pre-polymerization complex solution, and then polymer film was deposited on a working electrode

under potentiodynamic conditions with five potential cycles over the potential range of 0.00 to 1.40 V vs. Ag quasi-reference electrode at a potential scan rate of 50 mV s⁻¹. The BioLogic SP-300 (Bio-Logic SAS, Seissinet-Pariset, France) potentiostat driven by EC-Lab v.10.37 software of the same manufacturer was used for this polymerization.

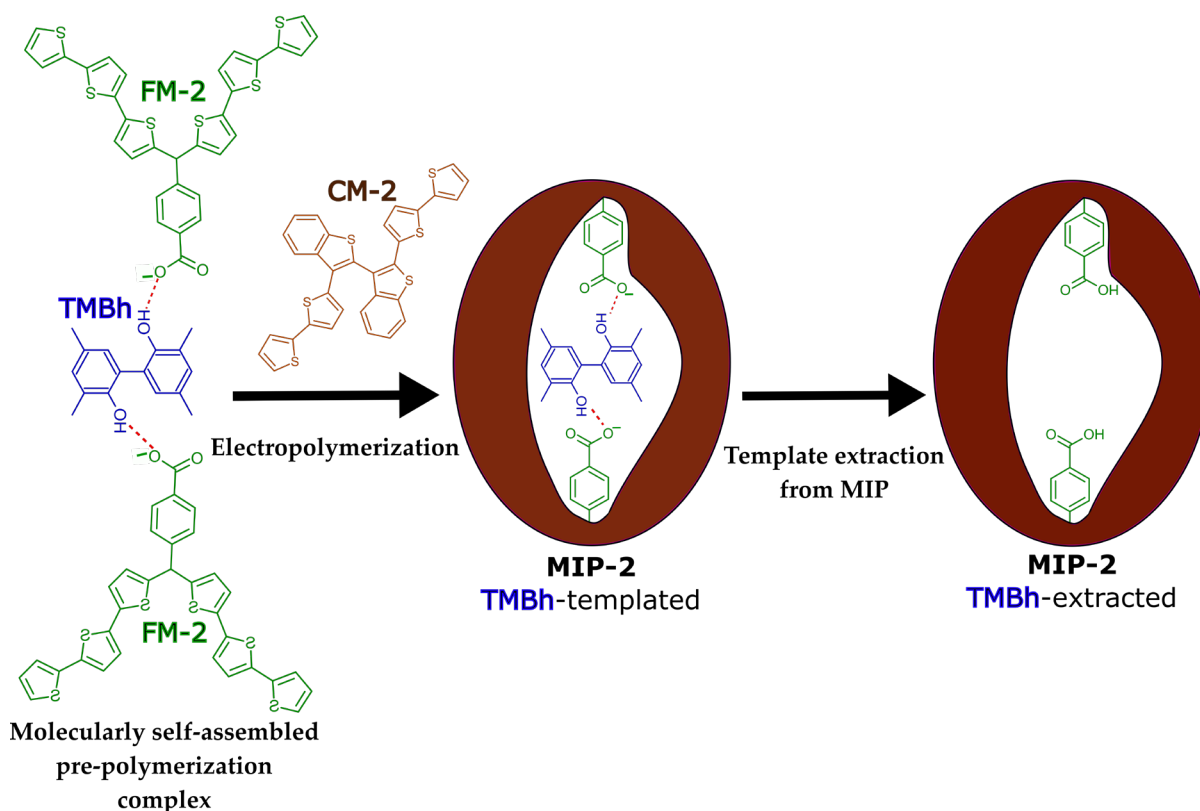
After the electropolymerization, the **TMBh** template was extracted from the **MIP-1** film. For that, the **MIP-1** film-coated electrode was immersed in the extraction (acetic acid) : methanol (1 : 1, v/v) solution for up to 400 min at room temperature, 25 (±1) °C. Acetic acid was used for extracting the **TMBh** template from the MIP because it more strongly interacts with the **TMBh** template than the **FM** and, therefore, can remove the template from the MIP. DPV measurements were performed on the **MIP-1** film-coated electrodes in 1 mM redox probe ferrocene and 100 mM (TBA)ClO₄ in ACN to confirm successful template extraction. The potential was swept between 0.00 and 0.80 V vs. Ag quasi-reference electrode with a potential step of 5 mV, the amplitude of 100-ms pulses of 2.5 mV. The CV and DPV experiments were performed using a three-electrode V-shaped glass minicell (Figure 2.28) using the Bio-Logic SP-300 potentiostat.

Synthesis of the control NIP-1 film was performed similarly to the **MIP-1** film but in the absence of the **TMBh** template. Then the extraction process was also applied to the NIP-1 films to maintain conditions similar to those used for template extraction from the **MIP-1** films.

(b) MIP-2 with newly synthesized functional monomer FM-2

The **MIP-2** preparation is presented in Scheme 2.2. Several concentrations of the **TMBh** template, **FM-2**, **CM-2**, and TEA were tested. MIPs were prepared with and without TEA. For **MIP-2a** film electrosynthesis, the optimized composition of a pre-polymerization complex solution involved 200 μM **TMBh** (template), 400 μM *p*-bis(2,2';5',2''-terthien-5'-yl)methylbenzoic acid (**FM-2**), 1000 μM 2,2'-bis(2,2'-bithiophene-5-yl)-3,3'-bithianaphthene (**CM-2**), 1000 μM TEA and 100 mM (TBA)ClO₄ (supporting electrolyte) in the ACN : DCM (9 : 1, v/v) mixed solvents. Based on the calculated standard Gibbs free energy gain due to complexation, the **TMBh** : **FM-2** molar ratio of 1 : 2 was selected. The **CM-2** was used in excess at a concentration five times higher than that of the template to ensure the MIP's uniform distribution of imprinted cavities. The pre-polymerization complex was prepared, then ultrasonicated for 15 min. Next, the Pt or Au electrodes were dipped into the pre-polymerization complex solution, and deposition was carried out under potentiodynamic conditions with five potential cycles over the potential range of 0.00 to 1.40 V vs. Ag quasi-reference electrode at a scan rate of 50 mV s⁻¹ also using the BioLogic SP-300 potentiostat.

Another set of thinner **MIP-2** film, denoted as **MIP-2b**, was prepared using a ten times diluted solution of the above pre-polymerization complex in the ACN : DCM (9 : 1, v/v) mixed solvents. The control NIP-2a and NIP-2b films were synthesized similarly to MIPs but without the **TMBh** template. DCM (10 vol.%) enhanced the solubility of **FM-2**. The **FM-2** is electropolymerized at a potential lower than the **TMBh** template, which is significant for maintaining the template integrity. TEA was used for deprotonating the **FM-2** to enable stronger electrostatic interactions between the **TMBh** template and **FM-2**. The **CM-2** provided rigidity to the **MIP-2** film because it polymerizes in three dimensions, yielding a three-dimensional networked rigid film.



Scheme 2.2. The flowchart of **MIP-2** film preparation for selective **TMBh** electrosynthesis.

The pre-polymerization complex for **MIP-2** preparation revealed aging. The mechanism of this aging is discussed in Section 3.5 of Chapter 3. The conditions were optimized to slow down aging. Toward that, solution storage at room temperature, 25 (\pm 1) °C, and protection with an aluminum foil from light illumination, significantly deterred the aging. Moreover, the pre-polymerization complex solution was ultrasonicated for 15 min before the electropolymerization.

After electropolymerization, the template was extracted from the **MIP-2** film. To this end, the **MIP-2** film-coated electrode was immersed in the (acetic acid) : methanol (1 : 1, *v/v*) extraction solution for up to 180 min at room temperature, 25 (\pm 1) °C. DPV measurements were performed with the **MIP-2** film-coated electrodes in the 1 mM ferrocene solution of 100 mM (TBA)ClO₄ in ACN : DCM (9 : 1, *v/v*) mixed solvents to confirm successful template extraction. Here, the potential was also swept between 0.00 and 0.80 V vs. Ag quasi-reference electrode with a potential step of 5 mV, the amplitude of 100-ms pulses of 2.5 mV. CV and DPV experiments were performed using the three-electrode V-shaped glass minicell exhibited in Figure 2.28 using the Bio-Logic SP-300 potentiostat.

2.2.1.b5 Electrosynthesis

The potentiodynamic characterization of **DMPH** was performed in ACN containing the (TBA)ClO₄ electrolyte at the bare Pt electrode. The **TMBh** electrosynthesis was carried out at room temperature, 25 (\pm 1) °C, through electro-oxidation of **DMPH** under potentiostatic or galvanostatic conditions in 100 mM (TBA)ClO₄ in 3 mL ACN : DCM (9 : 1, *v/v*). The MIP film thickness, electrosynthesis potential or current and time, and **DMPH** concentrations' effects on the reactant conversion and product yield were studied. Kinetic plots were obtained for electrosynthesis at bare, **MIP-2**, and NIP-2 film-coated electrodes to elucidate the performance of MIPs towards the selective electrosynthesis of **TMBh**. The experiments were performed using the three-electrode V-shaped glass minicell (Figure 2.28) using the Bio-Logic SP-300 potentiostat. Pt disk electrodes (diameter of 0.75 mm and area of 0.44 mm²) were used for preliminary optimization of electrosynthesis, and the 22 × 5 mm² Pt plates (2.74 cm² area) were used for large-scale electrosyntheses wherein the active surface area for electrosynthesis was 1.90 cm². An Ag wire was used as the quasi-reference electrode with ferrocene as the internal reference. A Pt wire or a 4-mm diameter 45-mm long graphite rod were used as the counter electrodes depending on the working electrode surface area. The solution was not stirred during the electrosynthesis. Notably, the polymer films were conditioned by cycling the potential ten times between 0.00 and 2.00 V vs. Ag quasi-reference electrode in the 100 mM (TBA)ClO₄ in the ACN : DCM (9 : 1, *v/v*) solution before electrosynthesis.

2.2.1.c Characterization techniques

2.2.1.c1 Proton nuclear magnetic resonance (^1H NMR) spectroscopy

^1H NMR spectroscopy was used to study the aging mechanism of the pre-polymerization complex of **MIP-2a** in ACN : DCM (9 : 1, v/v) with a Bruker AVANCE II 300 MHz spectrometer. Solutions of the pre-polymerization complex for **MIP-2a** preparation and individual components of the solution were analyzed on the day the solutions were freshly prepared and then under refrigeration at $\sim 4 (\pm 1)^\circ\text{C}$ after 1 and 10 days to monitor aging.

2.2.1.c2 UV-vis spectroscopy

The UV-vis spectroscopy analysis was used in titration experiments to investigate the effect of **TMBh** and **FM** binding on the absorbance of **TMBh** and **FM**. Mixed solutions of BP (**TMBh** analog) and **FM-1** were prepared at different molar ratios in ACN in the **MIP-1** system, and that of **TMBh** and **FM-2** were prepared at different molar ratios in ACN : DCM (9 : 1, v/v) in the **MIP-2** system with and without TEA. The spectra were acquired in the 190 to 800 nm region for solutions in quartz cuvettes with a path length of 1 cm. Moreover, the UV-vis spectroscopy analysis was performed for the BP, **TMBh**, **FM**, and TEA individual components as references for the peaks detected for the pre-polymerization complex. The Shimadzu UV-2501PC spectrophotometer with 0.5 nm resolution was used for recording the UV-vis spectra. Quartz cuvettes were used as the analysis was also performed in the UV region. Simulated spectra were calculated by the addition of the spectra of individual components. This analysis was performed for the **MIP-1** and **MIP-2** systems.

Moreover, the effect of aging on the pre-polymerization complex of the **MIP-2** system was studied using this technique. The pre-polymerization complex solution of **MIP-2a** was analyzed immediately after preparation in ACN : DCM (9 : 1, v/v) and after one day of aging at $4 (\pm 1)^\circ\text{C}$.

2.2.1.c3 Infrared spectroscopy

In all cases, the Vertex 80v (Bruker, Germany) FT-IR spectrophotometer was used for analysis, and the OPUS v. 7.2 software of Bruker was used to analyze the IR spectra recorded.

(a) Fourier transform infrared spectroscopy (FTIR)

The transmission FT-IR spectroscopy was used to understand the binding nature in the pre-polymerization complex with and without 1 mM TEA. The transmission FT-IR spectroscopy

measurements were performed on ZnSe windows coated with the pre-polymerization complex solution of **MIP-1** or **MIP-2**, and the solutions of their components with the pressure in the sample compartment decreased below 6 hPa. The ZnSe windows were drop-coated with the solutions, then dried under atmospheric conditions. The pre-polymerization complex solution and solutions of individual components of **MIP-1** were prepared in ACN and that of **MIP-2** in ACN : DCM (9 : 1, v/v).

(b) Grazing angle reflectance Fourier-transform infrared (GA-FTIR) spectroscopy

GA-FTIR spectroscopy was used to characterize the **MIP-2a** films. The films were deposited on Au-layered glass slides under potentiodynamic conditions, the same as those used for Pt electrodes, because the gold surface has excellent reflection properties in the IR spectral region. The GA-FTIR spectroscopy measurements were performed at the 70° angle with pressure decreased to 6 hPa in the sample compartment.

(c) Polarization-modulated infrared reflection-absorption spectroscopy (PM-IRRAS)

The PM-IRRAS spectra of the **MIP-2** and NIP-2 films deposited on Au-layered glass slides before and after exposure to (acetic acid)-methanol extraction solution were recorded using polarization-modulation. The spectrophotometer was equipped with a PMA50 PM-IRRAS module. The nitrogen-cooled MCT (Hg-Cd-Te) detector was used for a reasonably high signal-to-noise ratio. The PM-IRRAS measurements of the polymer films were performed at an 86° incidence angle in the atmosphere of dry nitrogen (evaporated from liquid N₂) under decreased pressure. The films on Au-layered glass slides were prepared according to the procedure reported for the **MIP-2** and NIP-2 films' preparation on Pt electrodes.

2.2.1.c4 Dynamic light scattering (DLS) analysis

The DLS analysis was used to monitor the changes related to the aging of the pre-polymerization complex solution. The DLS instrumentation used was ZetaSizer from Malvern Instruments Ltd. (UK), and the analysis was performed at room temperature, 20 (±1) °C. The pre-polymerization complex solution of **MIP-2a** in ACN : DCM (9 : 1, v/v) was analyzed immediately after preparation and then after aging for 7 days.

2.2.1.c5 Atomic force microscopy (AFM)

A p-doped Si cantilever and tip (RTESP Bruker) with a 43.3 N m⁻¹ force constant was used to image the polymer films deposited on Au-layered glass electrodes. The films were AFM

imaged using the TappingTM and PeakForce quantitative nanomechanical (PQNMTM) modes with a MultiMode 8 AFM microscope of Bruker controlled by a Nanoscope V controller and driven by Multimode v.8.15 software. Simultaneously, film topography and nanomechanical properties were measured. Further, the AFM analysis, which included the determination of film roughness, thickness, and phase changes within the film, was performed using NanoScope Analysis v.1.2 software of Bruker. The Derjaguin, Muller, and Toporov model was used to calculate Young modulus³⁶³ and unravel the nanomechanical properties.

AFM was used to characterize the solution aging wherein **MIP-2a** films, prepared using a fresh solution and the solution aged for one day, were imaged and analyzed. Furthermore, AFM was applied to observe differences between thick (**MIP-2a**, NIP-2a) and thin (**MIP-2b**, NIP-2b) films before and after exposure to (acetic acid) : methanol (1 : 1, v/v) extraction solution.

2.2.1.c6 High-performance liquid chromatography (HPLC)

The electrosynthesis was followed by an HPLC analysis on a Shimadzu Corp. (Kyoto, Japan) HPLC setup. This setup comprised a DGU-20A degassing unit, a liquid chromatography (LC) LC-20AT unit with controlled gradient mobile-phase elution, and an SPD-M20A UV-vis diode array detector. The compounds were separated using a Luna[®] 5 μm C18(2) 100 Å reversed-phase LC column (dimension $250 \times 4.6 \text{ mm}^2$ from Torrance, CA, USA). Gradient elution was performed with ACN (Solvent B) and Millipore water with a resistivity of 18.2 M Ω cm (at 25 °C) (Solvent A) mobile phase. A linear gradient was accomplished with the Solvent A to Solvent B volume ratio from the initial 50 : 50 to the final 5 : 95 value during 20 min. The compounds were separated at 30 (± 0.5) °C. Reference standards of the **DMP_h** reactant and the **TMB_h** desired product dissolved with 100 mM (TBA)ClO₄ in the ACN : DCM (9 : 1, v/v) solution were used for identification and calibration plots preparation. The HPLC system was controlled with LabSolutions software provided by the Shimadzu company.

2.2.2 Silver nanocomposites

2.2.2.a *Materials and chemicals*

The materials and chemicals used for the Silver nanocomposites project are as follows.

1. Silver nitrate, AgNO₃, purity 99.9% (POCH S.A.).
2. Brewery wastes from Jablonowo brewery (Wólka Kosowska, Poland).
3. Doubly distilled deionized water (resistivity 15 MΩ cm).
4. *N,N'*-Dimethylformamide, anhydrous, 99.8% purity (Sigma-Aldrich).
5. Potassium ferrocyanide, K₄[Fe(CN)₆]·3H₂O, p.a. (Chempur).
6. Potassium nitrate, KNO₃, p.a. (POCH S.A.).
7. Sodium hydroxide, NaOH, purity 98.8% (POCH S.A.).
8. di-Sodium hydrogen phosphate, Na₂HPO₄, anhydrous, p.a. (Chempur).
9. Sodium dihydrogen phosphate monohydrate, NaH₂PO₄ H₂O, p.a. (POCH S.A.).

2.2.2.b *Experimental techniques and methods*

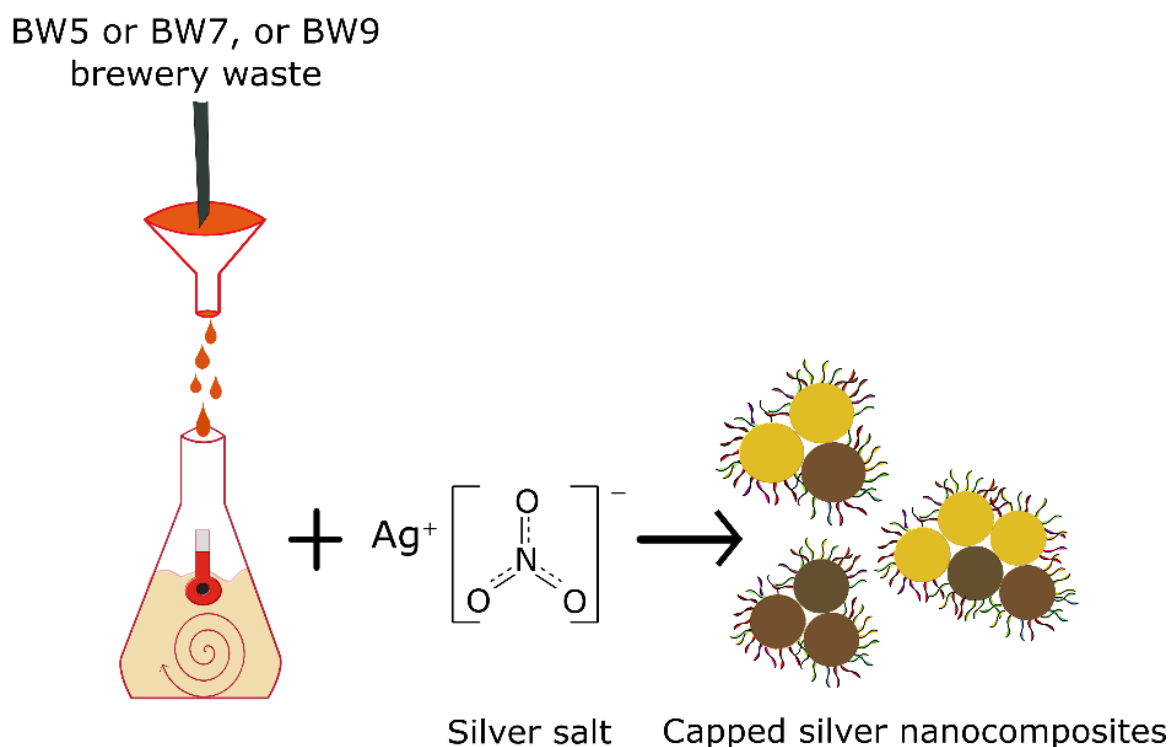
2.2.2.b1 Brewery wastes analysis methods

The total nitrogen, polyphenols, carbohydrates, sugars (fructose, glucose, maltose and sucrose, maltotriose, sulfate (SO₄²⁻), and TOC in brewery wastes were quantified. The elemental content of most elements was determined by a conventional combustion method. Chlorine was determined by argentometric titration with the AgNO₃ standard solution³⁶⁴. The total nitrogen content was determined using the Kjeldahl titration (PN-A-04018:1975)³⁶⁵. The total polyphenols content was determined using the spectrophotometric method (PN-A-79093-13:2000)³⁶⁶. The total carbohydrate content was determined using the spectrophotometric method according to Analytica EBC, 2.7.3 MEBAK (2013)³⁶⁷. The total sugar content was determined using HPLC with refractometric detection (HPLC-RID); external standards were used according to 9.27, 8.7 Analytica EBC, 2.7.2 MEBAK (2013)³⁶⁸. The sulfate content was determined using HPLC with conductometric detection (HPLC-CD) and an external standard according to 2.22.1 MEBAK (2013)³⁶⁹. The TOC was quantified using the spectrometric method according to CLA/SR/26/2012³⁷⁰. The pH of the brewery wastes was measured using an MP220 (Mettler-Toledo, USA) pH meter.

2.2.2.b2 Preparation of silver nanocomposites

Brewery wastes-mediated nanocomposite synthesis was a simple one-pot reaction (Scheme 2.3). The BW5, BW7, and BW9 unprocessed filtered brewery wastes were directly

used for NPs synthesis without any preliminary chemical processing. For the project's duration, the bulk brewery wastes were stored at 4 (\pm 1) °C. All of the brewery wastes were filtered using 150 mm Whatman filter paper (11 μ m) before using them for synthesis.



Scheme 2.3. Valorization of brewery wastes for nanoparticle (NP) synthesis.

A measured volume (50 mL) of the filtered brewery waste (BW5, BW7, or BW9) was heated under magnetic stirring at a constant rate of 100 revolutions per minute (rpm) until the desired temperature (25 or 50, or 80 °C) was attained. Subsequently, silver nitrate was added to the filtered waste to reach its final concentration of 100 mM. The syntheses were performed at various times (10, 30, or 120 min) at 80 (\pm 1) °C, as well as for 120 min at different temperatures, 25 (\pm 1) and 50 (\pm 1) °C. After the synthesis, the solution was cooled for up to 10 min to \sim 35 °C. Then, the solution was centrifuged at 10,000 rpm in a centrifuge model MPW 351R (MPW MED. INSTRUMENTS, Warsaw, Poland) for 40 min. The centrifugation temperature was maintained at 20 °C. The supernatant was discarded, following which doubly distilled deionized water was used to wash the NPs twice, sufficient to obtain pure nanocomposites. Each washing was followed by centrifugation at 10,000 rpm for 20 min. Finally, the NPs were kept for drying for 24 h at \sim 40 (\pm 2) °C in an oven (model SLN53 STD INOC/G, POL-EKO-APARATURA SP.J., Wodzisław Śląski, Poland) under natural airflow

conditions. Afterward, NPs in the ground powder form were directly used or dispersed in a solvent for further analyses.

2.2.2.b3 Preparation of silver nanocomposites' coatings

For photoelectrochemical characterization, fluorine-doped tin oxide (FTO) coated glass slides of $15 \times 35 \text{ mm}^2$ dimensions were rinsed with deionized water, then washed in methanol under ultrasonication for 15 min. Next, the nanocomposites were dispersed in *N,N*-dimethylformamide (DMF) using a probe ultrasonicator (amplitude 40%, model VCX 130 of SONICS Vibra-Cell, Newtown, CT, USA) in the pulse mode for 30 min to yield a concentration of 9 mg mL^{-1} . The pulse mode was used to prevent the solution from overheating. Then a 100- μL sample of the nanocomposite suspension was drop-cast on the FTO glass slide and dried at $50 (\pm 2) \text{ }^\circ\text{C}$ for 2 h in an air oven (model SLN53 STD INOC/G, POL-EKO-APARATURA SP.J., Wodzisław Śląski, Poland).

For the electrochemical ORR, 4 mg of the nanocomposites were dispersed in 1 mL of DMF using the probe ultrasonicator in the pulse mode for 30 min to 1.5 h, depending on the dispersibility of the nanocomposites. The RRDE [Pt ring / glassy carbon (GC) disk] electrode consisted of the GC disk of 4-mm diameter and Pt ring of 7-mm outer and 5-mm inner diameter with a 1-mm Teflon spacer. This electrode was first roughened using PP 2500 sandpaper to enhance coatings' adhesion. The GC disk was drop-coated with a 10- μL sample of the suspension and then allowed to dry for 30 min. The process was repeated thrice to reach optimum coverage. Finally, the RRDE was kept in the air for 15 min to dry the film entirely before electrochemical measurements. Noticeably, DMF was used because of high viscosity and hydrophobicity to enable stable coatings in aqueous solutions yet evaporated reasonably quickly. As DMF is not a green solvent, finding alternative ways to form stable nanocomposite coatings is imperative.

2.2.2.b4 Photoelectrochemistry

The nanocomposites were photoelectrochemically characterized using a three-electrode Teflon cell with a quartz window of 0.28 cm^2 surface area. The $15 \times 35 \text{ mm}^2$ FTO glass slides were used as working electrodes, a palladium sheet as the counter electrode, and an Ag/AgCl (3.0 M KCl) as the reference electrode. Sodium phosphate buffer solution (pH = 7.2) was used in all experiments to maintain the integrity of the nanocomposite structure. A 150 W Oriel AM1 Solar Simulator was used to provide illumination to activate the material with the light intensity of 100 mW cm^{-2} . A CHI Mod. 660E potentiostat (CH Instruments Inc., Austin, TX,

USA) was used to perform LSV experiments with a scan rate of 10 mV s^{-1} between 0.50 and 1.00 V vs. Ag/AgCl. The mechanical chopper was used to chop the light beam illuminating the electrode.

2.2.2.b5 Electrocatalytic oxygen reduction reaction (ORR)

The ORR was tested at an RRDE (model RRDE-3A of ALS Co. Ltd., Japan). The 100 mL electrochemical cell was made of glass with a Teflon cap containing ports for the three electrodes and inlets for pumping gas. Rubber gaskets were used to seal the cell. A 4-mm diameter 45-mm long graphite rod was used as the counter electrode and an Ag wire as the quasi-reference electrode. The potassium ferrocyanide redox probe formal potential was determined vs. the Ag quasi-reference electrode to standardize the measurements. The potential of 1 mM potassium ferrocyanide (0.165 V) vs. Ag quasi-reference electrode in the 0.1 M KNO_3 solution was shifted by $\sim 55 \text{ mV}$ in the negative direction compared to potassium ferrocyanide potential vs. Ag/AgCl. The reported formal potential of potassium ferrocyanide is $\sim 0.22 \text{ V}$ vs. Ag/AgCl in an aqueous solution of KCl or KNO_3 ³⁷¹⁻³⁷². Notably, this potassium ferrocyanide formal potential vs. Ag/AgCl is pH dependent.

The ORR experiments were performed in O_2 saturated 0.1 M KNO_3 or 0.1 M NaOH aqueous solutions at different rotation rates (0, 400, 800, 1000, 1200, 1600, and 2000 rpm). KNO_3 was chosen as the electrolyte because it ensured nanomaterials' stability. The pH effect on the electrocatalytic oxygen reduction by the nanocomposites was tested using NaOH. Oxygen was purged for 10 minutes before the experiment and 2 minutes before each measurement. The potential was swept between 0.00 and -1.00 V vs. Ag quasi-reference electrode. The experiments in a deaerated environment were performed by purging Ar gas into the cell for 15 minutes before starting and performing the experiments under Ar flow.

2.2.2.c Characterization techniques

2.2.2.c1 Attenuated total reflectance Fourier-transform infrared (ATR-FTIR) spectroscopy

The composition of the surface organic coating of nanocomposites can be understood through the FT-IR spectroscopy characteristic bands of functional groups that form a part of this capping on the Ag nanocomposite surface. Single-reflection Platinum ATR (Bruker) accessory was used for experiments with powder nanocomposites at decreased pressure (below 5 hPa). The FT-IR spectroscopy measurements for brewery waste solutions were carried out under dry nitrogen at decreased pressure (below 5 hPa) with the multi-reflection attenuated total

reflectance accessory A537-A/Q Overhead ATR unit (Bruker) involving multi-ATR and deuterated triglycine sulfate (DTGS) detector using Vertex 80V FT-IR spectrophotometer (Bruker Inc., Billerica, MA, USA). The spectra were recorded with 2 cm^{-1} resolution using 1024 scans.

2.2.2.c2 Ultraviolet-visible (UV-vis) spectroscopy

The Shimadzu UV-2501PC spectrophotometer recorded the UV-vis spectra of nanocomposites dispersed in deionized water between 190 and 800 nm with 0.5 nm resolution. The cuvettes were made of quartz, and the path length of the cuvettes was 1 cm. The nanocomposites were dispersed using a 35 kHz bath ultrasonicator (model RK52H, BANDELIN electronic GmbH & Co. KG, Berlin, Germany) for 20 min.

2.2.2.c3 X-ray diffraction (XRD)

The Empyrean D8 X-ray diffractometer (Bruker Inc., Billerica, MA, USA) was used to record polycrystalline nanomaterials' powder XRD (PXRD) patterns. This apparatus was equipped with Bragg-Brentano geometry, an X-ray tube (Cu K_{α} radiation) with K_{β} filters, and a goniometer in a θ - θ vertical system. The slits used were $1/4^{\circ}$ fixed divergence slit with anti-scatter slit and $1/8^{\circ}$ anti-scatter slit. The measurements were performed with spinning at the 40-kV voltage and 40 mA current settings. The chemical compounds and their phases in the NPs were identified using X'PertHighscore Plus software³⁷³. The phase composition was determined from the most intense PXRD reflexes representing each phase, i.e., (012) at $2\theta = 33.3^{\circ}$ for Ag_3PO_4 , (002) at $2\theta = 32.3^{\circ}$ for AgCl and (111) at $2\theta = 38.1^{\circ}$ for Ag metal (Ag_{met}). The method applying the reference intensity ratio (RIR) values to corundum was applied to calculate the phase content³⁷⁴. The Scherrer equation (Equation 2.11), using a constant of 0.94 and accounting for the reflexes of each phase in the 2θ range of 20° – 60° was applied to evaluate the average values of crystallite size and the respective standard deviations when considering more than one reflex.

2.2.2.c4 Energy-dispersive X-ray fluorescence spectroscopy (EDXRF)

A MiniPal 4 PW4025/00 EDXRF spectrometer (PANalytical Inc., Malvern, UK) with a rhodium lamp operating at a maximum voltage of 30 kV and a Si-PIN semiconductor detector was used to analyze the elemental composition of nanomaterials. The nanocomposite powders were placed in a plastic sample holder with a transparent bottom prepared using $4\text{ }\mu\text{m}$ Prolene 4™ film. The samples were irradiated for 120 s with X-rays produced by the rhodium

lamp under spinning. Filters inside the spectrometer blocked the bremsstrahlung backscatter radiation, thereby improving the signal-to-noise ratio. The PANalytical MiniPal software package was used to deconvolute the spectra and identify the peaks using the library of characteristic element lines. The quantification was performed automatically by the algorithms embedded in the package.

2.2.2.c5 Scanning electron microscopy (SEM)/energy-dispersive X-ray spectroscopy (EDXS)

The Nova NanoSEM 450 (FEI, Hillsboro, OR, USA) recorded images of the nanocomposites synthesized at 25 (± 1) and 80 (± 1) °C during 120 min at 10 kV accelerating voltage and 5 mm working distance in immersion imaging mode, including charge neutralization for nanocomposites with low electrical conductivity. The EDXS attachment was connected to the SEM instrument for surface elemental mapping of the silver nanocomposites at 10 kV. A 512 \times 512 matrix was recorded in 16 frames with a dwell time of 200 s. The powdered nanocomposites were deposited on 12-mm wide double-coated carbon-filled acrylic adhesive (Ted Pella, Inc., USA) and attached to the sample holder.

2.2.2.c6 Brunauer-Emmett-Teller (BET) analysis

The BET analysis of nanocomposites was performed using the Surface Area & Porosity Analyzer (model ASAP 2020, MJ Micrometrics, Norcross, GA, USA). First, ~100 – 400 mg nanocomposite powders were degassed at 100 °C for ~7 h. Then, the analysis was performed. For the evacuation step of degassing, the temperature was set at 50 °C with a ramp rate of 10 °C min⁻¹ while the pressure was decreased to 10 mm Hg. Next, the heating phase occurred at 100 °C with the same ramp rate for 6 hours. Liquid nitrogen Dewars were used for the degassing and analysis.

2.2.2.c7 Thermogravimetric analysis (TGA)

The TGA data were acquired using a Mettler Toledo TGA/differential scanning calorimetry (DSC) 3+ apparatus in the temperature ranging from room temperature, 25 (± 1) °C to 800 °C under nitrogen flow at 10 °C min⁻¹ heating rate.

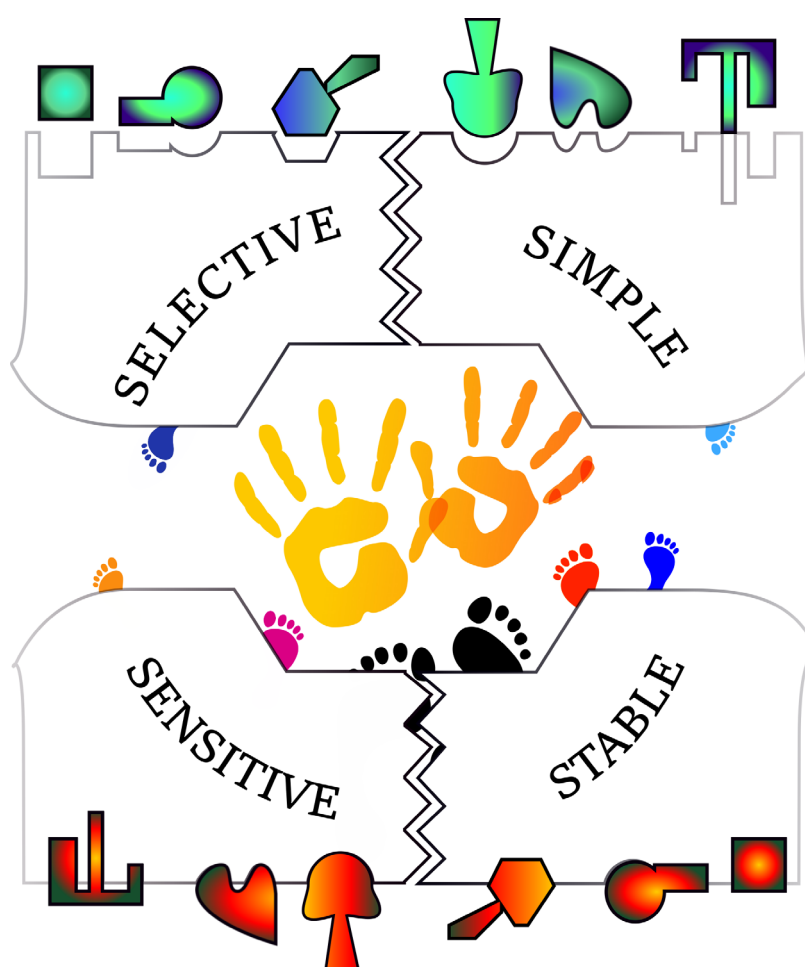
2.2.2.c8 Electron spin resonance (ESR) spectroscopy

Broker EMXplus X-band continuous wave spectrometer operating at 100 kHz field modulation and equipped with Teslameter, an ESR 4131VT temperature controller, and nitrogen cryostat was used for the ESR analysis. The ESR analysis parameters were 0.1 mT modulation amplitude, 1.28 ms time constant, 22.25 ms conversion time, 40 s sweep time for 30 mT field sweep, 500 mT sweep width, power 1 mW, spectra resolution 4000 points, and modulation frequency 100 kHz. The ESR spectroscopy analysis of nanocomposites was performed at room temperature, $25 (\pm 1) ^\circ\text{C}$. Gamma irradiation of 10 kGy at a dose rate of 1.87 kGy h^{-1} was also applied to the samples in the gamma chamber 5000 (BRIT, India) to examine the effect of irradiation on the exemplary nanocomposites synthesized at $80 (\pm 1) ^\circ\text{C}$ during 120 min. The absorbed dose was controlled with an alanine dosimeter according to ISO/ASTM 51607:2013(E)³⁷⁵. Cobalt 60 was used as the source for gamma radiation. Temperature-dependent measurements on γ -irradiated samples were accomplished starting from 100 K to room temperature with a step of 30 – 70 K.



3

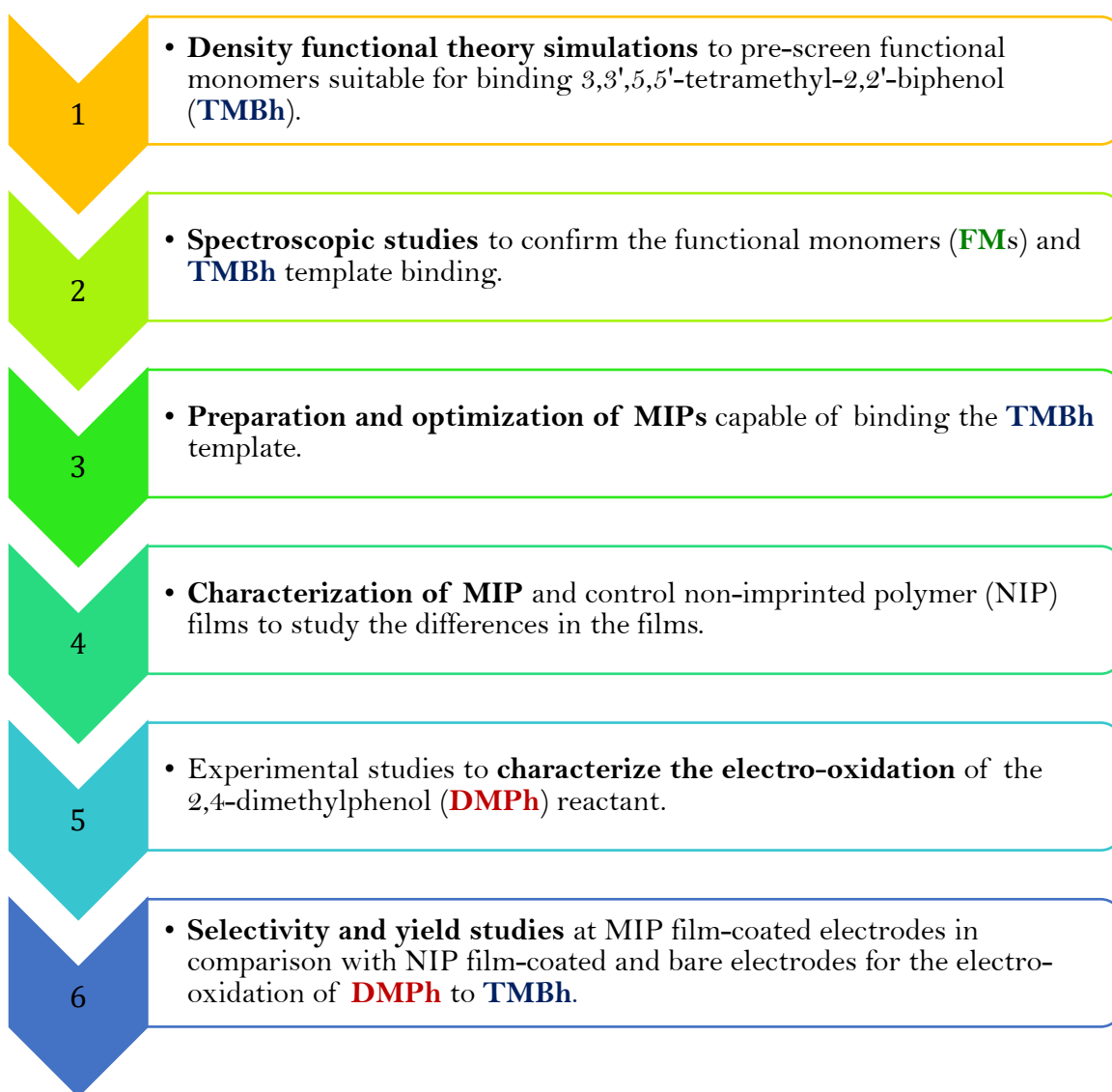
Molecularly imprinted polymers (MIPs) for selective electrosyntheses



† The image contains handprints sourced from www.freepik.com and footprints from www.stock.adobe.com.

3.1 Synopsis

The project aimed to develop MIPs for the selective electrosyntheses of 2,2'-biphenols, widespread motifs in natural products, catalysts, and pharmaceuticals. Our research focused on increasing the selectivity and yield of the electrosynthesis of these important chemicals. As a representative candidate, the electro-oxidation of **DMPH** to **TMBh** was chosen because this reaction's current yield and selectivity are quite low. The template for MIP preparation was our desired product, **TMBh**. The steps involved in this project are explained in Scheme 3.1.



Scheme 3.1. The project workflow for MIPs in selective electrosynthesis of **TMBh**.

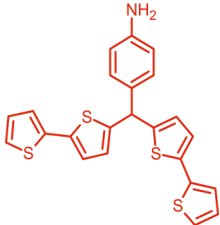
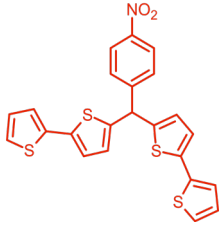
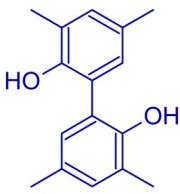
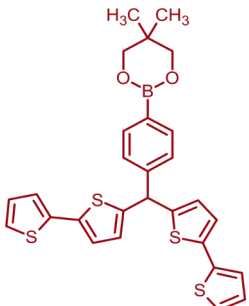
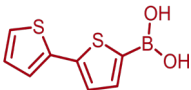
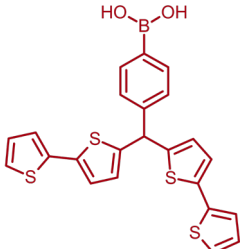
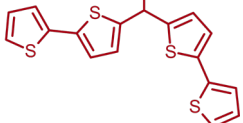
The major steps involved were DFT simulations to prescreen **FMs** that can bind the **TMBh** template, presented in **Section 3.2**. Further, **Section 3.3** describes experimental studies performed to confirm the binding of the **TMBh** template and **FM**. After confirming the binding, the MIPs were prepared, as **Section 3.4** reveals. Then, **Section 3.5** focuses on a phenomenon called 'solution aging' responsible for the irreproducibility of MIP film formation. Afterward, the optimized MIP and NIP films were characterized in **Section 3.6** to reveal their morphological characteristics and understand the extraction process's effect on the polymer films. Subsequently, these optimized films were applied for electro-oxidation of **DMPH**, and the products were identified using HPLC, as **Section 3.7** depicts. This section also elucidates a possible mechanism of selective electrosynthesis by MIPs. Finally, **Section 3.8** amasses the conclusions of the project.

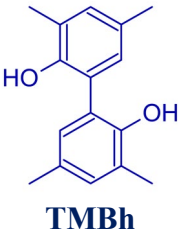
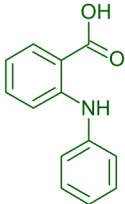
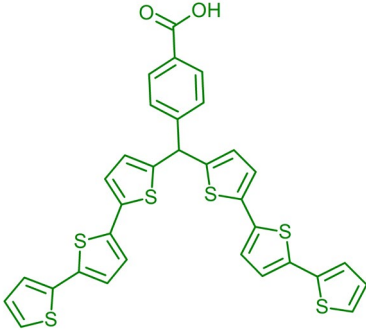
3.2 Density functional theory simulations to prescreen functional monomers (**FMs**)

The DFT calculations at the B3LYP/6-31g(d) basis set level were performed for compounds in a vacuum at room temperature (298.15 K) to screen **FMs** from the library based on non-covalent interactions. Interactions of several monomers containing various functional groups with the **TMBh** template were studied by comparing their standard Gibbs free energy change (ΔG_{bind}^0) accompanying the formation of pre-polymerization complexes (Table 3.1). The **FMs** containing nitrogen functional groups ($-\text{NH}_2$ and $-\text{NO}_2$) did not interact significantly with the **TMBh** yielding positive ΔG_{bind}^0 values. Furthermore, boron-based **FMs** were tested. The monomer with the protected boron atom reported here did not interact with the **TMBh** template, whereas the monomers containing unprotected boron-based functional group [$-\text{B}(\text{OH})_2$] very weakly interacted if the **TMBh** to **FM** molar ratio of 1 : 2 was used.

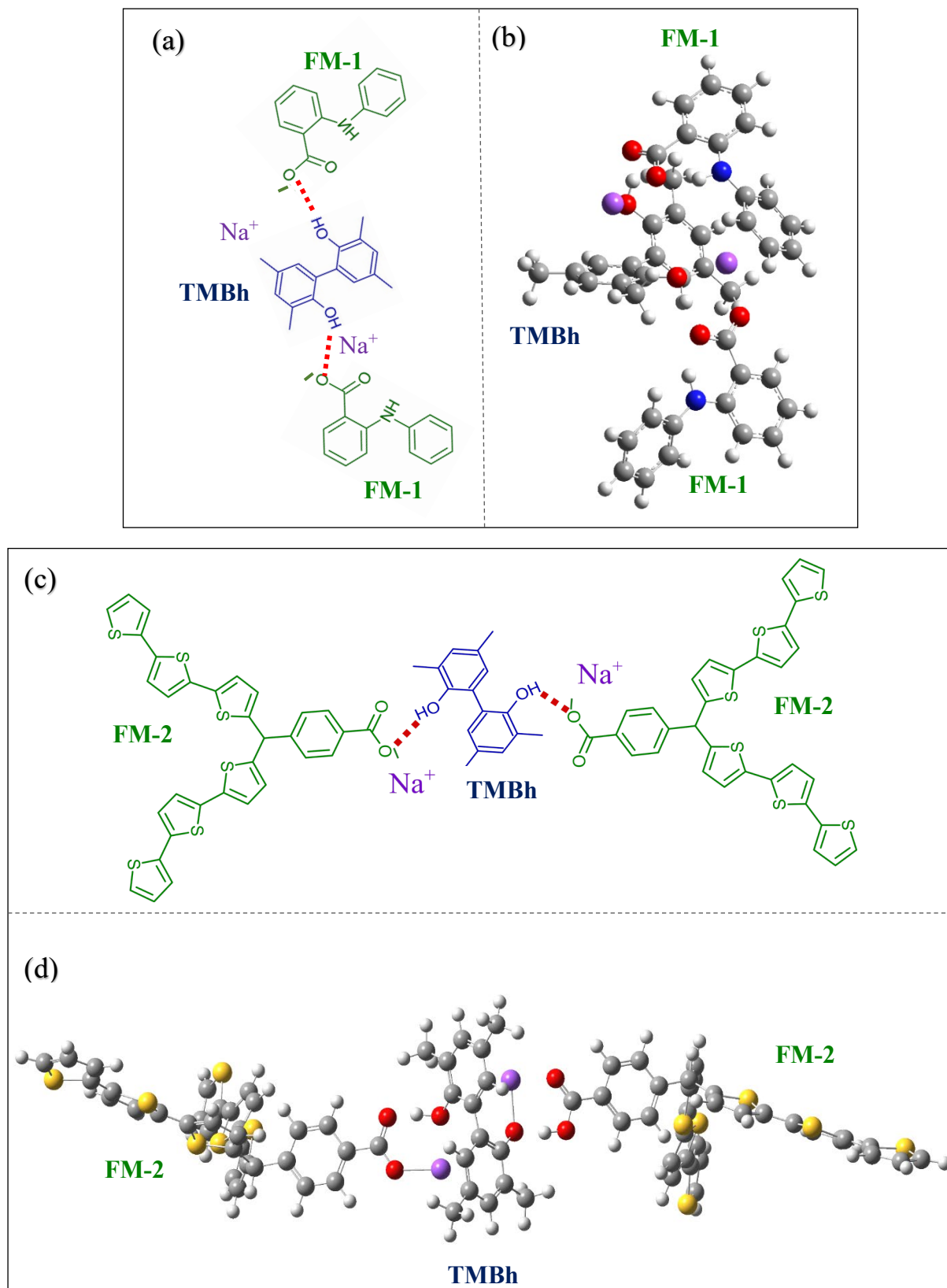
Finally, the $-\text{COOH}$ functional groups appeared most effective in binding the **TMBh** as their interactions resulted in high negative Gibbs free energy gain, especially in their carboxylate ($-\text{COO}^-$) form. The carboxylated form of the DACA commercial monomer (**FM-1**) most strongly interacted with the **TMBh** template revealing the ΔG_{bind}^0 value as high as -182 kJ mol^{-1} at the **TMBh** : **FM-1** molar ratio of 1 : 2. The ΔG_{bind}^0 value of the interaction of the newly synthesized monomer *p-bis(2,2';5',2''-terthien-5'-yl)methylbenzoic acid* (**FM-2**) with **TMBh** was about -68 kJ mol^{-1} at the **TMBh** : **FM-2** molar ratio of 1 : 2. If the carboxylate forms were used, the Na^+ ions were added for charge neutralization.

Table 3.1. Standard Gibbs free energy change (ΔG_{bind}^0) accompanying the interaction of the functional monomer (**FM**) with the **TMBh** template, calculated using DFT for compounds in vacuum at 298.15 K, at the B3LYP/6-31g(d) basis set level.

Template TMBh	Functional monomer FM	Complex stoichiometry TMBh : FM	ΔG_{bind}^0 kJ mol ⁻¹
	 <p><i>p</i>-Bis(2,2'-bithien-5-yl)methylaniline</p>	1 : 1	+21
	 <p><i>p</i>-Bis(2,2'-bithien-5-yl)methylnitrobenzene</p>	1 : 1	+15
 <p>TMBh</p>	 <p><i>p</i>-Bis(2,2'-bithien-5-yl)methylphenylboronic acid neopentylglycol ester</p>	1 : 1	+26
	 <p>2,2'-Bithiophene-5-boronic acid</p>	1 : 1	+2
	 <p><i>p</i>-Bis(2,2'-bithien-5-yl)methylphenylboronic acid</p>	1 : 1	+1
	 <p><i>p</i>-Bis(2,2'-bithien-5-yl)methylphenylboronic acid</p>	1 : 2	-1

Template TMBh	Functional monomer FM	Complex stoichiometry TMBh : FM	ΔG_{bind}^0 kJ mol ⁻¹	
 TMBh	 Diphenylamine-2-carboxylic acid (FM-1)	1 : 1	+6	
		1 : 2	+29	
		The carboxylate form interacts with Na ⁺ for charge neutralization		
		1 : 1	-85	
			↓	
			1 : 2	-182
	 <i>p</i> -Bis(2,2';5',2''-terthien-5'-yl)methylbenzoic acid (FM-2)	1 : 1	-9	
		1 : 2	-9	
		The carboxylate form interacts with Na ⁺ for charge neutralization		
		1 : 1	-63	
			↓	
			1 : 2	-68

The **TMBh** template with **FM** interaction plays a significant role in successfully preparing MIP films. Therefore, the two **FM**s, namely, diphenylamine-2-carboxylic acid, DACA (**FM-1**) and *p*-bis(2,2';5',2''-terthien-5'-yl)methylbenzoic acid (**FM-2**) with the carboxyl functional group were chosen based on their optimal interaction with the template at the **TMBh : FM** molar ratio of 1 : 2 (Scheme 3.2). The structural orientation of the DFT optimized structures is also shown in Scheme 3.2. Deprotonation of **FM** was crucial for strong interactions occurring. The **FM-1** is commercially available. Therefore, it is a preferred candidate for MIP preparation for electrosynthesis applications. However, **FM-2** is based on thiophene polymerization units known for effective electropolymerization and efficient conductive film formation³⁷⁶.



Scheme 3.2. (a, c) The structural formulae and (b, d) structure of the DFT B3LYP/6-31g(d) optimized pre-polymerization complex of the **TMBh** template with carboxylated forms of **FM-1** or **FM-2** at the molar ratio of 1 : 2 in a vacuum, including Na⁺ ions for charge neutralization.

3.3 **TMBh** template and functional monomers (**FMs**) binding

3.3.1 Ultraviolet-visible (UV-vis) spectroscopy titration

The UV-vis spectroscopic titrations were performed, and the resulting spectra were compared to those obtained by adding the spectra of pure components for the same complex stoichiometry. In these titrations, the complexation effects were relatively subtle, not producing clear isosbestic points. Moreover, the observed subtle shifts and other changes in the spectra were overlapped by the high-intensity bands of the components. UV-vis spectroscopy titrations (Figure 3.1 and 3.2) reveal the subtle effect of molecular interactions between the 2,2'-biphenol (BP) / **TMBh** template and **FMs** on the electronic transitions of molecules.

The BP with **FM-1** complexation has been studied in the absence (Figure 3.1a) and the presence of TEA (Figure 3.1b). BP was used as a **TMBh** template analog for preliminary studies as it is a cheaper, structurally similar alternative for **TMBh**. TEA was used as a strong base capable of deprotonating the carboxyl group of **FM-1**. In the absence of TEA, changes in the UV-vis spectra of the complex of BP with **FM-1** were insignificant up to the BP : **FM-1** molar ratio of 1 : 10, except for changes due to the superposition of the components' spectra (Figure 3.1a). However, there were some changes between the experimental spectrum for the BP : **FM-1** at the 1 : 10 molar ratio and the spectrum obtained by adding the components' spectra at the same ratio (Figure 3.1c). The bands at ~285 and ~350 nm were slightly shifted against those predicted theoretically. These shifts suggest weak interactions between the BP and **FM-1**, influencing the electronic structure of the aromatic system.

When TEA was added to the pre-polymerization complex solution, there were some visible changes in the spectrum of **FM-1** (Figure 3.1b). Notably, the band at ~285 nm was shifted to a higher wavelength (~290 nm), and the band at ~350 nm was shifted to a lower wavelength after TEA addition. Similar shifts can also be observed in the spectrum of BP. These shifts indicate some TEA interaction with the aromatic system of both components. Mixing both components led to a slight shift of the band at ~290 nm back to lower wavelengths. The broad band in the 325 – 400 nm region in the spectra of the pre-polymerization complex is asymmetric, consisting of superimposed bands. Moreover, the band maximum is shifted towards higher wavelengths when the components are mixed. This shift indicates more pronounced interactions between the BP and **FM-1** in the TEA presence. It also suggests the formation of two different forms of the complex. The band shape and position of its maximum changed with the BP : **FM-1** molar ratio increase from 1 : 1 to 1 : 10, indicating the formation

of the pre-polymerization complex. The comparison of the calculated and experimental spectra for the BP : **FM-1** molar ratio of 1 : 10 in the presence of TEA (Figure 3.1d) clearly shows the band shifts and band intensity differences, supporting the conclusion of stronger interactions between the BP and **FM-1** in the TEA presence.

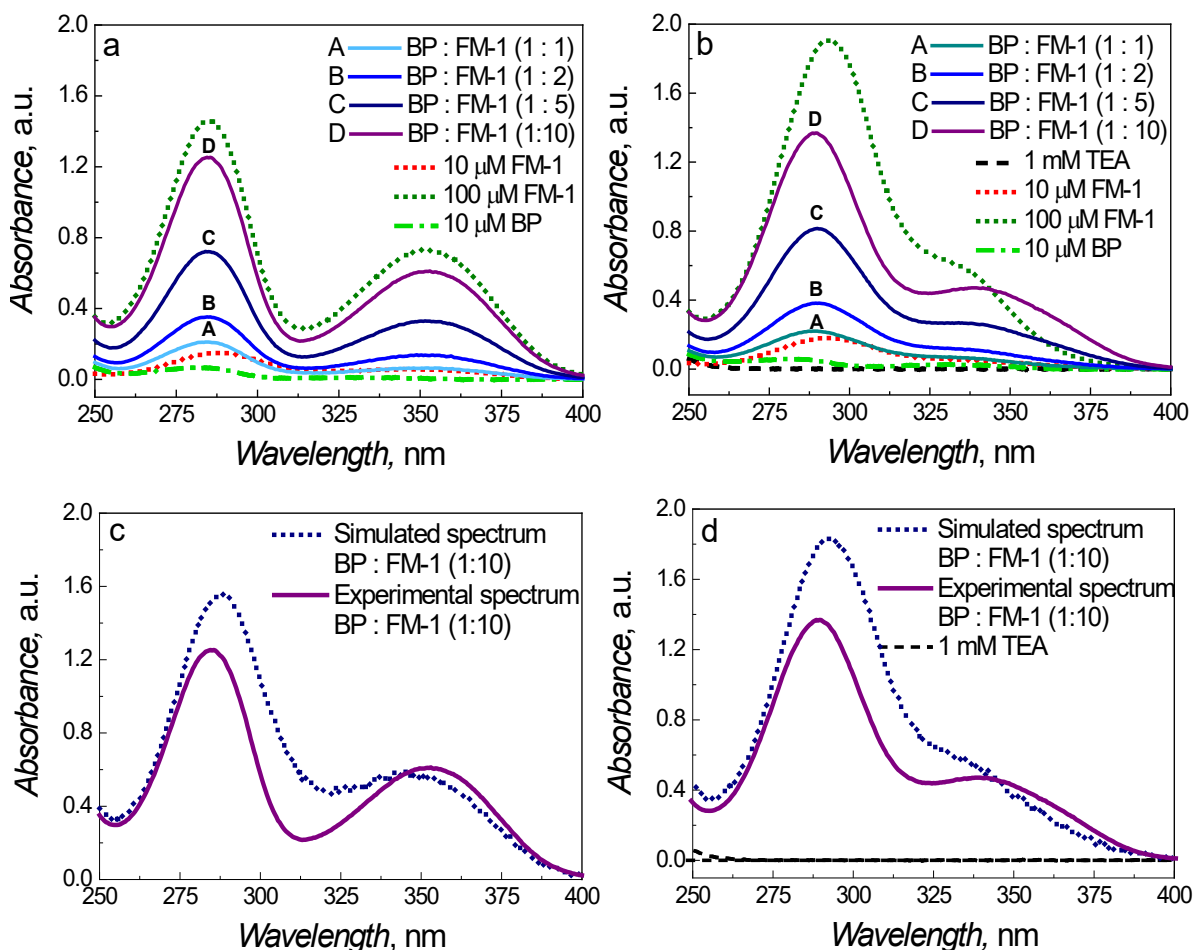


Figure 3.1. Experimental UV-vis spectra for complexation of BP and **FM-1** at different molar ratios compared with the spectra of BP and **FM-1** alone (a) in the TEA absence and (b) in 1 mM TEA. Comparison of experimental and simulated UV-vis spectra of BP and **FM-1** complexation at the BP : **FM-1** molar ratio of 1 : 1 (c) in the TEA absence and (d) in 1 mM TEA.

The complexation of the **TMBh** template and **FM-2** has also been studied in the TEA absence (Figure 3.2a) and presence (Figure 3.2b). The π - π transition bands of **FM-2** were very intense between 300 and 400 nm, overlapping the subtle changes due to the complexation of the **TMBh** template and **FM-2** (Figure 3.2a and 3.2b). Therefore, the subtle changes between experimental and simulated spectra in the TEA presence and absence could only be observed in the region below 300 nm (Figure 3.2c and 3.2d). In the region below 230 nm, there was a subtle difference between the simulated and experimental spectra at the **TMBh** : **FM-2** molar

ratio of 1 : 1 and 1 : 2, both in the TEA absence and presence. The differences were slightly more pronounced for the **TMBh** : **FM-2** complex of the 1 : 2 molar ratio indicating weak binding that affected the electronic transitions of the –COOH and –OH groups in the **FM-2** and **TMBh**, respectively. However, the changes below 215 nm were inconclusive because of the limits of optical resolution. In the region below 230 nm, the overall absorbance intensity of the **FM-2** and the complex also increased upon TEA addition, supporting the inference that absorption is linked with the electronic transitions of the –C=O group.

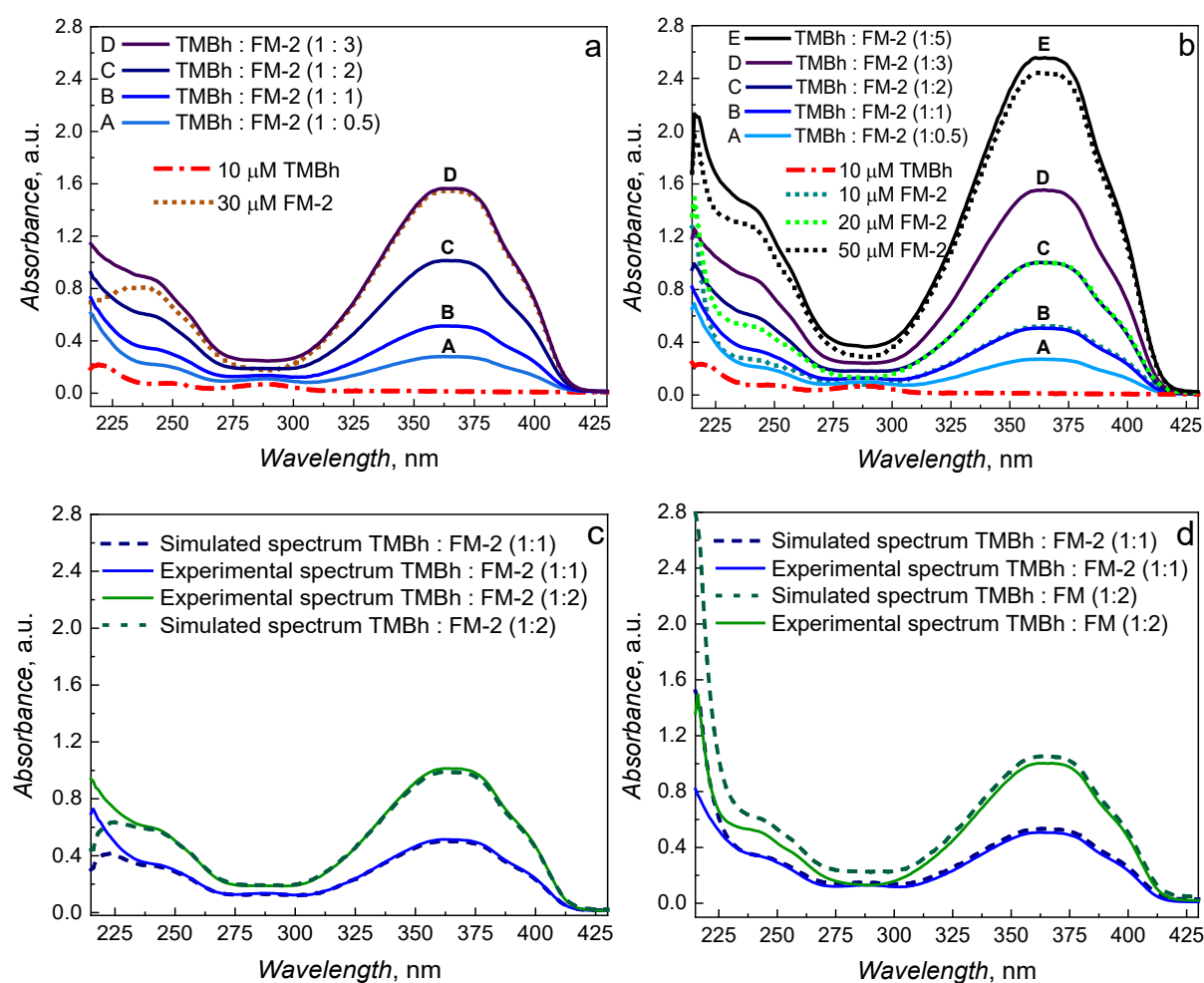


Figure 3.2. Experimental UV-vis spectra of complexation of **TMBh** and **FM-2** at different molar ratios compared with the spectra of **TMBh** and **FM-2** alone (a) in the TEA absence and (b) in 1 mM TEA. Comparison of experimental and simulated UV-vis spectra of **TMBh** and **FM-2** complexation at the **TMBh** : **FM-2** molar ratios of 1 : 1 and 1 : 2, (c) in the TEA absence and (d) in 1 mM TEA.

3.3.2 Fourier transform infrared (FT-IR) spectroscopic studies of monomer-template interactions

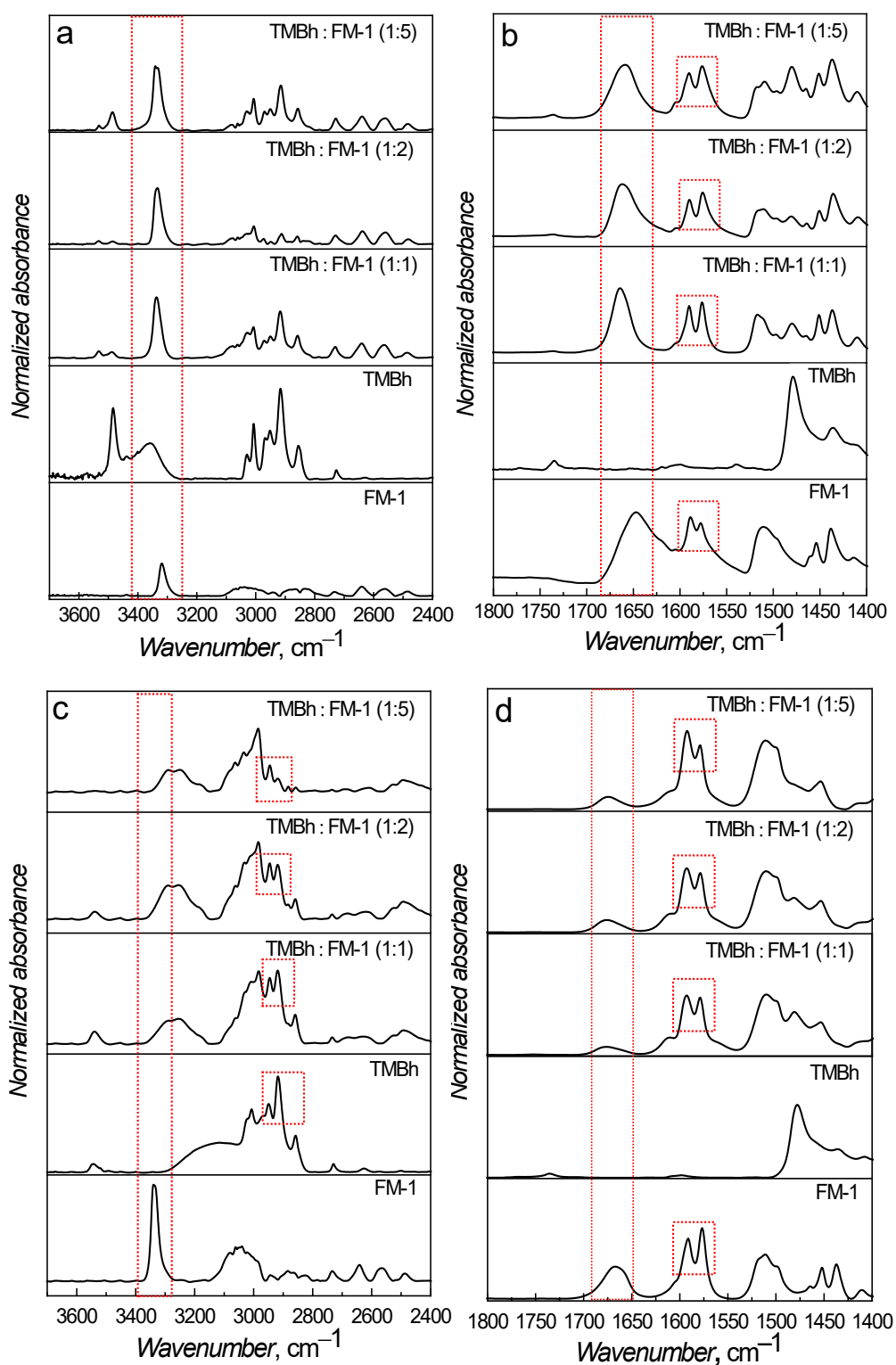


Figure 3.3. Experimental FT-IR spectra of complexation of **TMBh** and **FM-1**, in ACN, at different molar ratios compared with the spectra of **TMBh** and **FM-1** alone (a, b) without TEA and (c, d) in 1 mM TEA.

The FT-IR transmission spectroscopy titration was performed by drop-casting a pre-polymerization complex prepared in solution at different **TMBh**-to-**FM** molar ratios on ZnSe crystals. Strong and broad bands between 3200 and 3600 cm^{-1} , assigned to intermolecular-bonded OH stretching vibration of **FM-1**, were affected by the addition of the **TMBh** template (Figure 3.3a). Moreover, these bands' frequencies shifted to higher wavenumbers upon TEA addition (Figure 3.3c). Their intensities decreased relative to the alkene C–H stretching vibration band, indicating partial deprotonation of the **FM-1** carboxyl group. After the **TMBh** addition, the broad band at 1650 cm^{-1} , ascribed to vibrations of the carboxyl group of the **FM-1** monomer, shifted to higher frequencies by $\sim 25 \text{ cm}^{-1}$ (Figure 3.3b). Notably, this band also shifted to higher wavenumbers in the presence of TEA (Figure 3.3d). The **TMBh** addition, in this case, led to a further shift of this band to higher wavenumbers by $\sim 10 \text{ cm}^{-1}$ and a significant decrease in the relative band intensity. Furthermore, relative intensities of the characteristic doublet at $\sim 1570 \text{ cm}^{-1}$ representing the carboxyl C–O group vibration coupled to aromatic skeleton vibrations in **FM-1** changed after complexation with **TMBh** (Figure 3.3b and 3.3d). These changes were more pronounced for complexation in the TEA presence (Figure 3.3d). The spectra below 1400 cm^{-1} differed negligibly; therefore, they were not considered.

The **TMBh** and **FM-2** complexation slightly changed the bands representing the –OH and –COOH stretching vibrations (Figure 3.4). The broad stretching vibration bands between 3600 and 3200 cm^{-1} , representative of the –OH group, were slightly shifted to higher wavenumbers for the **TMBh** : **FM-2** complex of the 1 : 1 and 1 : 2 stoichiometry compared to the **FM-2** (Figure 3.4a). The differences in the band positions were more pronounced in the TEA presence (Figure 3.4c). Furthermore, the characteristic C=O vibration at $\sim 1700 \text{ cm}^{-1}$ was also affected, revealing the influence of binding on the molecular vibrations (Figure 3.4b). This band is a doublet of components at 1716 and 1696 cm^{-1} . The relative intensities of this two-component band decreased after **TMBh** addition. Moreover, the band's intensity at 1696 cm^{-1} increased compared to other bands present in the spectrum. Noticeably, the band at higher wavenumber (1716 cm^{-1}) increased after the interaction of **FM-2** with TEA (Figure 3.4d). Then, the **TMBh** addition led to further change in these two bands' relative intensities.

These differences in the UV-vis and FT-IR spectra of the pre-polymerization complex components (**FM-1** and **FM-2**, and BP / **TMBh**) and the (BP / **TMBh**) : **FM-1** and **TMBh** : **FM-2** complexes suggest that **TMBh** and **FM-1** / **FM-2** bind indeed, thereby confirming the predictions from DFT simulations. Although the observed changes are relatively small, they

indicate the presence of the binding, albeit not very strong, especially in the case of **FM-2**. Notably, the FT-IR bands' assignment was based on performed DFT simulations.

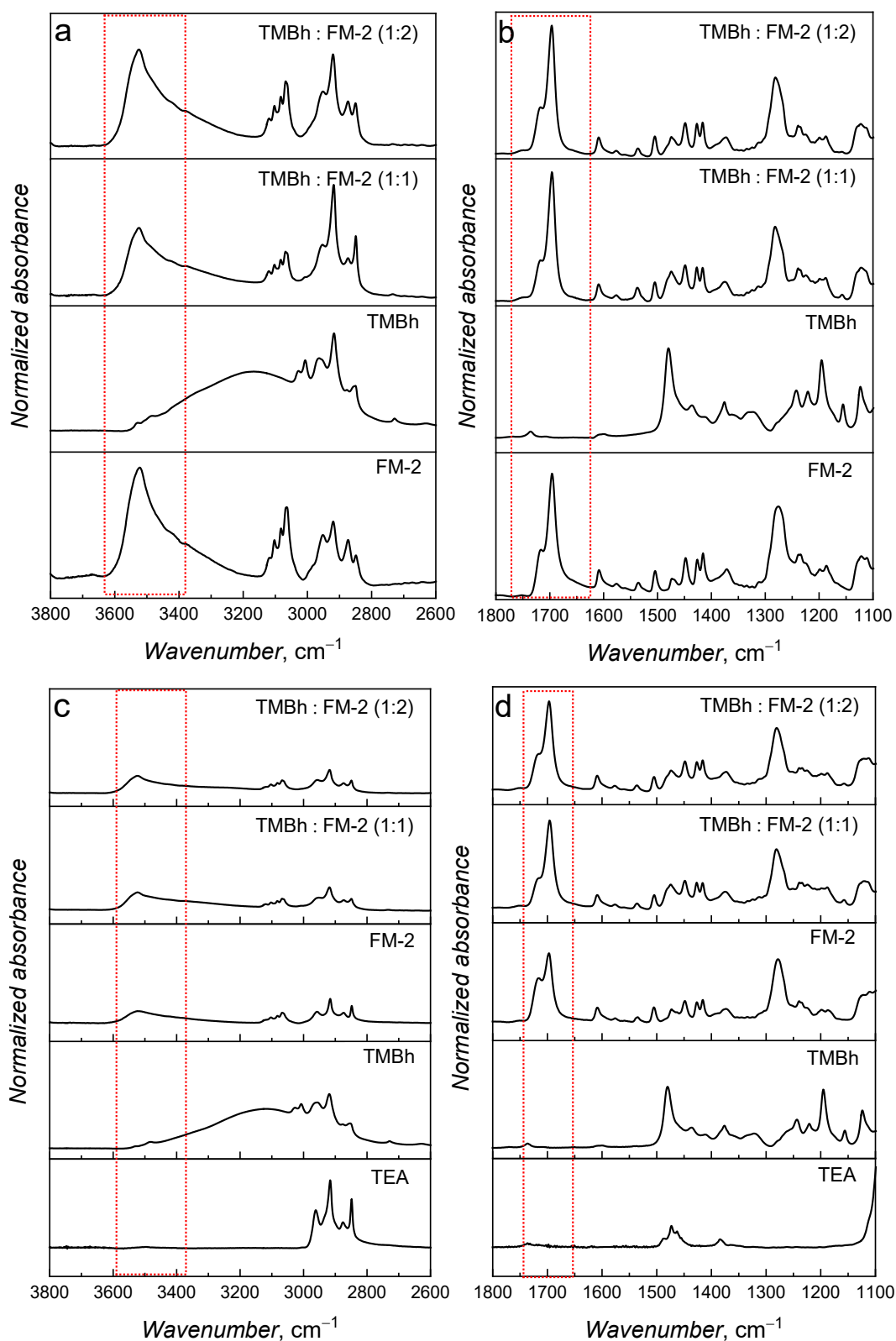
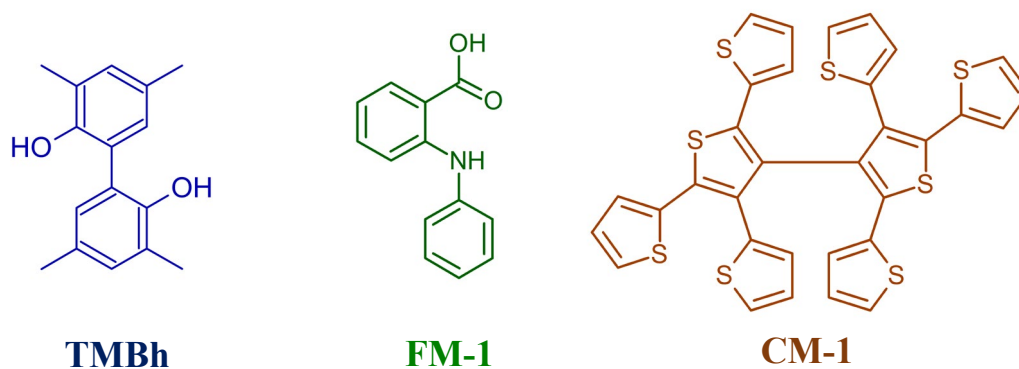


Figure 3.4. Experimental FT-IR spectra of complexation of **TMBh** with **FM-2** at different molar ratios compared with the spectra of **TMBh** and **FM-2** alone (a, b) without TEA and (c, d) in 1 mM TEA in ACN : DCM (9 : 1, v/v).

3.4 Preparation of molecularly imprinted polymer (MIP) and control non-imprinted polymer (NIP) films

3.4.1 MIP-1 films preparation



Scheme 3.3. Polymerization solution components, namely, 3,3',5,5'-tetramethyl-2,2'-biphenol - **TMBh** (template), diphenylamine-2-carboxylic acid, DACA - **FM-1**, and 2,4,5,2',4',5'-hexa(thiophen-2-yl)-3,3'-bithiophene - **CM-1**, for **MIP-1** films preparation.

The **MIP-1** film was prepared using the diphenylamine-2-carboxylic acid (DACA) **FM-1**, imprinted with the **TMBh** template. The advantage of using **FM-1** is that it is commercially available and, therefore, is beneficial for large-scale electrosyntheses. Following the results from experimental titrations confirming the formation of the pre-polymerization complex, MIP films were deposited on 0.75-mm diameter platinum disk electrodes in a three-electrode electrochemical cell. The complex was prepared by mixing the **TMBh** template, **FM-1** and **CM-1** at the molar ratio of 1 : 2 : 5 in ACN (Scheme 3.3). The electrolyte used was 0.1 M (TBA)ClO₄. The polymerization was carried out under potentiodynamic conditions with the potential cycled between 0.00 and 1.40 V vs. Ag quasi-reference electrode. These potential limits were imposed to prevent oxidation of the template, which is electro-oxidized at ~1.50 V vs. Ag quasi-reference electrode. The **MIP-1** films, prepared in both the absence (Figure 3.5a) and presence (Figure 3.5c) of TEA, were conductive, as indicated by the current increase with each cycle.

Interestingly, deposited polymer oxidation currents were observed at slightly lower potentials in the TEA presence than in the TEA absence. This effect indicates the formation of polymers with longer conjugation in the TEA presence. The template was extracted from the prepared **MIP-1** films with an (acetic acid)-methanol (1 : 1 v/v) solution. The extraction involved placing the electrode in the solution under stirring for a predetermined time. According to the "gate effect" principle explained in detail in Section 2.1.1.c of Chapter 2, an

increase in the DPV peak of the redox probe would indicate successful template extraction, leaving vacated molecular cavities in the MIP, which would result in easier transport of the redox probe through the film to the electrode surface. The **MIP-1** films, however, showed almost no change in the DPV peak initially up to 60-min extraction time and then a decrease in DPV peak currents of the redox probe (Figure 3.5b) after every extraction step up to 400 min. This behavior indicates that cavities are not formed, or the redox probe diffusion through the film is blocked because of either charge repulsion at the polymer surface or film swelling, leading to the blocking of available pores and cavities in the film.

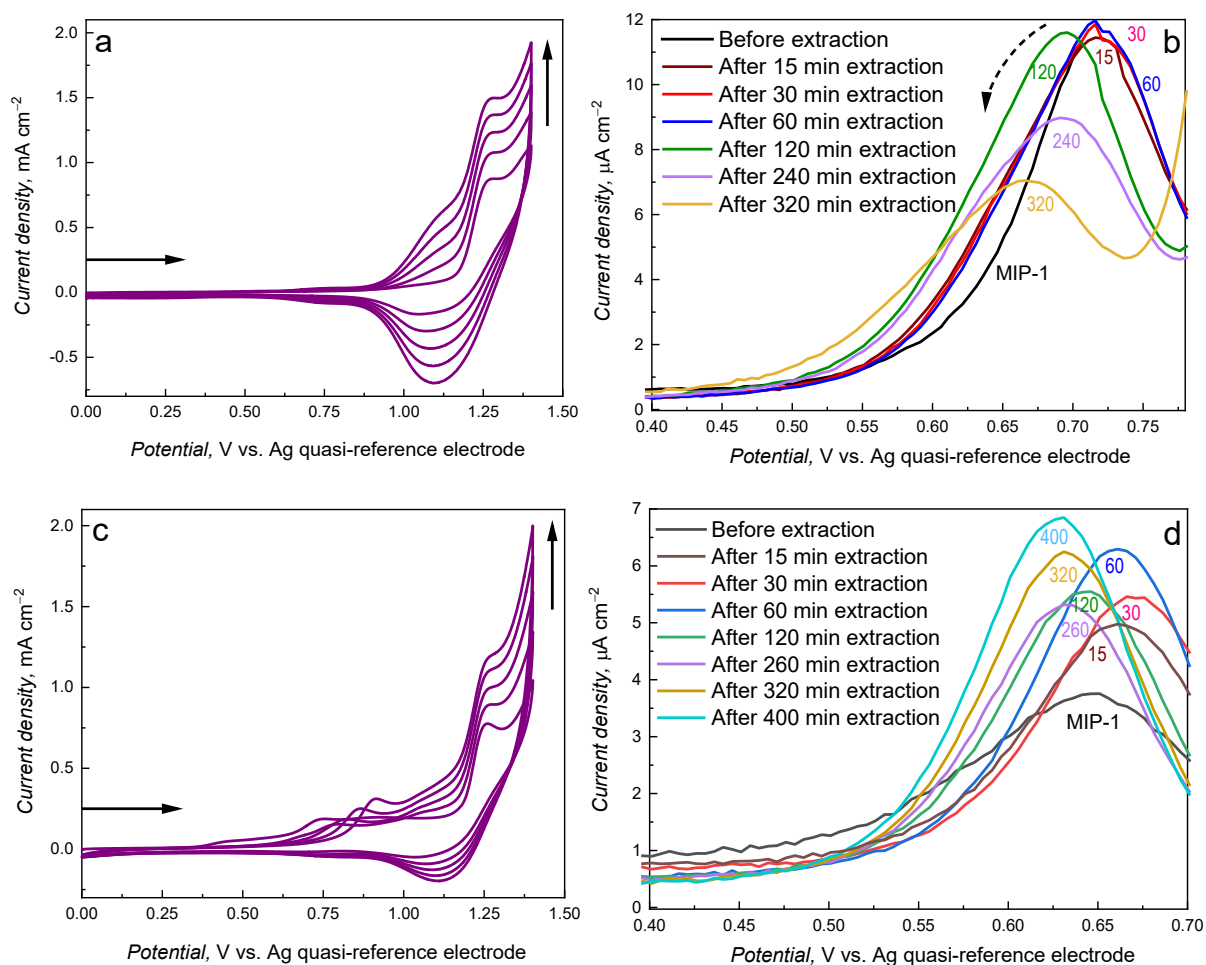


Figure 3.5. Multi-cyclic current-potential curves for potentiodynamic electropolymerization of the **MIP-1** film with five consecutive potential cycles at 50 mV s^{-1} scan rate in the ACN solution of $100 \text{ }\mu\text{M}$ **TMBh**, $200 \text{ }\mu\text{M}$ **FM-1**, $500 \text{ }\mu\text{M}$ **CM-1**, and 100 mM (TBA) ClO_4 (a) without and (c) with 1 mM TEA. DPV curves of 1 mM ferrocene redox probe at the **MIP-1** film-coated electrodes prepared (b) without TEA and (d) with TEA in 100 mM (TBA) ClO_4 in ACN before and after **TMBh** template extraction with (acetic acid) : methanol ($1 : 1, \text{ v/v}$) for up to 400 min.

On the other hand, the **MIP-1** films prepared in the presence of TEA (Figure 3.5c), added to deprotonate the **FM-1**, showed an increasing trend in the DPV peak of the redox probe (Figure 3.5d), which could be indicative of molecular cavity formation. This increase was observed up to 60 min of extraction. Then the DPV signal dropped and raised again, indicating a quite complex behavior, including at least partially destroying the polymer film. Notably, the DPV peak for the as-deposited **MIP-1** film prepared in the TEA absence was approximately four times higher (Figure 3.5b) than the DPV peak for the film deposited in the TEA presence (Figure 3.5d). This lower intensity peak indicates the formation of a more compact film in the presence of TEA. Several different **TMBh** : **FM-1** : **CM-1** ratios were tested, and the exemplary results are presented in Figure 3.5.

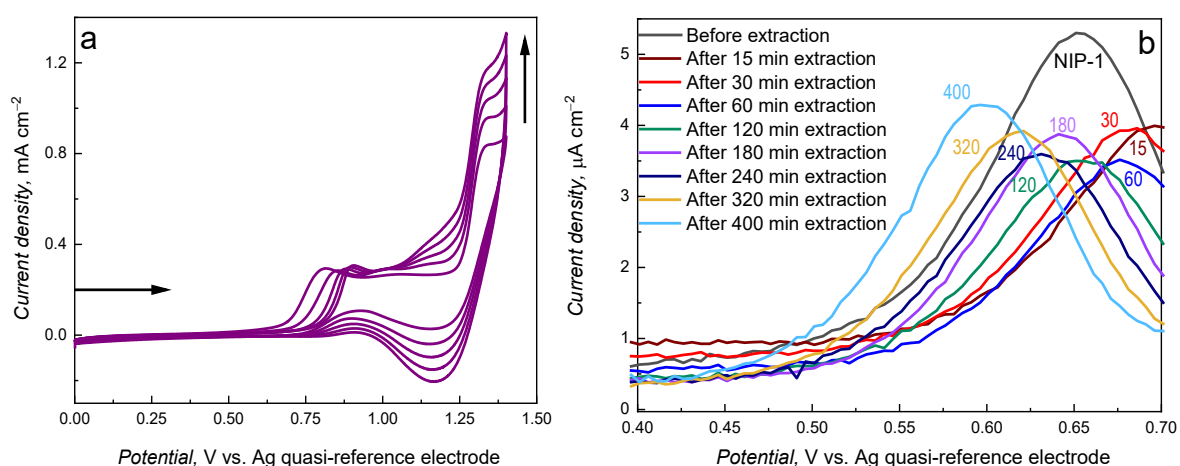


Figure 3.6. (a) Multi-cyclic current-potential curves for NIP-1 film deposition by potentiodynamic electropolymerization with five consecutive potential cycles at 50 mV s^{-1} using the ACN solution of $200 \text{ } \mu\text{M}$ **FM-1**, $500 \text{ } \mu\text{M}$ **CM-1**, 1 mM TEA, and 100 mM (TBA)ClO₄. (b) DPV curves for 1 mM ferrocene redox probe in 100 mM (TBA)ClO₄, in ACN, at the NIP-1 film-coated electrodes before and after exposure to the (acetic acid) : methanol (1 : 1, v/v) extraction solution for up to 400 min.

Moreover, NIP-1 films were deposited similarly to **MIP-1** films. Then the films were exposed to the same (acetic acid) : methanol (1 : 1, v/v) extraction solution (Figure 3.6a). Furthermore, a conductive polymer film was deposited in this case, similar to the **MIP-1** film. Unfortunately, the DPV studies of the template extraction from the NIP-1 films prepared in the TEA presence showed a peak for the as-prepared NIP-1 film similar to that for the **MIP-1** film prepared in the TEA presence. Furthermore, the decrease in the DPV peak after template extraction (Figure 3.6b) was seen up to 120 min of the extraction time. Then the peak increased. The evolution of the DPV peaks for **MIP-1** and NIP-1 films indicates complex film changes during the extractions, suggesting possible films' decomposition.

Furthermore, the **FM-1** electropolymerization ability was low (Figure 3.7). The well-polymerizing **CM-1** was added to prepare films using electrochemically initiated polymerization of the **FM-1**. However, this approach may lead to a small number of imprinted cavities as the dominant component of the polymer formed is the **CM-1**. Besides, the intramolecular H-bonding of the **FM-1** could be sufficiently strong to affect the intermolecular H-bonding with the **TMBh** template adversely. Given these issues, we decided to change the polymerization system.

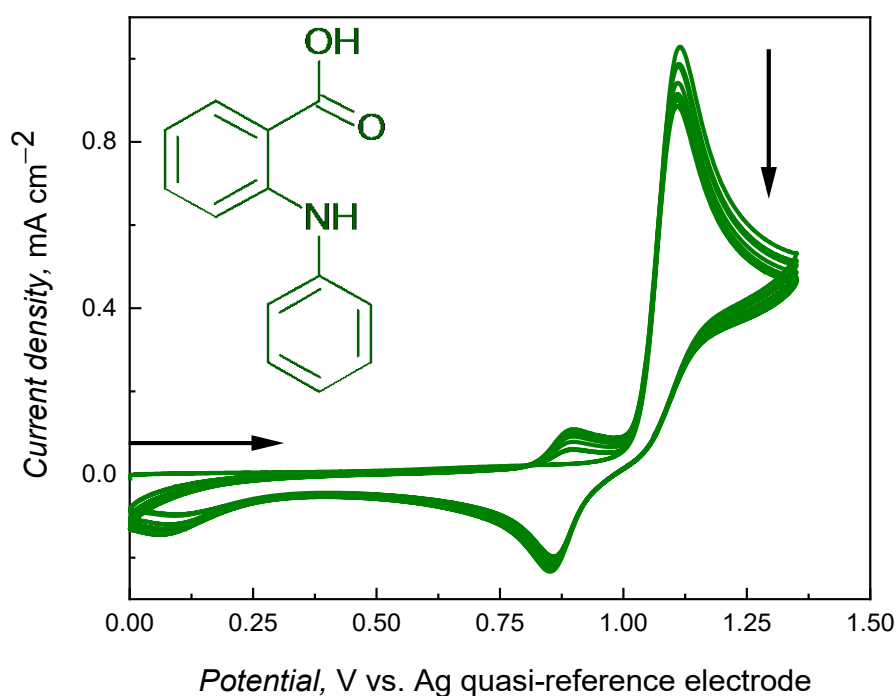
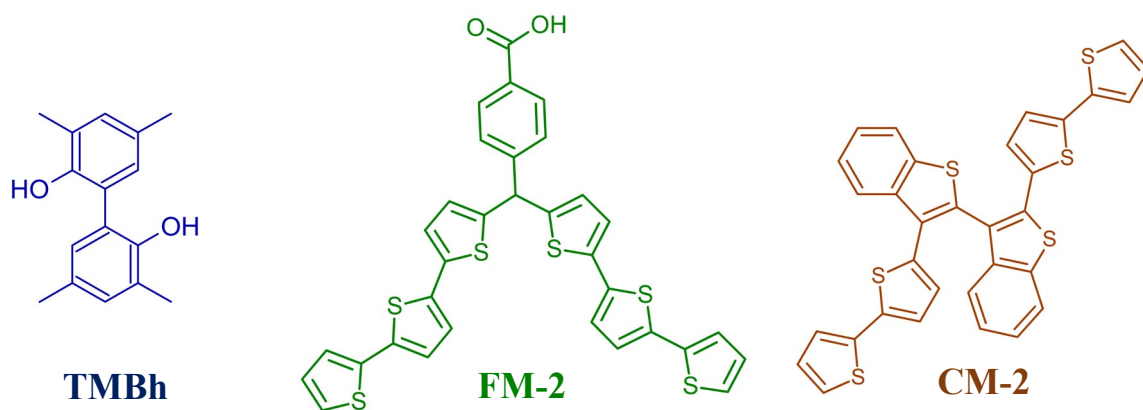


Figure 3.7. Multi-cyclic current-potential curves for the potentiodynamic electropolymerization of 1 mM diphenylamine-2-carboxylic acid (DACA) **FM-1**, recorded at a Pt bare electrode at a scan rate of 100 mV s^{-1} in 100 mM (TBA)ClO₄, in ACN.

3.4.2 MIP-2 films preparation

The new pre-polymerization complex for **MIP-2** deposition contained the **TMBh** template, newly synthesized [*p*-bis(2,2';5',2''-terthien-5'-yl)methylbenzoic acid] **FM-2** and [2,2'-bis(2,2'-bithiophene-5-yl)-3,3'-bithianaphthene] **CM-2** (Scheme 3.4). The calculated **FM-2** binding of the **TMBh** template was weaker, but it was easier to polymerize. The **MIP-2** films were also deposited under potentiodynamic conditions by oxidative electropolymerization.



Scheme 3.4. Structural formulae of polymerization solution components, namely, the **TMBh** template as well as the functional [*p*-bis(2,2';5',2''-terthien-5'-yl)methylbenzoic acid] **FM-2** and cross-linking [2,2'-bis(2,2'-bithiophene-5-yl)-3,3'-bithianaphthene] **CM-2** monomers for the preparation of **MIP-2** films.

The films were deposited within five consecutive cycles between 0.00 and 1.40 V vs. Ag quasi-reference electrode from 0.1 M (TBA)ClO₄ in ACN : DCM (9 : 1, v/v). The **TMBh** : **FM-2** : **CM-2** starting ratio was 1 : 2 : 10 (Figure 3.8a). An anodic peak starting at ~1.20 V vs. Ag quasi-reference electrode appeared during the electro-oxidation. It represented radical cation formation due to the electro-oxidation of the terthiophene and bithiophene units of **FM-2** and **CM-2**, respectively. In subsequent cycles, the anodic current between 0.80 and 1.10 V vs. Ag quasi-reference electrode grew, indicating the formation of polythiophene chains, oxidized at lower potentials more readily than bithiophene and terthiophene units³⁷⁷. The current increase with each consecutive cycle indicated conductive film deposition.

The **TMBh** template was then removed from the **MIP-2** film by extracting with the (acetic acid) : methanol (1 : 1, v/v) solution. Acetic acid was used for this extraction as it interacts with the template more strongly than the **FM-2**. Therefore, it can remove the template from the MIP film. This extraction was monitored via the same "gate effect" with DPV measurements using the ferrocene redox probe, as described previously¹²¹. The MIP film initially blocked the redox probe, enabling a very small DPV peak to flow (Figure 3.8b). After the extraction, the DPV peak increased and shifted to lower potentials, indicating a less restricted electron exchange with the electrode. The DPV peak reached a maximum after 180-min extraction, although it was significantly lower than that for **MIP-1** films.

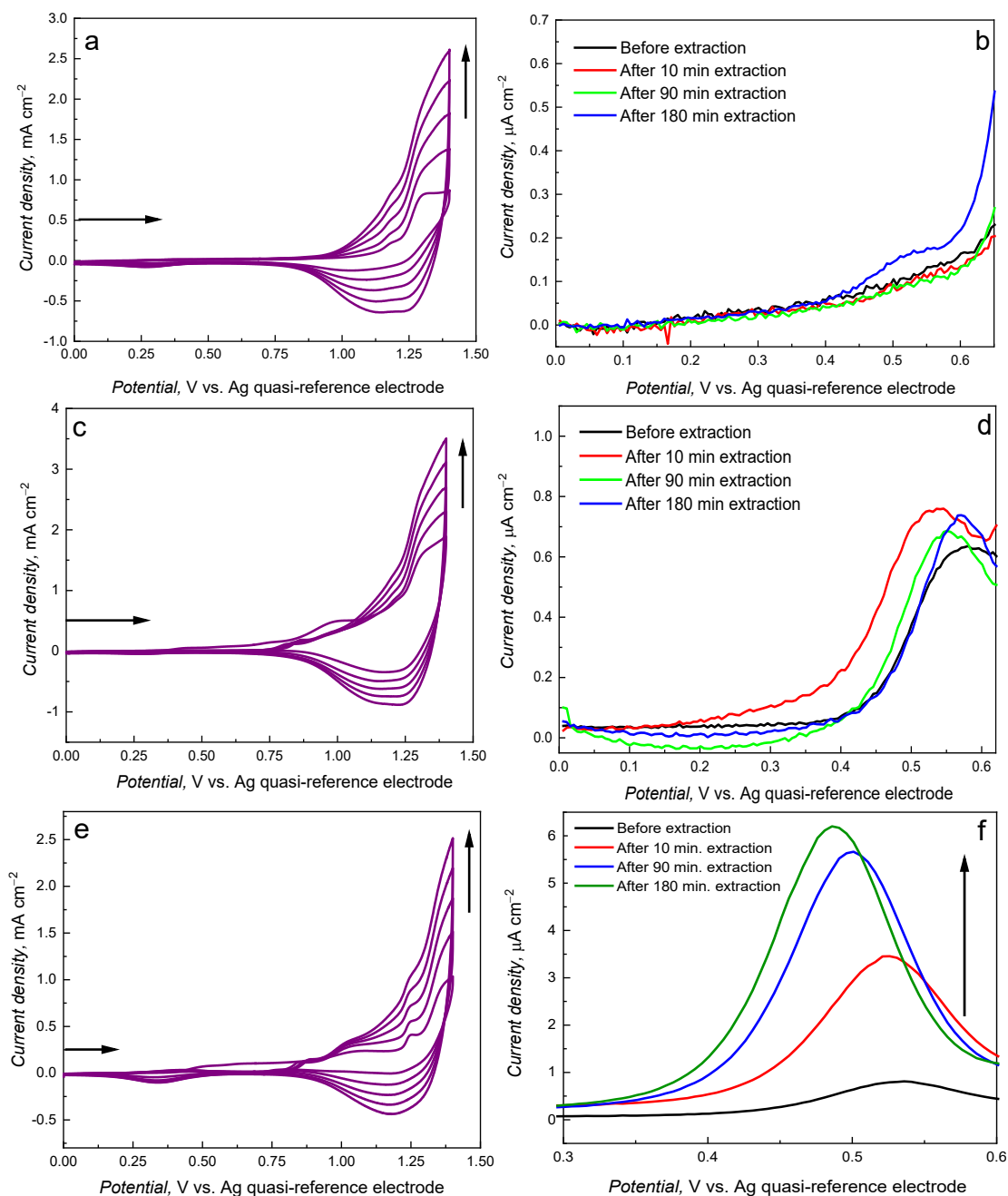


Figure 3.8. Multi-cyclic current-potential curves for **MIP-2** films deposition via potentiodynamic electropolymerization with five consecutive potential cycles at 50 mV s^{-1} scan rate in the ACN : DCM (9 : 1, v/v) solution of $100 \mu\text{M}$ **TMBh**, $200 \mu\text{M}$ **FM-2**, $1000 \mu\text{M}$ **CM-2**, and 100 mM (TBA)ClO₄ (**a**) without TEA and (**c**) in 1 mM TEA. The **TMBh** template extraction from the respective films (**b**, **d**) with (acetic acid) : methanol (1 : 1, v/v) for up to 180 min followed by a DPV measurement of 1 mM ferrocene redox probe in 100 mM (TBA)ClO₄ in the ACN : DCM (9 : 1, v/v) solution. (**e**) Multi-cyclic current-potential curves for optimized **MIP-2a** film deposition using potentiodynamic electropolymerization with five consecutive potential cycles at 50 mV s^{-1} in the ACN : DCM (9 : 1, v/v) solution of $200 \mu\text{M}$ **TMBh**, $400 \mu\text{M}$ **FM-2**, $1000 \mu\text{M}$ **CM-2**, and 100 mM (TBA)ClO₄ in 1 mM TEA, and (**f**) template extraction with the (acetic acid) : methanol (1 : 1, v/v) solution for up to 180 min followed by a DPV measurement of 1 mM ferrocene redox probe in 100 mM (TBA)ClO₄, in the ACN : DCM (9 : 1, v/v) solution.

After 180 min, the DPV peak did not increase further, indicating complete extraction. Noticeably, longer extraction times affected polymer films' integrity. Therefore, the extraction time of 180 min was selected for further studies. However, a measured small DPV peak increase indicated either a small number of cavities formed or high film thickness, significantly hindering the redox probe mass transport.

Therefore, TEA was used to deprotonate the **FM-2**, thus enabling stronger **TMBh** and **FM-2** interaction. The MIP film formation at the **TMBh** : **FM-2** : **CM-2** molar ratio of 1 : 2 : 10 in 1 mM TEA is shown in Figure 3.8c. In this case, also, a conductive film was deposited. The template extraction from this film resulted in much higher DPV peaks, indicating that the film was more permeable to the redox probe. A DPV peak increase with the extraction time indicates that the template extraction is more efficient (Figure 3.8d). However, the DPV peak is still much smaller than that for the **MIP-1** film, suggesting either a very compact film or a relatively lower number of cavities. Notably, the TEA concentration was optimized and kept at 1 mM, as increasing the TEA concentration further significantly restricted the **MIP-2** film formation. Therefore, the MIP film was not formed at higher TEA concentrations.

To improve the **MIP-2** film performance further by increasing the number of imprinted cavities in the film deposited, the **TMBh** : **FM-2** : **CM-2** molar ratio was changed to 1 : 2 : 5. The electropolymerization appeared similar to that previous, and a conductive film was formed (Figure 3.8e). From the DPV peak evolution, it follows that decreasing the (**FM-2**)-to-**CM-2** ratio improves the permeability of the redox probe through the polymer film (Figure 3.8f). Moreover, the peak considerably increased with the extraction time. This increase suggests that the number of cavities formed in this film was relatively higher. Therefore, the molar ratio of **TMBh** : **FM-2** : **CM-2** was kept at 1 : 2 : 5 in further experiments. The films prepared at this ratio in the TEA presence were called **MIP-2a**. Moreover, another set of films (**MIP-2b**) was prepared by diluting the pre-polymerization complex solution ten times to obtain thinner films. The electropolymerization and extraction conditions were the same as those used for preparing **MIP-2a** films.

Control NIP-2 films were prepared similarly to **MIP-2** films but without the template and then extracted under the same conditions as that for MIP films (Figure 3.9). The NIP-2a (Figure 3.9a) films were also conductive, and oxidation currents were slightly higher than for **MIP-2a** deposition may indicate higher film conductivity for the former. However, the films blocked the electrode strongly, as the ferrocene redox probe current was very small (Figure 3.9b). Significantly, the redox probe current did not increase even after 180-min

extraction with the (acetic acid) : methanol (1 : 1, v/v) solution. This behavior supports the conclusion regarding the formation of molecular cavities in **MIP-2a** film. Therefore, the **MIP-2** system (**MIP-2a** and **MIP-2b**) was further used to test the selective **TMBh** electrosynthesis.

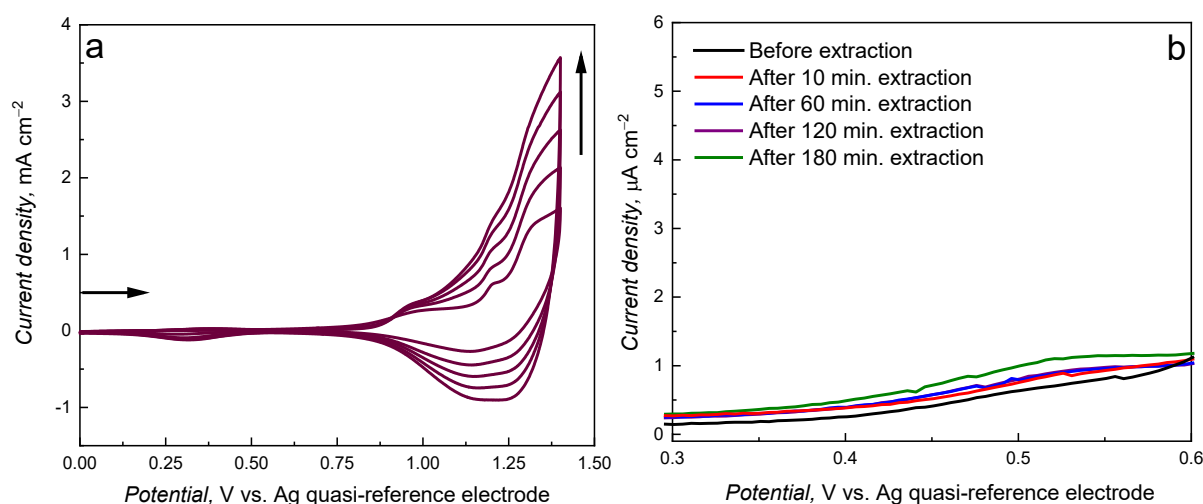


Figure 3.9. (a) Multi-cyclic current-potential curves for NIP-2a film deposition via potentiodynamic electropolymerization with five consecutive potential cycles at 50 mV s^{-1} in the ACN : DCM (9 : 1, v/v) solution of $400 \mu\text{M}$ **FM-2**, $1000 \mu\text{M}$ **CM-2**, and 100 mM (TBA)ClO₄, and 1 mM TEA. (b) DPV curves for 1 mM ferrocene redox probe in 100 mM (TBA)ClO₄ in the ACN : DCM (9 : 1, v/v) solution at the electrode coated with the NIP-2a film, prepared in the TEA presence before and after exposure to the (acetic acid) : methanol (1 : 1, v/v) extraction solution for up to 180 min.

3.5 Solution aging

The mechanism of the so-called 'aging' of the optimized pre-polymerization complex was studied to understand the observed irreproducibility in the **MIP-2** film preparation. The **MIP-2a** film deposition using the pre-polymerization complex, prepared by mixing the **TMBh** template, **FM-2**, and **CM-2** at the molar ratio of 1 : 2 : 5 in 0.1 M (TBA)ClO₄ and 1 mM TEA in the ACN : DCM (9 : 1, v/v) solvent mixture and subsequent template extraction from this MIP film, was irreproducible. Potentiodynamic curves for depositing **MIP-2a** films using freshly prepared pre-polymerization complex solution (Figure 3.8e) and aged solution stored at $4 (\pm 1) ^\circ\text{C}$ for one or two days (Figure 3.10a) differed only slightly. Mainly, a cathodic peak at 0.37 V vs. Ag quasi-reference electrode was more pronounced during film deposition from the aged solution. However, the DPV curves of the redox probe recorded during the template extraction from these two films differed significantly (Figures 3.8f and 3.10b). The DPV peak for the ferrocene redox probe at **MIP-2a** polymer film-coated electrodes prepared

from the fresh solution significantly increased with extraction time and negatively shifted, indicating an easier mass transport to the electrode through the polymer film. The DPV peaks for the redox probe at as-prepared **MIP-2a** polymer film-coated electrodes, prepared using the aged solution, were higher than those for films deposited from freshly prepared solutions.

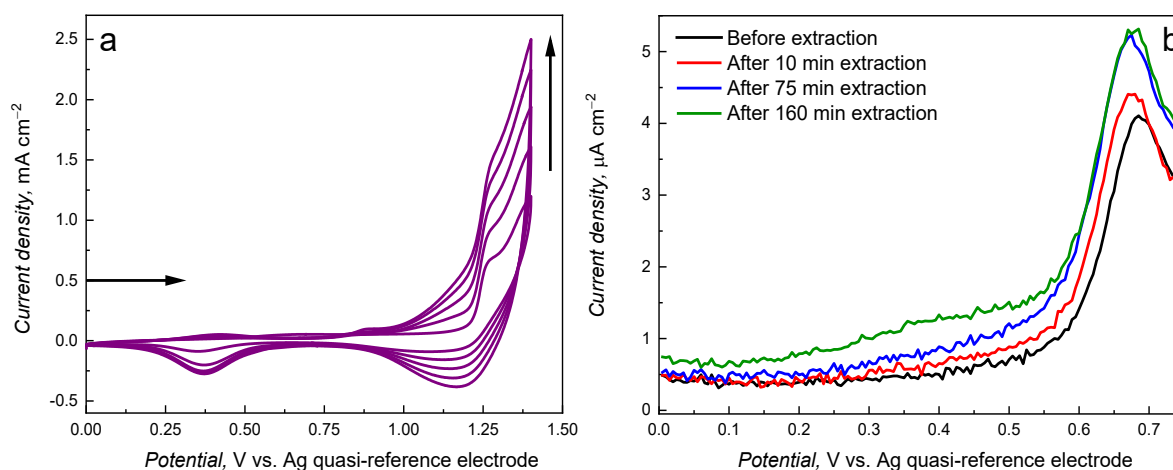


Figure 3.10. (a) Multi-cyclic current-potential curves for **MIP-2a** film deposition by potentiodynamic electropolymerization with five consecutive potential cycles at 50 mV s^{-1} in the 1-day aged ACN : DCM (9 : 1, v/v) solution of $200 \text{ }\mu\text{M}$ **TMBh**, $400 \text{ }\mu\text{M}$ **FM-2**, $1000 \text{ }\mu\text{M}$ **CM-2**, 100 mM (TBA)ClO₄, and 1 mM TEA. (b) DPV curves for 1 mM ferrocene redox probe in 100 mM (TBA)ClO₄ in the ACN : DCM (9 : 1, v/v) solution at the electrode coated with the **MIP-2a** film, deposited from the TEA-containing solution before and after template extraction with (acetic acid) : methanol (1 : 1, v/v) solution for up to 160 min.

Moreover, the DPV peak for **MIP-2a** films prepared from the aged solution increased with the extraction time. However, the increase was less pronounced, and there was no negative potential shift. The films prepared from fresh solutions contained more imprinted cavities, or template extraction was more efficient. The films prepared from aged solutions, i.e., those kept at $4 (\pm 1) \text{ }^\circ\text{C}$, might reveal organizational changes because of changes in the interaction between the solution components over time. These changes might lead to a decrease in the efficiency of template removal. They can be called the aging of the pre-polymerization complex solution. Therefore, attempts were made to study this aging mechanism using UV-vis and NMR spectroscopy and the DLS techniques.

3.5.1 Characterization of the pre-polymerization complex changes with time

The "solution aging" was examined with a freshly prepared **MIP-2a** pre-polymerization complex solution, then after aging this solution for 1, 7, and 10 days. Overall, NMR and UV-vis spectra (Figure 3.11) do not exhibit significant band shifts or band

appearance/disappearance over time. That shift lacking indicates no decomposition, dissociation, or formation of new compounds if the solution is kept at 4 (\pm 1) °C for up to 10 days.

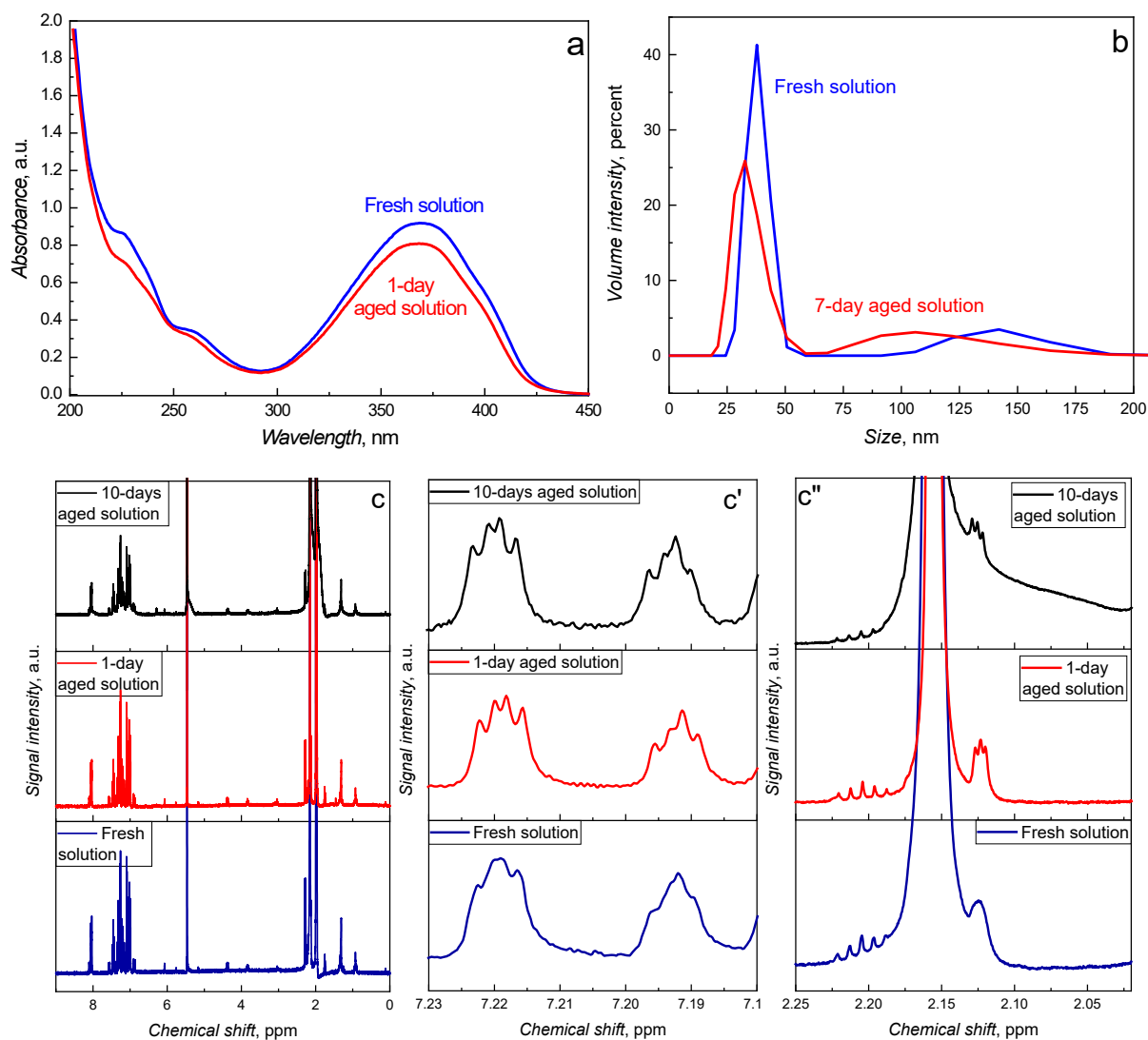


Figure 3.11. (a) UV-vis spectra, (b) DLS data, and (c, c', c'') NMR spectra for the freshly prepared and aged pre-polymerization complex in the ACN : DCM (9 : 1, v/v) solution of 200 μ M **TMBh**, 400 μ M **FM-2**, 1000 μ M **CM-2**, and 1 mM TEA.

The UV-vis absorbance bands (Figure 3.11a) for a freshly prepared solution were slightly higher than bands for a 1-day-old solution, presumably related to the solution components' de-aggregation by either decomposition or precipitation of larger aggregates. For example, several aromatic rings of the pre-polymerization complex components could be engaged in weak π - π stacking interactions, not resulting in significant conformational or structural changes. With time, these interactions could weaken, leading to the aggregates' breaking down.

As the spectroscopic measurements were performed in the transmission mode, the effects of diffused light could be an additional effect in this output spectra. Therefore, the bigger aggregates in the freshly prepared solution would diffuse more light so that less light would be transmitted. Consequently, the apparent absorbance would be higher. The smaller aggregates in the aged solution would diffuse light to a lesser extent, leading to higher transmittance. Therefore, the observed apparent absorbance would be relatively lower.

The DLS analysis of the pre-polymerization complex solution (Figure 3.11b) reveals the presence of some smaller and larger aggregates. The peak intensity decreased with the solution aging, indicating the decrease in the aggregate hydrodynamic size. However, a relatively high noise in DLS measurements restricts the possibility of drawing definite conclusions.

In the NMR spectra, there are no significant peak shifts or differences in peak intensities (Figure 3.11c). However, the freshly prepared solution reveals relatively broad featureless peaks at ~ 7.20 and ~ 2.12 ppm (Figure 3.11c' and 3.11c'', respectively). Those peaks become sharper and better developed with aging, proving to be two quadruplets at ~ 7.20 ppm and a triplet at ~ 2.12 ppm. Such broad features are typical for fast proton exchange with the respective functional groups indicating that the proton transfer is fast in the NMR time-scale³⁷⁸, which could be representative of large aggregates with molecules closely related. The proton exchange of those groups is slower in the aged solutions, indicating smaller aggregates interacting relatively weakly.

From DLS, UV-vis, and NMR spectroscopy analyses of the fresh and aged **MIP-2a** pre-polymerization complex solution, one can postulate that the freshly prepared solution contains bigger aggregates that decompose over time. The above studies indicate that imaging the deposited polymer films with techniques such as SEM and AFM would be essential to study further the phenomenon of stabilization or aggregation of components in the pre-polymerization complex solution.

3.5.2 Characterization of the **MIP-2a** film

The **MIP-2a** film, used as a model, was imaged with AFM in the Tapping™ mode (Figure 3.12) to unravel the morphology of the films deposited from fresh and aged solutions. The imaging yielded important information regarding the differences in the two films' surface morphology and surface parameters. Globally, the films were very rough (Table 3.2).

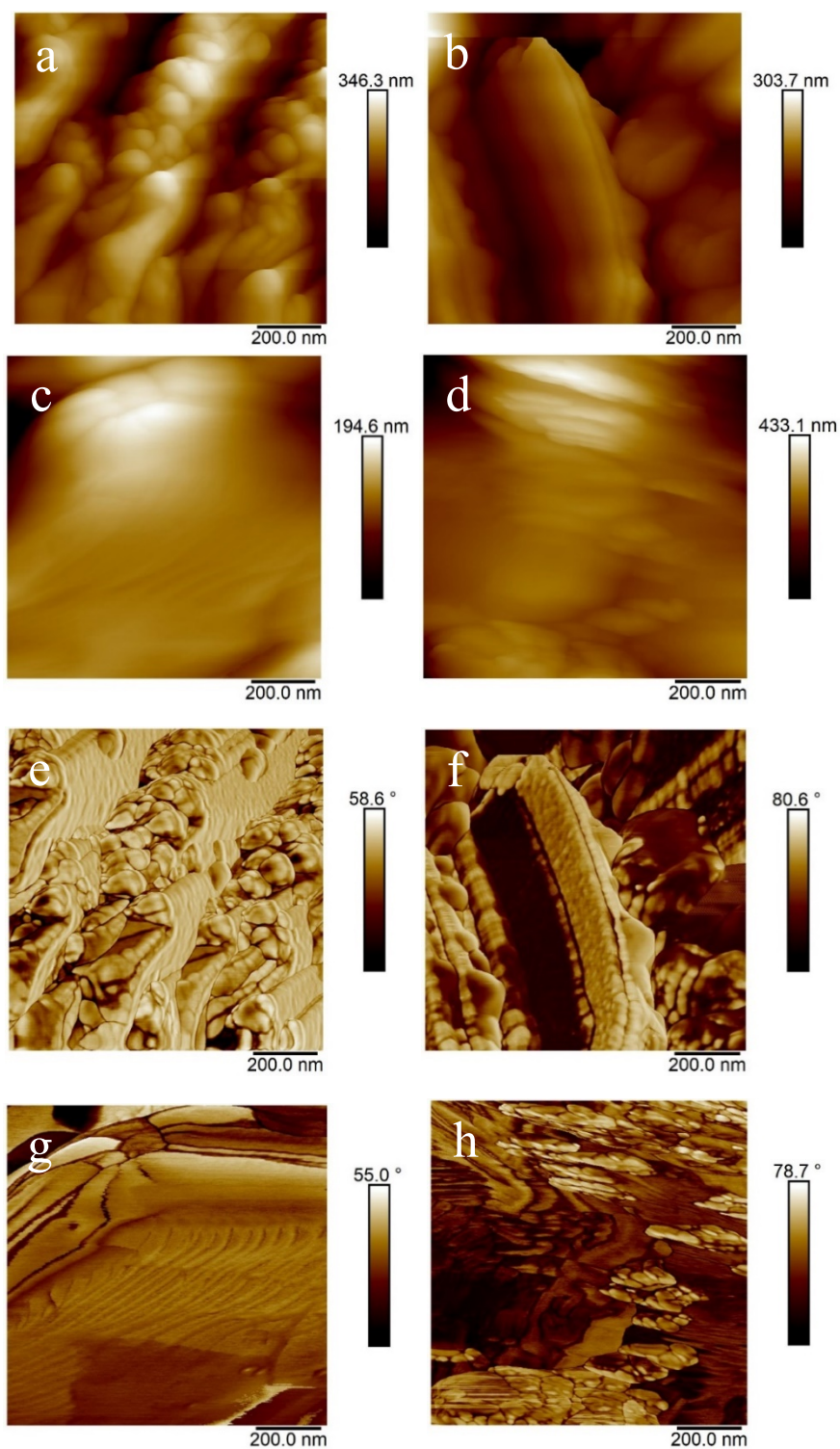


Figure 3.12. AFM morphology analysis of **MIP-2a** films prepared using fresh and 1-day aged solutions (**a**, **c**, respectively) before and (**b**, **d**, respectively) after **TMBh** template extraction for 180 min in the (acetic acid) : methanol (1 : 1, v/v) solution. Phase imaging of **MIP-2a** films prepared using respective fresh and 1-day aged solutions (**e**, **g**, respectively) before and (**f**, **h**, respectively) after **TMBh** template extraction for 180 min in the (acetic acid) : methanol (1 : 1, v/v) solution.

The morphology of the films prepared using fresh and aged solutions differed pronouncedly (Figure 3.12a and 3.12c, respectively). The films deposited from the aged solution were smoother (Figure 3.12c). Grainy structures were present in the films prepared from fresh solutions (Figure 3.12a). These structures were confirmed by a significantly lower roughness of the film prepared from the aged solution (Table 3.2).

Extraction of the template using the (acetic acid) : methanol (1 : 1, v/v) solution altered the morphological structure of both fresh and aged solution-based films (Figure 3.12b and 3.12d, respectively). The effect of template extraction was more pronounced in films deposited from aged solutions as they became much grainier after extraction (Figure 3.12d). However, this feature does not translate into DPV peak changes (Figure 3.10b), which are quite small. Phase images indicative of the viscoelastic properties of the film exhibit significantly different properties of both the films before and after extraction (Figure 3.12e, 3.12f, 3.12g, and 3.12h). Yet, the average phase shift is relatively small, indicating rigid films (Table 3.2). Noticeably, there are significant variances in the phase shift across the image, indicating different regions with different viscoelastic properties.

Table 3.2. AFM analysis of morphological and nanomechanical properties of **MIP-2a** films prepared using respective fresh and 1-day aged solutions before and after **TMBh** template extraction for 180 min in the (acetic acid) : methanol (1 : 1, v/v) solution.

Polymer film	Roughness, R_a, nm	Phase, deg.
MIP-TEA, fresh	286 ± 119	6.0 ± 1.0
MIP-TEA, fresh, template extracted	201 ± 32	7.0 ± 7.0
MIP-TEA, aged	160 ± 81	19.0 ± 2.0
MIP-TEA, aged, template extracted	204 ± 56	1.1 ± 0.4

Hence, it can be concluded that the solution aging affects the MIP film formation, possibly leading to irreproducibility in the film's template extraction. The MIP films deposited from aged solutions are smoother and more compact, possibly inhibiting the template extraction. Smooth films are formed in the absence of aggregates or the presence of very small aggregates. This observation is in accord with the characterization of the **MIP-2a** pre-polymerization complex solution, wherein it was postulated that the aggregates' size decreased over time. This

study points to the critical role of organic solution stability on MIP films. For this problem's partial overcoming, the vials with solutions were wrapped with aluminum foil, kept at room temperature of 25 (\pm 1) °C, and ultrasonicated for 15 min in a bath sonicator before the electropolymerization. These precautions helped produce films with higher repeatability in template extraction. Moreover, the aged solution was used to prepare films for testing the selective electrosynthesis to enable the reuse of the solution.

3.6 Characterizing optimized **MIP-2** and **NIP-2** films

The prepared **MIP-2** and **NIP-2** films were characterized using FT-IR spectroscopy and AFM to confirm successful film deposition and study the effect of the extraction process on their properties.

3.6.1 Fourier-transform infrared (FT-IR) spectroscopy analysis

Two sources of differences in the **MIP-2** and **NIP-2** spectra can be identified, i.e., the difference between MIP and NIP films and the extraction treatment effect on the films (Figure 3.13a). Significant differences are observed in the bands of thinner **MIP-2b** and **NIP-2b** films between 2800 and 3000 cm^{-1} , representing the $-\text{CH}$ stretching (Region 1 in Figure 3.13a)³⁷⁹. These bands are substantially more intense for **MIP-2b** films than **NIP-2b** films. The bands' intensities markedly decreased after exposure of **MIP-2b** and **NIP-2b** films to the (acetic acid) : methanol (1 : 1, v/v) solution. Moreover, new bands appeared in the region of 3000 – 3500 cm^{-1} , which can be attributed to the appearance of $-\text{OH}$ groups in the films³⁷⁹. Another characteristic region exhibiting differences between **MIP-2b** and **NIP-2b** films is that of 1600 – 1800 cm^{-1} (Region 2 in Figure 3.13a). In this region, there are two bands centered at 1760 and 1733 cm^{-1} and a weak broad band centered at \sim 1655 cm^{-1} in **MIP-2b** before extraction. They represent vibrations of the $\text{C}=\text{O}$ group that can interact with the **TMBh** template³⁷⁹. After template extraction, the band at 1760 cm^{-1} disappeared, while that at 1733 cm^{-1} shifted to a lower wavenumber of \sim 1722 cm^{-1} and decreased in intensity. The broad band at \sim 1655 cm^{-1} was still present in this spectrum. Those bands' evolution indicates a change in the interaction of the $\text{C}=\text{O}$ group in the polymer, presumably because of the template removal. For **NIP-2b**, the band at 1722 cm^{-1} and a broad one at 1655 cm^{-1} were initially present, and no changes in these bands were observed after exposure to the extraction solution. Regions 3 and 4 in Figure 3.13a mainly reveal the extraction process effect on **MIP-2b** and **NIP-2b** films, i.e., two major bands at 1430 and 1120 cm^{-1} appeared in these regions after exposure to extraction

solution. These two bands' origins are unknown; however, they indicate extraction-incurred changes in the studied films.

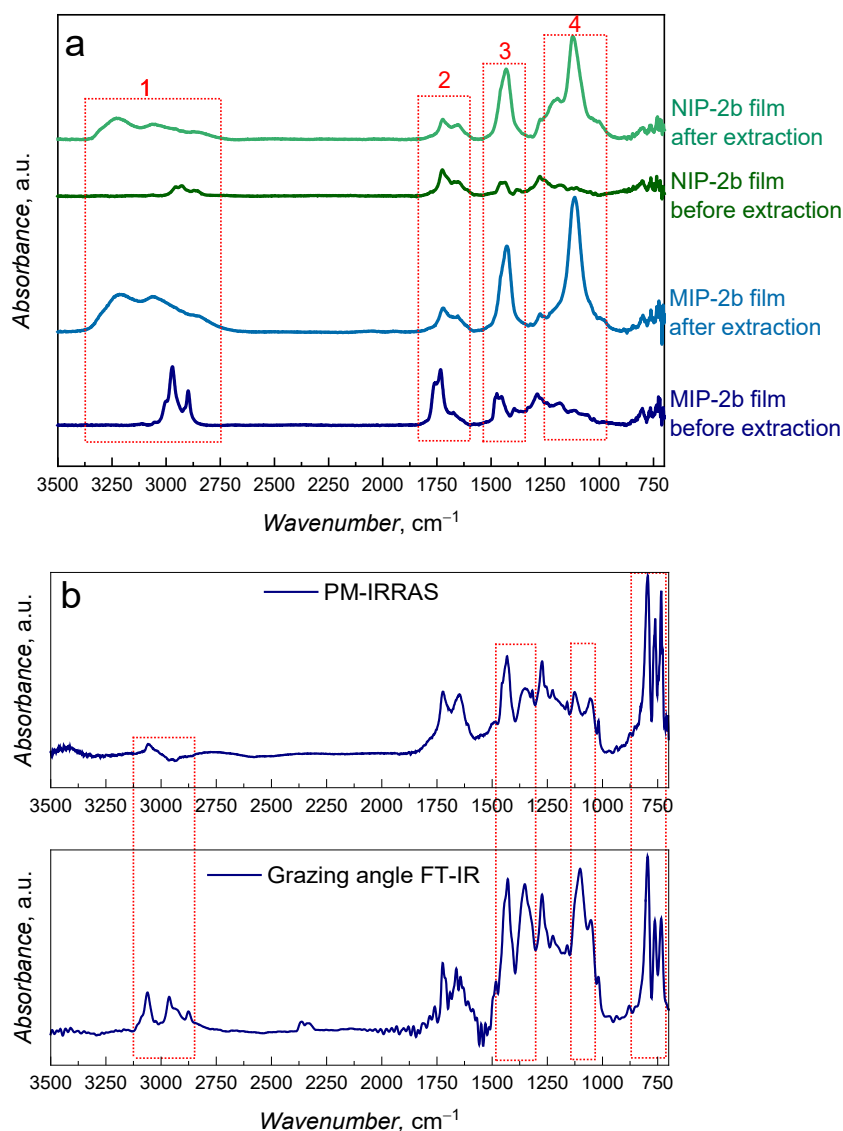


Figure 3.13. (a) PM-IRRAS spectra for **MIP-2b** and **NIP-2b** film-coated Au electrodes before and after exposure to (acetic acid) : methanol (1 : 1, v/v) extraction solution for 180 min and (b) comparison of PM-IRRAS and grazing angle FT-IR spectra of **MIP-2a** film-coated Au electrodes before template extraction.

Interestingly, there are significant differences in the PM-IRRAS and grazing angle FT-IR spectra of the thicker **MIP-2a** film (Figure 3.13b). The four regions (marked with vertical red dotted lines) reveal bands with different relative intensities in PM-IRRAS and grazing angle FT-IR spectroscopy. The bands in the 2800 – 3100 cm⁻¹ region have significantly diminished along with those in the two subsequent regions (bands centered at ~1350 and ~1105 cm⁻¹). The band centered at ~735 cm⁻¹ has intensified relative to its neighboring bands in PM-IRRAS

spectra. This difference can be explained as revealing the oriented growth of the polymer film. The intensity of bands corresponding to vibrations with in-plane transition dipole moments decreases in PM-IRRAS, and the intensity of bands corresponding to vibrations with transition dipole moment oriented out-of-plane increases. Therefore, the change in the relative intensities of the bands indicates local ordering in the films. Such orientations were not apparent in the thinner **MIP-2b** film as grazing angle FT-IR was not very sensitive.

3.6.2 Atomic force microscopy (AFM) analyses

The AFM analysis was performed for the **MIP-2a**, NIP-2a, **MIP-2b**, and NIP-2b films before and after exposure to (acetic acid) : methanol (1 : 1, v/v) extraction solution to study the film morphology and the extraction treatment effect on the film properties. The AFM imaging revealed the MIP and NIP films' surface morphology and nanomechanical properties. The **MIP-2a** and NIP-2a films were very thick and rough (Figure 3.14a, 3.14c, respectively, and Table 3.3).

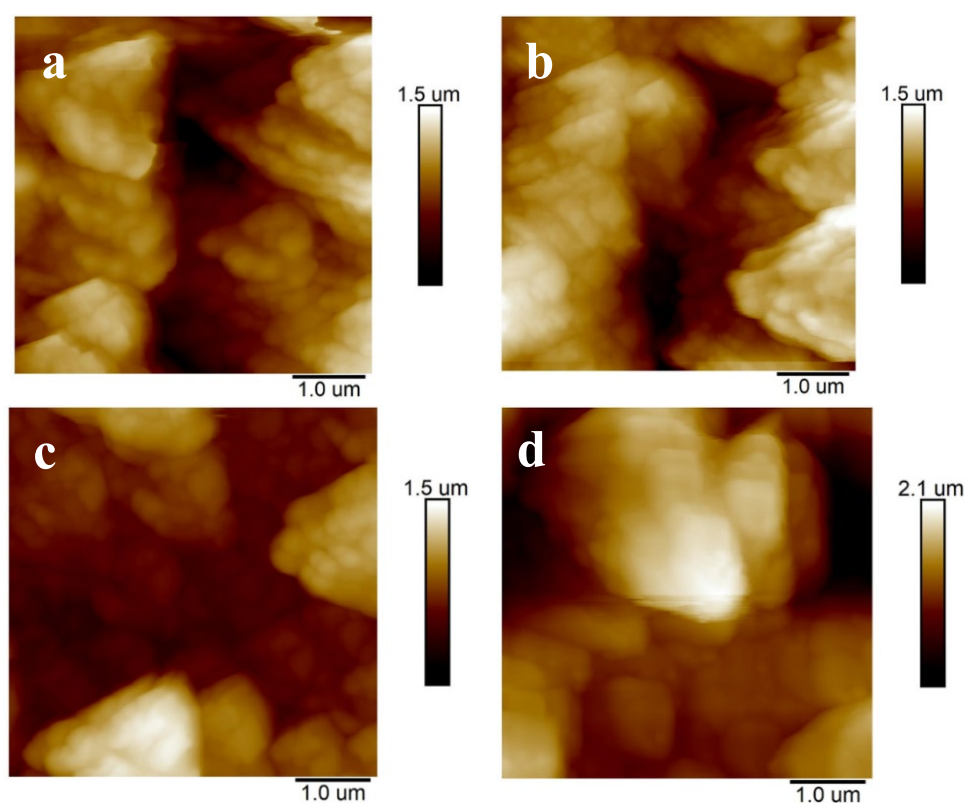


Figure 3.14. Atomic force microscopy images of the thick (a) as prepared and (b) template-extracted **MIP-2a**, as well as (c) as prepared and (d) extracted NIP-2a films. All films were deposited on Au-layered glass slides using potentiodynamic electropolymerization with five consecutive potential cycles at 50 mV s^{-1} in the ACN : DCM (9 : 1, v/v) solution of $200 \text{ }\mu\text{M}$ **TMBh**, $400 \text{ }\mu\text{M}$ **FM-2**, $1000 \text{ }\mu\text{M}$ **CM-2**, $100 \text{ }\mu\text{M}$ TEA, and 100 mM (TBA)ClO₄. The template was extracted in the (acetic acid) : methanol (1 : 1, v/v) solution for 180 min.

The average film thickness ranged from 657 to 883 nm for **MIP-2a** and NIP-2a films. Both films' roughness was quite similar, slightly exceeding 200 nm. The films were composed of granular aggregates forming a layered structure. Exposure to extraction solution altered the structure of both **MIP-2a** and NIP-2a films slightly (Figure 3.14b and 3.14d, respectively), though the **MIP-2a** film thickness and roughness increased after template extraction, presumably indicating film swelling (Table 3.3).

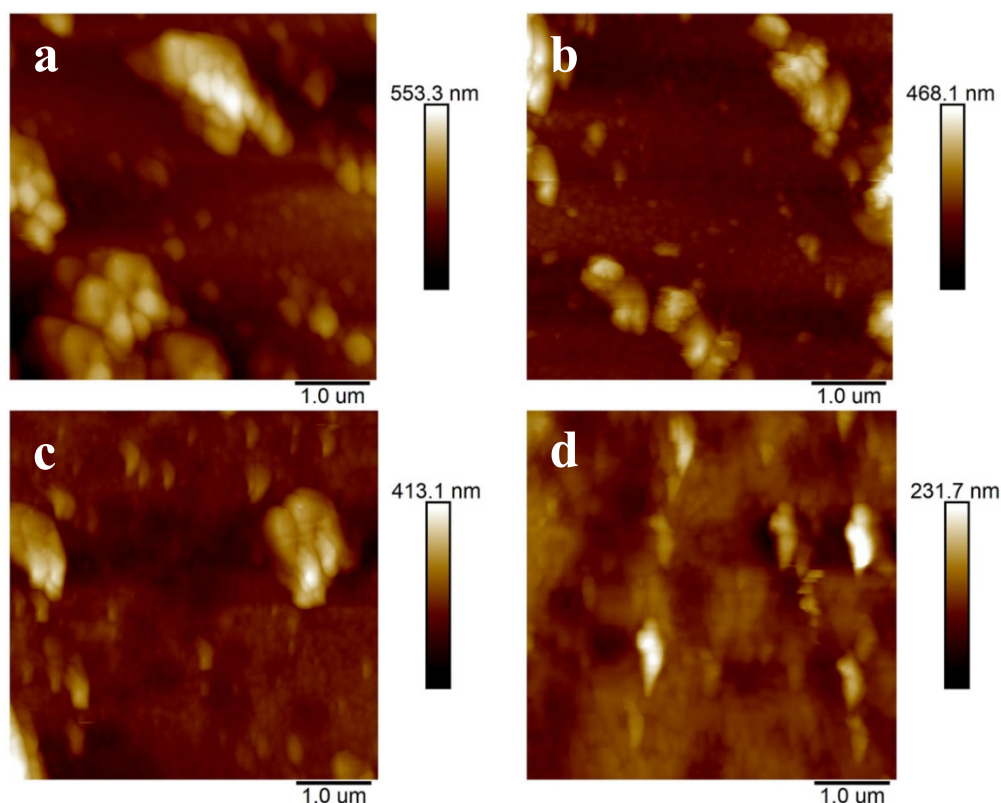


Figure 3.15. Atomic force microscopy images of the thin (a) as prepared and (b) template-extracted **MIP-2b**, as well as (c) as prepared and (d) extracted NIP-2b films. All films were deposited by potentiodynamic electropolymerization on Au-layered glass slides during five consecutive potential cycles at 50 mV s^{-1} in the ACN : DCM (9 : 1, v/v) solution of $20 \text{ } \mu\text{M}$ **TMBh**, $40 \text{ } \mu\text{M}$ **FM-2**, $100 \text{ } \mu\text{M}$ **CM-2**, $100 \text{ } \mu\text{M}$ TEA, and 100 mM (TBA)ClO₄.

The **MIP-2b** and NIP-2b films deposited from 10-times diluted solution for electropolymerization were markedly thinner and less rough (Figure 3.15 and Table 3.3). The average thickness of the **MIP-2b** film was 488 nm, while its roughness reached 45 nm. The NIP-2b film was relatively thinner, with an average thickness of 384 nm and much less roughness ($\sim 20 \text{ nm}$). **MIP-2b** and NIP-2b were composed of a compact homogeneous layer with clusters of aggregates on top (Figure 3.15a and 3.15c). Exposure of **MIP-2b** and NIP-2b films to (acetic acid) : methanol (1 : 1, v/v) extraction solution mainly led to the removal of top

aggregates (Figure 3.15b and 3.15d, respectively), more pronounced for the **MIP-2b** film (Figure 3.15b). For the **MIP-2b** film, the average film thickness significantly decreased upon template extraction, and the average roughness increased slightly (Table 3.3). Exposure of NIP-2b film to extraction solution slightly increased the film thickness and average roughness (Table 3.3).

Table 3.3. Atomic force microscopy (AFM) analyses of morphological and nanomechanical properties of **MIP-2a**, **MIP-2b**, NIP-2a, and NIP-2b films before and after exposure to (acetic acid) : methanol (1 : 1, v/v) extraction solution for 180 min.

Polymer film	Extraction condition	Film thickness, nm	Roughness, R_a , nm	Young modulus, GPa	Dissipation, keV
MIP-2a	Before extraction	657 ± 54	205 ± 70	0.87 ± 0.42	33.0 ± 10.5
	After extraction	900 ± 104	255 ± 60	1.15 ± 0.39	62.0 ± 38.8
MIP-2b	Before extraction	488 ± 18	45 ± 14	1.11 ± 0.23	NA
	After extraction	355 ± 21	51 ± 21	1.90 ± 0.09	2.40 ± 0.98
NIP-2a	Before extraction	883 ± 91	214 ± 29	7.39 ± 4.00	25.3 ± 10.9
	After extraction	748 ± 86	212 ± 78	2.11 ± 1.00	19.0 ± 5.6
NIP-2b	Before extraction	384 ± 31	20 ± 13	2.30 ± 0.62	5.21 ± 1.33
	After extraction	419 ± 29	34 ± 20	4.05 ± 0.60	5.70 ± 1.16

The recorded Young modulus maps of **MIP-2** and NIP-2 films (Figure 3.16) indicate non-uniform properties and co-existence of softer and harder regions in all the films deposited. The average Young modulus of the films ranged from 1 to 7 GPa (Table 3.3). The literature values of Young modulus for polythiophene films are also typically in the range of few GPa³⁸⁰⁻³⁸¹. The average Young modulus values for all the studied films were higher for NIP-2 than **MIP-2**, indicating that the imprinting led to the formation of a softer film.

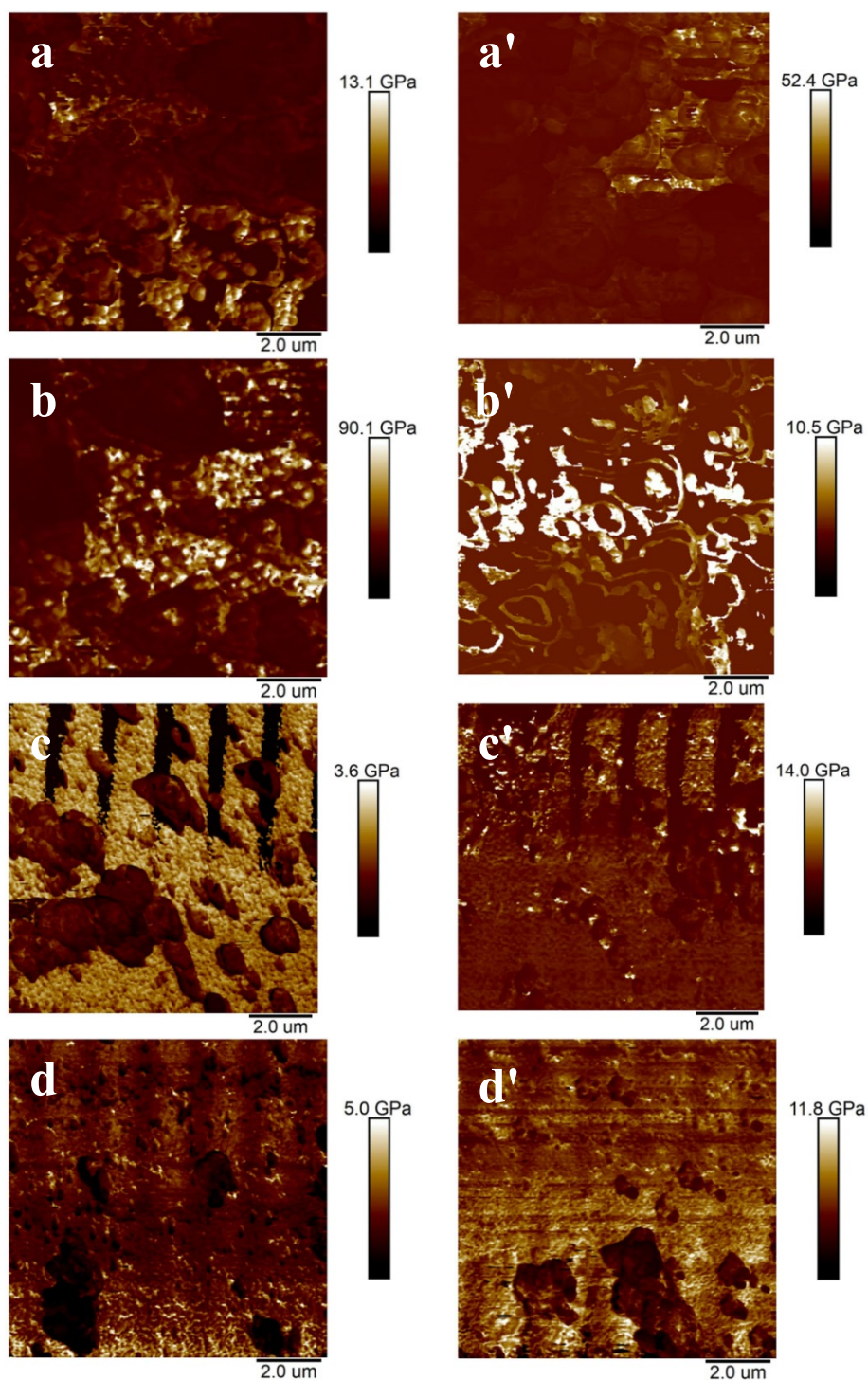


Figure 3.16. Young modulus maps recorded during AFM imaging of as prepared (a) **MIP-2a**, (b) **MIP-2b**, (c) **NIP-2a**, and (d) **NIP-2b** films and extracted (a') **MIP-2a**, (b') **MIP-2b**, (c') **NIP-2a**, and (d') **NIP-2b** films. All films were deposited on Au-layered glass slides by potentiodynamic electropolymerization.

3.7 Selective **TMBh** electrosynthesis

3.7.1 Film processing for **TMBh** electrosynthesis

Before **TMBh** electrosynthesis, the **MIP-2** and NIP-2 films were conditioned by cycling the potential ten times between 0.00 and 2.00 V vs. Ag quasi-reference electrode in the 100 mM (TBA)ClO₄ in the ACN : DCM (9 : 1, v/v) solution (Figure 3.17). The current dropped significantly after the first cycle, and the film became increasingly non-conductive with each consecutive cycle. This step ensured that the **DMPH** reactant did not poison the film during electro-oxidation.

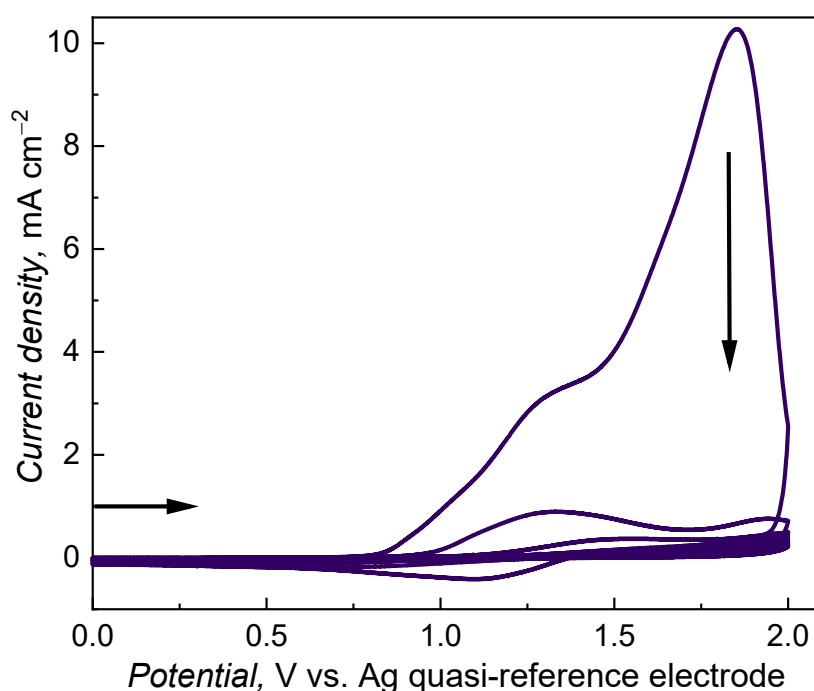


Figure 3.17. MIP-2a film-coated Pt electrode conditioning in 100 mM (TBA)ClO₄ in the ACN : DCM (9 : 1, v/v) solution for 10 cycles at 100 mV s⁻¹.

3.7.2 Electro-oxidation of **DMPH** at bare Pt electrode

The potentiodynamic characterization of the **DMPH** reactant in ACN containing the (TBA)ClO₄ electrolyte revealed an anodic peak with onset at 1.00 V vs. Ag quasi-reference electrode representing the **DMPH** electro-oxidation (Figure 3.18). Therefore, it is essential to run electrosynthesis at potentials exceeding 1.00 V vs. Ag quasi-reference electrode to obtain the desired **TMBh** product.

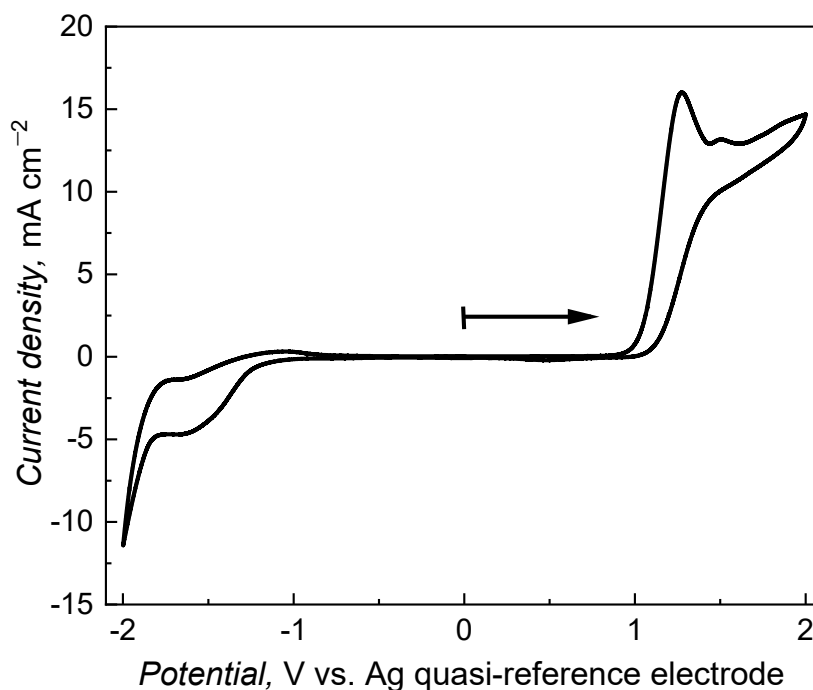


Figure 3.18. Cyclic voltammogram for 20 mM **DMPH** recorded at a Pt bare electrode in 100 mM (TBA)ClO₄ in ACN at 100 mV s⁻¹.

The anodic oxidation results in a radical cation which is a strong acid. This acid spontaneously expels the proton, leading to the phenoxy radical formation. The radical with spin densities at several positions can further be converted to phenoxonium species. Then, the phenoxy and phenoxonium species attack the substrate or other nucleophiles produced during electro-oxidation, resulting in bond formation³⁸². The C–C coupling proceeds via the reactive unsubstituted site of the **DMPH** substrate. However, as several reactive sites on the intermediate species exist, several by-products can be formed, apart from the desired **TMBh** product³⁸³. Moreover, the primary oxidation products can undergo further oxidation.

3.7.3 High-performance liquid chromatography (HPLC) analysis of substrate and product

The **DMPH** reactant and the **TMBh** product reference standards were used to construct HPLC calibration plots (Figure 3.19). For that, peak areas were measured at the retention times of **DMPH** equal to ~7.6 min and **TMBh** to ~14.1 min at 280-nm light to identify their concentrations after electrosynthesis.

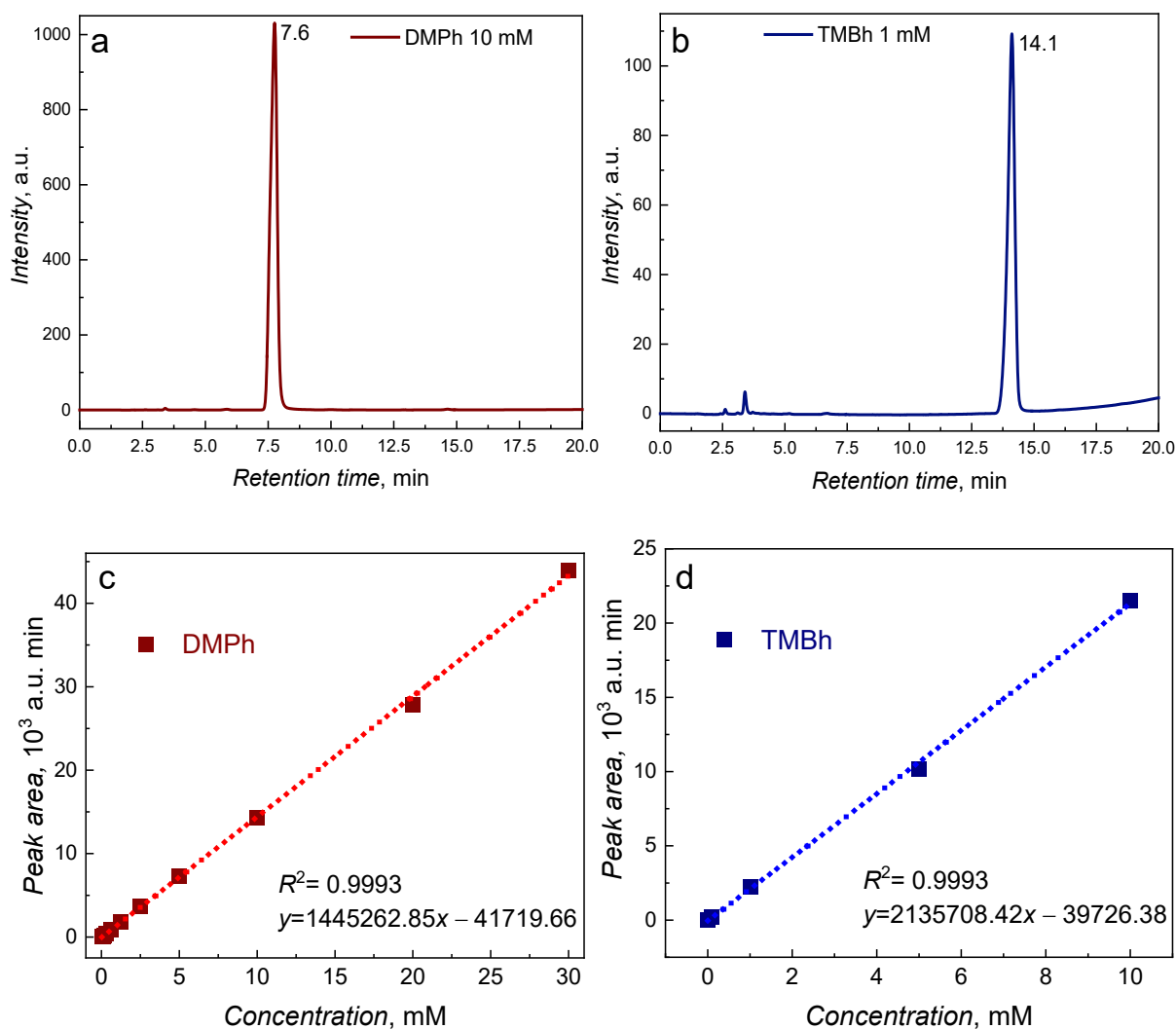


Figure 3.19. HPLC chromatograms of (a) the **DMPH** reactant and (b) the desired **TMBh** product. HPLC calibration plots for (c) the **DMPH** reactant and (d) the **TMBh** desired product at 280 nm.

3.7.4 Optimization of **TMBh** electrosynthesis

The platinum electrodes coated with an optimized MIP film, templated with **TMBh**, were used to perform electrosynthesis. The optimized pre-polymerization complex solution was prepared by mixing **TMBh**, **FM-2**, and **CM-2** at the molar ratio of 1 : 2 : 5 in 0.1 M (TBA)ClO₄ and 1 mM TEA in the ACN : DCM (9 : 1, v/v) solution. All films were prepared using electropolymerization, then treated with (acetic acid) : methanol (1 : 1, v/v) extraction solution for 180 min, and then conditioned before electrosynthesis.

The **TMBh** electrosynthesis was performed using 0.1 M (TBA)ClO₄ supporting electrolyte in ACN : DCM (9 : 1, v/v) solution. Pt disk electrodes with a small area of 0.44 mm² were used for preliminary experiments. The **MIP-2a** film-coated electrode was immersed in 10 mM **DMPH** solution for electrosynthesis of **TMBh**. The Pt wire and the Ag

wire were used as the counter and quasi-reference electrodes, respectively. The electrosynthesis at the **MIP-2a** film-coated electrode was compared to those at the bare and NIP-2a film-coated electrodes. Two methods of electrosynthesis, namely, potentiostatic and galvanostatic, were applied (Figure 3.20).

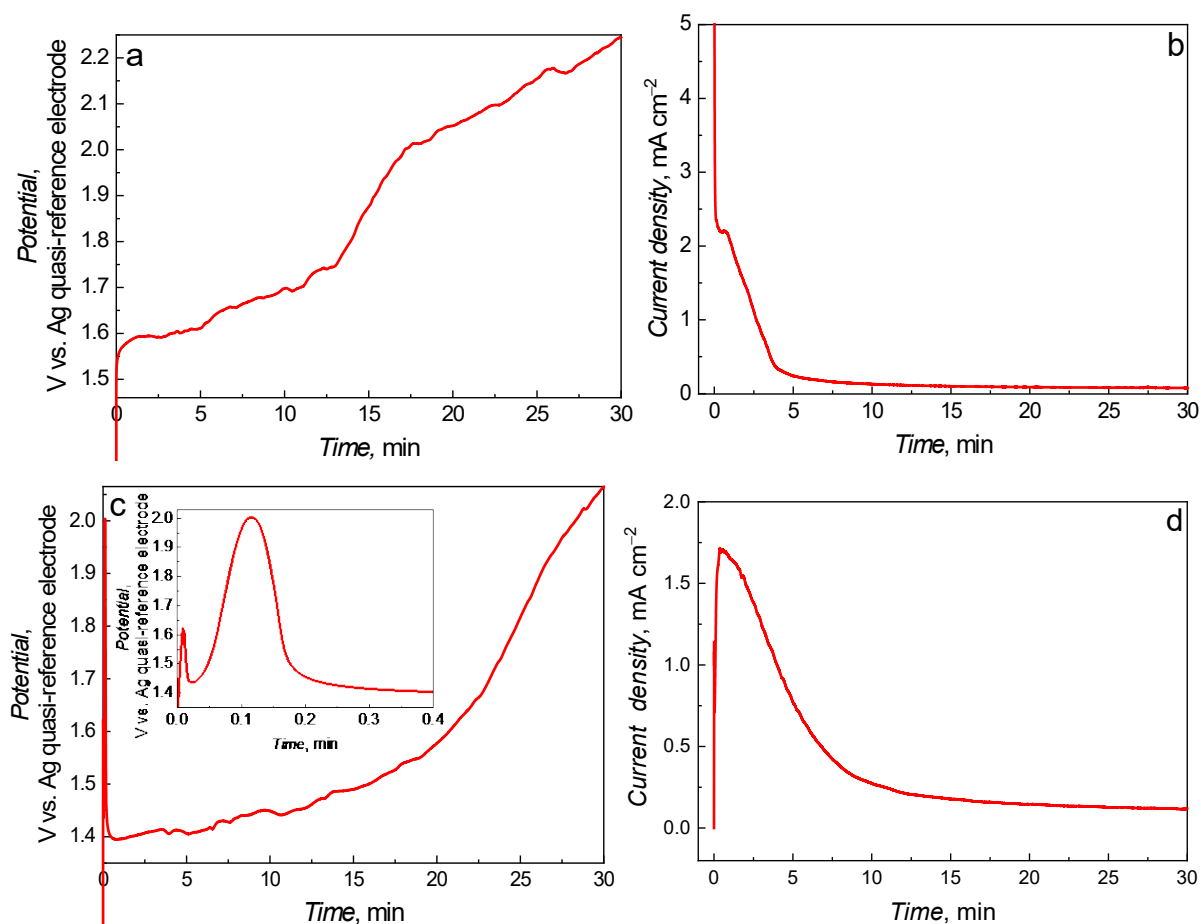


Figure 3.20. Potential transients for galvanostatic **TMBh** electrosynthesis at 0.34 mA cm^{-2} for 30 min at the (a) bare and (c) **MIP-2a** film-coated 0.44-mm^2 Pt disk electrode as well as current transients for potentiostatic **TMBh** electrosynthesis at $2.00 \text{ V vs. Ag quasi-reference electrode}$ for 30 min at the (b) bare and (d) **MIP-2a** film-coated 0.44-mm^2 Pt disk electrode. Solution composition: 10 mM DMPH and 0.1 M (TBA)ClO_4 in the $\text{ACN} : \text{DCM} (9 : 1, v/v)$ solution.

The potential changes vs. time for bare and **MIP-2a** film-coated electrodes differed markedly in galvanostatic electrosynthesis (Figure 3.20a and 3.20c). For the **MIP-2a** film-coated electrode, a potential peak reaching 2.00 V was formed at the beginning of the electrosynthesis, and then the potential steadily increased with time (Figure 3.20c). After ~ 20 min, the potential increased faster. The curve at the bare electrode was similar except for the presence of the potential peak at the beginning of the electrosynthesis (Figure 3.20a). Moreover, the potential for the bare electrode reached 2.20 V after 30 min, while **MIP-2a**

film-coated electrode potential reached only 2.00 V after 30 min. The observed potential peak most likely indicates the accumulation of the electrosynthesis intermediates in the polymer film, which undergo further reactions. In potentiostatic electrosynthesis, the current rapidly decreased and remained constant for electrosyntheses at the **MIP-2a** film-coated (Figure 3.20d) and bare electrodes (Figure 3.20b). However, a peak is also seen here for the **MIP-2a** film-coated electrode.

Table 3.4. Results of the HPLC determination of the **TMBh** electrosynthesized product at the bare, thick **MIP-2a** and NIP-2a film-coated electrodes.

Electrosynthesis type	Potential or current density	Time, h	Electrode surface	Conversion, %	Selectivity, %
Potentiostatic	2.00 V	0.5	Bare	2.3	27.8
	2.00 V	0.5	MIP-2a	3.5	50.3
	2.00 V	0.5	NIP-2a	1.8	27.0
	2.00 V	2	Bare	4.2	22.8
	2.00 V	2	MIP-2a	5.6	52.3
	2.00 V	2	NIP-2a	4.3	20.7
Galvanostatic	0.34 mA cm ⁻²	0.5	Bare	2.3	25.7
	0.34 mA cm ⁻²	0.5	MIP-2a	2.2	26.9

The product determination using HPLC peak areas (Table 3.4) indicated that the use of the electrode coated with the **MIP-2a** film improved the selectivity of the electrosynthesis of the **TMBh** product (~50%) as compared to that at the bare (27.8%) and NIP-2a film-coated (27%) electrodes under potentiostatic conditions at 2.00 V after 30-min synthesis. The selectivity at the **MIP-2a** film-coated electrode to the **TMBh** product under potentiostatic conditions after 2-h synthesis was also relatively high (52.3%). Noticeably, the low conversion yield arose from using Pt disk electrodes of a small (0.44 mm²) area. Alternately, under galvanostatic conditions, the selectivity and yield at the MIP film-coated electrode were similar to those at the bare electrode despite a peak forming at the beginning of the electrosynthesis at the **MIP-2a** film-coated electrode (Figure 3.20c). Therefore, potentiostatic electrosynthesis was applied in further studies.

3.7.5 Large-scale TMBh electrosynthesis

Large-scale **TMBh** electrosynthesis was performed at bare as well as **MIP-2a**, **MIP-2b**, and NIP-2a film-coated Pt plate electrodes, with an active surface area of $\sim 1.90 \text{ cm}^2$, under potentiostatic conditions. The charge passing through the electrode was measured during the electrosynthesis (Figure 3.21). The shapes of charge transients over time for **MIP-2a** and NIP-2a film-coated electrodes were somewhat different from the shape for the bare electrode. For both MIP and NIP film-coated electrodes, the charge increased slowly for the first 2 hours, then rose faster, finally reaching a plateau. Initially, the slow charge increase was much less pronounced for bare electrodes. This slow increase may indicate accumulation of the first synthesis intermediate product followed by faster electro-oxidation of this product. The charge passed through the system during electrosynthesis was the lowest for the NIP-2a film and reached a plateau after ~ 3 -h synthesis. Then, the charge increased very slowly (Figure 3.21). The charges passed for the **MIP-2a** film-coated electrode and the bare electrode were comparable, with the **MIP-2a** electrode reaching a plateau after ~ 10 -h synthesis.

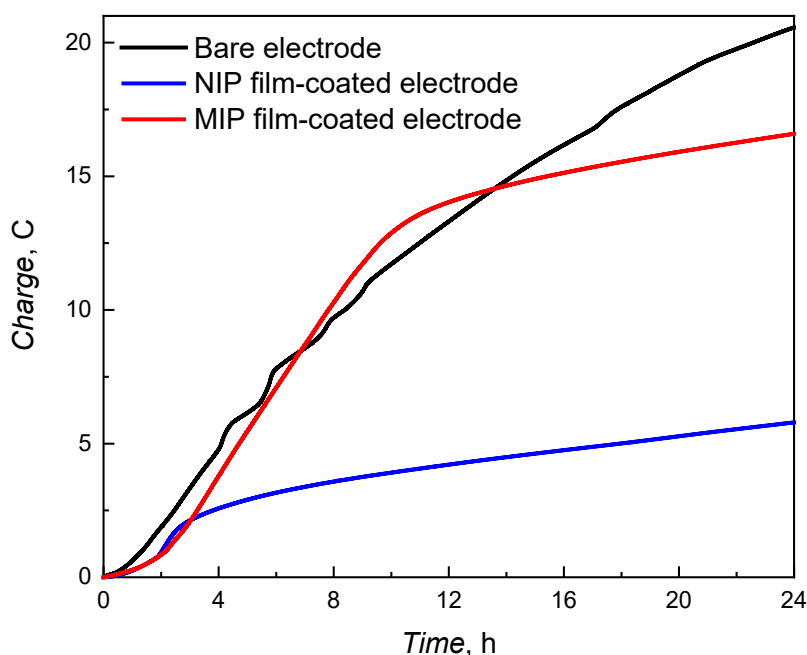


Figure 3.21. The charge passed as a function of electrosynthesis time during electro-oxidation of 20 mM **DMPH** at the bare, **MIP-2a**, and NIP-2a film-coated 1.90-cm^2 active area Pt plate electrode at 1.20 V vs. Ag quasi-reference electrode in 100 mM (TBA)ClO₄ in the ACN : DCM (9 : 1, v/v) solution.

The reaction mixture samples were taken at various time intervals and analyzed using HPLC. The exemplary chromatograms of solutions obtained after electro-synthesis are seen in Figure 3.22.

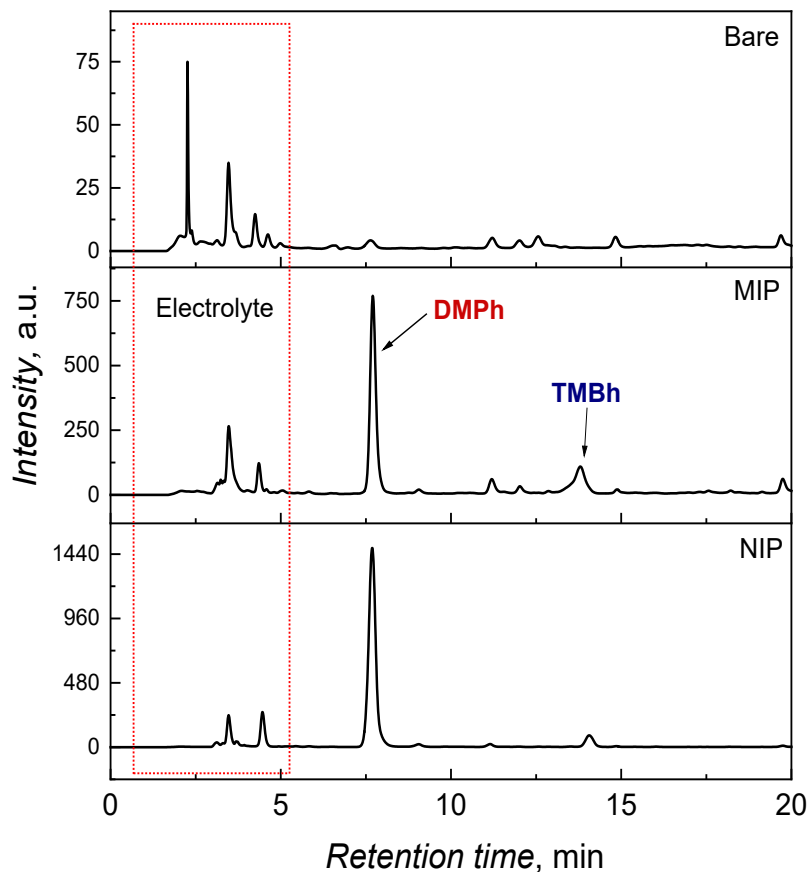


Figure 3.22. Exemplary high-performance liquid chromatography (HPLC) chromatograms at 280 nm wavelength of solutions obtained after 14-h electro-synthesis at the bare, as well as **MIP-2a** and **NIP-2a** film-coated electrodes.

The **DMPH** conversion and **TMBh** product yield as a function of synthesis time at the bare, as well as **MIP-2** and **NIP-2** film-coated electrodes, can be seen in Figure 3.23. The potentiostatic electro-oxidation at 1.20 V vs. Ag quasi-reference electrode led to ~75% **DMPH** conversion at the **MIP-2a** film-coated electrode after 24-h electro-synthesis time, whereas at **NIP-2a** film-coated electrode, the conversion was significantly lower (up to 40%) (Figure 3.23a). **DMPH** completely converted at the bare electrode after a 14-h synthesis. However, the **TMBh** product yield was the highest at the **MIP-2a** film-coated electrode after 14-h electro-synthesis. The **TMBh** amount very slightly increased with a further increase in synthesis time. Apparently, the bare electrode is not selective to the **TMBh** product. The MIPs entirely provides selectivity. Moreover, in the case of **NIP-2a**, it appears as if the film is

blocking the electrode. Therefore, the substrate conversion efficiency and product yield are very low.

Furthermore, the **MIP-2a** film-coated electrode provided higher **DMPH** conversion, but the **TMBh** yield was slightly lower than the **MIP-2b** film-coated electrode (Figure 3.23b). Therefore, the selectivity of the thinner **MIP-2b** films towards **TMBh** electro-synthesis is higher and reaches up to 39% at 24-h synthesis time.

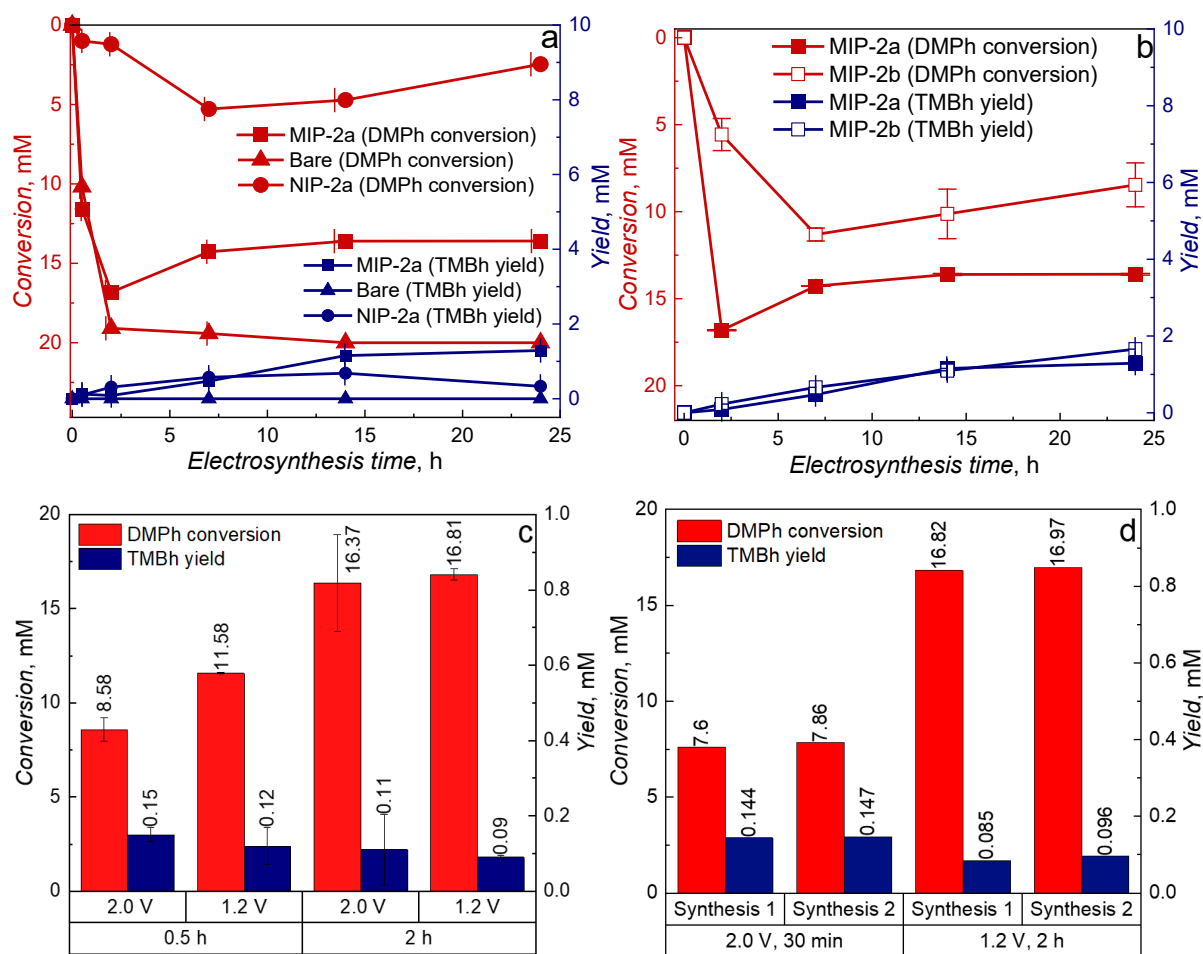


Figure 3.23. Kinetic plot for potentiostatic electro-oxidation of 20 mM **DMPH** at 1.20 V vs. Ag quasi-reference electrode in 100 mM (TBA)ClO₄ in ACN : DCM (9 : 1 v/v) for (a) **DMPH** conversion and **TMBh** product yield as a function of synthesis time for the bare as well as **MIP-2a** and **NIP-2a** film-coated Pt electrodes and (b) **DMPH** conversion and **TMBh** product yield as a function of synthesis time for **MIP-2a** and **MIP-2b** film-coated electrodes. Comparison of potentiostatic electro-oxidation of 20 mM **DMPH** in 100 mM (TBA)ClO₄ in ACN : DCM (9 : 1, v/v) at **MIP-2a** film-coated electrodes at (c) different potentials and for (d) different synthesis cycles.

When comparing electro-synthesis at different potentials (Figure 3.23c), one can see that electro-oxidation at 2.00 V vs. Ag quasi-reference electrode led to unexpected relative lower

DMPH conversion and slightly higher **TMBh** yield than at 1.20 V vs. Ag quasi-reference electrode at **MIP-2a** film-coated electrode. However, longer synthesis times (> 2 h) at 2.00 V vs. Ag quasi-reference electrode affect the film irreversibly. Disparately, the **MIP-2a** films appear stable in repeated electro-synthesis runs up to 2 hours. As seen in Figure 3.23d, the **MIP-2a** films retained the conversion and yield efficiency for two cycles at 1.20 (2-h synthesis) and 2.00 V vs. Ag quasi-reference electrode (30-min synthesis). This behavior indicates that these **MIP-2** systems can be used to scale up electro-synthesis.

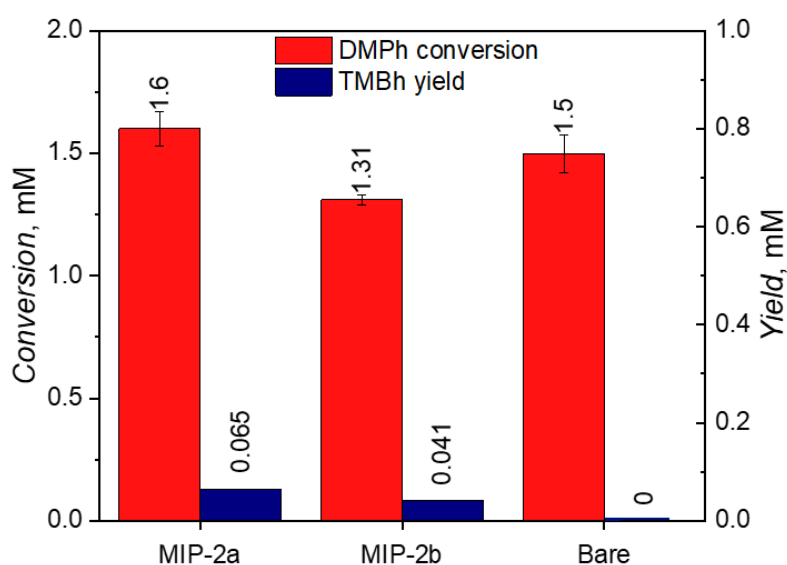
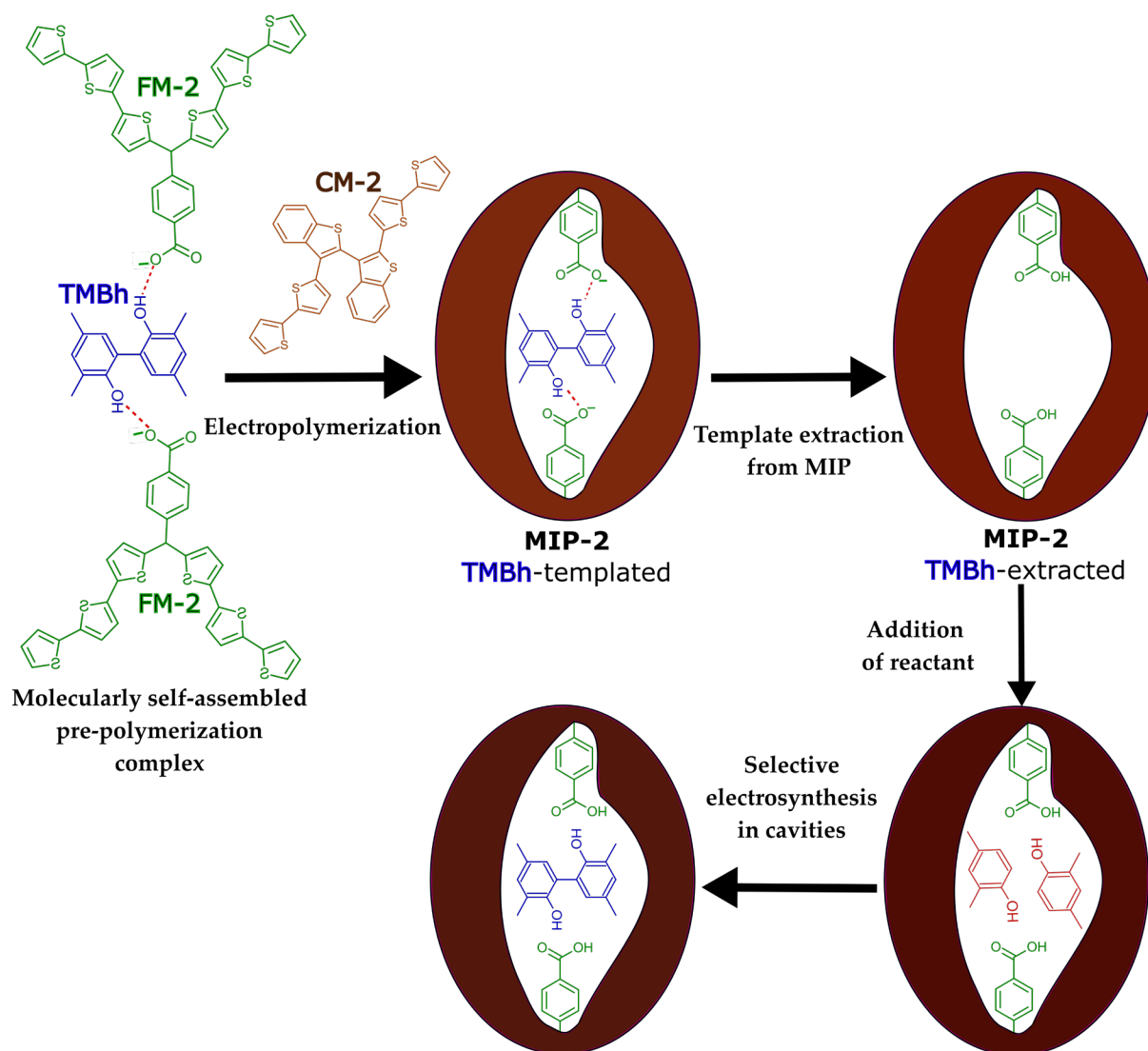


Figure 3.24. Comparison of potentiostatic electro-oxidation of 2 mM **DMPH** in 100 mM (TBA)ClO₄ in ACN : DCM (9 : 1, v/v) at bare, **MIP-2a**, and **MIP-2b** film-coated electrodes at 1.20 V vs. Ag quasi-reference electrode after 7 h.

Furthermore, if a lower concentration of the **DMPH** reactant is used, the yield of the desired **TMBh** product is also equivalently lower (Figure 3.24). The lower reactant concentration does not help improve the yield of the desired product. Moreover, even at lower **DMPH** concentrations, the bare Pt electrode was not selective to the desired **TMBh** product, although the **DMPH** conversion was high. That presumably indicates that the phenolic compound polymerizes or degrades at bare electrodes, as HPLC chromatograms (Figure 3.22) also do not show at 280 nm wavelength a significant quantity of products of the electro-synthesis at the bare electrode.

In conclusion, the thinner **MIP-2b** film is slightly more selective toward the desired **TMBh** electro-synthesis product. Moreover, higher electro-oxidation potential positively affects this selectivity of electro-synthesis. However, an optimized value must be determined by focusing on the integrity of the films.

3.7.6 Theoretical simulations of selective **TMBh** electrosynthesis at **MIP-2** films-coated electrodes



Scheme 3.5. A flowchart of preparation of MIPs selective to **TMBh** and a tentative mechanism of selective electrosynthesis of **TMBh** in the **MIP-2** system.

Scheme 3.5 proposes a selective electrosynthesis mechanism. After preparing **MIP-2** film-coated electrodes and conditioning them, the **DMPH** reactant is added to 100 mM (TBA)ClO₄ in ACN : DCM (9 : 1, v/v). The electrosynthesis is performed under potentiostatic conditions, and selective coupling is expected in the cavities where two **DMPH** molecules are converted to a **TMBh** molecule through radical cation formation followed by coupling. To further elucidate the selectivity of the MIPs for this reaction, computational simulations were applied, and attempts have been made to explain the process in depth.

Insight into the cavity formed in MIP-2

The **MIP-2** cavity model was created by the simulations of electropolymerization of the **FM-2** functional monomer and the **CM-2** cross-linking monomer in the **TMBh** template presence (Figure 3.25). The cavity surfaces were colored according to all components' molecular electrostatic potential (MEP) distribution. The positive potential was generated on the edges of the cavity, whereas the neutral potential was near the thiophene rings derived from **FM-2** and **CM-2**. A slightly negative potential was close to the benzene rings of **FM** and **CM**. In turn, strongly negative regions were near the O atoms of the carboxyl group in **FM-2**.

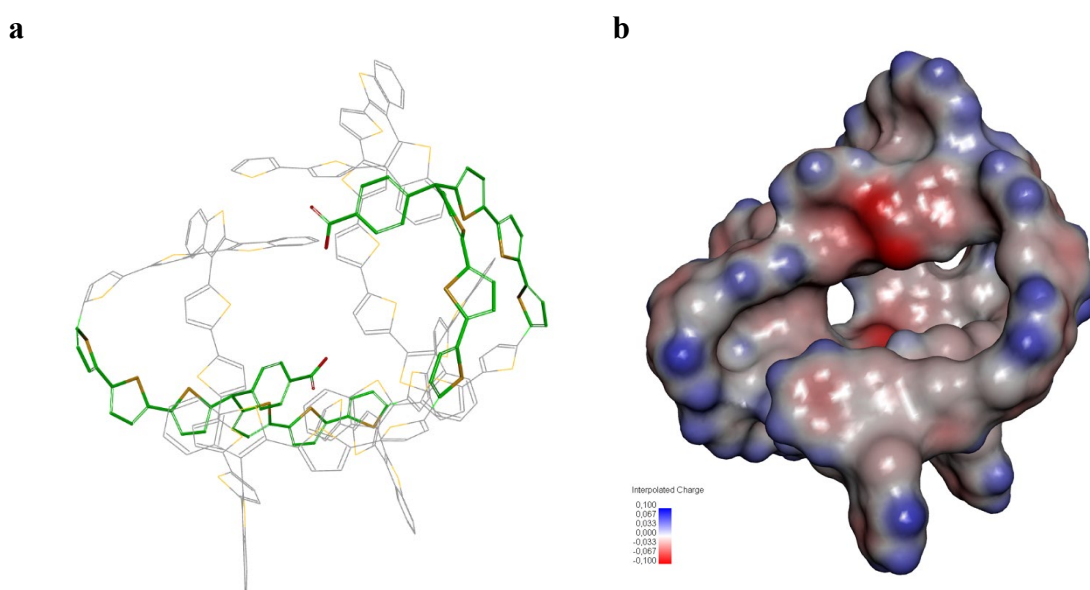


Figure 3.25. A simulated structure of the molecular cavity imprinted in the (**MIP-2**)-**TMBh** film. (a) A skeleton model and (b) molecular electrostatic potential (MEP) surface, colored according to the interpolated charge (blue/red represent the positive/negative charge, respectively).

Processes in the cavity

The **DMPH** molecules should diffuse into the cavity from the solvent for the **TMBh** electrosynthesis. Therefore, these molecules were inserted into the cavity one by one to simulate this diffusion. This simulation allowed for examining their alignment in the cavity and checking whether their positions favor the **DMPH** conversion into **TMBh**. The results are shown in Figure 3.26. The first **DMPH** molecule locates itself deep in the cavity, with the hydroxy and *ortho* methyl groups oriented toward the cavity center and the *para* methyl group oriented toward the cavity wall. The second **DMPH** molecule enters the space left in the cavity, and its methyl and hydroxyl groups are directed outside the cavity. The second **DMPH**

molecule changes the orientation of the first molecule. The first **DMPH** molecule is still located deep in the cavity, but two methyl groups are oriented toward the cavity center, while the hydroxyl group is oriented toward the cavity wall. The distance between C–C atoms for neutral **DMPH** molecules is predicted to be 3.33 Å (Figure 3.26a). We postulate that the sorbed neutral **DMPH** molecules are electro-oxidized to the radical cations **DMPH^{•+}** and then converted to the desired product **TMBh** presumably in a few steps, which are associated with the proton H⁺ removal. Initial and final steps were simulated and analyzed based on systems in which the intermediate radical cations and the **TMBh** product, together with 2 H⁺ ions, are located inside the cavity one after the other.

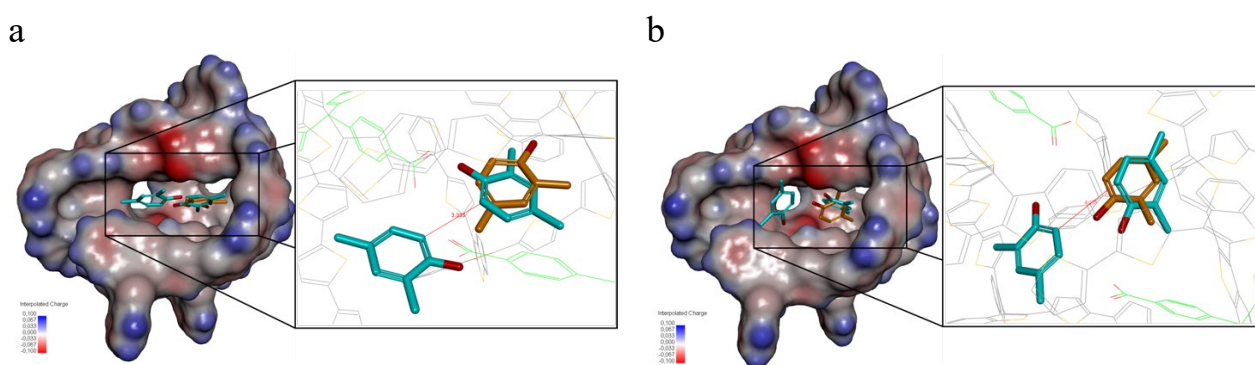


Figure 3.26. The positions of the substrates in the **MIP-2** cavity after MD simulations. (a) The position of one neutral **DMPH** molecule (orange) in the **DMPH**-(**MIP-2**) system and the position of two neutral **DMPH** molecules (turquoise) in the 2×**DMPH**-(**MIP-2**) system. (b) The position of one radical cation **DMPH^{•+}** molecule (orange) in the **DMPH^{•+}**-(**MIP-2**) system and the position of two radical cations **DMPH^{•+}** molecules (turquoise) in the 2×**DMPH^{•+}**-(**MIP-2**) system.

Two molecules of the radical cation of **DMPH^{•+}** (Figure 3.26b) are in the same cavity part as the neutral **DMPH** molecules, but their arrangement somewhat differs. The first **DMPH^{•+}** radical cation is located deep in the cavity, with its methyl substituents oriented toward the cavity center and the hydroxyl group directed toward the outside of the cavity. The second **DMPH^{•+}** radical cation is situated in the space left in the cavity, with both methyl substituents directed toward the outside of the cavity, while the hydroxyl group is directed inside the cavity. Hence, the arrangement of two substrates in the polymer cavity can promote the formation of a C–C bond between them. The distance between these atoms is predicted as 4.03 Å (Figure 3.26b). The ΔG_{bind}^0 value calculated after MD simulations is $-183.7 \text{ kJ mol}^{-1}$ for the electro-oxidized substrates system in the **MIP-2** cavity, while for the neutral substrates, it is

-152.9 kJ mol⁻¹. It means that the system after electro-oxidation is more stable, which can favor the anodic oxidation.

MIP surface impact on the reaction from QM/MM simulations

The cavity's effect on the **TMBh** synthesis was investigated by comparing the standard Gibbs free energy changes, $\Delta G_{\text{reaction}}^0(298 \text{ K})$ for the reaction inside the **MIP-2** cavity and in a free environment. The computation was made on the DFT/Amber level of the QM/MM theory. The results are shown in Table 3.5.

Table 3.5. The standard Gibbs free energy and standard enthalpy changes accompanying the **TMBh** synthesis.

Reaction	$\Delta G_{\text{reaction}}^0(298 \text{ K})$ kJ mol ⁻¹	$\Delta H_{\text{reaction}}^0(298 \text{ K})$ kJ mol ⁻¹
Free molecules		
DMP^{h+} + DMP^{h+} → TMBh + 2H ⁺	+1141.6	+1149.5
Molecules in the MIP cavity		
DMP^{h+} + DMP^{h+} → TMBh + 2H ⁺	-573.5	-588.1

The $\Delta G_{\text{reaction}}^0(298 \text{ K})$ value is highly positive for **DMP^{h+}** dimerization in the ACN : DCM (9 : 1, v/v) mixed solvents, reflecting a very low dimerization possibility. In contrast, the $\Delta G_{\text{reaction}}^0(298 \text{ K})$ value for the reaction on the electrode coated with the **MIP-2** film is highly negative, substantiating the favorable impact of cavities on the **TMBh** synthesis.

Interaction between reagents and the cavity

Analyzing the interactions between the cavity and the reagents can highlight the MIP impact on the synthesis pathway. Figure 3.27 schematically shows the intermolecular interactions as dashed segments. The **DMP^{h+}** radical cations form three hydrogen bonds and two non-classical bonds (π -donor) between the hydroxyl groups of **DMP^{h+}** and sulfur atoms of the thiophene from **FM-2** and benzothiophene rings of the two **CM-2** (length of 3.54 to 3.77 Å). The interactions with OH groups can help orient the substrates per the structure of the desired product. Additionally, the position of the carboxyl groups from the **FM-2** in the cavity allows

for the creation of electrostatic interactions (π -anion) between the aromatic rings of both **DMP^{h+}** radical cations (lengths of 4.56 and 4.66 Å), which supported the favorable positions of **DMP^{h+}**. Other interactions reinforce the molecular arrangement. There are hydrophobic interactions (π - π sigma, π - π T-shaped, and π -alkyl types) between the thiophene and benzothiophene rings of **CM-2** and the methyl groups of **DMP^{h+}** (length of 3.57 to 5.48 Å).

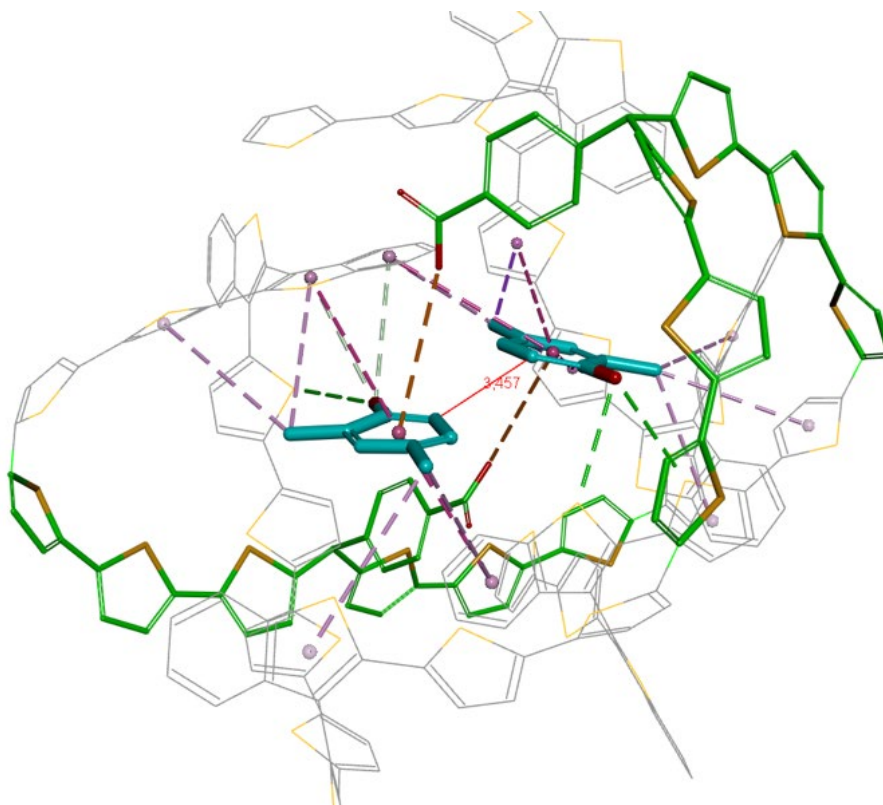


Figure 3.27. The interactions of two **DMP^{h+}** substrate radical cations, indicated with dash segments, in the skeleton model of the **MIP-2** cavity.

Therefore, it can be concluded that the interaction of the reactant molecule with the **MIP-2** cavity is favorable for the selective electrosynthesis of the **TMBh** desired product. This yields selectivity of the **MIP-2** system toward **TMBh**.

3.8 Conclusions

The 3,3',5'5'- tetramethyl-2,2'-biphenol (**TMBh**) desired product of electro-oxidation of 2,4-dimethylphenol (**DMPH**) was imprinted in molecularly imprinted polymer (MIP) film deposited by electropolymerization. Although the diphenylamine-2-carboxylic acid functional monomer (**FM-1**) strongly binds the **TMBh** template in simulations and experiments, it failed to form a stable MIP film with sufficient strong binding of the template in cavities. The successful MIP (**MIP-2**) preparation utilized interactions between the **TMBh** template and *p*-bis(2,2';5',2''-terthien-5'-yl)methylbenzoic acid functional monomer (**FM-2**) with the carboxylic acid functional group. The **FM-2** was deprotonated as the carboxylate more strongly binds **TMBh** at the **TMBh** : **FM-2** molar ratio of 1 : 2. The calculations allowed the selection of *p*-bis(2,2';5',2''-terthien-5'-yl)methylbenzoic acid as one of the effective functional monomers. FT-IR and UV-vis spectroscopy probed the interaction between the template and the functional monomer. Both techniques showed interactions between pre-polymerization complex components. The study of the "aging" mechanism of the pre-polymerization complex solution of **MIP-2** revealed possible instabilities in the film formation, presumably because of aggregation changes in the pre-polymerization solution. Measures were taken to ascertain reproducible film formation. Both **MIP-2** and NIP-2 films were successfully deposited on the electrodes using electrochemical polymerization. The films deposited were relatively thick (400 – 900 nm) and rough. Nanomechanical properties mapping allowed distinguishing softer and more rigid domains in the films. The PM-IRRAS spectra of the films before and after template extraction and the indirect using DPV of the redox probe employing the "gate effect" confirmed successful template extraction.

Finally, the polymer film-coated electrodes were used for the electrosynthesis of **TMBh**. The effect of film thickness, the potential applied, and **DMPH** concentration on the electrosynthesis yield and selectivity toward the desired **TMBh** product were studied. The **MIP-2** film-coated electrodes exhibited a higher yield toward the desired C–C coupled product than non-imprinted polymer (NIP) film-coated and bare electrodes. The selectivity of the electrosynthesis performed at 1.20 V vs. Ag quasi-reference electrode reached 39% at the thinner **MIP-2b** film-coated electrode. Compared to literature data, the highest selectivity (yield %) of ~17% was reported for electro-oxidation of **DMPH** to **TMBh** in aqueous/organic solvents at room temperature ³⁸³. The selectivity has been further increased to ~56% by performing the electrosynthesis at 70 °C in the presence of ammonium salts ³⁸³, then to ~67% by using fluorinated additives at 30 °C ¹⁷³, and then to ~70% using oxidizers like SeO₂ at

85 °C³⁸⁴ to name a few. Recently, the highest selectivity of 60% has also been reported for electrosynthesis performed in the presence of radical-stabilizing hexafluoroisopropan-2-ol solvent at low temperatures¹⁶⁷. Therefore, it can be concluded that the MIPs are promising for selective electrosynthesis. Optimizing the electrode and electrolyte solutions could be prospective future paths to enhance electrosynthesis selectivity further.

The MIPs could maintain the electrosynthesis yield and selectivity even in the second electrosynthesis cycle up to 2 h, indicating the stability of the material suitable for electrosynthesis. Higher electrode potential increased the reaction yield, but the films became poisoned by reaction products at a longer (> 2 h) synthesis time. Therefore, the desired high selectivity should be balanced with maintaining the MIP film integrity. Theoretical simulations confirmed the selectivity of MIP cavities toward the formation of **TMBh**, yielding a deeper understanding of the possible mechanism inside the cavities. The MIP technology combination with electrosynthesis led to a significant enhancement in the selectivity of the phenol C–C coupling toward the desired biphenol compound.



4

Green silver nanocomposites for catalytic applications



4.1 Synopsis

The present work deals with the recycling of the large amounts of wastes produced from stages 5 (BW5), 7 (BW7), and 9 (BW9) of the brewing industry for preparing nanocatalyst materials. The project workflow is shown in Scheme 4.1. The project was initiated by analyzing brewery wastes in **Section 4.2** to understand their composition and determine the wastes' value-added compounds. The nanocomposites were synthesized, then their structure, composition, and morphology were characterized in **Sections 4.3.1 - 4.3.5**. Furthermore, the thermal stability of these materials was examined and described in **Section 4.3.6**, and representative nanocomposites were studied for their catalytic activity depicted in **Section 4.3.7**. The work is concluded in **Section 4.4**.



Scheme 4.1. The project workflow for brewery wastes-mediated nanocomposites for catalytic applications.

4.2 Analysis of the brewery wastes composition[‡]

The composition and elemental analysis results of brewery wastes from three production stages, i.e., the fifth stage (BW5 - wort precipitate), the seventh stage (BW7 - Brewer's spent yeast), and the ninth stage (BW9 - filtration waste) are summarized in Table 4.1.

[‡] The brewery wastes analyses reported in Table 4.1 were performed by Dr. Dorota Michałowska and Prof. Marek Ł. Roszko at the Institute of Agriculture and Food Biotechnology - State Research Institute, Warsaw, Poland, and the TOC analysis was performed at the Central Research Laboratory of the University of Life Sciences, Lublin, Poland and included for description purposes jointly with the thesis, entitled "Unraveling the chemistry behind the biological activity of green silver nanocomposites" by M.Sc. Neha Venkatesh Rangam under the supervision of Dr. hab. Beata Lesiak-Orłowska from the Structures and Dynamics of Nanocrystalline Materials Research Group at the Institute of Physical Chemistry, Polish Academy of Sciences, Warsaw, Poland.

Table 4.1. Composition analysis of brewery wastes BW7, BW9, and BW5 in solution form.

Analysis	Subtype	Brewery waste		
		BW7	BW9	BW5
Total nitrogen, mg L ⁻¹		7454.5	443.8	975.8
Total polyphenols, mg L ⁻¹		181.2	87.75	92.65
Total sulfates, mg L ⁻¹		193.03	103.4	119.65
Total carbohydrates, mg L ⁻¹		4500	1200	156700
Fermentable sugars, mg L ⁻¹	Total	1600	600	115,800
	Fructose	700	100	2100
	Glucose	300	100	12,500
	Maltose + Sucrose	500	200	76,500
	Maltotriose	100	200	24,700
Elemental content, mg L ⁻¹	K	2710 ± 460	284 ± 48.3	657 ± 111
	P	97 ± 3,9	149 ± 6	525 ± 20
	Cl	<4	165 ± 1.0	365 ± 1.0
	Mg	228.3 ± 38.8	56.1 ± 9.5	125.9 ± 21.4
	Ca	55.0 ± 8.3	68.0 ± 10.2	69.3 ± 10.4
	Na	64.0 ± 6.4	42.9 ± 4.3	58.0 ± 5.8
	Mn	1.64 ± 0.13	0.22 ± 0.02	0.73 ± 0.06
	Fe	0.8 ± 0.11	6.0 ± 0.84	0.3 ± 0.04
	Zn	2.6 ± 0.36	0.01 ± 0.01	0.43 ± 0.06
	Cu	0.32 ± 0.03	<0.05	0.08 ± 0.01
	Al	0.01 ± 0.01	<0.05	0.01 ± 0.01
Ni	<0.05	<0.05	<0.05	
Total organic carbon, %		7.24	2.84	7.78

The BW7 brewery waste is richer in nitrogen, polyphenols, and sulfates than BW5 and BW9. BW5, disparately, has a significant carbohydrate content. The BW7 and BW9 are relatively

deficient in carbohydrates. The BW7 also has high potassium, magnesium, sodium, and manganese content, whereas the BW5 has significantly more phosphorous content. BW9 contains smaller amounts of most of the compounds and elements. However, the quantity of some elements, i.e., P, Cl, Ca, Na, and Fe, is higher. The influence of these composition changes on the nanocomposite formation is discussed in Section 4.4 in detail.

Moreover, small amounts of zinc and copper are present in brewery wastes. Similar carbon content is determined in the BW7 and BW5 wastes in the TOC analysis, and BW9 organic carbon content is substantially lower, which is not surprising considering the substantially smaller amount of organic compounds in this filtration waste. The total fermentable sugars can be equated to reducing sugars present in brewery wastes, as the sucrose contents in BW5, BW7, and BW9 were negligible.

Significant differences are in the FT-IR spectra of BW5 compared to BW7 and BW9 (Figure 4.1), indicating that the fermentation leads to substantial changes in the functional moieties in the brewing liquids.

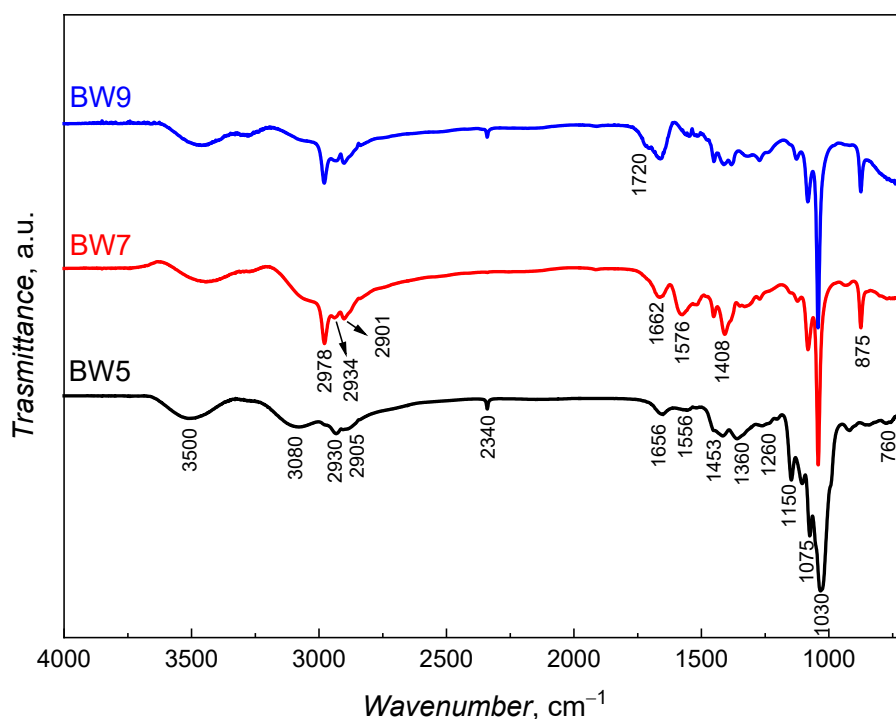


Figure 4.1. Fourier transform infrared (FT-IR) spectra of BW5, BW7, and BW9 brewery wastes in a solution form.

The broad band between ~ 3700 and 3300 cm^{-1} is related to strong intramolecular H-bonded O–H group stretching vibrations of polyphenols combined with the N–H stretching vibrations for hydrogen-bonded NH groups³⁷⁹. For BW5, this band is more intense and slightly

shifted to higher wavenumbers than BW7 and BW9. The broad band at 3080 cm^{-1} can be related to the C–H stretching vibrations for compounds built from carbon atoms of sp^2 hybridization³⁷⁹. The C–H alkane stretching vibrations are found in the $2990 - 2850\text{ cm}^{-1}$ region in all the wastes³⁷⁹. However, additional bands with a higher intensity in BW7 and BW9, especially the band at 2978 cm^{-1} , can be assigned to stretching vibrations in the $-\text{CH}_3$ substituent³⁷⁹.

The bands at $1650 - 1670$ and $1550 - 1580\text{ cm}^{-1}$ can be attributed to amide I (C=O stretching with some N–H bending) and amide II (N–H bending with C–N stretching), respectively³⁸⁵⁻³⁸⁶. The amide I band position is varied in the different wastes indicating the possible presence of different secondary structures³⁸⁵. These bands are more pronounced for BW7, indicating a higher protein/peptide content, possibly from the yeast. An additional band at $\sim 1720\text{ cm}^{-1}$ only for BW9 could originate from C=O vibrations of the carbonyl group in carboxylic acids or aldehydes. The C–H alkane bending vibrations are at ~ 1450 and $\sim 1360\text{ cm}^{-1}$. Bands at ca. 1260 , 1150 , 1075 , and 1030 cm^{-1} could represent C–O vibrations or O–H bending of primary, secondary, and tertiary alcohols. These vibrations can also relate to the C–O bending of the C–OH groups in carbohydrates, especially in BW5, as it does not contain fermented alcohols³⁸⁷. Below 1000 cm^{-1} , the out-of-plane X–H bending ($X = \text{C, O, N}$) or $-\text{NH}_2$ rocking and wagging bands appear^{379, 388} like the sharp bands at 875 cm^{-1} for BW7 and BW9. The absence of this band in the waste before the fermentation, BW5, could result from the lack of yeast and fermentation products³⁸⁸.

The rich spectra for all the wastes indicate the possibility of the presence of alcohols, amides, peptides, and polyphenols. The functional groups can also be associated with carbohydrates (~ 1150 to 900 cm^{-1}), lipids (~ 2950 to 2850 cm^{-1}), and proteins (~ 1690 to 1635 cm^{-1}) in the wastes, along with polyphenols³⁸⁵⁻³⁹¹. Considering the rich composition of brewery wastes containing various compounds, one may conclude that these wastes can be used to synthesize NPs, as they contain both capping and reducing agents. The pH of BW7, BW9, and BW5 was 4.85, 3.29, and 4.3, respectively.

4.3 Characterization of nanocomposites

Five different nanomaterials were synthesized by varying the temperature ($25 (\pm 1)$, $50 (\pm 1)$, and $80 (\pm 1)^\circ\text{C}$) and time (10, 30, and 120 min) of synthesis using each brewing waste, namely BW7, BW9, and BW5. The notations of these nanomaterials are given in Table 4.2.

Table 4.2. Designation and synthesis conditions of nanomaterials synthesized using brewery wastes BW7, BW9, and BW5.

Nanocomposite	Synthesis temp., °C	Synthesis time, min
BW7Ag1	25	120
BW7Ag2	50	120
BW7Ag3	80	120
BW7Ag4	80	30
BW7Ag5	80	10
BW9Ag1	25	120
BW9Ag2	50	120
BW9Ag3	80	120
BW9Ag4	80	30
BW9Ag5	80	10
BW5Ag1	25	120
BW5Ag2	50	120
BW5Ag3	80	120
BW5Ag4	80	30
BW5Ag5	80	10

4.3.1 X-ray diffraction (XRD) analysis of crystal structure and phase composition[§]

The X-ray diffraction patterns (Figure 4.2) provided important information on the key differences between the NPs precipitated using different brewery wastes (BW5, BW7, and BW9). The PXRD patterns showed reflexes characteristics for the Ag₃PO₄ (ICDD 98-002-7843), AgCl (ICDD 98-005-6538), and Ag (ICDD 98-060-4629) phases. The average values of crystallite size and the respective standard deviations are listed in Table 4.3.

[§] The XRD diffraction patterns and analyses are produced in common with the thesis, entitled: "Unraveling the chemistry behind the biological activity of green silver nanocomposites" by M.Sc. Neha Venkatesh Rangam under the supervision of Dr. hab. Beata Lesiak-Orłowska from the Structures and Dynamics of Nanocrystalline Materials Research Group at the Institute of Physical Chemistry, Polish Academy of Sciences, Warsaw, Poland.

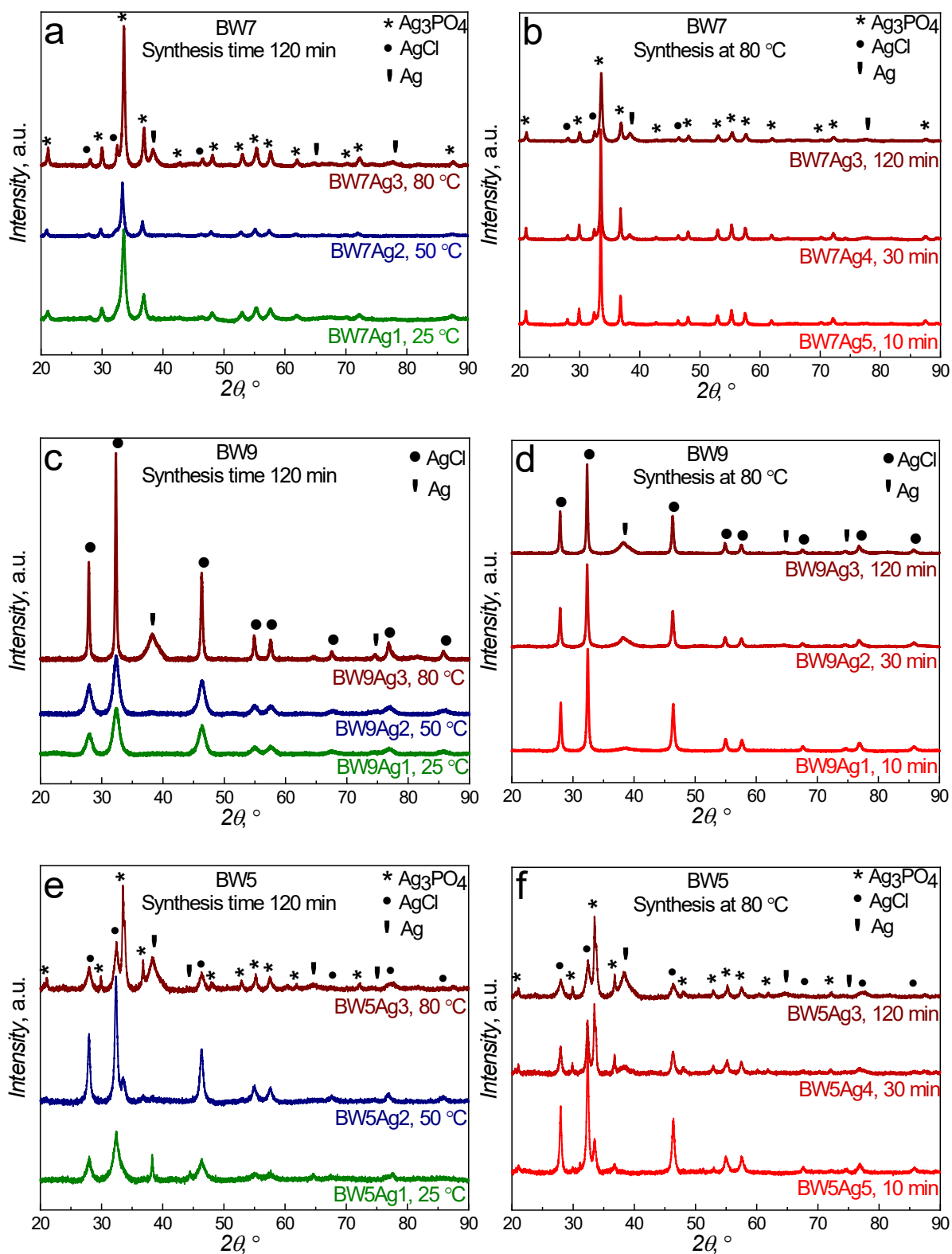


Figure 4.2. X-ray diffractograms of nanomaterials synthesized at different temperatures and times using brewery wastes (a, b) BW7, (c, d) BW9, and (e, f) BW5. (Nanocomposites syntheses conditions are denoted as follows: Ag1 - 25 °C, 120 min; Ag2 - 50 °C, 120 min; Ag3 - 80 °C, 120 min; Ag4 - 80 °C, 30 min; Ag5 - 80 °C, 10 min).

Table 4.3. The PXRD analysis determined phase content and nanocrystallites size of BW7, BW9, and BW5 nanocomposites.

Nanocomposite	Synthesis temp., °C	Synthesis time, min	Ag phase content, %			Nanocrystallites size, nm		
			Ag ₃ PO ₄	AgCl	Ag _{met}	Ag ₃ PO ₄	AgCl	Ag _{met}
BW7Ag1	25	120	90.0	10.0	-	9.9 ± 2.3	5.5 ± 3.6	-
BW7Ag2	50	120	88.7	11.3	-	15.5 ± 4.2	7.5	-
BW7Ag3	80	120	77.1	11.8	11.1	16.2 ± 3.3	16.5 ± 5.9	7.3
BW7Ag4	80	30	79.2	12.0	8.8	25.3 ± 4.0	26.2 ± 5.2	12.2
BW7Ag5	80	10	86.6	10.8	2.6	22.7 ± 3.8	21.0 ± 8.3	15.1
BW9Ag1	25	120	-	100	-	-	5.6 ± 0.5	-
BW9Ag2	50	120	-	97.0	3.0	-	5.6 ± 0.6	2.9
BW9Ag3	80	120	-	73.2	26.8	-	19.4 ± 3.1	3.6
BW9Ag4	80	30	-	75.7	24.3	-	15.6 ± 2.7	3.2
BW9Ag5	80	10	-	92.9	7.1	-	16.0 ± 2.7	2.5
BW5Ag1	25	120	5.9	91.5	2.6	4.8	4.0 ± 0.5	18.1
BW5Ag2	50	120	13.8	85.7	0.5	5.6	8.1 ± 0.8	14.0
BW5Ag3	80	120	30.0	41.5	28.5	12.1 ± 6.2	6.7 ± 0.4	3.2
BW5Ag4	80	30	28.5	46.0	25.6	15.9 ± 6.2	10.2 ± 1.7	1.4
BW5Ag5	80	10	13.1	86.9	-	11.8 ± 0.7	11.9 ± 1.0	-

The **BW7** waste predominantly yielded NPs of silver orthophosphate, Ag₃PO₄ (Figure 4.2a, 4.2b, and Table 4.3) with reflections corresponding to the cubic structure with space group P4-3n. The characteristic Ag₃PO₄ reflexes are at 2θ values of 20.9° (011), 29.7° (002), 33.3° (012), 36.6° (112), 47.9° (013), 52.8° (222), 55.1° (023), 57.4° (123), 61.7° (004), 72.0° (124), and 87.4° (234). An additional reflex at 69.98° (024) 2θ is present in the patterns for samples synthesized at 80 (±1) °C. The evolution of new reflexes and narrowing of all crystalline reflexes with increasing synthesis temperature indicated that the phase crystallinity increases with increasing temperature. The crystal structure consists of a body-centered cubic lattice formed by regular isolated PO₄ tetrahedrons. The Ag atom experiences fourfold coordination by four O atoms³⁹². The P atoms have fourfold coordination surrounded by four O atoms, while the O atoms have fourfold coordination surrounded by three Ag atoms and one P atom.

The polyhedron structure consists of one PO₄ tetrahedron and three tetrahedral AgO₄ combined through the corner oxygen atom. The Ag₃PO₄ phase content decreased from 90 to 77.1% when the synthesis temperature increased to 80 (±1) °C. The size of these crystallite Ag₃PO₄ NPs increased from 9.9 (±2.3) to 16.2 (±3.3) nm with the increasing synthesis temperature (Table 4.3).

Minor quantities (10%) of silver chloride NPs with an average crystallite size of 5.5 (±3.6) nm (Table 4.3) were identified in the BW7Ag1 nanocomposite synthesized at room temperature, 25 (±1) °C. The reflexes at 2θ values of ~27.8° (111), 32.3° (002), and 46.3° (022) are ascribed to AgCl. The AgCl has a body-centered cubic structure with the Fm-3m space group. The crystallinity of the Ag₃PO₄ and AgCl phases increased with the synthesis temperature increase. The AgCl phase content slightly grew from 10 to 11.8%, and the size of the crystallites grew with the temperature increase.

A relatively small AgCl content is not surprising, given a relatively insignificant amount of chlorine in BW7 (Table 4.1). When the synthesis temperature was increased to 80 (±1) °C, Ag_{met} NPs were also formed, indicating that high temperature facilitates the reduction of Ag cations in the precursor silver nitrate from +1 to 0 oxidation state. This effect can indicate that the actual reducing agent is formed or activated in BW7 components at this temperature. Reflexes of Ag are present at 2θ values of 38.1° (111), 64.5° (022), and 77.4° (113). The Ag phase steadily increased at 80 (±1) °C from 10 to 120 min during the synthesis at the expense of the major phase, Ag₃PO₄. The synthesis temperature increase favored the AgCl and Ag₃PO₄ crystallite growth. The Ag₃PO₄ and AgCl crystallite sizes increased with increased synthesis time from 10 to 30 minutes, then decreased when the synthesis time was increased to 120 minutes. This unusual trend might indicate that the synthesis time affects two competing mechanisms: nucleation and crystal growth. The Ag crystallite size decreased with the synthesis time, indicating that the Ag nucleation rate is higher than the Ag phase's crystal growth rate.

In contrast, the **BW9** formed pure AgCl NPs (73.2 to 100%) at room temperature, 25 (±1) °C. At synthesis temperatures exceeding 50 (±1) °C, Ag_{met} up to 26.8% was also incorporated into the structure (Figure 4.2c and 4.2d). The characteristic AgCl reflexes were observed at 27.8° (111), 32.3° (002), 46.3° (022), 54.9° (113), 57.5° (222), 67.5° (004), 76.8° (024), and 85.8° (224). The silver chloride crystallized into a face-centered cubic NaCl-like structure with the Fm-3m space group. As the synthesis temperature was increased, the Ag_{met} NP phases growth was evidenced with the peaks at 38.1° (111), 64.5° (022), and 77.4° (113)

2θ . These peaks were attributed to cubically structured silver NPs, strongly depending on the synthesis temperature. The Ag_{met} phase increased with an increase in synthesis time and temperature at the expense of the AgCl phase. The AgCl NP crystallite size (Table 4.3) increased from 5.6 (± 0.5) nm at room temperature, 25 (± 1) °C, synthesis to 19.4 (± 3.1) nm at elevated temperature, 80 (± 1) °C, synthesis, while that of Ag NPs remained almost constant. This behavior indicates that increasing the synthesis temperature favors the AgCl NPs' growth over the nucleation.

Diversely, **BW5** gave rise to the mixed composite with the AgCl domination. The AgCl phase content up to 91.5% could be obtained via a room temperature, 25 (± 1) °C, synthesis. The Ag and Ag_3PO_4 NPs were found in minor amounts (Figure 4.2e, 4.2f, and Table 4.3). With time and increasing synthesis temperature, more Ag_3PO_4 NPs (up to 30%) and Ag (up to 28.5%) were introduced into the composite. The crystallographic structures of various NPs in these composites were similar to those for NPs obtained using BW7 and BW9. The Ag_3PO_4 NPs' crystallite size increased, and that of Ag NPs decreased with the temperature increase. Elevating the synthesis temperature favored the growth of Ag_3PO_4 crystallites and nucleation of Ag crystallites as observed for BW7 nanocomposites. The Ag and Ag_3PO_4 phases grew with time at the expense of AgCl at the 80 (± 1) °C synthesis temperature. The crystallites' size of these two phases also increased with time; however, that of AgCl decreased. This effect was similar to that of the synthesis temperature effect on AgCl crystallites. The synthesis time favored the growth of nanocrystallites of minor phases, such as Ag and Ag_3PO_4 .

Therefore, it is observed that a wide variety of compositions of nanocomposites can be obtained using these three different brewery wastes, namely, BW7, BW9, and BW5. Increasing synthesis temperatures favored the minor phases' growth and the reduction of Ag cations. Evidently, this synthesis can lead to a composite system with three silver-based phases. Noteworthy, silver oxides' signals were not seen in PXRD diffractograms, presumably because their content was below the detection limit.

4.3.2 Elemental analysis by energy dispersive X-ray fluorescence (EDXRF) spectroscopy**

The elemental content analysis of the nanocomposites obtained using BW7, BW9, and BW5 brewery wastes revealed silver (Ag), chlorine (Cl), phosphorus (P), and sulfur (S) presence. Table 4.4 shows the calculated weight percentages of these elements in the samples.

Table 4.4. Elemental composition of BW7, BW9, and BW5 nanocomposites determined by the energy dispersive X-ray fluorescence (EDXRF) analysis.

Nanocomposite	Synthesis temp., °C	Synthesis time, min	Elemental composition, %			
			Ag	P	Cl	S
BW7Ag1	25	120	93.5	4.8	1.0	0.8
BW7Ag2	50	120	93.7	4.3	1.1	0.8
BW7Ag3	80	120	94.4	3.9	1.0	0.8
BW7Ag4	80	30	94.4	4.0	1.0	0.6
BW7Ag5	80	10	93.8	4.2	1.2	0.8
BW9Ag1	25	120	83.1	0.1	15.1	1.6
BW9Ag2	50	120	83.8	0.2	14.6	1.5
BW9Ag3	80	120	89.3	0.6	9.3	0.8
BW9Ag4	80	30	88.0	0.4	10.7	0.9
BW9Ag5	80	10	84.4	0.3	14.5	0.8
BW5Ag1	25	120	86.5	5.3	7.7	0.5
BW5Ag2	50	120	88.4	2.9	8.1	0.6
BW5Ag3	80	120	92.2	3.0	4.4	0.5
BW5Ag4	80	30	91.6	2.9	5.0	0.6
BW5Ag5	80	10	87.6	2.9	8.8	0.6

The area under the peak for Ag in the EDXRF spectrum was the highest, confirming that Ag-containing NPs were formed. The Ag content was similar in all the nanocomposites

**The EDXRF analyses is produced in common with the thesis, entitled: "Unraveling the chemistry behind the biological activity of green silver nanocomposites" by M.Sc. Neha Venkatesh Rangan under the supervision of Dr. hab. Beata Lesiak-Orłowska from the Structures and Dynamics of Nanocrystalline Materials Research Group at the Institute of Physical Chemistry, Polish Academy of Sciences, Warsaw, Poland.

synthesized using the BW7 fraction. Slight differences are related to the growth of minor amounts of Ag phases (up to 11.1%) with temperature and time observed in PXRD (Table 4.3). The P content decreased with the time and temperature increase, in accord with Ag_{met} NPs formation at higher temperatures, manifested by PXRD (Table 4.3). The Cl and S contents were almost constant in all the BW7 nanocomposites. Only a minor (~1%) amount of Cl (Table 4.4) is coherent with the low AgCl phase content (up to 12%) (Table 4.3).

The Ag's content increased, and that of Cl decreased with the synthesis time and temperature increase for nanocomposites synthesized using the BW9 fraction. This Cl content decrease is consistent with the Ag phase content increase in the PXRD analysis of BW9 nanocomposites (Table 4.3). Phosphorous is present only in trace amounts in BW9 nanocomposites, indicating they could be a part of the carbonaceous shell. Worth mentioning that the sulfur content is the highest in BW9 nanocomposites.

In nanocomposites synthesized using the BW5 fraction, the Ag content increased from 86.5 to 92.2% with the synthesis temperature increase (Table 4.4). The growth of a larger amount of Ag_{met} NPs in the composite (up to 28.5%) (Table 4.3) competes with this increase. The Cl content in BW5 nanocomposites decreased with the synthesis temperature and time increase because the Ag_{met} NPs formation was favored. This behavior aligns with the decrease in the AgCl phase observed in PXRD (Table 4.3). The phosphorous content change does not entirely agree with the PXRD analysis, possibly indicating the presence of this element in the organic capping as well. The sulfur, present in trace amounts in all the samples, is most likely included in the organic layer stabilizing the NPs.

4.3.3 Morphological analysis

The morphology of nanocomposites synthesized at 25 (± 1) and 80 (± 1) °C after 120 min, using BW7, BW9, and BW5 wastes as representatives, was analyzed with SEM. The imaging of an Ag₃PO₄-rich sample, BW7Ag1, obtained using BW7 at 25 (± 1) °C (Figure 4.3a and 4.3b), revealed globular structures composed of several smaller balls. As the AgCl and Ag particles content increased in the structures with the synthesis temperature increase (BW7Ag3), the flakey aggregated layers were fused with balls, as observed in the areas marked in red in Figure 4.3c and 4.3d. The size of these globular structures ranged from ~10 to 350 nm in BW7 nanocomposites. BW9 nanocomposites, prepared at 25 (± 1) °C (BW9Ag1), were mainly composed of aggregated layers (Figure 4.3e and 4.3f). Silver incorporation in the BW9Ag3 structure accompanying the synthesis temperature increase to 80 (± 1) °C yielded some small

round particles growing on layers (Figure 4.3g and 4.3h). The BW5 nanocomposite, prepared at $25 (\pm 1) ^\circ\text{C}$ (BW5Ag1), revealed aggregated layers. These layers are characteristic of AgCl, as seen for BW9 nanocomposites, along with some small balls and globules characteristic of Ag_3PO_4 as found in BW7 nanocomposites (Figure 4.3i and 4.3j).

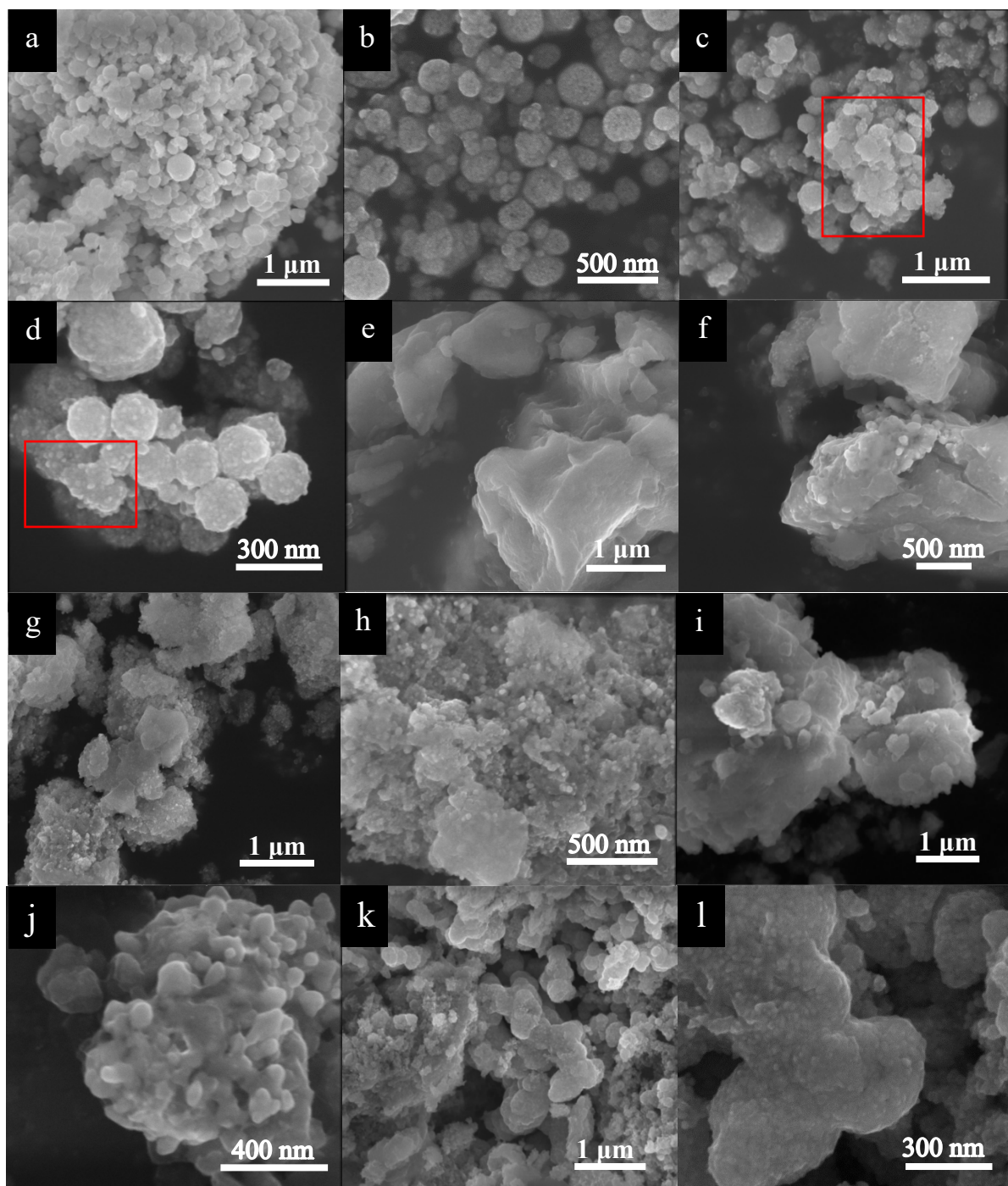
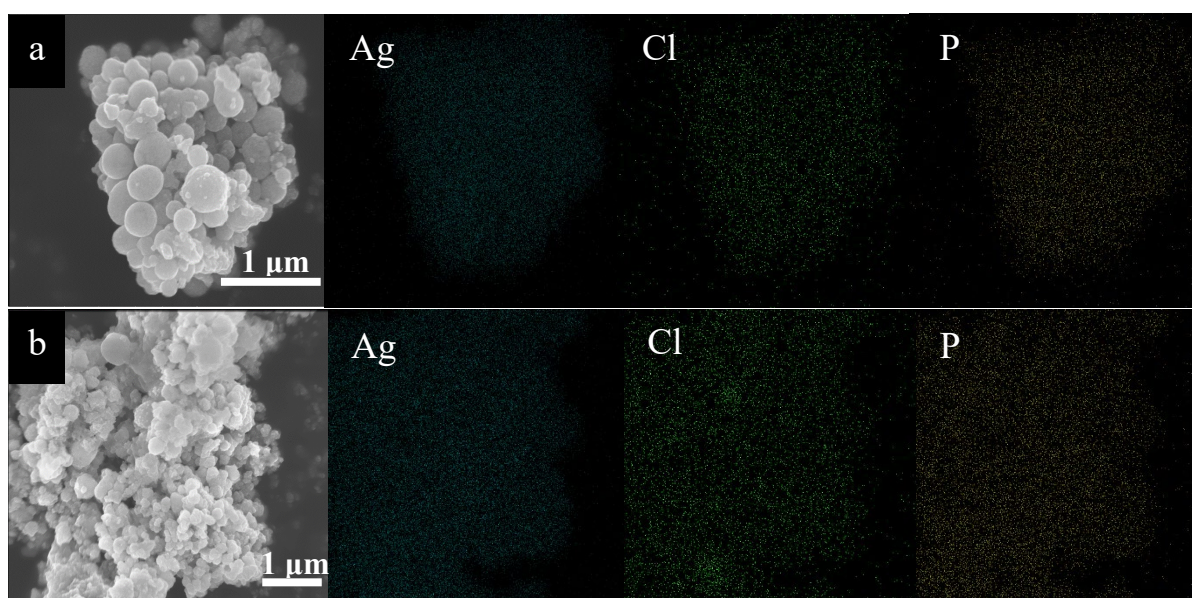


Figure 4.3. SEM images of nanocomposites of (a, b) BW7Ag1, (c, d) BW7Ag3, (e, f) BW9Ag1, (g, h) BW9Ag3, (i, j) BW5Ag1, and (k, l) BW5Ag3. (Nanocomposites syntheses conditions are denoted as follows: Ag1 - $25 ^\circ\text{C}$, 120 min, and Ag3 - $80 ^\circ\text{C}$, 120 min).

With increasing Ag_3PO_4 content in the structure, fused morphology similar to that of BW7 nanocomposites was observed (Figure 4.3k and 4.3l). In Figure 4.3l, the particles' surface morphology is similar to the Ag_3PO_4 balls in BW7 nanocomposites. All the nanocomposites are aggregated, possibly because of a thin organic overlayer formed using weak capping agents that were not entirely sufficient for preventing aggregation.

The elemental mapping of BW7, BW9, and BW5 nanocomposites synthesized at $25 (\pm 1)$ and $80 (\pm 1)$ °C after 120 min is presented in Figure 4.4. This mapping indicates that the elemental distribution of the significant components of the nanocomposites, namely, Ag, Cl, and P, on the surface of the BW7 (Figure 4.4a and 4.4b), BW9 (Figure 4.4c and 4.4d) and BW5 nanocomposites (Figure 4.4e and 4.4f) was sufficiently homogeneous. This distribution indicates that the NPs' morphological changes in shapes and sizes are due to incorporating certain phases in the structure; however, these phases are not present independently but predominately as a mixed phase composite. Only Ag and Cl are visible for BW9 nanocomposites synthesized at $25 (\pm 1)$ °C (BW9Ag1) and $80 (\pm 1)$ °C (BW9Ag3), while Ag, Cl, and P can be found in BW5 and BW7 nanocomposites synthesized at $25 (\pm 1)$ °C (BW5Ag1 and BW7Ag1) and $80 (\pm 1)$ °C (BW5Ag3 and BW7Ag3), in accord with the PXRD analysis results (Table 4.3).



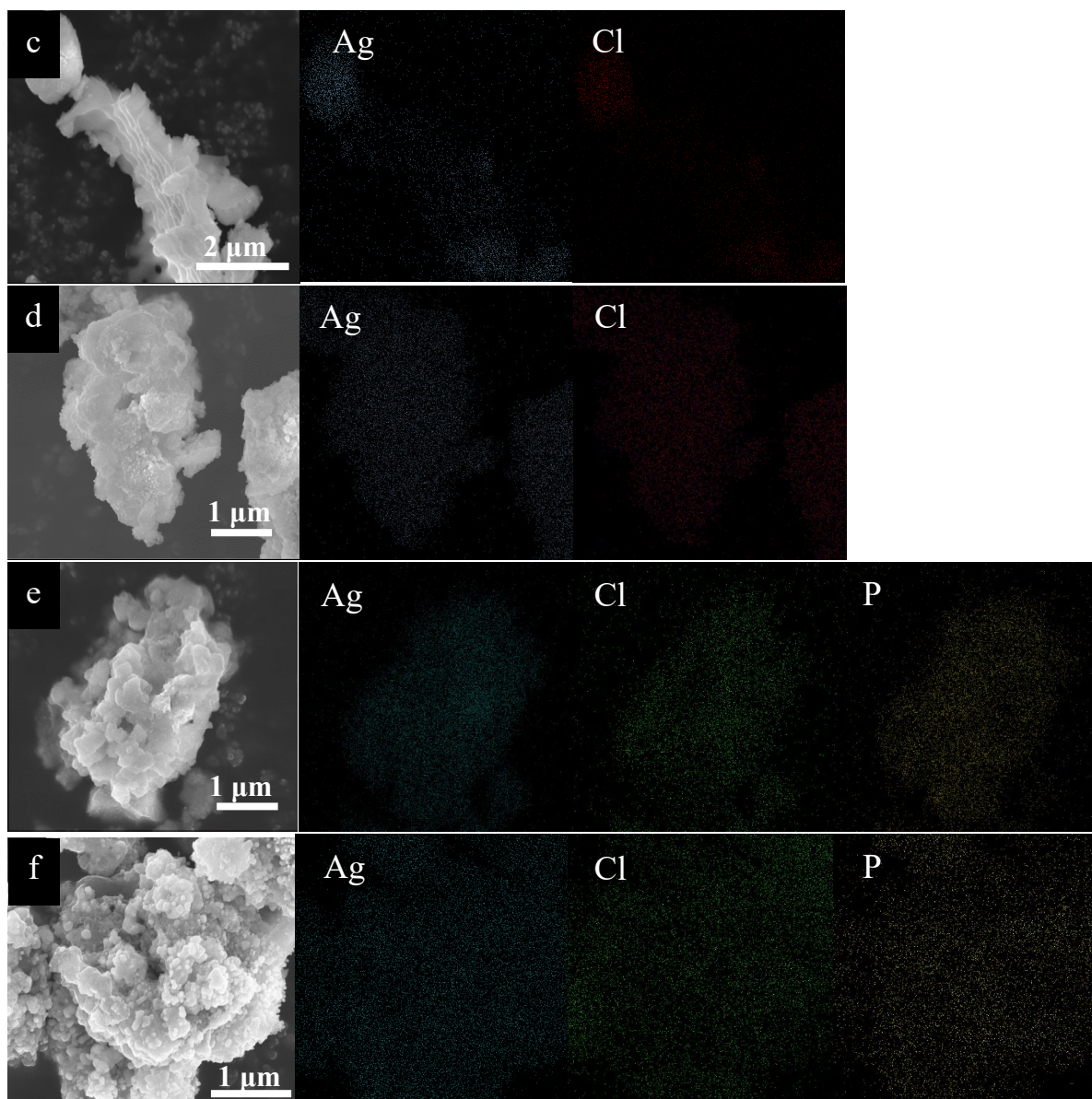


Figure 4.4. Elemental mapping of (a) BW7Ag1, (b) BW7Ag3, (c) BW9Ag1, (d) BW9Ag3, (e) BW5Ag1 and (f) BW5Ag3 nanocomposites. (Nanocomposites syntheses conditions are denoted as follows: Ag1 - 25 °C, 120 min, Ag3 - 80 °C, 120 min).

4.3.4 Spectral analysis

4.3.4.a UV-vis spectroscopy analysis

The UV-vis absorption spectra of the nanocomposites synthesized using BW7, BW9, and BW5 at different temperatures and 120-min synthesis are shown in Figure 4.5. Free electrons in Ag_{met} NPs exhibited an SPR absorption band. This band is seen if the vibration of the electrons in the NPs is in resonance with incoming light radiation³⁹³. The bands between 400 and 500 nm represents the characteristic SPR of the Ag_{met} NPs in all nanocomposites. Moreover, the presence of Ag_3PO_4 in BW7 and BW5 nanocomposites affected the UV-vis absorption in

the region below 530 nm as Ag_3PO_4 is a semiconductor sensitive to UV-vis radiation (Figure 4.5a and 4.5c). The Ag_3PO_4 irradiation removes electrons from the valence shell of oxygen³⁹⁴. These electrons are scavenged by silver cations (Ag^+), forming metallic silver (Ag^0) NPs. The Ag_{met} absorption bands in the BW7 and BW5 nanocomposites containing Ag_3PO_4 follow a decreasing intensity with increasing synthesis temperature (Figure 4.5a and 4.5c), which is a bit puzzling as the Ag_{met} amount in the structure is higher at higher synthesis temperatures, as seen in PXRD (Table 4.3). The absorption trend is appropriate only for BW9 nanocomposites (Figure 4.5b) that do not contain Ag_3PO_4 , wherein the absorption band becomes more intense with increasing Ag_{met} introduction at higher synthesis temperatures. Therefore, it can only be speculated that the presence of Ag_3PO_4 disrupts the collective resonance of the SPR band leading to the observed trend.

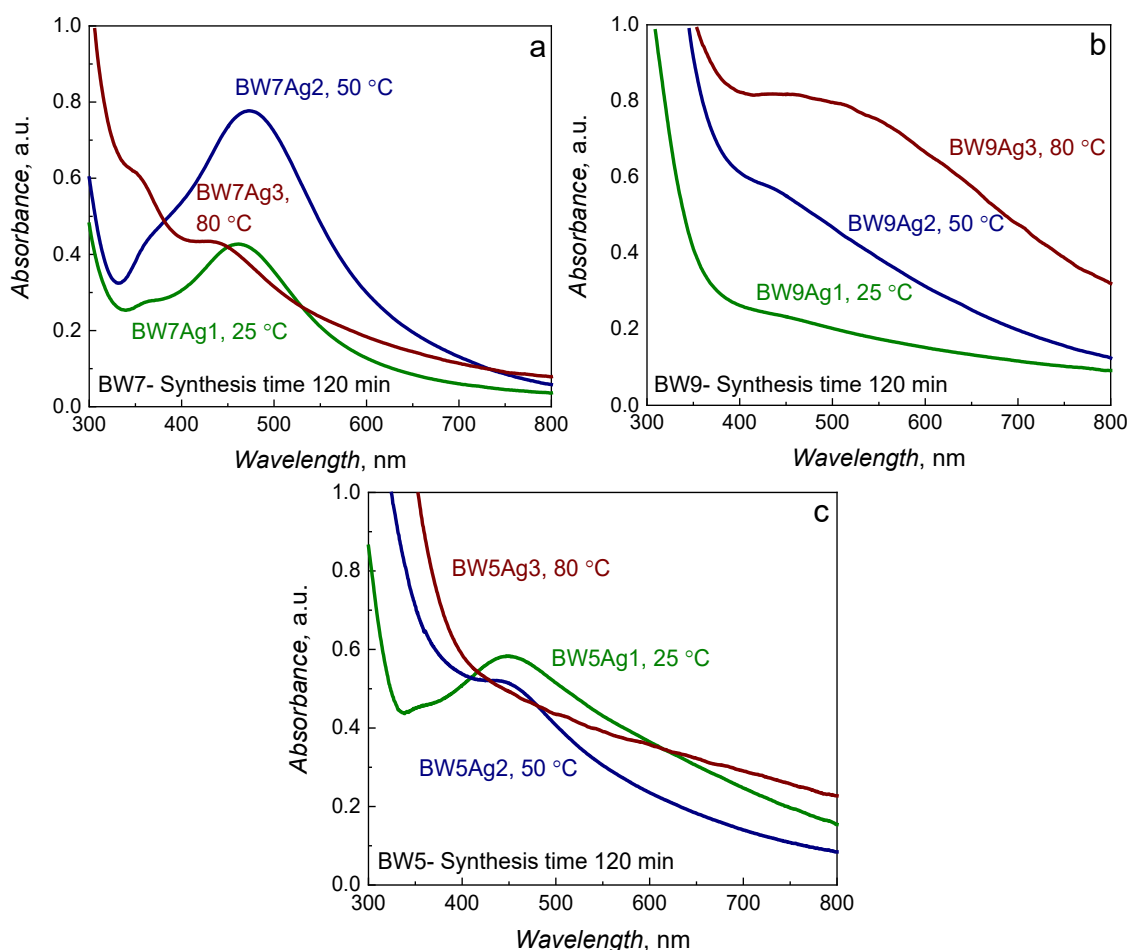


Figure 4.5. UV-vis spectra for nanocomposites synthesized using (a) BW7, (b) BW9, and (c) BW5. (Nanocomposites syntheses conditions are denoted as follows: Ag1 - 25 °C, 120 min, Ag2 - 50 °C, 120 min, and Ag3 - 80 °C, 120 min).

4.3.4.b *Fourier-transform infrared (FT-IR) spectroscopy analysis*

All three sets of nanocomposites show a broad band between 3500 and 3000 cm^{-1} , representing stretching vibrations of the hydrogen-bonded –OH group of polyphenols, although the relative intensities of these bands vary depending on the nanocomposite (Figure 4.6). This broad band can also be attributed to the amide's N–H stretching vibration. This vibration band in BW5 and BW9 nanocomposites is stronger than in the BW7 nanocomposites, indicating more surface-bound hydroxyl and other hydrogen-bonded functional groups. Compared to its position in brewery wastes, this band shift to lower frequencies in NPs (Figures 4.1 and 4.6) is related to the complexation of the functional groups to NPs. Moreover, many sharp bands between 2840 and 3000 cm^{-1} arise from symmetric and asymmetric C–H stretching vibrations of alkanes in various chemical environments. These vibrations are also significantly intense in BW5 (Figure 4.6e and 4.6f) nanocomposites but are almost absent in BW7 nanocomposites (Figure 4.6a and 4.6b).

Interestingly, the BW7 spectrum bands assigned to the C–H bond-containing compounds are more pronounced than the BW5 spectrum bands (Figure 4.1). However, the BW7 nanocomposites exhibit only very weak bands in this region (Figure 4.6a and 4.6b). BW5 nanocomposites show important bands in this region, and the dominant bands at 2915 – 2920 and 2850 cm^{-1} indicate mainly the –CH₂– moieties presence (Figure 4.6e and 4.6f). BW9 nanocomposites also exhibit these bands representing the –CH₂– moieties (Figure 4.6c and 4.6d). The amide I and II bands at 1630 – 1650 and ~1540 cm^{-1} , respectively, related to peptide/protein binding, are also present in the spectra of nanocomposites. These bands are intense for BW9 nanocomposites (Figure 4.6c and 4.6d), followed by BW5 nanocomposites (Figure 4.6e and 4.6f), and very weak for BW7 nanocomposites (Figure 4.6a and 4.6b). This effect also contradicts the wastes' behavior, where the intensity of those bands for BW5 and BW9 is weaker than for BW7 (Figure 4.1). Considering the NP composition, one can infer that the protein/peptide adsorption on AgCl NPs is more predominant than for Ag₃PO₄. The intense band between 1030 and 1040 cm^{-1} representing C–O vibration is in the BW5 (Figure 4.6e and 4.6f) and BW9 nanocomposites (Figure 4.6c and 4.6d). The BW5 and BW9 nanocomposites' capping resulted in more functional groups in the FT-IR spectroscopy analysis, indicating that these materials' surface composition is richer than the BW7 nanocomposites. The functional group vibrations for these NPs are from the brewery wastes BW7, BW9, and BW5, indicating a successful capping of the NPs.

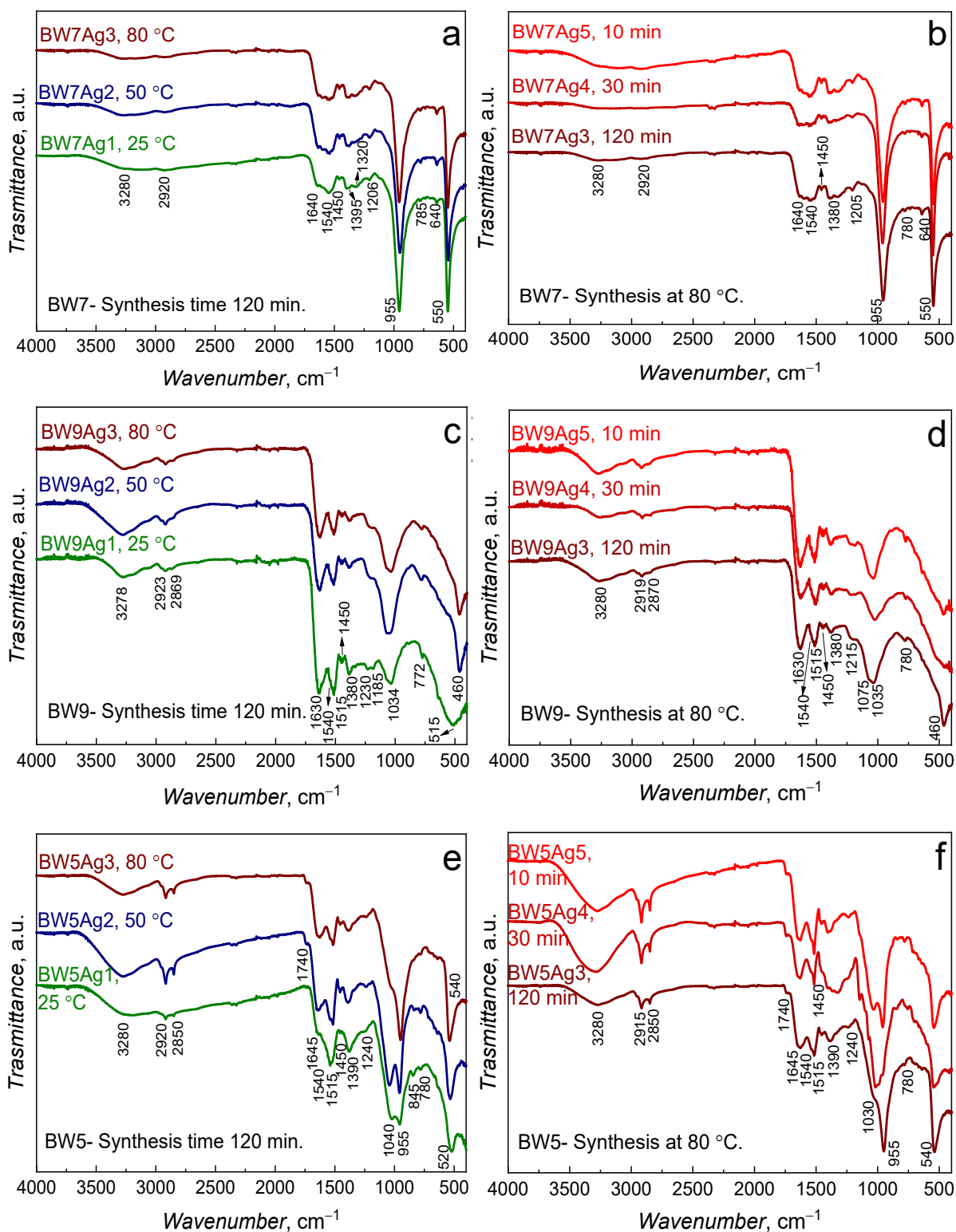


Figure 4.6. FT-IR spectra of nanocomposites synthesized at different temperatures and times using brewery wastes (a, b) BW7, (c, d) BW9, and (e, f) BW5. (Nanocomposites syntheses conditions are denoted as follows: Ag1 - 25 °C, 120 min, Ag2 - 50 °C, 120 min, Ag3 - 80 °C, 120 min, Ag4 - 80 °C, 30 min, and Ag5 - 80 °C, 10 min).

Furthermore, the frequencies' shifts of these vibrations in NPs (Figure 4.6) compared to that in the brewery wastes (Figure 4.1) indicate extensive complexation of the functional

groups with the NPs. Not all functional groups aid in the capping of NPs, and depending on the brewery waste, different groups have been attached to the NPs' surface. The binding of protein/peptide and polyphenols is preferred on the surface of AgCl NPs.

The nanocomposites' spectra have additional vibrations related to Ag_3PO_4 and silver oxides. The band for BW7 (Figure 4.6a and 4.6b) and BW5 (Figure 4.6e and 4.6f) nanocomposites in the region of ~ 520 to 550 cm^{-1} represent Ag–O stretching modes. The band at $\sim 550\text{ cm}^{-1}$ is also attributed to a bending vibration of O=P–O, whereas that at $\sim 960\text{ cm}^{-1}$ is ascribed to asymmetric stretching of the OP–O bridge^{392, 395-396}. These PO_4^{3-} modes are relatively sharp for BW7 nanocomposites (Figure 4.6a and 4.6b) at all synthesis temperatures and times, providing evidence of Ag_3PO_4 as the major phase. Characteristic vibration modes for Ag_3PO_4 become more prominent with the temperature and time increase for BW5 nanocomposites (Figure 4.6e and 4.6f), indicating the growth of Ag_3PO_4 in the nanocomposite. The band also shifts from 520 to 540 cm^{-1} as phosphate groups grow in the BW5 nanocomposites with increasing synthesis temperature. The vibration frequency for the BW5Ag3 nanocomposite is lower than for the BW7Ag3 nanocomposite because Ag_3PO_4 is a minor phase. Therefore, it has a more complex environment that influences its vibration. The vibrations around these two regions are broad in BW9 nanocomposites (Figure 4.6c and 4.6d), indicating that these materials do not have Ag_3PO_4 in their structure. A possible silver oxides' presence in BW9 nanocomposites may account for the broad band between ~ 450 and 500 cm^{-1} .

4.3.5 Brunauer-Emmett-Teller (BET) sorption analysis

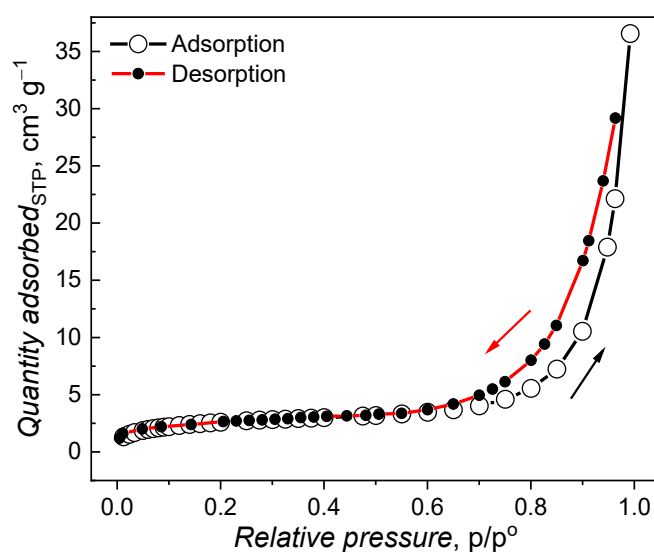


Figure 4.7. Exemplary Brunauer-Emmett-Teller (BET) adsorption-desorption isotherms for BW7Ag3 nanocomposites synthesized at $80 (\pm 1)\text{ }^\circ\text{C}$ for 120 min.

The surface nature and surface area of materials used as catalysts play an important role as the reactions primarily occur at the catalyst surface. Therefore, the larger surface area available for reaction can enable higher conversion of reactants, thereby improving the efficiency of the process. All nanocomposites exhibited a Type II isotherm, as shown for BW7Ag3 as an exemplary nanocomposite (Figure 4.7), indicating unlimited multilayer adsorption on non-porous / macroporous structures.

Table 4.5. The Brunauer-Emmett-Teller (BET) specific surface area of nanocomposites synthesized using BW7, BW9, and BW5 brewery wastes.

Nanocomposite	Synthesis temp., °C	Synthesis time, min	BET specific surface area, m ² g ⁻¹
BW7Ag1	25	120	2.19
BW7Ag2	50	120	3.21
BW7Ag3	80	120	9.51
BW7Ag4	80	30	11.35
BW7Ag5	80	10	5.84
BW9Ag1	25	120	2.37
BW9Ag2	50	120	7.48
BW9Ag3	80	120	10.09
BW9Ag4	80	30	5.48
BW9Ag5	80	10	6.79
BW5Ag1	25	120	0.91
BW5Ag2	50	120	8.56
BW5Ag3	80	120	8.92
BW5Ag4	80	30	4.41
BW5Ag5	80	10	7.82

The multi-point BET surface area analysis of the nanocomposites revealed that their specific surface areas depended on the synthesis temperature (Table 4.5). The specific surface area of nanocomposites synthesized at 80 (±1) °C (~8.5 – 11.4 m² g⁻¹) was higher than those synthesized at room temperature, 25 (±1) °C (0.9 – 2.4 m² g⁻¹). The observed growth of the Ag_{met} phase in the nanocomposites with increasing synthesis temperature might be affecting

the specific surface area. Although small, these differences in the BET-specific surface areas of the nanocomposites could affect the catalytic performance of these nanomaterials. Notably, however, the surface area of the materials tested is relatively small for BET measurements, and the quantity of powder available for analysis was also small³⁹⁷. Therefore, the isotherms' shape is irregular, with the desorption isotherm intersecting the adsorption isotherm for most nanocomposites. This behavior is presumably due to the low degassing temperature that might be insufficient to clean the surfaces achieved through the removal of the physisorbed species and the "entrapment" of adsorbed gases in the pores.

4.3.6 Thermogravimetric analysis (TGA)

Thermogravimetric analysis was performed to understand the thermal stability of nanocomposites. There are three major TGA decomposition stages (Figure 4.8). The TGA curves for nanocomposites started with removing surface water, followed by the decomposition of organic moieties over the nanocomposite surface as the major decomposition part. Subsequently, there were changes in Ag phase compositions. Noteworthy, the decomposition did not complete at 800 °C.

Three clear decomposition stages can be observed for **BW7 nanocomposites** (Figure 4.8a and 4.8b). The overall weight loss is the highest for samples synthesized at 25 (± 1) °C, BW7Ag1 (27.7%), followed by samples synthesized at 50 (± 1) °C, BW7Ag2 (25.9%), and 80 (± 1) °C, BW7Ag3 (24.4%). The first decomposition stage, up to 140 °C for BW7Ag1 and BW7Ag2 and 150 °C for BW7Ag3, resulted in a weight loss between 2.2 and 3.3%. The major decomposition occurred up to ~450 °C exhibiting weight losses of ~16% and 14.4% for BW7Ag1 and BW7Ag2. This stage extended only to 370 °C for BW7Ag3, yielding a loss of ~13%. A weight loss of ~8 to 9% was for all three samples in the last stage of decomposition, although the last stage was slow and not finished in the studied temperature range. The anomalous behavior in the decomposition temperature range observed for the BW7Ag3 synthesized at 80 (± 1) °C can be attributed to the metallic Ag NPs growth in the composite structure and oxidation of the surface Ag.

Moreover, **BW9 nanocomposites'** three-stage decomposition was like BW7 nanocomposites' decomposition (Figure 4.8c and 4.8d). The overall weight loss of 30 to 45% was for all nanocomposites synthesized using BW9. The weight loss for BW9 nanocomposites higher than for BW7 nanocomposites indicates a higher organic capping over the AgCl

nanocomposites in the former, in agreement with the FT-IR observations of the richness of functional groups in AgCl-based nanocomposites (Figure 4.6).

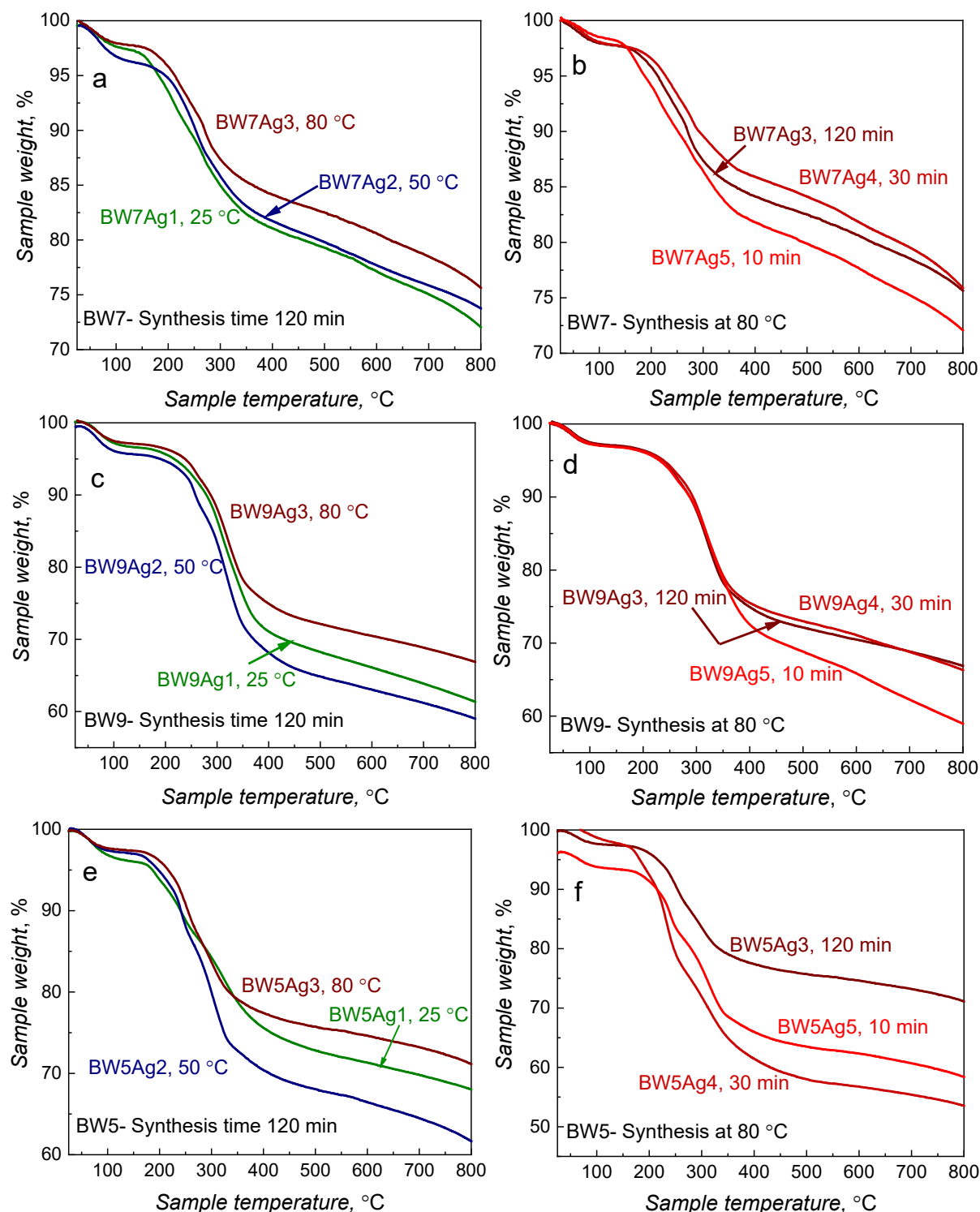


Figure 4.8. Thermogravimetry analysis (TGA) curves for nanocomposites synthesized at different temperatures and times using brewery wastes (a, b) BW7, (c, d) BW9, and (e, f) BW5. (Nanocomposites syntheses conditions are denoted as follows: Ag1 - 25 °C, 120 min, Ag2 - 50 °C, 120 min, Ag3 - 80 °C, 120 min, Ag4 - 80 °C, 30 min, Ag5 - 80 °C, 10 min).

The weight loss for BW9Ag2 nanocomposite, synthesized at 50 (± 1) °C was the highest, equalling ~41%, followed by the BW9Ag1 nanocomposite synthesized at 25 (± 1) °C, and the least weight loss was for BW9Ag3 nanocomposite synthesized at 80 (± 1) °C for 120 min. This result indicates that the synthesis at 50 (± 1) °C results in a higher organic coating that decomposes in the second stage. The first decomposition stage led to ~3.5 to 4.5% weight loss, followed by 23.7 to 30.1% weight loss in the second stage, and finally ~6% for BW9Ag2 and BW9Ag3 nanocomposites synthesized at higher temperatures and a relatively higher 8% weight loss for BW9Ag1 nanocomposite synthesized at 25 (± 1) °C. The higher weight loss by BW9Ag1 could be ascribed to the pure AgCl phase present with possible some silver oxide impurities. Therefore, the presence of phases such as Ag₃PO₄ and Ag_{met} is beneficial for improving the stability of the nanocomposites.

In contrast, **BW5 nanocomposites** exhibited four decomposition stages for the BW5Ag1 sample synthesized at 25 (± 1) °C and the BW5Ag2 sample synthesized at 50(± 1) °C, and three stages for the sample synthesized at 80 (± 1) °C (Figure 4.8e and 4.8f). The overall weight loss increased from BW5Ag1 (~32%) to BW5Ag2 (38.8%). Subsequently, the total weight loss markedly decreased to 28.8% for BW5Ag3, wherein the Ag_{met} NPs and Ag₃PO₄ contributions were significantly high. The decomposition in the region between ~260 and ~500 °C strongly influences the overall weight loss trend, wherein weight was lost by 14.4, 17.9, and 10.5% for BW5Ag1, BW5Ag2, and BW5Ag3, respectively. A trend in the last decomposition stage beyond 500 °C is similar, and the weight loss of BW5Ag2 (6.7%) is high compared to BW5Ag1 (4.3%) and BW5Ag3 (4.7%). However, this stage indicates the start of slow decomposition here as well. The decomposition trend in BW5 nanocomposites indicates that synthesis at 50 (± 1) °C results in higher organic matter content in the nanocomposite compared to other synthesis temperatures. Noticeably, the weight loss of nanocomposites with a high AgCl content is higher than those with high Ag₃PO₄ content. Therefore, it can be concluded that the organic overlayer composition and thickness strongly depend on the nanocomposites' composition, which agrees with the FT-IR spectroscopy analysis (Figure 4.6).

The weight loss of BW5 nanocomposites synthesized at 80 (± 1) °C for different time spans largely varied (Figure 4.8f). The reaction for 120 min led to the Ag and Ag₃PO₄ rich structure resulting in significantly higher stability at temperatures between 260 and 500 °C. The BW7 nanocomposites' stability was almost similar, with the samples prepared within a 10-min synthesis showing the lowest stability in the series (Figure 4.8b). Moreover, the BW9 nanocomposites' stability trend was like BW7 nanocomposites, with a 10-min reaction leading

to the highest organic content, resulting in higher weight loss (Figure 4.8d). Therefore, increasing the synthesis time at 80 (± 1) °C is favorable for improving the materials' thermal stability, which could also indirectly point to the significance of Ag_{met} phase growth.

The weight loss up to 100 °C results from surface-bound water removal. Ag₃PO₄ remains thermally stable up to ~900 °C with only a minor (<1%) portion converting to Ag and Ag oxide³⁹⁸⁻³⁹⁹, whereas AgCl NPs remain stable up to 650 °C⁴⁰⁰⁻⁴⁰¹. The DSC and temperature-programmed reaction (TPR) studies provided information on the decomposition process of silver oxides⁴⁰². A minor decomposition could be the surface AgO thermal reduction to metallic silver in the 100 to 200 °C range, and this reaction's product remained stable up to ~350 °C. The Ag₂O intermediate completely decomposes to Ag and O₂ at 400 °C. However, a major weight loss for Ag NPs at ~200 °C has been related to the decomposition of organic capping agents⁴⁰³. At ~470 °C, decompositions of hydroxyl (C–OH) and carbonyl (C=O) groups were reported, whereas above 600 °C, mainly C=O groups decompose⁴⁰⁴.

The BW7 nanocomposites' weight loss was the smallest, followed by BW9 and BW5 nanocomposites. The major differences are in the second decomposition stage up to 500 °C, wherein the BW5 nanocomposites' weight loss was the highest, followed by BW9 and BW7 nanocomposites, indicating that BW5 nanocomposites contain the highest organic overlayer content. The variation in the weight loss is related to different phase compositions of samples synthesized using various brewery wastes at different synthesis temperatures and times.

4.3.7 Characterization of catalytic properties of nanocomposites

4.3.7.a Electron spin resonance (ESR) analysis

To characterize the electronic properties of synthesized nanocomposites and elucidate their catalytic capabilities, electron spin resonance (ESR) spectroscopy has been used. Worth mentioning that the electronic properties of nanocomposites play a crucial role in heterogeneous catalysis and electrocatalysis⁴⁰⁵. The ESR spectrum parameters (the first derivative of the absorption spectrum) are indicated in Figure 4.9, where $A_{\text{ESR}} = A_1 + A_2$ is the amplitude, $\Delta H_{\text{pp}} = H_1 + H_2$ is the linewidth, and B_0 is the resonant magnetic induction. The A_{ESR} amplitude, normalized to the sample weight, reflects the content of paramagnetic centers. The g-factor is evaluated from conditions of resonance according to Equation 2.19

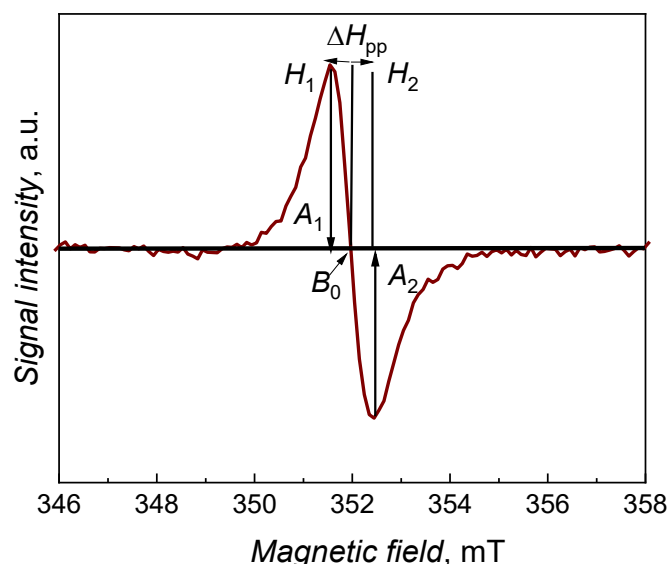


Figure 4.9. Exemplary electron spin resonance (ESR) spectrum for BW7Ag3 nanocomposite [synthesized at 80 (± 1) $^{\circ}$ C for 120 min], indicating the analyzed parameters.

The ESR spectra recorded for nanocomposites, synthesized using BW7, BW9, and BW5 brewery wastes at different times and temperatures, do not have any subtle structures relating to Ag. In all the spectra, there is a single sharp resonance band of varying intensity depending on the nanocomposites synthesis conditions, with a 0.8 to 1.0 mT width and a 2.0044 to 2.0055 g -factor (Figure 4.10). These values are typical for zero-valent silver aggregates with a conduction band⁴⁰⁶⁻⁴⁰⁷. For BW5Ag1 and BW5Ag5 nanocomposites, i.e., nanocomposites synthesized using the BW5 brewery waste at 25 (± 1) $^{\circ}$ C for 120 min and 80 (± 1) $^{\circ}$ C for 10 min, respectively, the sharp band overlaps with a broad band of the ~

50 mT linewidth and 2.011 g -factor (Figure 4.10c). This wide band is seen for other BW5 and BW9 nanocomposites, albeit with low intensity. The origin of this broad band could not be precisely identified. However, it could be attributed to small silver clusters occurring due to highly mobile Ag^+ ions undergoing auto reduction under different environmental conditions, like exposure to light⁴⁰⁸⁻⁴¹⁰. Notably, this broad band is a feature prominent in mixed Ag/AgCl/Ag₃PO₄ phases. Apparently, the nanocomposite structure stabilizes the clusters, as the pronounced band is visible even at room temperature. This band stabilization points to the importance of domain formation in the structures that can isolate the active species for a longer time, stabilizing the ESR signal⁴¹⁰. Moreover, this signal is visible for the BW5Ag5 nanocomposites, not exhibiting a silver phase in PXRD (Table 4.3). That might indicate that these small clusters are present in tiny amounts below the detection limit of XRD.

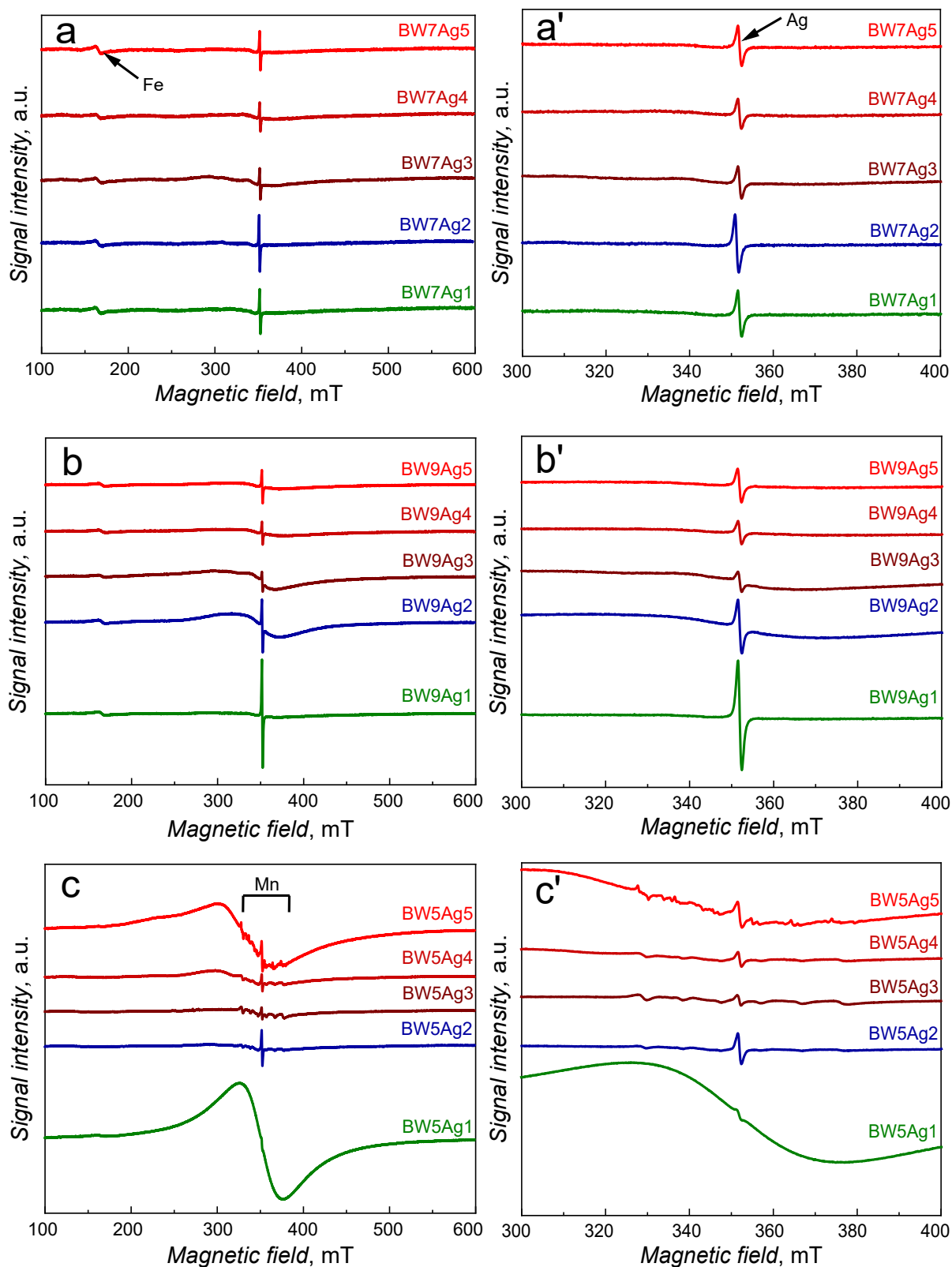


Figure 4.10. Electron spin resonance (ESR) spectra for (a, a') BW7, (b, b') BW9, and (c, c') BW5 nanocomposites synthesized at different temperatures and times. (Nanocomposites syntheses conditions are denoted as follows: Ag1 - 25 °C, 120 min, Ag2 - 50 °C, 120 min, Ag3 - 80 °C, 120 min, Ag4 - 80 °C, 30 min, Ag5 - 80 °C, 10 min). a', b', and c' are scaled in spectra of a, b, and c, respectively, to show the sharp band at ~350 mT.

Moreover, interestingly, there is a band for a Fe complex with organic matter in the BW7 and BW9 nanocomposites at a g -factor of ~ 4.3 (Figure 4.10a and 4.10b), indicating that the Fe is present in the organic capping of the nanocomposites⁴¹¹⁻⁴¹². The ESR band for Mn^{2+} in BW5 nanocomposites reveals hyperfine splitting, resulting in six lines with a g -factor close to the Ag conduction band singlet (Figure 4.10c and 4.10c')⁴¹¹. The bands for Fe and Mn could be observed because the ESR spectroscopy is exceptionally sensitive to these metals. Because of their scarce content, these metals are undetectable with other analytical techniques. Fe and Mn in brewery wastes are the sources of these elements in the nanocomposites. This result shows that elements present in the brewery wastes are differently attached to the organic content. Hence, some elements are selectively present in some nanocomposites.

Table 4.6. The parameters of the sharp Ag singlet at ~ 350 mT in electron spin resonance (ESR) spectra, namely, g -factor, amplitude normalized to weight, linewidth, amplitude asymmetry, linewidth asymmetry of BW7, BW9, and BW5 nanocomposites synthesized at different temperatures and times. (Nanocomposites syntheses conditions are denoted as follows: Ag1 - 25 °C, 120 min, Ag2 - 50 °C, 120 min, Ag3 - 80 °C, 120 min, Ag4 - 80 °C, 30 min, Ag5 - 80 °C, 10 min).

Nanocomposite	g -factor	Amplitude, a.u.	Linewidth, mT	Amplitude asymmetry	Linewidth asymmetry
BW7Ag1	2.0044	34.63	0.89	1.13	1.19
BW7Ag2	2.0048	43.51	0.98	1.15	1.46
BW7Ag3	2.0048	24.04	0.91	1.08	0.90
BW7Ag4	2.0047	22.43	0.81	1.17	0.88
BW7Ag5	2.0052	30.4	0.88	1.17	0.63
BW9Ag1	2.0046	237.9	0.88	1.10	0.91
BW9Ag2	2.0052	113.8	0.92	1.15	0.84
BW9Ag3	2.0050	41.8	0.89	1.13	1.23
BW9Ag4	2.0055	49.85	0.81	1.04	0.93
BW9Ag5	2.0055	72.53	0.99	1.05	0.87
BW5Ag1	2.0051	11.5	0.98	0.95	0.91
BW5Ag2	2.0051	52.37	0.83	1.17	1.03
BW5Ag3	2.0053	17.51	0.91	1.38	1.45
BW5Ag4	2.0049	24.87	0.81	1.28	0.99
BW5Ag5	2.0049	42.6	1.04	1.26	0.80

The parameters of the sharp ESR singlet of the 2.0044 to 2.0055 *g*-factor, recorded for all BW7, BW9, and BW5 nanocomposites, indicate that they depend on sample phase and elemental composition (Table 4.6). For BW5 and BW9 nanocomposites of Ag, the ESR parameters' dependence on the nanocomposite synthesis conditions is significant, while the BW7 nanocomposites' spectral changes are smaller. That could indicate that the silver chloride environment in the nanocomposite is favorable for silver paramagnetic activity, as literature reports include the importance of the environment on the ESR signal intensity of silver aggregates⁴¹³. The number of paramagnetic centers in BW7 and BW9 nanocomposites decreases with the synthesis temperature increase. This effect can be related to the increase in the size of silver aggregates, as small-size silver aggregates predominantly contribute to the ESR signal⁴¹⁰. Therefore, the number of paramagnetic centers, proportional to the normalized amplitude, is lower for BW7 and BW9 nanocomposites synthesized at 80 (± 1) °C (samples Ag3, Ag4, and Ag5) because of large-sized Ag crystallites observed in PXRD (Table 4.3).

Amplitude (A_1/A_2) and linewidth (H_1/H_2) asymmetry indicate anisotropy, being higher for BW5 nanocomposites synthesized at elevated temperatures (samples Ag3, Ag4, and Ag5) and BW7 and BW9 nanocomposites synthesized at 25 (± 1) and 50 (± 1) °C (samples Ag1 and Ag2, respectively). That is attributed to the broad heterogeneous distribution of NPs sizes⁴¹⁴. Presumably, a larger number of larger silver aggregates are formed in BW7 and BW9 nanocomposites at elevated synthesis temperatures. Most likely, these larger aggregates have non-interacting spins that are more localized, and the high synthesis temperatures give rise to more homogeneous silver beyond the size limit required to generate an ESR signal. Therefore, the number of paramagnetic centers observed in ESR spectroscopy and the anisotropy of the sharp singlet for BW7 and BW9 nanocomposites synthesized at 80 (± 1) °C are lower. Contrastingly, higher synthesis temperatures of 50 (± 1) and 80 (± 1) °C result in the formation of smaller silver crystallites in BW5 nanocomposites (Table 4.3). Possibly, these smaller size aggregates capable of exhibiting paramagnetic properties, having a more heterogeneous size distribution, lead to higher anisotropy.

A 10-kGy γ -irradiation of BW7Ag3, BW9Ag3, and BW5Ag3 nanocomposites [synthesized at 80 (± 1) °C for 120 min] enhances the sharp singlet peak of *g*-factor of 2.0044 to 2.0055. That indicates the formation of new paramagnetic centers, presumably because of electrons and holes generated locally in the materials or Ag clusters (Figure 4.11)⁴¹⁰.

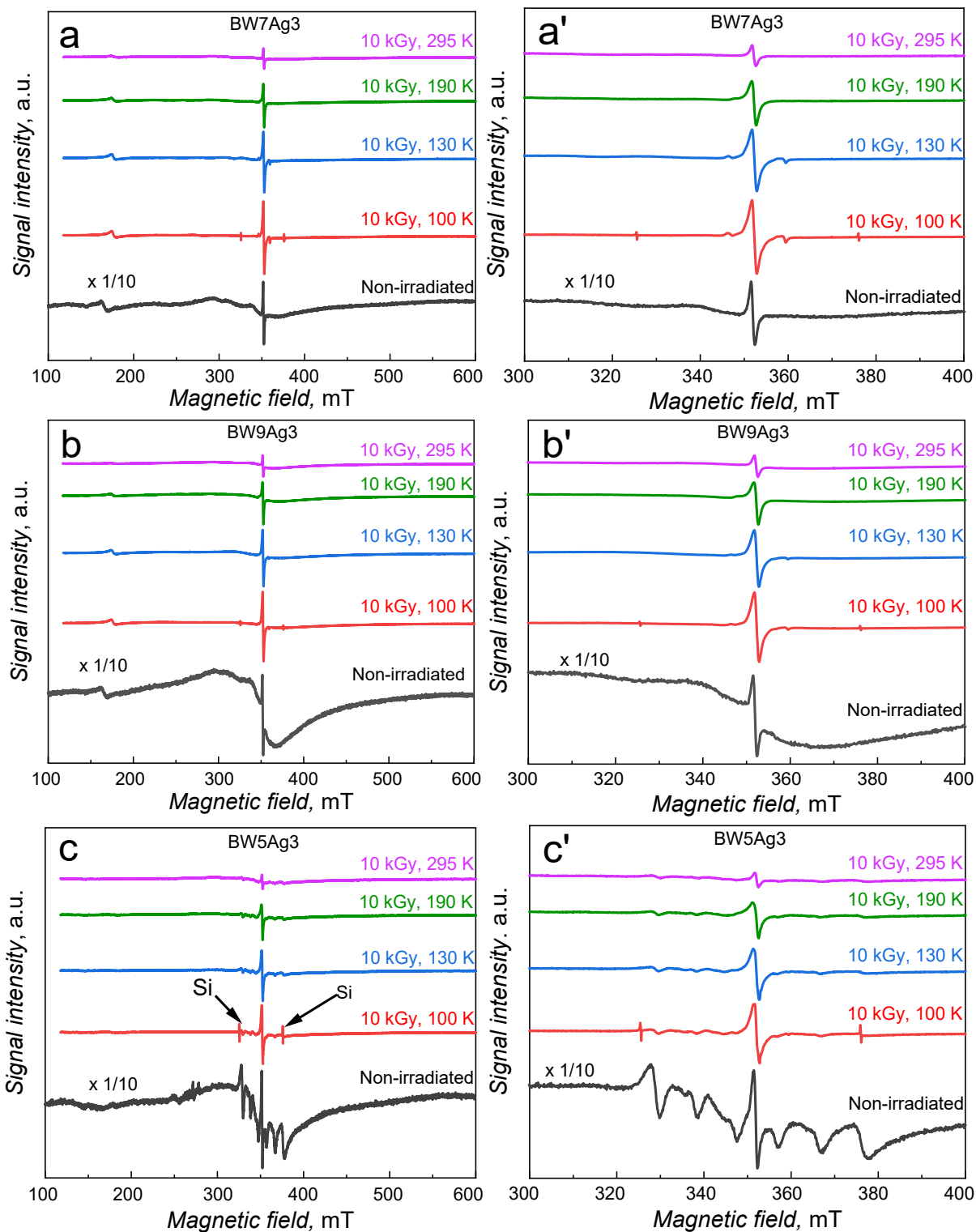


Figure 4.11. ESR spectra for (a, a') BW7Ag3, (b, b') BW9Ag3, and (c, c') BW5Ag3 non-irradiated nanocomposites synthesized at $80 (\pm 1) ^\circ\text{C}$ for 120 min, measured at room temperature, $25 (\pm 1) ^\circ\text{C}$, and after 10-kGy γ -irradiation measured in the temperature range of 100 to 295 K. The spectra in panels a', b', and c' are the magnified spectra presented in panels a, b, and c, respectively; they show a sharp band at ~ 350 mT.

γ -irradiated silver halides do not produce any ESR bands, but clusters synthesized from silver nitrate exhibit a singlet line after irradiation. That is most likely due to silver clusters forming or generating electrons localized in the AgCl-like conduction band^{410, 415}. When the analysis was performed at low temperatures, a signal from the silicon in the quartz tube was detected in all samples.

Parameters of the singlet band of the 2.0044 to 2.0055 g -factor in the ESR spectra are temperature dependent, and the rate of change depends on sample composition (Figure 4.12). The g -factor does not vary significantly with temperature (Figure 4.12a). The number of paramagnetic centers in the γ -irradiated nanocomposite samples decreased with the analysis temperature increase from 100 to 295 K (Figure 4.12b). That is likely because of generated silver clusters decomposition resulting from faster movement at higher temperatures. Moreover, the spins get more localized, limiting the clusters' interactions with the environment.

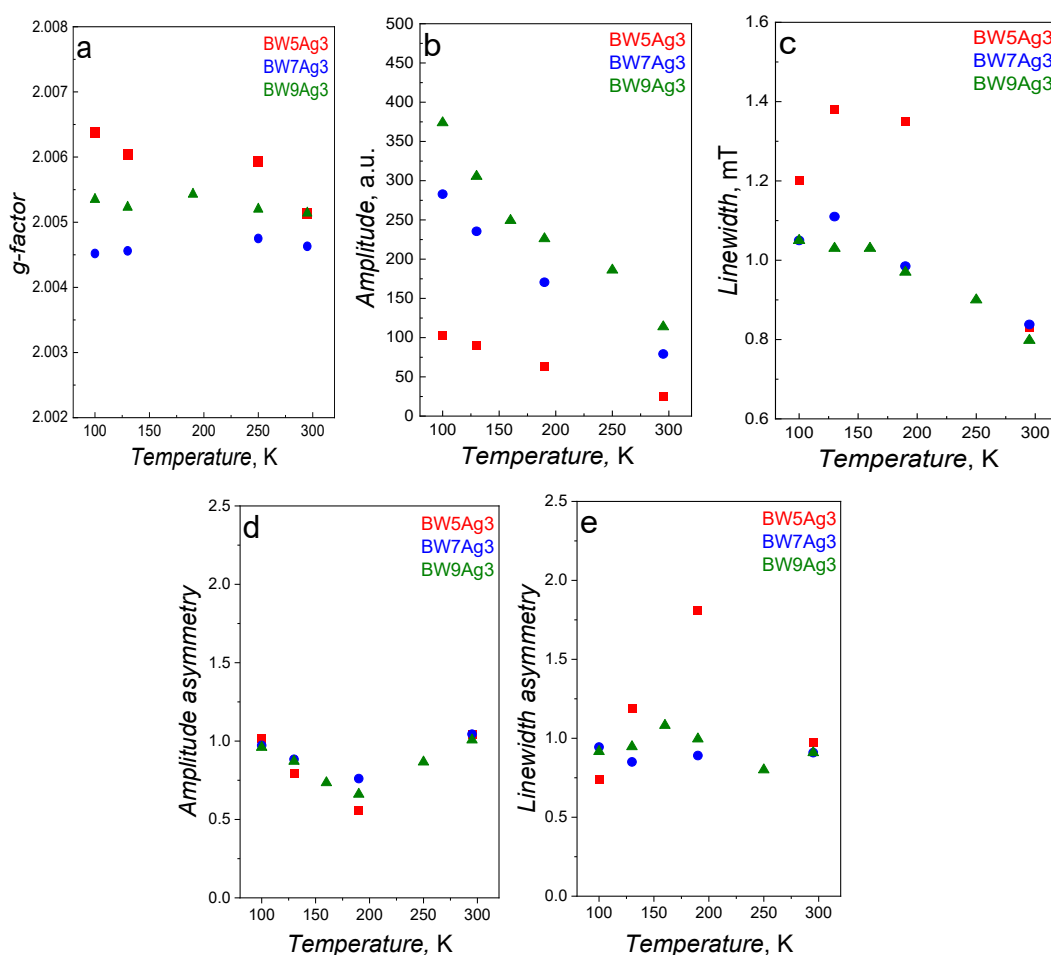


Figure 4.12. Temperature dependence (in the range of 100 – 295 K) of parameters of the sharp Ag singlet at ~ 350 mT in ESR spectra (a) g -factor, (b) amplitude normalized to weight, (c) linewidth, (d) amplitude asymmetry, and (e) linewidth asymmetry recorded for 10-kGy γ -irradiated BW5, BW7, and BW9 nanocomposites Ag₃ synthesized at $80 (\pm 1)$ °C for 120 min.

The amplitude and linewidth decrease with increasing analysis temperature, accompanied by a slight increase in the amplitude and linewidth asymmetry above 200 K for BW7Ag3 and BW9Ag3 nanocomposites (Figure 4.12b, 4.12c, 4.12d, and 4.12e). The trend is not very clear for BW5Ag3, which could be due to the overlap of the broad band of the ~50 mT linewidth and the 2.011 g-factor.

4.3.7.b Photoelectrochemistry

The photoelectrochemical activity of selected nanocomposites was studied. That was because Ag_3PO_4 is a highly photoactive material effective in OER and the degradation of organic pollutants^{392, 416-418}. Moreover, AgCl has been applied as an efficient catalyst for photocatalytic organic pollutants' degradation⁴¹⁹.

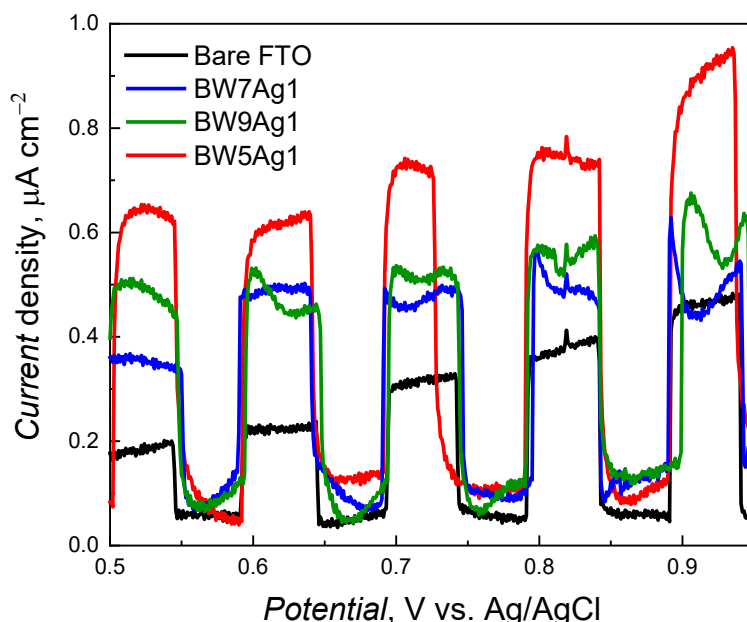


Figure 4.13. Linear sweep voltammetry curves with light chopping for bare FTO electrodes and electrodes coated with nanocomposites synthesized at $25 (\pm 1) ^\circ\text{C}$ for 120 min, using the BW7, BW9, and BW5 brewery wastes in sodium phosphate buffer solution ($\text{pH} = 7.2$) at a 10-mV s^{-1} scan rate.

The samples synthesized at $25 (\pm 1) ^\circ\text{C}$ for 120 min using BW5 (BW5Ag1), BW7 (BW7Ag1), and BW9 (BW9Ag1) were taken as initial test samples for determining the photoelectrochemical activity due to their significant composition variations and the interesting ESR spectra for the BW5Ag1 nanocomposite (Figure 4.10c). The LSV curves for bare and nanocomposites-coated FTO electrodes, in the potential range of 0.50 to 1.00 V vs. Ag/AgCl, are shown in Figure 4.13. The experiment was performed by illuminating the FTO electrodes

at certain time intervals while scanning the potential between 0.50 and 1.00 V vs. Ag/AgCl. The photocurrent density increased at a bare FTO electrode from 0.2 to 0.4 $\mu\text{A cm}^{-2}$ with the applied potential increase. That is not surprising as the FTO is a semiconductor. The photocurrents at nanocomposites-coated FTO electrodes also increased with the applied potential. However, the nanocomposites-coated FTO electrodes revealed photocurrents higher than those at the bare electrode, at least up to 0.85 V vs. Ag/AgCl.

The BW9Ag1 nanocomposite with pure AgCl in the structure and BW7Ag1 nanocomposite with the highest Ag_3PO_4 content in the structure exhibited almost similar activity in the potential range of 0.60 to 1.00 V vs. Ag/AgCl. Interestingly, the shape of the photocurrent curve during illumination at the potential above 0.60 V becomes rather complex, indicating the formation of charge trapping states under light irradiation. For the BW5Ag1 nanocomposite containing Ag_3PO_4 in minor amounts and AgCl in significant amounts, together with a small amount of Ag NPs, photocurrent densities were higher than for all other samples studied. A maximum photocurrent density of 0.93 $\mu\text{A cm}^{-2}$ was at a potential between 0.90 and 1.00 V vs. Ag/AgCl at the BW5Ag1 nanocomposite-coated FTO. In view of the literature data on the photoactivity of the AgCl/Ag composites⁴¹⁹ and $\text{Ag}_3\text{PO}_4/\text{Ag}$ composites⁴²⁰⁻⁴²¹, this result stresses the importance of metallic Ag NPs' presence in the composite and the mixed-phase composite presence. Moreover, the presence of Ag clusters in the BW5Ag1 nanocomposite of a structure, suggested by the ESR spectroscopy results, most likely plays a role in a relatively higher photoactivity of this nanomaterial. However, the obtained photocurrents remain relatively small for the nanocomposites fabricated. Although it is not uncommon for photocurrent densities to amount $\sim 1 \mu\text{A cm}^{-2}$ ^{260, 422-423}, silver-based materials can reach even higher photoactivity⁴²⁰⁻⁴²¹. The poor internal organization of the nanocomposite components could inhibit the electron-hole separation, leading to their fast recombination. Furthermore, this structural arrangement can hinder electron transport to the electrode. A combination of both of these effects might lead to low photocurrents measured.

Therefore, the nanocomposites' synthesis and materials deposition procedures need further optimization to improve their photoactivity. Moreover, a relevant support material might be introduced to mediate the electron transfer, increasing the photocurrents⁴²⁴⁻⁴²⁵. Furthermore, these materials' application for photocatalytic waste removal, especially for organic pollutants' degradation, may be envisaged in future studies. Consequently, this application route was not further pursued because of time constraints.

4.3.7.c Electrocatalytic oxygen reduction reaction (ORR)

Silver-based compounds have also found application as catalysts in oxygen reduction reaction (ORR). Therefore, attempts were made to apply the synthesized nanocomposites as ORR electrocatalysts.

Firstly, the behavior of bare and nanocomposite-coated electrodes in O₂ saturated and deaerated (Ar saturated) aqueous solution was compared (Figure 4.14). Apparently, in the dissolved oxygen absence in the NaOH solution, the cathodic peak is absent for both bare and BW7 nanocomposite-coated electrodes, indicating that the peak recorded for the O₂ saturated solution is due to ORR.

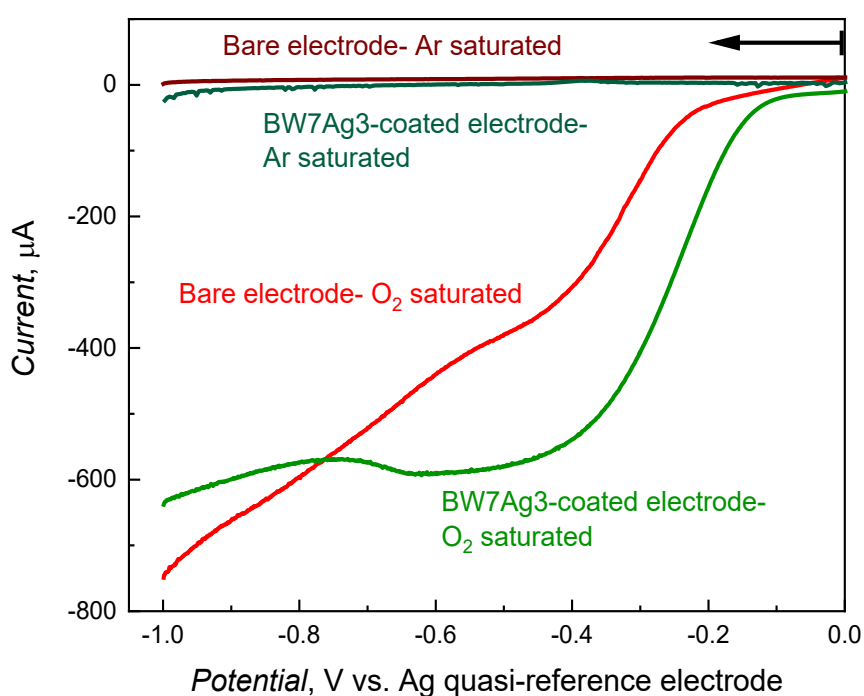


Figure 4.14. Comparison of linear sweep voltammetry curves for ORR at a bare and exemplary BW7Ag3 [synthesized at 80 (\pm 1) °C for 120 min] nanocomposite-coated GC disk electrode of RRDE at a rotation rate of 2000 rpm and 10 mV s⁻¹ scan rate in O₂ and Ar saturated 0.1 M NaOH.

Subsequently, the ORR experiments were performed using an RRDE, a neutral solution of 0.1 M KNO₃, and a basic solution of 0.1 M NaOH to understand the pH effect on the ORR at the nanocomposites-coated electrode surface. The 1 mM potassium ferrocyanide formal potential (0.165 V) vs. Ag quasi-reference electrode in 0.1 M KNO₃ was shifted by ~55 mV in the negative direction compared to the potassium ferrocyanide formal potential vs. Ag/AgCl. The curves in Figure 4.15 correspond to the current at the RRDE, wherein the GC disk was coated with nanocomposites synthesized at different temperatures for 120 min, and the

potential was linearly swept between 0.00 and -1.00 V vs. Ag quasi-reference electrode at a scan rate of 10 mV s^{-1} under 0, 400, 800, 1000, 1200, 1600, 2000 rpm rotation rates in 0.1 M KNO_3 . The Au ring electrode potential was fixed at a value of 1.00 V vs. Ag quasi-reference electrode to oxidize hydrogen peroxide that could be generated at the disk electrode. As the disk potential was swept from 0.00 to -1.00 V vs. Ag quasi-reference electrode, the onset ORR potential yielded a cathodic current measured between -0.25 and -0.32 V vs. Ag quasi-reference electrode for nanocomposite-coated electrodes (Figure 4.15).

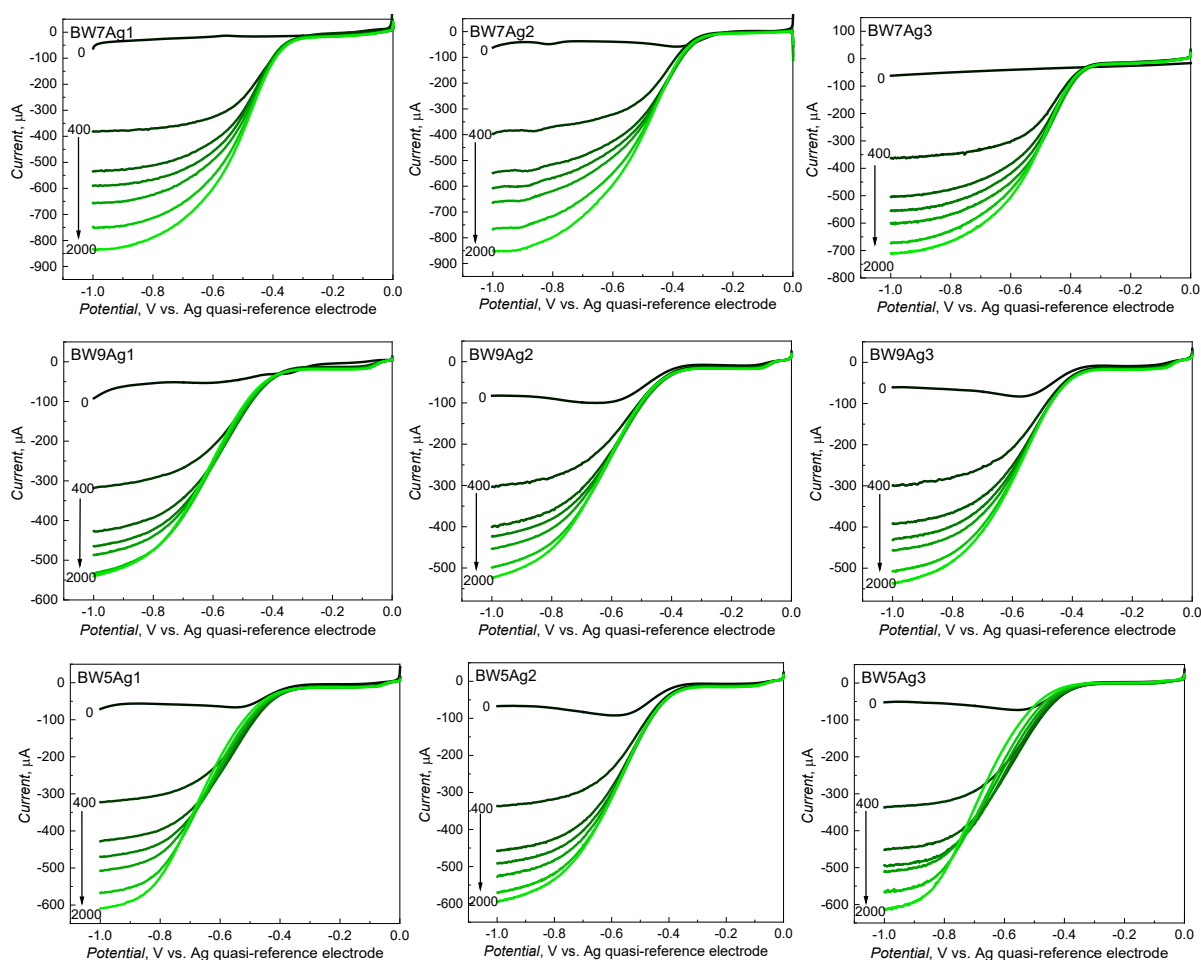


Figure 4.15. Linear sweep voltammety curves recorded at the RRDE at rotation rates of 0 to 2000 rpm and 10 mV s^{-1} scan rate in 0.1 M KNO_3 using the GC disk electrode coated with nanocomposites synthesized at different temperatures for 120 min. (Nanocomposites syntheses conditions are denoted as follows: Ag1 - $25 \text{ }^\circ\text{C}$, 120 min, Ag2 - $50 \text{ }^\circ\text{C}$, 120 min, Ag3 - $80 \text{ }^\circ\text{C}$, 120 min).

The current gradually increased with a further potential decrease and formed a plateau between -0.60 and -1.00 V vs. Ag quasi-reference electrode. This plateau is the mass transfer-limited range of the LSV voltammogram, wherein the ORR reaction rate is limited by the oxygen availability at the electrode surface. The cathodic current increased with the ω increase, as

expected. For all studied composites, the voltammograms' shapes were similar. At a given rotation rate, the highest currents were measured for the GC electrode coated with the BW7 nanocomposites (BW7Ag1, BW7Ag2, and BW7Ag3), followed by BW5 nanocomposites (BW5Ag1, BW5Ag2, and BW5Ag3) and BW9 nanocomposites (BW9Ag1, BW9Ag2, and BW9Ag3), which yielded lower currents.

When oxygen starts to reduce at the GC disk electrode, reaction products, including H_2O_2 , are carried away by centrifugal forces from the disk electrode and transported to the ring electrode for subsequent electrode reaction. Suppose H_2O_2 is produced during ORR at the disk electrode. In that case, it is then oxidized at the ring electrode resulting in an anodic current coinciding with the oxygen reduction current. That way, one can determine if the ORR reaction is a 2 or 4-electron process. In the latter case, no signal of H_2O_2 oxidation would be seen. Figure 4.16 shows disk and ring electrodes' currents for the bare and exemplary BW7Ag3 nanocomposite-coated electrodes.

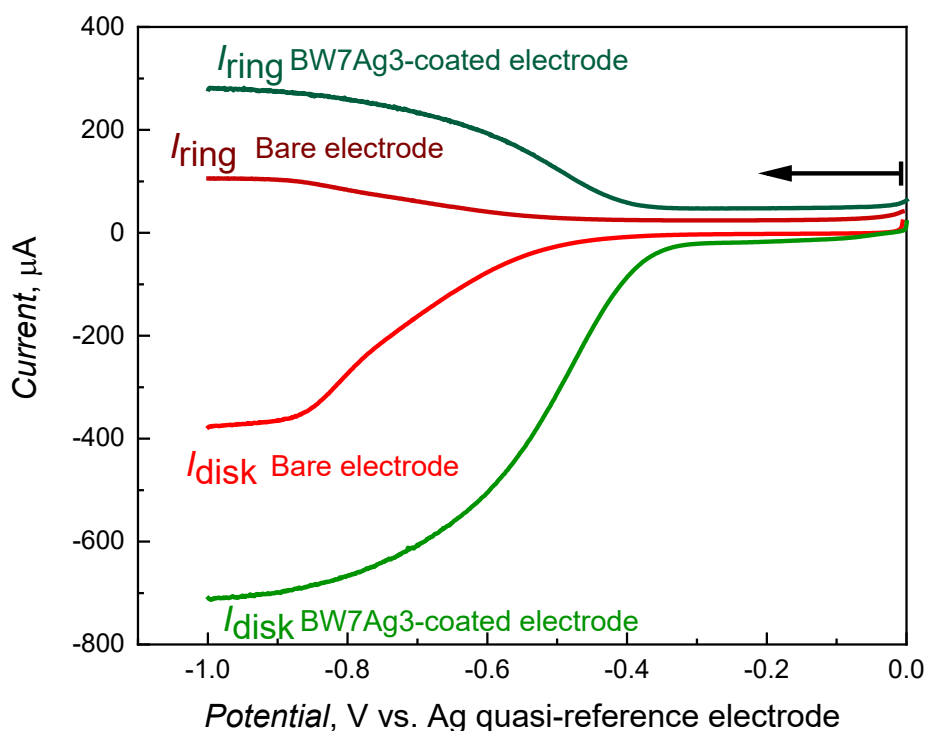


Figure 4.16. Comparison of linear sweep voltammetry curves for ORR at the bare and exemplary BW7Ag3 [synthesized at $80 (\pm 1) ^\circ\text{C}$ for 120 min] nanocomposite-coated GC disk electrodes of RRDE in 0.1 M KNO_3 at a rotation rate of 2000 rpm and a scan rate of 10 mV s^{-1} .

A clear positive potential shift by $\sim 100 \text{ mV}$ of the onset ORR potential for the nanocomposite-coated electrode is evident compared to the bare GC electrode. The anodic current at the ring

electrode appears simultaneously with the oxygen reduction current at the disk electrode. This behavior indicates the formation of H_2O_2 , i.e., two-electron oxygen reduction. Noticeably, the collection efficiency of this RRDE system, evaluated using potassium ferrocyanide in 0.1 M KNO_3 , was $\sim 40\%$. Therefore, the anodic ring current of H_2O_2 electro-oxidation should be $\sim 40\%$ of that of the ORR cathodic disk current. It is the case for both bare and nanocomposite-coated electrodes. All other nanocomposites behaved similarly. The Koutecký-Levich plots were constructed to confirm the number of electrons involved in the ORR in KNO_3 (Figure 4.17). Slopes of the plots for all nanocomposites are similar. The number of electrons transferred and the kinetic current densities in the ORR were determined using these plots.

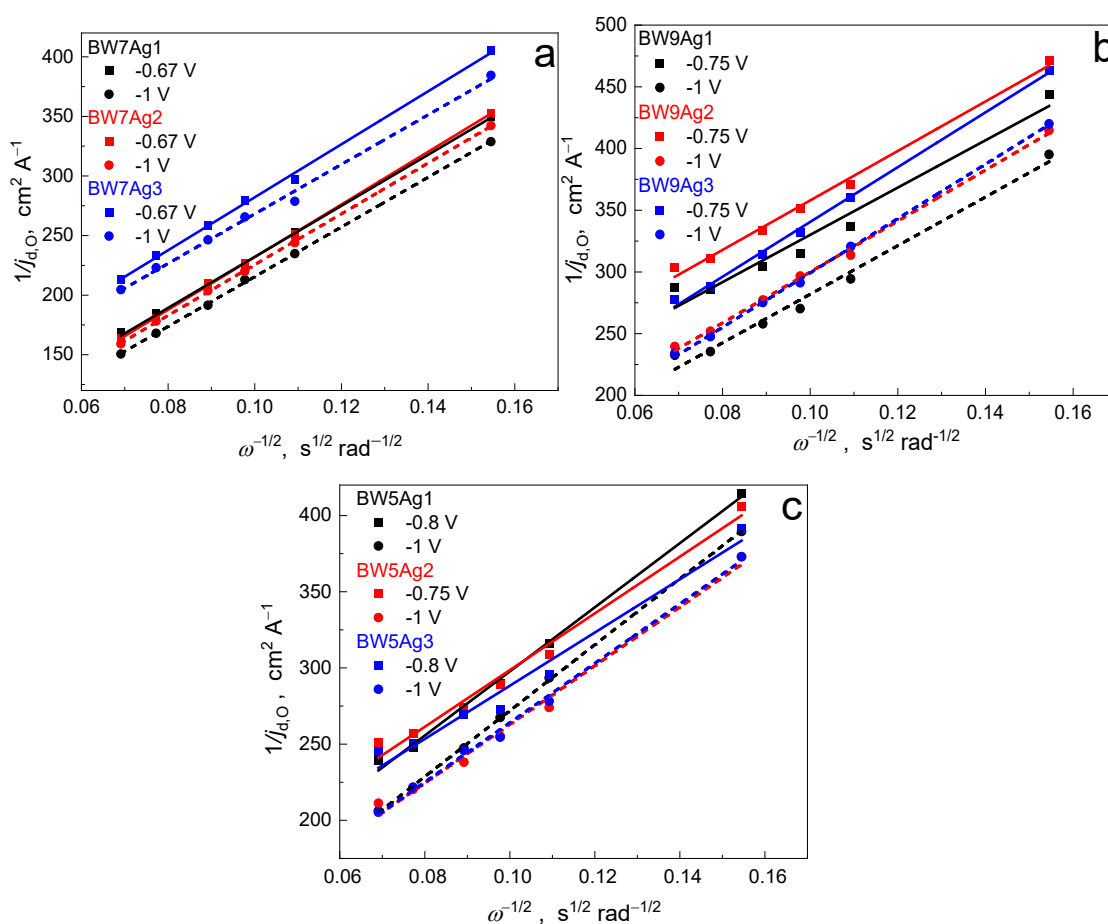


Figure 4.17. Koutecký-Levich plots for the ORR in 0.1 M KNO_3 at (a) BW7, (b) BW9, and (c) BW5 nanocomposites-coated GC disk electrodes of RRDE at two different potentials after the onset of the plateau range. (Nanocomposites syntheses conditions are denoted as follows: Ag1 - 25 °C for 120 min, Ag2 - 50 °C for 120 min, Ag3 - 80 °C for 120 min).

The following values of parameters used in the calculations, i.e., $F = 96\,487 \text{ C mol}^{-1}$ ⁴²⁶, $D_{\text{O}} = 2.0 \times 10^{-5} \text{ cm}^2 \text{ s}^{-1}$ ⁴²⁷, $\nu_k = 1.27 \times 10^{-2} \text{ cm}^2 \text{ s}^{-1}$ ⁴²⁸, and $C_{\text{O}}^0 = 1.10 \times 10^{-6} \text{ mol cm}^{-3}$ ⁴²⁸ were applied in Equation 2.3 to obtain the number of electrons transferred and kinetic current

densities in the ORR using the slope and intercept values, respectively, determined from the Koutecký-Levich plots; the GC disk electrode surface area being 0.1256 cm² (Table 4.7). All ORRs were 2-electron processes indicating that the ORR proceeds via the H₂O₂ intermediate formation. The number of electrons determined for some nanocomposite-coated electrodes is slightly lower than two, indicating possible parasite reactions occurring at the composite surface. Moreover, the kinetic current densities were the highest for the BW7 nanocomposites followed by BW5, and BW9 nanocomposites. This indicates that BW7 nanocomposites facilitate faster electrode transfer, in agreement with higher Ag₃PO₄ concentration and thinner organic overlayer in this material.

Table 4.7. Parameters derived from the Koutecký-Levich plots for ORR in 0.1 M KNO₃ at the BW7, BW9, and BW5 nanocomposites-coated electrodes at two different potentials after the onset of the plateau range. (Nanocomposites syntheses conditions are denoted as follows: Ag1 - 25 °C for 120 min, Ag2 - 50 °C for 120 min, Ag3 - 80 °C for 120 min).

Sample	Potential, E_v V vs. Ag quasi-ref.	Number of electrons transferred, n	Kinetic current density, $j_{k,O}$ mA cm ⁻²
BW7Ag1	-0.67	1.81	6.95
	-1.00	1.85	18.47
BW7Ag2	-0.67	1.75	11.46
	-1.00	1.81	10.07
BW7Ag3	-0.67	1.74	2.10
	-1.00	1.86	2.08
BW9Ag1	-0.75	1.84	0.91
	-1.00	1.79	1.48
BW9Ag2	-0.75	2.08	0.80
	-1.00	2.01	1.34
BW9Ag3	-0.75	2.21	1.06
	-1.00	1.98	1.59
BW5Ag1	-0.80	2.02	1.44
	-1.00	1.96	2.26
BW5Ag2	-0.75	1.93	1.12
	-1.00	1.87	1.78
BW5Ag3	-0.80	1.74	1.10
	-1.00	1.76	1.82

A similar effect was observed when the experiments were performed using a highly basic solution of 0.1 M NaOH. Basic solutions promote ORR, and therefore these tests were performed. In Figure 4.18, the LSV curves correspond to the current at the RRDE electrode, wherein the GC disk electrode was coated with nanocomposites synthesized for 120 min at different temperatures as the potential was swept between 0.00 and -1.00 V vs. Ag quasi-reference electrode at 10 mV s^{-1} scan rate at 0, 400, 800, 1000, 1200, 1600, and 2000 rpm electrode rotation rates in 0.1 M NaOH. The Au ring electrode potential was kept at 1.00 V vs. Ag quasi-reference electrode.

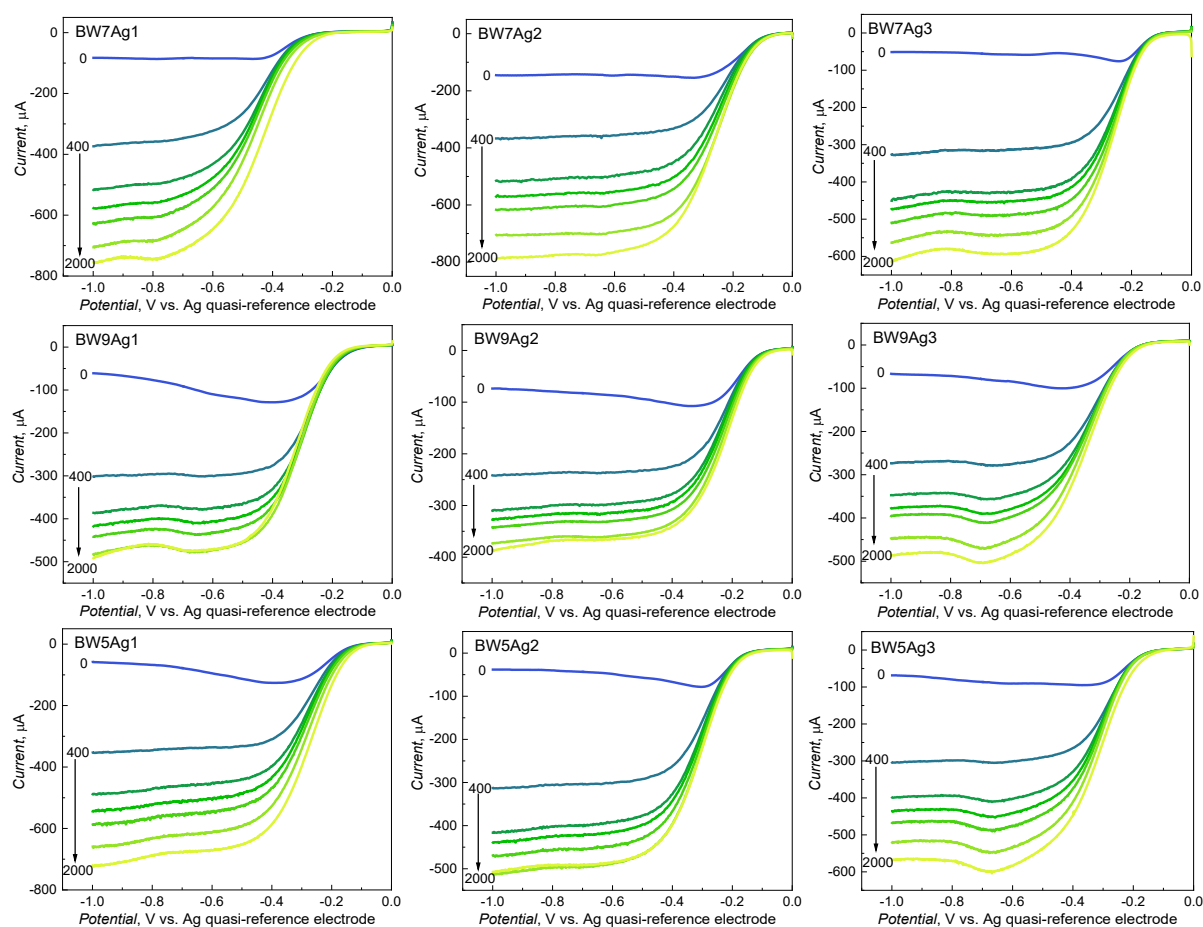


Figure 4.18. Linear sweep voltammetry curves recorded at the RRDEs in 0.1 M NaOH at rotation rates of 0 to 2000 rpm and 10 mV s^{-1} scan rate using GC disk electrodes coated with different nanocomposites, synthesized at different temperatures for 120 min. (Nanocomposites syntheses conditions are denoted as follows: Ag1 - $25 \text{ }^{\circ}\text{C}$ for 120 min, Ag2 - $50 \text{ }^{\circ}\text{C}$ for 120 min, Ag3 - $80 \text{ }^{\circ}\text{C}$ for 120 min).

The onset potential of ORR at the nanocomposite-coated electrodes was between -0.01 and -0.11 V vs. Ag quasi-reference electrode. The current plateau range was between -0.40 and -1.00 V vs. Ag quasi-reference electrode. Moreover, peak-like features appeared in the voltammograms at potentials more negative than -0.40 V vs. Ag quasi-reference electrode for

some nanocomposites, predominantly those synthesized at 25 (± 1) and 80 (± 1) °C (Ag1 and Ag3 samples). Herein, also, the highest currents were for BW7 nanocomposites (BW7Ag1, BW7Ag2, and BW7Ag3), followed by BW5 nanocomposites (BW5Ag1, BW5Ag2, and BW5Ag3), while BW9 nanocomposites (BW9Ag1, BW9Ag2, and BW9Ag3) yielded lower currents.

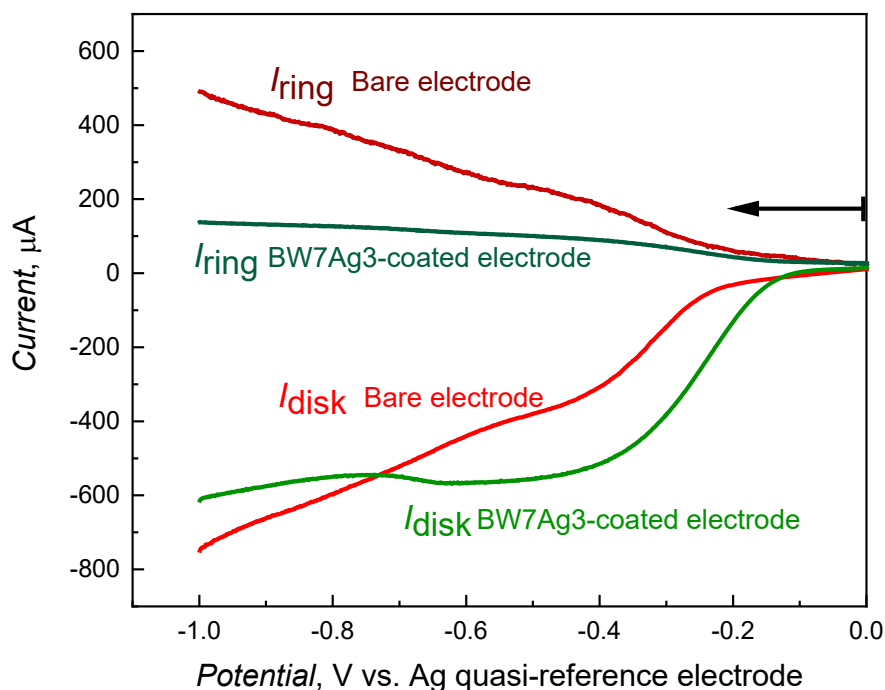


Figure 4.19. Comparison of linear sweep voltammetry curves for the ORR at the bare and exemplary BW7Ag3 [synthesized at 80 (± 1) °C for 120 min] nanocomposite-coated GC disk electrode of RRDE in 0.1 M NaOH at a rotation rate of 2000 rpm and 10 mV s⁻¹ scan rate. (Note: The I_{ring} vs. E_v curves were offset to start at 0 μ A).

Figure 4.19 compares the bare and exemplary BW7Ag3 nanocomposite-coated electrodes for ORR. The currents at the bare GC electrode in 0.1 M NaOH (Figure 4.19) are higher than in 0.1 M KNO₃ (Figure 4.16). The ORR onset potential at the nanocomposites-coated electrode is by ~ 100 mV more positive than at the bare GC electrode, similar to that observed in 0.1 M KNO₃ (Figure 4.16). The positive shift of the onset potential at the bare and nanocomposite-coated electrodes in NaOH, compared to KNO₃, is not surprising as basic solutions promote the ORR. There is a significant difference between the ring currents of bare and nanocomposite-coated disk electrodes for the NaOH system. The anodic current at the ring electrode appears together with the cathodic current at the disk electrode for ORR at the bare GC disk electrode, which indicates the formation of H₂O₂, i.e., two-electron ORR. However, there is a notably diminished anodic current for the BW7Ag3-coated electrode despite a clear

cathodic current associated with the ORR. This lower current indicates that either H₂O₂ is not produced in sufficient quantities in the ORR at the nanocomposite-coated disk electrode or the transport of the H₂O₂ through the coating is slower and therefore cannot be observed at the ring electrode for the given ω values. For clarification, Koutecký-Levich plots were prepared to confirm the number of electrons involved in the reaction.

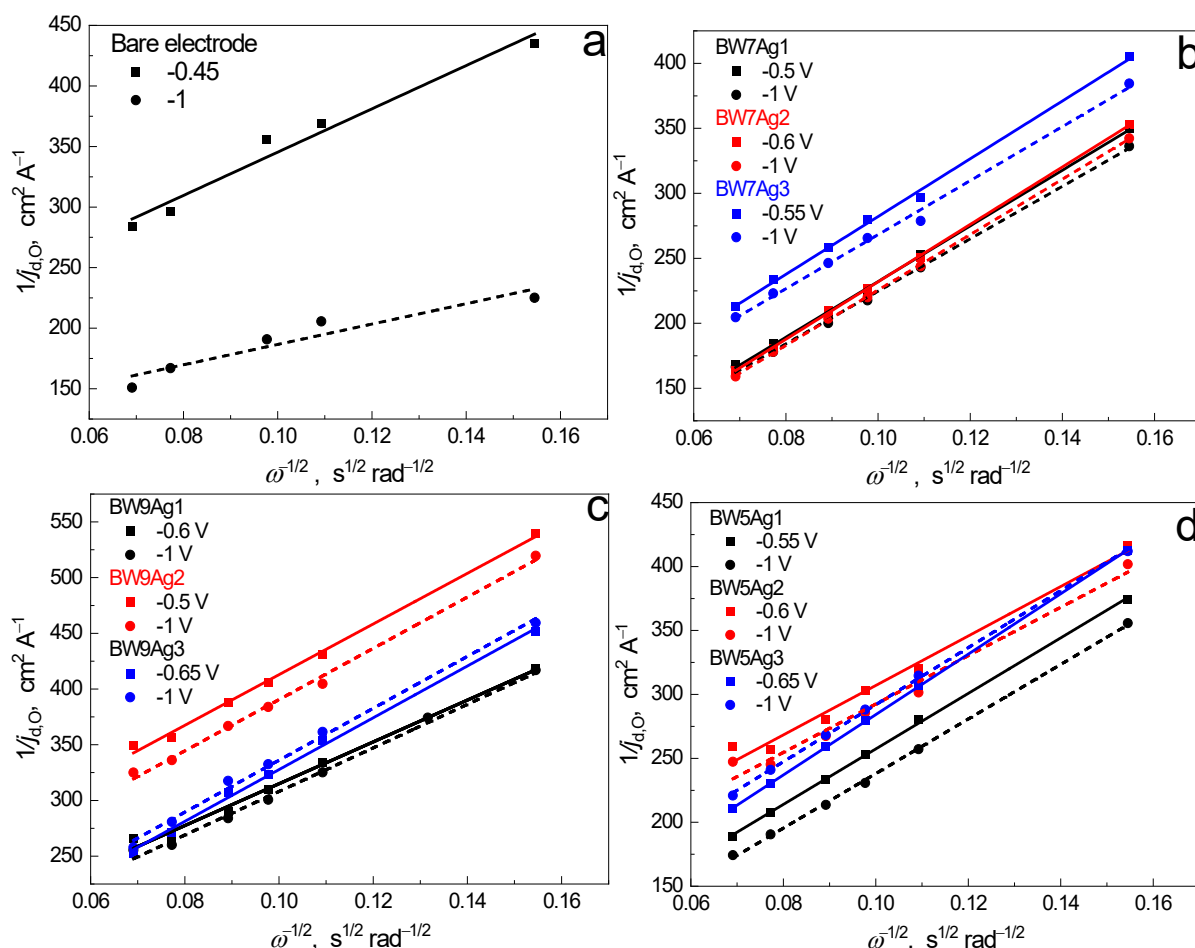


Figure 4.20. Koutecký-Levich plots for ORR in 0.1 M NaOH at (a) the bare GC disk electrode of RRDE, as well as (b) BW7, (c) BW9, and (d) BW5 nanocomposites-coated electrodes at two different potentials after the onset of the potential range of the plateau. (Nanocomposites syntheses conditions are denoted as follows: Ag1 - 25 °C for 120 min, Ag2 - 50 °C for 120 min, Ag3 - 80 °C for 120 min).

Figure 4.20 shows the Koutecký-Levich plots for the ORR in 0.1 M NaOH. For this solution, plot slopes for all nanocomposite-coated electrodes are also similar. The parameters' values, applied in Equation 2.3 to obtain the number of electrons passed and kinetic current densities during the ORR at the electrode, were $F = 96\,487\text{ C mol}^{-1}$ ⁴²⁶, $D_0 = 2.22 \times 10^{-5}\text{ cm}^2\text{ s}^{-1}$ ⁴²⁸, $\nu_k = 1.27 \times 10^{-2}\text{ cm}^2\text{ s}^{-1}$ ⁴²⁸, and $C_0^0 = 1.08 \times 10^{-6}\text{ mol cm}^{-3}$ ⁴²⁸.

The bare electrode shows a 2-electron process at a lower plateau potential which turned into a 4-electron process at a higher plateau potential (Table 4.8).

Table 4.8. Parameters derived from the Koutecký-Levich plots for ORR in 0.1 M NaOH at a bare GC disk electrode of RRDE and the BW7, BW9, and BW5 nanocomposites-coated electrodes at two different potentials after the onset of the plateau range. (Nanocomposites syntheses conditions are denoted as follows: Ag1 - 25 °C for 120 min, Ag2 - 50 °C for 120 min, Ag3 - 80 °C for 120 min).

Sample	Potential, E_v V vs. Ag quasi-ref.	Number of electrons transferred, n	Kinetic current density, $j_{k,O}$ mA cm^{-2}
Bare electrode	-0.45	2.06	0.75
	-1.00	4.37	1.23
BW7Ag1	-0.50	1.72	6.95
	-1.00	1.82	5.53
BW7Ag2	-0.60	1.66	11.46
	-1.00	1.72	10.07
BW7Ag3	-0.55	1.65	2.10
	-1.00	1.77	2.08
BW9Ag1	-0.60	1.96	0.99
	-1.00	1.88	1.12
BW9Ag2	-0.50	1.62	0.68
	-1.00	1.60	0.78
BW9Ag3	-0.65	1.58	1.32
	-1.00	1.58	1.22
BW5Ag1	-0.55	1.69	3.12
	-1.00	1.72	5.09
BW5Ag2	-0.60	1.90	1.11
	-1.00	1.94	1.22
BW5Ag3	-0.65	1.56	2.62
	-1.00	1.65	1.82

The nanocomposites exhibited a 2-electron process at all plateau potentials, which is surprising considering the diminished ring currents for nanocomposites-coated electrodes (Figure 4.19). Moreover, herein the number of electrons transferred is slightly lower than two, indicating that some side reactions occur at the nanocomposites' surfaces. To further examine

the mechanism of the ORR at these nanocomposite-coated electrodes, it is essential to explore techniques like ESR spectroelectrochemistry.

The kinetic current densities in the NaOH solution are still the highest for BW7 nanocomposites (Table 4.8), which indicates these materials with relatively thinner overlayer coatings and higher Ag_3PO_4 in their structure could be the most effective cheap alternatives for ORR electrocatalysis. Similar onset potentials have been reported for silver-based nanomaterials. However, as the ORR on silver is strongly shape- and structure-dependent, the comparison of activities is a bit complex²³⁷. The 2-electron pathway of ORR has been observed for NPs containing a protective organic shell that leads to the passivation of the surface for electron charge transfer⁴²⁹. Moreover, defective and angular surfaces result in a smaller number of electrons transferred but exhibit higher activity of O_2 reduction compared to smooth Ag surfaces⁴³⁰.

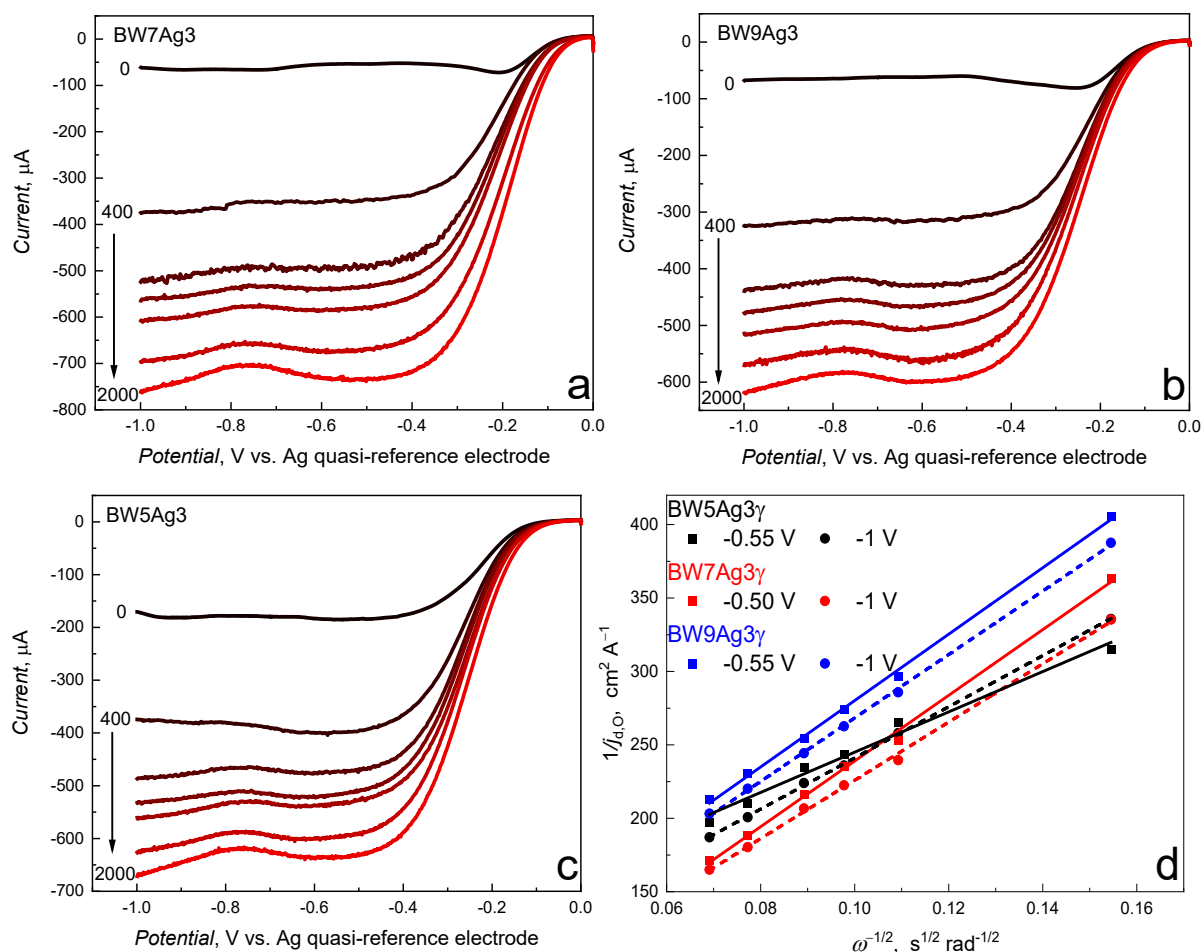


Figure 4.21. Linear sweep voltammetry curves recorded at GC disk electrodes of RRDE coated with films of (a) BW7 (BW7Ag3), (b) BW9 (BW9Ag3), and (c) BW5 (BW5Ag3) nanocomposites, synthesized at $80 (\pm 1)^\circ\text{C}$ for 120 min, then γ -irradiated with the 10 kGy dose, at rotation rates of 0 to 2000 rpm, and 10 mV s^{-1} scan rate in 0.1 M NaOH and (d) their Koutecký-Levich plots.

The ORR was also accomplished for three nanocomposites synthesized at 80 (± 1) °C for 120 min, i.e., BW7Ag3, BW9Ag3, and BW5Ag3, after γ -irradiation with a dose of 10 kGy to examine the irradiation effect on the samples' properties. After the irradiation, the RRDE curves yielded higher currents for these nanocomposites, and the onset potential was slightly more positive (Figure 4.21a-c). That could point to the significance of paramagnetic centers in the materials as γ -irradiation led to an increased number of paramagnetic centers in the composites, as seen in the ESR spectroscopy characterization (Figure 4.12 and Table 4.6).

Moreover, some interesting variations exist in the Koutecký-Levich analysis of the irradiated materials (Figure 4.21d). Although the nanocomposites' electro-reduction still exhibits a 2-electron process, the number of electrons transferred in the BW5Ag3 nanocomposite electro-reduction exceeded 2 in 0.1 M NaOH after γ -irradiation. Interestingly, the irradiation also led to markedly improved electron transfer kinetics for BW7 and BW9 materials while did not change much electron transfer kinetics at BW5 modified electrodes (Table 4.9). That suggests the possibility of exposure of nanocomposites to γ -irradiation to improve their electron transfer kinetics and change the reaction mechanism.

Table 4.9. Parameters derived from the Koutecký-Levich plots for ORR in 0.1 M NaOH at the γ -irradiated BW7Ag3, BW9Ag3, and BW5Ag3 nanocomposites-coated GC disk electrodes of RRDE at two different potentials after the onset of the plateau range.

Sample	Potential, E_v V vs. Ag quasi ref.	Number of electrons transferred, n	Kinetic current density, $j_{k,O}$ mA cm^{-2}
BW7Ag3	-0.55	1.64	8.18
	-1.00	1.85	4.19
BW9Ag3	-0.65	1.63	3.42
	-1.00	1.70	2.40
BW5Ag3	-0.65	2.68	1.16
	-1.00	2.11	1.88

4.4 Discussion and conclusions

Brewery wastes from stages 5 (BW5), 7 (BW7), and 9 (BW9) of the brewing process were successfully valorized for the synthesis of green silver nanocomposites. For growth mechanism understanding, several nanocomposites were prepared at different temperatures [25 (\pm 1), 50 (\pm 1), and 80 (\pm 1) °C] and synthesis times at 80 (\pm 1) °C (10, 30, and 120 min). The synthesis temperature and time affected the relative compositions of the three silver phases, namely, Ag₃PO₄, AgCl, and Ag_{met}, in the BW5 and BW7 nanocomposites and the relative compositions of AgCl and Ag_{met} in BW9 nanocomposites. The lack of chlorine in BW7 and the abundance of phosphorus-based compounds caused silver phosphate formation. The presence of yeast and a nitrogen-rich environment can also be instrumental in the growth of silver phosphate. Contrastingly, BW5 and BW9 are rich in phosphorous and chlorine; therefore, competing reactions favored the growth of majorly AgCl. BW9 yields only AgCl and Ag_{met} NPs. The Ag₃PO₄ phase is absent in all BW9 nanocomposites. The spontaneous formation of AgCl results from the exchange reaction between silver nitrate and a source of halide present in the brewery wastes. Therefore, at high amounts of Cl in the BW5 and BW9 wastes, AgCl is obtained in significant quantities. After AgCl formation, the excess silver nitrate follows another exchange reaction with the phosphate source leading to Ag₃PO₄ in BW5 nanocomposites⁴³¹. The conversion of silver salts by all brewery wastes led to a more diversified composition of the nanocomposite structure with increasing synthesis temperature and time.

Increasing the synthesis temperature can promote reactions that may not be spontaneous under room temperatures, including several parallel reactions yielding a composite structure. The Ag_{met} growth in all the nanocomposites is favored only at elevated temperatures. In the case of BW7 nanocomposite, the Ag_{met} is observed only at 80 (\pm 1) °C (BW7Ag3). At lower temperatures, the formation of Ag₃PO₄ predominates. In BW9 nanocomposites, increasing synthesis temperature incorporates more Ag_{met} into the structure, starting from 50 (\pm 1) °C. However, a substantial amount of Ag_{met} is evident only at 80 (\pm 1) °C. Because of increasing synthesis temperature, reaction with BW5 yields Ag_{met} NPs with smaller crystallite sizes, and reaction with BW7 and BW9 yields Ag_{met} NPs with larger crystallite sizes. Moreover, substantial amounts of Ag_{met} are obtained here at 80 (\pm 1) °C. The most favored reaction at 25 (\pm 1) °C is the formation of AgCl and Ag₃PO₄, depending on the type of BW precursor. Although Ag_{met} is obtained at 25 (\pm 1) °C synthesis temperatures in some nanocomposites like BW5Ag1, the growth of the phases is promoted at 80 (\pm 1) °C (BW5Ag3). With increasing

synthesis temperature, particles become more highly aggregated. The reducing agents in BW5, BW7, and BW9 are either activated or formed at higher temperatures, reducing Ag cations from the +1 to 0 oxidation state.

Amino acids, carbohydrates, polyphenols, and sugars are well-known agents responsible for reducing silver cations to silver metal and capping NPs⁴³²⁻⁴³³. However, different compounds present in BW5, BW7, and BW9 are responsible for NP synthesis. In alkaline solutions, sugars are potent reducing agents⁴³⁴. The added effect of hydroxyl radicals in silver cation reduction is also evident at high pH values. Therefore, the reducing capacity of these agents is not prominent in our synthesis as the brewery wastes are acidic. The Ag⁺ reduction by polyphenols is also affected by the system's pH, which impacts the NP size and shape. At low pH, this reduction leads to larger-size NPs⁴³⁵. Therefore, the low pH in our system led to the formation of a small amount of large-sized Ag_{met} NPs in the composite structure primarily due to polyphenol-induced reduction.

Amino acids and proteins contain carbonyl groups with a strong affinity toward metal NPs⁴³⁶. Therefore, they are some of the critical capping agents. Proteins are present in all the wastes. Thus, the overlayer of BW5 and BW9 nanocomposites contain protein moieties. However, the intensity of the BW7 nanocomposites' overlayer vibrations attributed to protein amide I and II vibrations are relatively small. This IR spectroscopy activity indicates that the surface of Ag₃PO₄ and AgCl NPs plays a significant role in determining the organic groups that will form a part of the overlayer. The protein peptides preferentially attach to nanocomposites with considerable AgCl in the structure. Several organic functional groups have participated in the capping, forming a rich overlayer. BW5 nanocomposites have the thickest overlayer capping, followed by BW9 nanocomposites and then BW7 nanocomposites with the smallest thickness of the overlayer coating. The overlayer is the thickest if the synthesis temperature is 50 (±1) °C. This high temperature facilitates the organic groups' attachment to the NP surface.

Nanocomposites were characterized in several ways to understand their catalytic activity. The presence of Ag aggregates and the environmental influence on the paramagnetic centers in nanocomposites was observed, as BW9 nanocomposite with majorly silver chloride in the structure contained the highest number of paramagnetic centers. Silver clusters present in BW5 nanocomposites (BW5Ag1) appeared to play a significant role in photocatalytic activity. Moreover, γ -irradiation significantly increased the number of paramagnetic centers in the nanocomposites. The synthesized nanocomposites exhibit photoactivity in the water-splitting reaction, albeit the photocurrents were up to 0.9 $\mu\text{A cm}^{-2}$. Presumably, the photocurrent is low

because of significant structural defects and a low degree of organization in the composite structure, which favors electron-hole recombination and hinders charge transport to the electrode. Interestingly, the photocurrent of the AgCl/Ag/Ag₃PO₄ composite, prepared using the BW5 reagent, was the highest of all studied composites. Therefore, it seems that the presence of the Ag NPs and clusters in the composite positively affects the photoactivity of the material. Photoactivity of the Ag₃PO₄ phase in major amounts and pure AgCl was quite similar.

Besides, the synthesized nanomaterials exert a promising effect as ORR catalysts. The onset of ORR at the nanocomposite-coated electrode is by ~100 mV positively shifted compared to the ORR onset potential at the bare GC electrode. Furthermore, the nanocomposites favor the two-electron oxygen reduction process. BW7 nanocomposites with high Ag₃PO₄ content and thin organic capping favored faster electron transfer kinetics. The nanocomposite synthesis needs some optimization, especially in view of synthesizing non-agglomerated nanocomposites with higher levels of monodispersity and uniformity, preparing stable coatings of the nanocomposites on GC electrodes, and removing the organic overlayer. However, it can be concluded that with optimized structure and composition, these materials can be promising cheap alternatives for large-scale OER and ORR.



5

Overview, summary, and future prospective

Catalytic materials are the foundations of a sustainable future. Therefore, developing green synthetic routes for catalytic materials and rendering the catalytic process eco-friendlier is the need of the hour. In this regard, electrosynthesized MIPs for application in electrocatalysis are certainly greener than conventional catalytic methods. It can be seen that the electrosynthesis of organic conductive MIPs is a simple and cost-effective method owing to the ease of their preparation. Furthermore, combining MIP technology with electrosynthesis excludes toxic oxidants and initiators, yielding a cleaner process. The MIP layer would allow for selective synthesis of the desired products. Organic MIPs yielding shape-selective catalytic activity have not been widely explored for synthetic applications. Therefore, the present research demonstrated that conducting MIPs prepared by electropolymerization can mimic enzymes for selective synthesizing value-added compounds.

To this end, biphenols were chosen as initial targets as C–C coupling reactions are widespread in industrial applications. The challenges faced in preparing organic conducting MIPs have been studied mechanistically, and the successful pathways to obtain catalytic MIPs have been revealed. The MIPs were efficient in the selective electro-oxidation of the 2,4-dimethylphenol (**DMP_h**) to the desired C–C coupled 3,3',5,5'-tetramethyl-2,2'-biphenol

(**TMBh**). A 5 to 7-fold increase in the desired product yield was obtained for MIP film-coated electrodes over NIP film-coated and up to 39% increase compared to bare electrodes. This selectivity increase indicates that organic MIPs could be considered prospective materials for preparing efficient and selective catalytic technologies. The theoretical simulations confirm this experimentally observed selectivity of MIPs towards the **TMBh** product.

However, tackling the aging issue and possibly replacing laboratory synthesized monomers with commercial monomers is required to further advance this technology to an industrial scale. Moreover, the stability of the organic MIP films is a concern if they have to be applied for repeated synthesis due to electrode film poisoning effects, although the MIP films exhibited high stability for synthesis up to 2 h. Additionally, replacing the currently used Pt electrodes for materials that would exhibit selectivity towards the desired product and performing the electrosynthesis in ionic liquids or media that stabilize the reaction intermediates would be the potential future paths for further improving the selectivity of the electrosynthesis and lowering the environmental footprint. Toward this, theoretical simulations could be applied to check the reaction's spontaneity in various solvents and electrode surfaces, thereby providing pre-optimized systems to start experiments. As the procedure for preparing organic MIPs for electrosynthesis has been elucidated, further C–C coupling reactions can also be studied following the guidance of this project.

There is also increasing awareness that catalytic materials should be prepared using greener, resource-efficient, and environmental-friendly methods. To this end, using industrial wastes as precursors for NP synthesis enables the recycling of the wastes and greener synthesis of the variety of NPs. The brewing industry wastes are produced in large quantities globally, and there is an imminent need to find alternative recycling options for these wastes to prevent the growing environmental pollution. Therefore, using these brewery wastes from different stages of the brewing process for synthesizing silver nanomaterials was an exciting goal. Surprisingly, nanocomposites of Ag_3PO_4 , AgCl , and Ag_{met} were obtained using the brewing stage 7 (BW7) and stage 5 (BW5) wastes. The formation of Ag_3PO_4 is not generally observed in the green synthesis of silver nanomaterials. Therefore, the composition and properties of the studied brewery wastes are unique for obtaining the Ag_3PO_4 phase. The composition and properties of the wastes were studied in detail to understand their effect on formed nanocomposite. Disparately, the BW9 waste from final stage 9 of brewing converted the silver salt to mainly AgCl with minor amounts of Ag_{met} . Ergo, an interesting variation in the nanocomposite phases could be obtained using the different wastes and performing synthesis under different conditions. The Ag^+ ion reduction was promoted only at higher temperatures,

possibly because the reducing agents were activated or created at higher temperatures. The highest Ag_3PO_4 content (90%) was obtained using BW7 at room temperature [$25 (\pm) ^\circ\text{C}$] synthesis for 120 min, and the highest AgCl content (100%) was obtained using BW9 at room temperature [$25 (\pm) ^\circ\text{C}$] synthesis for 120 min. All other variations in synthesis temperature and time led to mixed nanocomposites. BW5 yielded mixed nanocomposites under all synthesis conditions. The organic surface capping was rich in functional groups observed in the brewery wastes. Preferential adsorption of functional groups on AgCl was observed. Increasing the synthesis temperature led to incorporating higher amounts of the minor components in the nanocomposite structures. The organic capping was the thinnest on BW7 nanocomposites followed by BW9 and then BW5 nanocomposites.

The nanocomposites were efficient electrocatalysts for the ORR as they positively shifted the oxygen reduction potential by ~ 100 mV compared to the bare electrode. Moreover, the nanocomposites showed photoactivity, albeit observed photocurrents were up to $0.9 \mu\text{A cm}^{-2}$. This smaller photoactivity was probably because of a lack of structural orientation, leading to more defects and charge trapping states. Therefore, further accuracy in the control over the phase composition and NP size would help prepare well-defined uniform nanomaterials with enhanced catalytic activity. Consequently, further optimization of the synthetic process is required to obtain precisely engineered NPs. Moreover, removing surface organic coating or converting them to carbon nanomaterials, for example, through heat treatment, would be an exciting perspective to enhancing these nanomaterials' catalytic properties. After optimization, these NPs could also be combined with the organic MIPs to develop the electrosynthesis methods leading to the selective and effective synthesis of value-added compounds like the biphenols.

By developing these two technologies, the present dissertation aims to bring about aspiration for greener research technologies enabling a route for a sustainable future. Although there is a long way ahead, a journey of a thousand miles begins with a single step, and this work hopes to be one of those few steps.



Annex

The analyses included in this Annex relate to electrosyntheses at **MIP-2** film-coated electrodes in **Chapter 3**.

Mass spectrometry (MS) experiments

Introduction

The mass spectrometry (MS) analyses were performed for different species obtained after the **DMPH** electro-oxidation at **MIP-2** film-coated Pt plate electrodes in ACN : DCM (9 : 1, v/v) solvent with (TBA)ClO₄ to identify the products of the reaction.

Technique

MS is a powerful analytical technique widely applied for identifying unknown compounds and determining detected molecules' chemical and structural properties. The samples are converted into gaseous ions by high-energy ionizing radiations, sometimes with fragmentation. These ions are then separated and characterized according to their mass-to-charge ratios (m/z)⁴³⁷. Ionic or neutral species can be formed depending on the chemical reactions occurring in the gas phase. The ions' relative abundances are also exhibited in the MS spectra. The ions provide essential information about the nature and structure of the parent molecules. Generally, the MS spectrometer has three major components (Figure A1-a)⁴³⁸.

1. The ion source produces the ionizing radiation for converting the sample into gaseous ions/neutral species.
2. The mass analyzer sorts the ions based on their m/z ratios.
3. The ion detection system detects and records the relative abundance of the separated ions.

Additionally, a sample introduction system, vacuum pumps to maintain a high vacuum ($\sim 10^{-6} - 10^{-8}$ mm Hg), and a computer to control the equipment and data analysis are also included in the MS instrument setup⁴³⁹. The MS spectrum displays a plot of ion abundance vs. mass-to-charge ratio (Figure A1-b). The obtained m/z values in MS spectra can either be compared to the reference libraries or reference compounds.

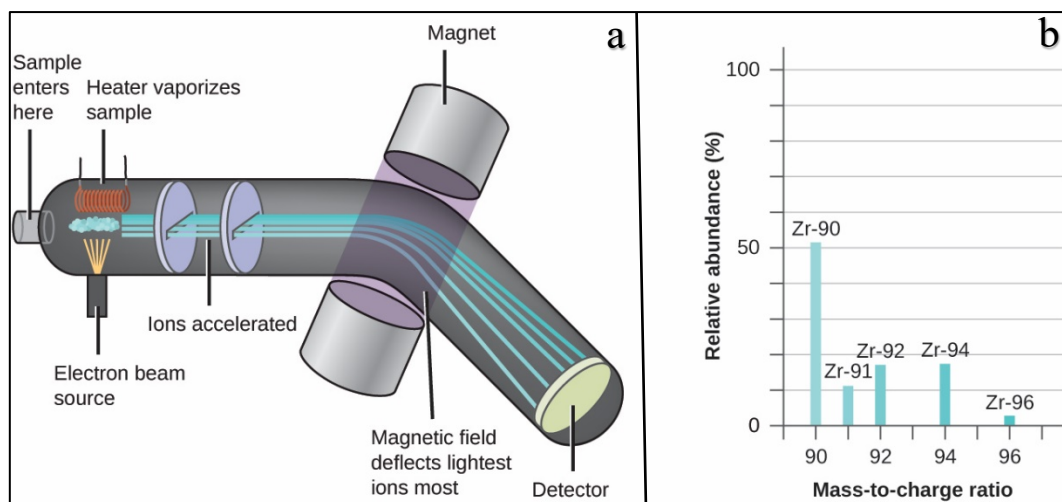


Figure A1. (a) Instrumentation and (b) spectra obtained in mass spectrometry (MS) ⁴⁴⁰.

Materials and method

(a) Separation of electro-oxidation products

A Shimadzu Corp. (Kyoto, Japan) HPLC setup was used for electro-oxidation products' separation. Initially, the HPLC chromatogram of the solution at 254 nm obtained after **DMPH** electro-oxidation was collected to detect the different fractions. The detailed HPLC analysis is explained in Chapter 2, Section 2.2.1.c6. Following this, a fraction collector FRC-10A from Shimadzu attached to the HPLC system was used to collect different fractions at retention times of 6.7, 11.0, 14.1, 14.9, and 19.7 min. These fractions were then passed through a silica gel 60 for column chromatography (0.040 – 0.063 mm, mesh 230 – 400, Merck KGaA) filled 50-mm long homemade column with 10 mm diameter using dichloromethane as the mobile phase to remove the tetrabutylammonium cations and perchlorate anions from the solution. Following this, the dichloromethane was evaporated, and then the solid was resuspended in 1 mL of an ACN : DCM (9 : 1, v/v) solution. The reference compound **DMPH** was used directly after diluting in ACN : DCM (9 : 1, v/v) solution for MS analysis.

(b) Mass spectrometry (MS) analysis

MS analyses were performed using a Synapt G2-S mass spectrometer (Waters, Milford, MS, USA) equipped with an atmospheric pressure chemical ionization (APCI) system and a quadrupole-time-of-flight (TOF) mass analyzer. The whole system is located in the Laboratory of Mass Spectrometry of the Institute of Organic Chemistry, Polish Academy of Sciences, Warsaw, Poland. Samples were dissolved in methanol (Honeywell, LC-MS Chromasolv™, purity ≥ 99.9%) and then injected into the APCI ion source. The injection volume was

1 – 8 μL , depending on the concentration of the samples. Methanol was used as a mobile phase with a 100 $\mu\text{L}/\text{min}$ flow rate. The measurement was performed in the negative ion mode with the resolving power of the qTOF analyzer at 20,000 full widths at half maximum. The lock-spray source generated the lock-spray spectrum of Leucine-enkephalin, and the recorded spectra in the range of $m/z = 50 - 1200$ were corrected. The desolvation and cone gas used was nitrogen, and their flow values were set to 600 L/h and 100 L/h, respectively. The source temperature was set to 120°C, and the probe temperature was 550°C. The nebulizer gas pressure was set to 5.0 bar. The corona current was set to 12.0 μA , and the sampling cone voltage and source offset were 30 V. The instrument was controlled, and the data were processed using the MassLynx V4.1 software package (Waters).

Results and discussion

Different fractions of the reaction products at retention times of 6.7, 11, 14.1, 14.9, and 19.7 min, obtained after electrosynthesis at **MIP-2a** film-coated electrodes, and the **DMPH** reference compound were analyzed by MS. In all recorded spectra signals at m/z of 98.94 and 100.94 Da are observed, which arise from ClO_4^- ion fragmentation (Figure A2). This result indicates that removing the supporting electrolyte ions was only partially successful. Nevertheless, the presence of those ions did not obscure the signal from other ions.

The 14.1-min fraction should contain the desired **TMBh** product as seen from HPLC reference spectra (Figure 3.19b). Therefore, the 14.1 min fraction spectrum (Figure A2-a) can be taken as the reference for **TMBh**. The fractions at 14.1 (Figure A2-a) and 14.9 min (Figure A2-b) show some similarities in the fragmentation patterns with a most pronounced ion at m/z of 241.12 Da, being compatible with **TMBh** structure with removed proton, and a less intense signal at m/z of 144.97 Da. The origin of the ions at m/z of 144.97 is not clear yet. However, the fraction at 14.1 min contains an intense signal at m/z of 220.97 Da, which is absent in the fraction collected at 14.9 min. Spectra of both fractions have small intensity signals at m/z above 250 Da, which can be attributed to coupling products of the primary fragmentation ions. This result suggests that both fractions contain compounds with similar structures, possibly isomers of **TMBh**, which is also supported by their similar retention times.

The fraction at the retention time of 19.7 min (Figure A2-c) shows a dominant signal at m/z of 144.97 Da and a weaker signal at 253.23 Da. It also exhibits several peaks of similar intensity at 168.99, 220.89, 241.12, 283.26, and 289.11 Da. The signal with m/z of 289.11 Da is almost equal to 2×144.97 Da, indicating a dimeric structure.

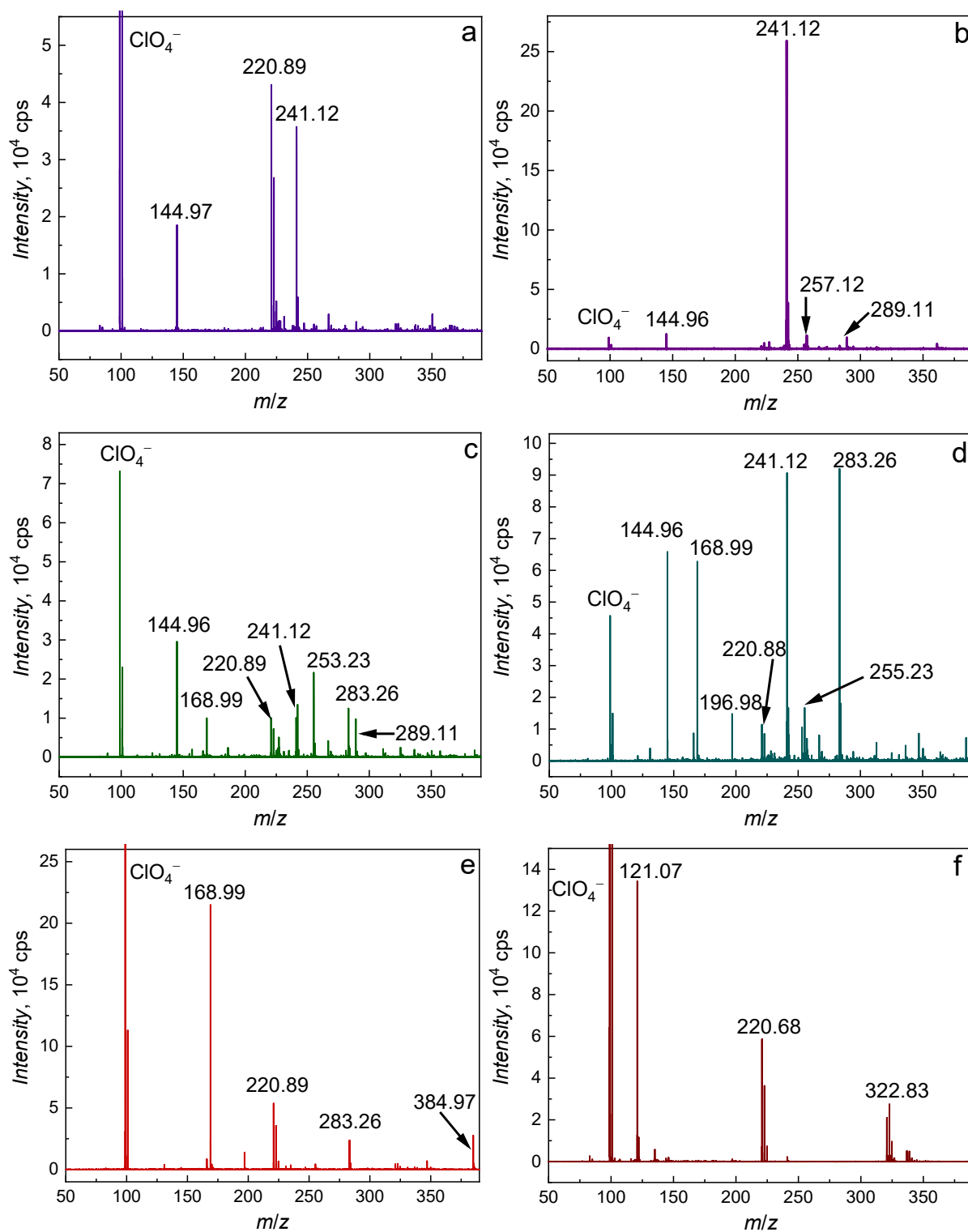


Figure A2. Mass spectra of HPLC separated fractions at (a) 14.1, (b) 14.9, (c) 19.7, (d) 11.0, and (e) 6.7 min retention time and mass spectra of (f) reference **DMPH** compound. All spectra were recorded in negative ion mode using atmospheric pressure chemical ionization (APCI).

There are also medium-sized signals at 504.51, 537.51, and 666.05 Da (not shown) which could be products of the primary ions coupling. The more complex fragmentation pattern for this fraction compared to that of fractions at 14.1 and 14.9 min indicate the breaking of a more complex molecule, including the **TMBh** unit. This fragmentation pattern, along with a higher retention time of the fraction, indicates a higher mass and less polar compound.

Mass spectrum of fraction collected at retention time 11.0 min (Figure A2-d) shows signals at m/z of 283.26 and 241.12 Da together with less intense signals at 144.96 and 168.99 Da, as well as several weak signals at 196.98, 220.88 and 255.23 Da. It also contains weak signals at m/z values above 350 Da (mainly at 410.36 and 537.51 Da), which are most probably products of the coupling of formed primary ions. The complex fragmentation pattern and lower retention time indicate that this product is a more polar derivative of **TMBh** containing a higher number of polar groups in its structure. This fraction was formed in relatively significant amounts during electrosynthesis at bare electrodes.

Finally, the fraction at 6.7 min (Figure A2-e) shows a strong signal at m/z of 168.99 Da and weaker signals at 220.89, 283.26, and 384.97 Da. This result suggests that the compound molecular mass is lower than **TMBh**, closer to the **DMPH**. Lower retention time also indicates a more polar compound, most probably a non-coupled product of **DMPH** oxidation. This fraction, as well, was a major product of electrosynthesis at bare electrodes. The MS of the **DMPH** pure compound (Figure A2-f) was performed to understand the fragmentation pattern in phenols as a reference.

In conclusion, MS analysis yielded some information on the possible side-products formed in electrosynthesis by the **MIP-2** system. However, further analysis is essential for determining the exact structure of the compounds formed.



References

1. Vlot, A. H. C.; de Witte, W. E. A.; Danhof, M.; van der Graaf, P. H.; van Westen, G. J. P.; de Lange, E. C. M., Target and tissue selectivity prediction by integrated mechanistic pharmacokinetic-Target binding and quantitative structure activity modeling. *AAPS J.* **2017**, *20*, 11.
2. Castel, A. D.; Humphreys, K. L.; Lee, S. S.; Galvan, A.; Balota, D. A.; McCabe, D. P., The development of memory efficiency and value-directed remembering across the life span: a cross-sectional study of memory and selectivity. *Dev. Psychol.* **2011**, *47*, 1553-1564.
3. Mencher, S. K.; Wang, L. G., Promiscuous drugs compared to selective drugs (promiscuity can be a virtue). *BMC Clin. Pharmacol.* **2005**, *5*, 3.
4. Vessman, J.; Stefan, R. I.; Staden, J. F. V.; Danzer, K.; Lindner, W.; Burns, D. T.; Fajgelj, A.; Muller, H., Selectivity in analytical chemistry. *Pure Appl. Chem.* **2001**, *73*, 1381–1386.
5. *Selectivity in catalysis*. American Chemical Society: Washington, DC, USA, 1993; Vol. 517.
6. Hagen, J., *Industrial catalysis. A practical approach*. John Wiley & Sons, Inc.: Weinheim, Germany, 2006.
7. Chorkendorff, I.; Niemantsverdriet, J. W., Introduction to catalysis. In *Concepts of modern catalysis and kinetics*, 3rd ed.; John Wiley & Sons, Inc.: 2017; pp 1-21.
8. Clime, K. Beyond sauerkraut: A brief history of fermented foods. <https://www.lhf.org/2014/03/beyond-sauerkraut-a-brief-history-of-fermented-foods/> (accessed 10 January 2022).
9. Smith, J. K., History of catalysis. In *Encyclopedia of catalysis*, Horváth, I. T., Ed. John Wiley & Sons, Inc.: 2010.
10. *Kent and Riegel's handbook of industrial chemistry and biotechnology*. 11th ed.; Springer: New York, NY, USA, 2007; Vol. 1.
11. *Metal nanoparticles for catalysis: advances and applications*. Royal Society of Chemistry: Cambridge, UK, 2014; Vol. 17.
12. Khoury, C.; Gadipelly, C.; Pappuru, S.; Shpasser, D.; Gazit, O. M., Progress in the design of cooperative heterogeneous catalytic materials for C–C bond formation. *Adv. Funct. Mater.* **2019**, *30*, 1901385.
13. Friend, C. M.; Xu, B., Heterogeneous catalysis: A central science for a sustainable future. *Acc. Chem. Res.* **2017**, *50*, 517-521.
14. Chorkendorff, I.; Niemantsverdriet, J. W., *Concepts of modern catalysis and kinetics*. John Wiley & Sons, Inc.: Weinheim, Germany, 2003.
15. Busca, G., *Heterogeneous catalytic materials: Solid state chemistry, surface chemistry and catalytic behaviour*. Elsevier Science: 2014.
16. *ENZYMES- A practical introduction to structure, mechanism, and data analysis*. 2nd ed.; John Wiley & Sons, Inc.: 2000.
17. Tripathi, A.; Bankaitis, V. A., Molecular docking: From lock and key to combination lock. *J. Mol. Med. Clin. Appl.* **2017**, *2*, PMC5764188.
18. Ben-Naim, A. The lock and key model for molecular recognition. Is it time for a paradigm shift? 2018. <https://arxiv.org/abs/1806.03499>.
19. Liu, L.; Corma, A., Metal catalysts for heterogeneous catalysis: From single atoms to nanoclusters and nanoparticles. *Chem. Rev.* **2018**, *118*, 4981-5079.

20. Védrine, J. C., Heterogeneous catalysis on metal oxides. *Catalysts* **2017**, *7*, 341.
21. Thomas, J. M.; Raja, R.; Lewis, D. W., Single-site heterogeneous catalysts. *Angew. Chem. Int. Ed.* **2005**, *44*, 6456-6482.
22. Ho Lee, C.; Uck Lee, S., Theoretical basis of electrocatalysis. In *Electrocatalysts for fuel cells and hydrogen evolution- Theory to design*, Ray, A.; Mukhopadhyay, I.; Pati, R. K., Eds. IntechOpen: London, UK, 2018.
23. Oriakhi, C. O., Fundamentals of electrochemistry. In *Chemistry in quantitative language: fundamentals of general chemistry calculations*, Oxford University Press: 2009.
24. *Electrocatalysis: Theoretical foundations and model experiments*. John Wiley & Sons, Inc.: Weinheim, Germany, 2013; Vol. 14.
25. *Electrocatalysis: Computational, experimental, and industrial aspects*. CRC Press Taylor & Francis Group: Boca Raton, FL, USA, 2010; Vol. 149.
26. Ashik, U. P. M.; Viswan, A.; Kudo, S.; Hayashi, J.-i., Nanomaterials as catalysts. In *Applications of nanomaterials*, Mohan Bhagyaraj, S.; Oluwafemi, O. S.; Kalarikkal, N.; Thomas, S., Eds. Woodhead Publishing: 2018; pp 45-82.
27. Zeng, K.; Zhang, D., Recent progress in alkaline water electrolysis for hydrogen production and applications. *Prog. Energy Combust. Sci.* **2010**, *36*, 307-326.
28. Bockris, J. O. M.; Minevski, Z. S., Electrocatalysis: a futuristic view. **1992**, *17* (*Int. J. Hydrog. Energy*), 423-444.
29. Boudjemaa, A., History, progress, and development of electrocatalysis. In *Methods for electrocatalysis: Advanced materials and allied applications*, Inamuddin; Boddula, R.; Asiri, A. M., Eds. Springer International Publishing, Cham: 2020; pp 401-424.
30. Andújar, J. M.; Segura, F., Fuel cells: History and updating. A walk along two centuries. *Renew. Sust. Energ. Rev.* **2009**, *13*, 2309-2322.
31. Li, H.; Chen, C.; Yan, D.; Wang, Y.; Chen, R.; Zou, Y.; Wang, S., Interfacial effects in supported catalysts for electrocatalysis. *J. Mater. Chem. A* **2019**, *7*, 23432-23450.
32. Schafer, H. J., Contributions of organic electrosynthesis to green chemistry. *C. R. Chim.* **2011**, *14*, 745-765.
33. Yuan, Y.; Lei, A., Is electrosynthesis always green and advantageous compared to traditional methods? *Nat. Commun.* **2020**, *11*, 802.
34. Suib, S. L., *New and future developments in catalysis. Catalysis by nanoparticles*. Elsevier Amsterdam, The Netherlands, 2013.
35. Jin, R., The impacts of nanotechnology on catalysis by precious metal nanoparticles. *Nanotechnol. Rev.* **2012**, *1*, 31-56.
36. Mirata, F.; Resmini, M., Molecularly imprinted polymers for catalysis and synthesis. In *Molecularly imprinted polymers in biotechnology*, Mattiasson, B.; Ye, L., Eds. Springer International Publishing, Cham: 2015; pp 107-129.
37. *Molecularly imprinted polymers: Man-made mimics of antibodies and their applications in analytical chemistry*. Elsevier: Amsterdam; New York, 2001.
38. Dickey, F. H., Specific adsorption. *J. Phys. Chem.* **1955**, *59*, 695-707.
39. Sellergren, B.; Lepisto, M.; Mosbach, K., Highly enantioselective and substrate-selective polymers obtained by molecular imprinting utilizing noncovalent interactions. NMR and chromatographic studies on the nature of recognition. *J. Am. Chem. Soc.* **1988**, *110*, 5853-5860.
40. Andersson, L.; Sellergren, B.; Mosbach, K., Imprinting of amino acid derivatives in macroporous polymers. *Tetrahedron Lett.* **1984**, *25*, 5211-5214.

41. Sellergren, B.; Ekberg, B.; Mosbach, K., Molecular imprinting of amino acid derivatives in macroporous polymers: Demonstration of substrate- and enantio-selectivity by chromatographic resolution of racemic mixtures of amino acid derivatives. *J. Chromatogr. A* **1985**, *347*, 1-10.
42. Wulff, G.; Sarhan, A.; Zabrocki, K., Enzyme-analogue built polymers and their use for the resolution of racemates. *Tetrahedron Lett.* **1973**, *14*, 4329-4332.
43. Mayes, A. G.; Mosbach, K., Molecularly imprinted polymers: Useful materials for analytical chemistry? *Trends Anal. Chem.* **1997**, *16*, 321-332.
44. Wulff, G., Molecular imprinting in cross-linked materials with the aid of molecular templates—A way towards artificial antibodies. *Angew. Chem. Int. Ed. Engl.* **1995**, *34*, 1812-1832.
45. *Molecularly imprinted catalysts*. Elsevier: Oxford, UK, 2015.
46. Kriz, D.; Ramström, O.; Mosbach, K., Peer reviewed: Molecular imprinting: New possibilities for sensor technology. *Anal. Chem.* **1997**, *69*, 345A-349A.
47. Yan, M., *Molecularly imprinted materials: Science and technology*. CRC Press: 2004.
48. Dickey, F. H. In *The preparation of specific adsorbents*, National Academy of Sciences, USA, National Academy of Sciences: USA, 1949; pp 227-229.
49. Katz, A.; Davis, M., Molecular imprinting of bulk, microporous silica. *Nature* **2000**, *403*, 286–289.
50. Diaz-Garcia, M. E.; Laino, R. B., Molecular imprinting in sol-gel materials: Recent developments and applications. *Mikrochim. Acta* **2004**, *149*, 19-36.
51. Ye, L., Synthetic strategies in molecular imprinting. In *Molecularly imprinted polymers in biotechnology*, Mattiasson, B.; Ye, L., Eds. Springer International Publishing, Cham: 2015; pp 1-24.
52. Andrew G. Mayes, K. M., Molecularly imprinted polymer beads: suspension polymerization using a liquid perfluorocarbon as the dispersing phase. *Anal. Chem.* **1996**, *68*, 3769-3774.
53. Resmini, M.; Flavin, K.; Carboni, D., Microgels and nanogels with catalytic activity. In *Molecular imprinting*, Haupt, K., Ed. Springer: Berlin, Heidelberg, Germany, 2012; pp 307-342.
54. Yoshikawa, M., Molecularly imprinted polymeric membranes. *Bioseparation* **2002**, *10*, 277-286.
55. Shen, X.; Ye, L., Interfacial molecular imprinting in nanoparticle-stabilized emulsions. *Macromolecules* **2011**, *44*, 5631-5637.
56. Schweitz, L.; Andersson, L. I.; Nilsson, S., Capillary electrochromatography with predetermined selectivity obtained through molecular imprinting. *Anal. Chem.* **1997**, *69*, 1179-1183.
57. Wackerlig, J.; Schirhagl, R., Applications of MIP nanoparticles and their advances towards industrial use—A review. *Anal. Chem.* **2016**, *88*, 250–261.
58. Dong, C.; Shi, H.; Han, Y.; Yang, Y.; Wang, R.; Men, J., Molecularly imprinted polymers by the surface imprinting technique. *Eur. Polym. J.* **2021**, *145*, 110231.
59. Wulff, G., Enzyme-like catalysis by molecularly imprinted polymers. *Chem. Rev.* **2002**, *102*, 1-28.
60. *Molecularly imprinted polymers in biotechnology*. Springer: Switzerland, 2015.
61. Xu, J.; Miao, H.; Wang, J.; Pan, G., Molecularly imprinted synthetic antibodies: From chemical design to biomedical applications. *Small* **2020**, *16*, 1906644.
62. Alexander, C.; Davidson, L.; Hayes, W., Imprinted polymers: Artificial molecular recognition materials with applications in synthesis and catalysis. *Tetrahedron* **2003**, *59*, 2025-2057.
63. Saylan, Y.; Yilmaz, F.; Ozgur, E.; Derazshamshir, A.; Yavuz, H.; Denizli, A., Molecular imprinting of macromolecules for sensor applications. *Sensors* **2017**, *17*, 898.

64. Haupt, K.; Linares, A. V.; Bompart, M.; Bui, B. T., Molecularly imprinted polymers. *Top. Curr. Chem.* **2012**, *325*, 1-28.
65. Whitcombe, M. J.; Chianella, I.; Larcombe, L.; Piletsky, S. A.; Noble, J.; Porter, R.; Horgan, A., The rational development of molecularly imprinted polymer-based sensors for protein detection. *Chem. Soc. Rev.* **2011**, *40*, 1547-1571.
66. Bossi, A.; Bonini, F.; Turner, A. P.; Piletsky, S. A., Molecularly imprinted polymers for the recognition of proteins: The state of the art. *Biosens. Bioelectron.* **2007**, *22*, 1131-1137.
67. Culver, H. R.; Peppas, N. A., Protein-imprinted polymers: The shape of things to come? *Chem. Mater.* **2017**, *29*, 5753-5761.
68. Pasquardini, L.; Bossi, A. M., Molecularly imprinted polymers by epitope imprinting: A journey from molecular interactions to the available bioinformatics resources to scout for epitope templates. *Anal. Bioanal. Chem.* **2021**, *413*, 6101-6115.
69. Madikizela, L.; Tavengwa, N.; Pakade, V., Molecularly imprinted polymers for pharmaceutical compounds: synthetic procedures and analytical applications. In *Recent research in polymerization*, Cankaya, N., Ed. IntechOpen: London, UK, 2018.
70. Xiao, D.; Jiang, Y.; Bi, Y., Molecularly imprinted polymers for the detection of illegal drugs and additives: A review. *Mikrochim. Acta* **2018**, *185*, 247.
71. Zarejousheghani, M.; Lorenz, W.; Vanninen, P.; Alizadeh, T.; Cammerer, M.; Borsdorf, H., Molecularly imprinted polymer materials as selective recognition sorbents for explosives: A review. *Polymers* **2019**, *11*, 888.
72. McCluskey, A.; Holdsworth, C. I.; Bowyer, M. C., Molecularly imprinted polymers (MIPs): Sensing, an explosive new opportunity? *Org. Biomol. Chem.* **2007**, *5*, 3233-3244.
73. Villa, C. C.; Sánchez, L. T.; Valencia, G. A.; Ahmed, S.; Gutiérrez, T. J., Molecularly imprinted polymers for food applications: A review. *Trends Food Sci. Technol.* **2021**, *111*, 642-669.
74. Gao, M.; Gao, Y.; Chen, G.; Huang, X.; Xu, X.; Lv, J.; Wang, J.; Xu, D.; Liu, G., Recent advances and future trends in the detection of contaminants by molecularly imprinted polymers in food samples. *Front. Chem.* **2020**, *8*, 616326.
75. Azizi, A.; Bottaro, C. S., A critical review of molecularly imprinted polymers for the analysis of organic pollutants in environmental water samples. *J. Chromatogr. A* **2020**, *1614*, 460603.
76. Tse Sum Bui, B.; Auroy, T.; Haupt, K., Fighting antibiotic-resistant bacteria: Promising strategies orchestrated by molecularly imprinted polymers. *Angew. Chem. Int. Ed.* **2022**, *61*, e202106493.
77. Amorim, M. S.; Sales, M. G. F.; Frasco, M. F., Recent advances in virus imprinted polymers. *Biosens. Bioelectron.: X* **2022**, *10*, 100131.
78. Cheong, W. J.; Yang, S. H.; Ali, F., Molecular imprinted polymers for separation science: A review of reviews. *J. Sep. Sci.* **2013**, *36*, 609-628.
79. Wackerlig, J.; Lieberzeit, P. A., Molecularly imprinted polymer nanoparticles in chemical sensing— Synthesis, characterisation and application. *Sens. Actuators B Chem.* **2015**, *207*, 144-157.
80. Wang, N. X.; von Recum, H. A., Affinity-based drug delivery. *Macromol. Biosci.* **2011**, *11*, 321-332.
81. Piletsky, S.; Canfarotta, F.; Poma, A.; Bossi, A. M.; Piletsky, S., Molecularly imprinted polymers for cell recognition. *Trends Biotechnol.* **2020**, *38*, 368-387.
82. Vasapollo, G.; Sole, R. D.; Mergola, L.; Lazzoi, M. R.; Scardino, A.; Scorrano, S.; Mele, G., Molecularly imprinted polymers: Present and future prospective. *Int. J. Mol. Sci.* **2011**, *12*, 5908-5945.
83. Liu, Z.; Xu, Z.; Wang, D.; Yang, Y.; Duan, Y.; Ma, L.; Lin, T.; Liu, H., A review on molecularly imprinted polymers preparation by computational simulation-aided methods. *Polymers* **2021**, *13*, 2657.

84. Haupt, K.; Linares, A. V.; Bompart, M.; Bui, B. T. S., Molecularly imprinted polymers. In *Molecular Imprinting*, Haupt, K., Ed. Springer Berlin Heidelberg: Berlin, Heidelberg, 2012; pp 1-28.
85. Karim, K.; Breton, F.; Rouillon, R.; Piletska, E. V.; Guerreiro, A.; Chianella, I.; Piletsky, S. A., How to find effective functional monomers for effective molecularly imprinted polymers? *Adv. Drug Deliv. Rev.* **2005**, *57*, 1795-1808.
86. Curk, T.; Dobnikar, J.; Frenkel, D., Rational design of molecularly imprinted polymers. *Soft Matter* **2016**, *12*, 35-44.
87. Cela-Pérez, M. C.; Lasagabáster-Latorre, A.; Abad-López, M. J.; López-Vilariño, J. M.; González-Rodríguez, M. V., A study of competitive molecular interaction effects on imprinting of molecularly imprinted polymers. *Vib. Spectrosc.* **2013**, *65*, 74-83.
88. Osmani, Q.; Hughes, H.; Flavin, K.; Hedin-Dahlstrom, J.; Allender, C. J.; Frisby, J.; McLoughlin, P., The use of FTIR and NMR spectroscopies to study prepolymerisation interactions in nitrogen heterocycles. *Anal. Bioanal. Chem.* **2008**, *391*, 1229-1236.
89. O'Mahony, J.; Molinelli, A.; Nolan, K.; Smyth, M. R.; Mizaikoff, B., Towards the rational development of molecularly imprinted polymers: ¹H NMR studies on hydrophobicity and ion-pair interactions as driving forces for selectivity. *Biosens. Bioelectron.* **2005**, *20*, 1884-1893.
90. Henry, O. Y.; Cullen, D. C.; Piletsky, S. A., Optical interrogation of molecularly imprinted polymers and development of MIP sensors: A review. *Anal. Bioanal. Chem.* **2005**, *382*, 947-956.
91. Subrahmanyam, S.; Karim, K.; Piletsky, S. A., Computational approaches in the design of synthetic receptors. In *Designing receptors for the next generation of biosensors*, Piletsky, S. A.; Whitcombe, M. J., Eds. Springer: Berlin Heidelberg, Germany, 2012; Vol. 12, pp 131-166.
92. Chianella, I.; Lotierzo, M.; Piletsky, S. A.; Tohill, I. E.; Chen, B.; Karim, K.; Turner, A. P. F., Rational design of a polymer specific for microcystin-LR using a computational approach. *Anal. Chem.* **2002**, *74*, 1288-1293.
93. Nicholls, I. A.; Andersson, H. S., Thermodynamic principles underlying molecularly imprinted polymer formulation and ligand recognition. In *Molecularly imprinted polymers - Man-made mimics of antibodies and their applications in analytical chemistry*, Elsevier: 2001; Vol. 23, pp 59-70.
94. Li, P.; Rong, F.; Zhu, X. L.; Hu, J. Z.; Yuan, C. W., Studies on the preparation of L-2-chloromandelic acid-imprinted polymer and its selective binding characteristics. *Acta Polym. Sin.* **2003**, 724-727.
95. Whitcombe, M. J.; Martin, L.; Vulfson, E. N., Predicting the selectivity of imprinted polymers. *Chromatographia* **1998**, *47*, 457-464.
96. Bompart, M.; Haupt, K., Molecularly imprinted polymers and controlled/living radical polymerization. *Aust. J. Chem.* **2009**, *62*, 751-761.
97. Yan, H.; Row, K. H., Characteristic and synthetic approach of molecularly imprinted polymer. *Int. J. Mol. Sci.* **2006**, *7*, 155-178.
98. Poma, A.; Turner, A. P.; Piletsky, S. A., Advances in the manufacture of MIP nanoparticles. *Trends Biotechnol.* **2010**, *28*, 629-637.
99. Walcarius, A.; Collinson, M. M., Analytical chemistry with silica sol-gels: Traditional routes to new materials for chemical analysis. *Annu. Rev. Anal. Chem.* **2009**, *2*, 121-143.
100. Mujahid, A.; Lieberzeit, P. A.; Dickert, F. L., Chemical sensors based on molecularly imprinted sol-gel materials. *Materials* **2010**, *3*, 2196-2217.
101. Hawker, C. J.; Bosman, A. W.; Harth, E., New polymer synthesis by nitroxide mediated living radical polymerizations. *Chem. Rev.* **2001**, *101*, 3661-3688.
102. Sajini, T.; Mathew, B., A brief overview of molecularly imprinted polymers: Highlighting computational design, nano and photo-responsive imprinting. *Talanta Open* **2021**, *4*, 100072.

103. Sharma, P. S.; Pietrzyk-Le, A.; D'Souza, F.; Kutner, W., Electrochemically synthesized polymers in molecular imprinting for chemical sensing. *Anal. Bioanal. Chem.* **2012**, *402*, 3177-3204.
104. Chiang, C. K.; Fincher, C. R.; Park, Y. W.; Heeger, A. J.; Shirakawa, H.; Louis, E. J.; Gau, S. C.; MacDiarmid, A. G., Electrical conductivity in doped polyacetylene. *Phys. Rev. Lett.* **1977**, *39*, 1098-1101.
105. Goodings, E. P., Conductivity and superconductivity in polymers*. *Chem. Soc. Rev.* **1976**, *5*, 95-123.
106. MacDiarmid, A. G., "Synthetic metals": A novel role for organic polymers (Nobel lecture)**. *Angew. Chem. Int. Ed.* **2001**, *40*, 2581-2590.
107. Schopf, G.; Kossmehl, G., *Polythiophenes: Electrically conductive polymers*. Springer: 1997.
108. Shirakawa, H., The discovery of polyacetylene film: The dawning of an era of conducting polymers (Nobel lecture)**. *Angew. Chem. Int. Ed.* **2001**, *40*, 2574-2580.
109. González-Tejera, M. J.; de la Blanca, E. S.; Carrillo, I., Polyfuran conducting polymers: Synthesis, properties, and applications. *Synth. Met.* **2008**, *158*, 165-189.
110. Sabouraud, G.; Sadki, S.; Brodie, N., The mechanisms of pyrrole electropolymerization. *Chem. Soc. Rev.* **2000**, *29*, 283-293.
111. Mark, H. F., *Encyclopedia of polymer science and technology, concise*. John Wiley & Sons, Inc.: 2013.
112. Kayser, L. V.; Lipomi, D. J., Stretchable conductive polymers and composites based on PEDOT and PEDOT:PSS. *Adv. Mater.* **2019**, *31*, 1806133.
113. Wang, P.-C.; Liu, L.-H.; Alemu Mengistie, D.; Li, K.-H.; Wen, B.-J.; Liu, T.-S.; Chu, C.-W., Transparent electrodes based on conducting polymers for display applications. *Displays* **2013**, *34*, 301-314.
114. Guo, X.; Facchetti, A., The journey of conducting polymers from discovery to application. *Nat. Mater.* **2020**, *19*, 922-928.
115. Xiao, L.; Chen, Z.; Qu, B.; Luo, J.; Kong, S.; Gong, Q.; Kido, J., Recent progresses on materials for electrophosphorescent organic light-emitting devices. *Adv. Mater.* **2011**, *23*, 926-952.
116. Meng, Q.; Cai, K.; Chen, Y.; Chen, L., Research progress on conducting polymer based supercapacitor electrode materials. *Nano Energy* **2017**, *36*, 268-285.
117. Saito, G.; Yoshida, Y., Frontiers of organic conductors and superconductors. In *Unimolecular and supramolecular electronics I: Chemistry and physics meet at metal-molecule interfaces*, Metzger, R. M., Ed. Springer: Berlin, Heidelberg, Germany, 2012; pp 67-126.
118. Hedborg, E.; Winqvist, F.; Lundstrom, I.; Andersson, L. I.; Mosbach, K., Some studies of molecularly-imprinted polymer membranes in combination with field-effect devices. *Sens. Actuators, A* **1993**, *37-38*, 796-799.
119. Piletsky, S. A.; Turner, A. P., Electrochemical sensors based on molecularly imprinted polymers. *Electroanalysis* **2002**, *14*, 317-323.
120. Haupt, K., Molecularly imprinted polymers in analytical chemistry. *Analyst* **2001**, *126*, 747-756.
121. Sharma, P. S.; Garcia-Cruz, A.; Cieplak, M.; Noworyta, K. R.; Kutner, W., 'Gate effect' in molecularly imprinted polymers: the current state of understanding. *Curr. Opin. Electrochem.* **2019**, *16*, 50-56.
122. Zaidi, S. A., Molecular imprinting polymers and their composites: A promising material for diverse applications. *Biomater. Sci.* **2017**, *5*, 388-402.
123. BelBruno, J. J., Molecularly imprinted polymers. *Chem. Rev.* **2019**, *119*, 94-119.

124. Apodaca, D. C.; Pernites, R. B.; Ponnappati, R. R.; Del Mundo, F. R.; Advincula, R. C., Electropolymerized molecularly imprinted polymer films of a bis-terthiophene dendron: Folic acid quartz crystal microbalance sensing. *ACS Appl. Mater. Interfaces* **2011**, *3*, 191-203.
125. Blanco-Lopez, M. C.; Gutierrez-Fernandez, S.; Lobo-Castanon, M. J.; Miranda-Ordieres, A. J.; Tunon-Blanco, P., Electrochemical sensing with electrodes modified with molecularly imprinted polymer films. *Anal. Bioanal. Chem.* **2004**, *378*, 1922-1928.
126. Ayerdurai, V.; Cieplak, M.; Noworyta, K. R.; Gajda, M.; Ziminska, A.; Sosnowska, M.; Piechowska, J.; Borowicz, P.; Lisowski, W.; Shao, S.; D'Souza, F.; Kutner, W., Electrochemical sensor for selective tyramine determination, amplified by a molecularly imprinted polymer film. *Bioelectrochemistry* **2021**, *138*, 107695.
127. Dutta, P.; Pernites, R. B.; Danda, C.; Advincula, R. C., SPR detection of dopamine using cathodically electropolymerized, molecularly imprinted poly-*p*-aminostyrene thin films. *Macromol. Chem. Phys.* **2011**, *212*, 2439-2451.
128. Sharma, P. S.; Dabrowski, M.; Noworyta, K.; Huynh, T.-P.; Kc, C. B.; Sobczak, J. W.; Pieta, P.; D'Souza, F.; Kutner, W., Fullerene derived molecularly imprinted polymer for chemosensing of adenosine-5'-triphosphate (ATP). *Anal. Chim. Acta* **2014**, *844*, 61-69.
129. Heinze, J., Electronically conducting polymers. In *Electrochemistry IV*, Steckhan, E., Ed. Springer: Berlin, Heidelberg, 1990; Vol. 152, pp 1-47.
130. Hasanah, A. N.; Safitri, N.; Zulfa, A.; Neli, N.; Rahayu, D., Factors affecting preparation of molecularly imprinted polymer and methods on finding template-monomer interaction as the key of selective properties of the materials. *Molecules* **2021**, *26*, 5612.
131. Shen, F.; Zhang, Q.; Ren, X., A triple-function zwitterion for preparing water compatible diclofenac imprinted polymers. *Chem. Commun.* **2015**, *51*, 183-186.
132. Włoch, M.; Datta, J., Chapter Two - Synthesis and polymerisation techniques of molecularly imprinted polymers. In *Comprehensive analytical chemistry*, Marć, M., Ed. Elsevier: 2019; Vol. 86, pp 17-40.
133. Mokni, M.; Mazouz, Z.; Attia, G.; Fourati, N.; Zerrouki, C.; Omezzine, A.; Bouslema, A.; Kalfat, R. In *Prime importance of the supporting electrolyte in the realization of molecularly imprinted polymers*, Conference on Molecular, Biomedical & Computational Sciences and Engineering, MDPI: 2018.
134. Bender, M. L.; Killheffer, J. V., Chymotrypsins. *CRC Crit. Rev. Biochem.* **1973**, *1*, 149-199.
135. Purdie, J. E.; Benoiton, N. L., The interaction of α -chymotrypsin with phenylalanine derivatives containing a free α -amino group. *Can. J. Biochem.* **1970**, *48*, 1058-1065.
136. Fastrez, J.; Pasteur, P. L., Mechanism of chymotrypsin: Concurrent chemical and enzymic aminolysis of an acyl-enzyme of methylchymotrypsin. Efficiency of acid-base catalysis. *J. Chem. Soc., Perkin Trans. 2* **1980**, 1067-1074.
137. Wulff, G.; Vietmeier, J., Enzyme-analogue built polymers, 26. Enantioselective synthesis of amino acids using polymers possessing chiral cavities obtained by an imprinting procedure with template molecules. *Makromol. Chem.* **1989**, *190*, 1727- 1735.
138. Zhang, H.; Piacham, T.; Drew, M.; Patek, M.; Mosbach, K.; Ye, L., Molecularly imprinted nanoreactors for regioselective Huisgen 1,3-dipolar cycloaddition reaction. *J. Am. Chem. Soc.* **2006**, *128*, 4178-4179.
139. Barbany, M.; Gutierrez-de-Teran, H.; Sanz, F.; Villa-Freixa, J.; Warshel, A., On the generation of catalytic antibodies by transition state analogues. *ChemBioChem.* **2003**, *4*, 277-285.
140. Wulff, G.; Gross, T.; Schonfeld, R., Enzyme models based on molecularly imprinted polymers with strong esterase activity**. *Angew. Chem. Int. Ed. Engl* **1997**, *32*, 1961-1964.

141. Wulff, G.; Liu, J., Design of biomimetic catalysts by molecular imprinting in synthetic polymers: The role of transition state stabilization. *Acc. Chem. Res.* **2012**, *45*, 239-247.
142. Matsui, J.; Nicholls, I. A.; Karube, I.; Mosbach, K., Carbon-carbon bond formation using substrate selective catalytic polymers prepared by molecular imprinting: An artificial class II aldolase. *J. Org. Chem.* **1996**, *61*, 5414-5417.
143. Hedin-Dahlstrom, J.; Rosengren-Holmberg, J. P.; Legrand, S.; Wikman, S.; Nicholls, I. A., A Class II Aldolase Mimic. *J. Org. Chem.* **2006**, *71*, 4845-4853.
144. Cammidge, A. N.; Baines, N. J.; Bellingham, R. K., Synthesis of heterogeneous palladium catalyst assemblies by molecular imprinting. *Chem. Comm.* **2001**, 2588-2589.
145. Viton, F.; White, P. S.; Gagne, M. R., Crown-ether functionalised second coordination sphere palladium catalysts by molecular imprinting. *Chem. Comm.* **2003**, 3040-3041.
146. Muratsugu, S.; Maity, N.; Baba, H.; Tasaki, M.; Tada, M., Preparation and catalytic performance of a molecularly imprinted Pd complex catalyst for Suzuki cross-coupling reactions. *Dalton Trans.* **2017**, *46*, 3125-3134.
147. Muratsugu, S.; Shirai, S.; Tada, M., Recent progress in molecularly imprinted approach for catalysis. *Tetrahedron Lett.* **2020**, *61*, 151603.
148. von Nussbaum, F.; Brands, M.; Hinzen, B.; Weigand, S.; Habich, D., Antibacterial natural products in medicinal chemistry--Exodus or revival? *Angew. Chem. Int. Ed. Engl.* **2006**, *45*, 5072-5129.
149. Bringmann, G.; Gulder, T.; Gulder, T. A. M.; Breuning, M., Atroposelective total synthesis of axially chiral biaryl natural products. *Chem. Rev.* **2011**, *111*, 563-639.
150. Lai, H.; Huang, Z.; Wu, Q.; Qin, Y., Synthesis of novel enantiopure biphenyl *P,N*-ligands and application in palladium-catalyzed asymmetric addition of arylboronic acids to *N*-benzylisatin. *J. Org. Chem.* **2009**, *74*, 283-288.
151. Cammidge, A. N.; Crepy, K. V. L., Application of the Suzuki reaction as the key step in the synthesis of a novel atropisomeric biphenyl derivative for use as a liquid crystal dopant. *J. Org. Chem.* **2003**, *68*, 6832-6835.
152. Imai, Y.; Zhang, W.; Kida, T.; Nakatsuji, Y.; Ikeda, I., Novel chiral bisoxazoline ligands with a biphenyl backbone: Preparation, complexation, and application in asymmetric catalytic reactions. *J. Org. Chem.* **2000**, *65*, 3326-3333.
153. Qiu, L.; Wu, J.; Chan, S.; Au-Yeung, T. T.; Ji, J. X.; Guo, R.; Pai, C. C.; Zhou, Z.; Li, X.; Fan, Q. H.; Chan, A. S., Remarkably diastereoselective synthesis of a chiral biphenyl diphosphine ligand and its application in asymmetric hydrogenation. *Proc. Natl. Acad. Sci. U. S. A.* **2004**, *101*, 5815-5820.
154. Alexakis, A.; Polet, D.; Benhaim, C.; Rosset, S., Biphenol-based ligands for Cu-catalyzed asymmetric conjugate addition. *Tetrahedron Asymmetry* **2004**, *15*, 2199-2203.
155. Monti, C.; Gennari, C.; Piarulli, U., Rh-catalyzed enantioselective conjugate addition of arylboronic acids with a dynamic library of chiral *tropos* phosphorus ligands. *Chemistry* **2007**, *13*, 1547-1558.
156. Mata, Y.; Pamies, O.; Dieguez, M., Screening of a modular sugar-based phosphite-oxazoline ligand library in asymmetric Pd-catalyzed heck reactions. *Chemistry* **2007**, *13*, 3296-3304.
157. Tsarev, V. N.; Kabro, A. A.; Moiseev, S. K.; Kalinin, V. N.; Bondarev, O. G.; Davankov, V. A.; Gavrilov, K. N., Complexing and catalytic properties of easily available chiral iminophosphite based on biphenyl-2,2'-diol. *Russ. Chem. Bull.* **2004**, *53*, 814-818.
158. Franke, R.; Selent, D.; Borner, A., Applied hydroformylation. *Chem. Rev.* **2012**, *112*, 5675-732.
159. Bringmann, G.; Mortimer, A. J. P.; Keller, P. A.; Gresser, M. J.; Garner, J.; Breuning, M., Atroposelective synthesis of axially chiral biaryl compounds. *Angew. Chem. Int. Ed. Engl.* **2005**, *44*, 5384-5427.

160. McDonald, P. D.; Hamilton, G. A., Mechanisms of phenolic oxidative coupling reactions. In *Oxidation in organic chemistry, part B*, Trahanovsky, W. S., Ed. Elsevier: 1973; Vol. 5, pp 97-134.
161. Dewar, M. J. S.; Nakaya, T., Oxidative coupling of phenols. *J. Am. Chem. Soc.* **1968**, *90*, 7134-7135.
162. Duprez, D.; Delanoe, F.; Barbier Jr, J.; Isnard, P.; Blanchard, G., Catalytic oxidation of organic compounds in aqueous media. *Catal. Today* **1996**, *29*, 317-322.
163. Lee, Y. E.; Cao, T.; Torruellas, C.; Kozlowski, M. C., Selective oxidative homo- and cross-coupling of phenols with aerobic catalysts. *J. Am. Chem. Soc.* **2014**, *136*, 6782-6785.
164. Shalit, H.; Dyadyuk, A.; Pappo, D., Selective oxidative phenol coupling by iron catalysis. *J. Org. Chem.* **2019**, *84*, 1677-1686.
165. Frontana-Uribe, B. A.; Little, R. D.; Ibanez, J. G.; Palma, A.; Vasquez-Medrano, R., Organic electrosynthesis: A promising green methodology in organic chemistry. *Green Chem.* **2010**, *12*, 2099-2119.
166. Horn, E. J.; Rosen, B. R.; Baran, P. S., Synthetic organic electrochemistry: an enabling and innately sustainable method. *ACS Cent. Sci.* **2016**, *2*, 302-308.
167. Selt, M.; Gleede, B.; Franke, R.; Stenglein, A.; Waldvogel, S. R., Electrosynthesis of 3,3',5,5'-tetramethyl-2,2'-biphenol in flow. *J. Flow Chem.* **2021**, *11*, 143-162.
168. Rockl, J. L.; Schollmeyer, D.; Franke, R.; Waldvogel, S. R., Dehydrogenative anodic C-C coupling of phenols bearing electron-withdrawing groups. *Angew. Chem. Int. Ed. Engl.* **2020**, *59*, 315-319.
169. Gleede, B.; Selt, M.; Franke, R.; Waldvogel, S. R., Developments in the dehydrogenative electrochemical synthesis of 3,3',5,5'-tetramethyl-2,2'-biphenol. *Chemistry* **2021**, *27*, 8252-8263.
170. Selt, M.; Mentizi, S.; Schollmeyer, D.; Franke, R.; Waldvogel, S. R., Selective and scalable dehydrogenative electrochemical synthesis of 3,3',5,5'-tetramethyl-2,2'-biphenol. *Synlett* **2019**, *30*, 2062-2067.
171. Waldvogel, S. R., Novel anodic concepts for the selective phenol coupling reaction. *Pure Appl. Chem.* **2010**, *82*, 1055-1063.
172. Malkowsky, I. M.; Fröhlich, R.; Griesbach, U.; Pütter, H.; Waldvogel, S. R., Facile and reliable synthesis of tetraphenoxyborates and their properties. *Eur. J. Inorg. Chem.* **2006**, *2006*, 1690-1697.
173. Kirste, A.; Hayashi, S.; Schnakenburg, G.; Malkowsky, I. M.; Stecker, F.; Fischer, A.; Fuchigami, T.; Waldvogel, S. R., Highly selective electrosynthesis of biphenols on graphite electrodes in fluorinated media. *Chemistry* **2011**, *17*, 14164-14169.
174. Kirste, A.; Nieger, M.; Malkowsky, I. M.; Stecker, F.; Fischer, A.; Waldvogel, S. R., ortho-Selective phenol-coupling reaction by anodic treatment on boron-doped diamond electrode using fluorinated alcohols. *Chemistry* **2009**, *15*, 2273-2277.
175. Holloczki, O.; Macchieraldo, R.; Gleede, B.; Waldvogel, S. R.; Kirchner, B., Interfacial domain formation enhances electrochemical synthesis. *J. Phys. Chem. Lett.* **2019**, *10*, 1192-1197.
176. Hollóczki, O.; Berkessel, A.; Mars, J.; Mezger, M.; Wiebe, A.; Waldvogel, S. R.; Kirchner, B., The catalytic effect of fluoroalcohol mixtures depends on domain formation. *ACS Catal.* **2017**, *7*, 1846-1852.
177. Narayanan, R., Synthesis of green nanocatalysts and industrially important green reactions. *Green Chem. Lett. Rev.* **2012**, *5*, 707-725.
178. Nanomaterials. <https://euon.echa.europa.eu/general-information> (accessed 1 April 2022).
179. Poole, C. P.; Owens, F. J., *Introduction to nanotechnology*. Wiley: 2003.

180. Feynman, R. P., Plenty of room at the bottom. Transcript talk presented to the American Physical Society. Pasadena, CA, USA, 1959.
181. Saratale, R. G.; Saratale, G. D.; Shin, H. S.; Jacob, J. M.; Pugazhendhi, A.; Bhaisare, M.; Kumar, G., New insights on the green synthesis of metallic nanoparticles using plant and waste biomaterials: Current knowledge, their agricultural and environmental applications. *Environ. Sci. Pollut. Res. Int.* **2018**, *25*, 10164-10183.
182. Uldrich, J.; Newberry, D., *The next big thing is really small: How nanotechnology will change the future of your business*. Random House: 2010.
183. Mihranyan, A.; Ferraz, N.; Strømme, M., Current status and future prospects of nanotechnology in cosmetics. *Prog. Mater. Sci.* **2012**, *57*, 875-910.
184. Emerich, D. F.; Thanos, C. G., Nanotechnology and medicine. *Expert Opin. Biol. Ther.* **2003**, *3*, 655-663.
185. *Introduction to nanoscale science and technology*. Springer: Boston, MA, USA, 2004.
186. Shamaila, S.; Sajjad, A. K. L.; Ryma, N.-u.-A.; Farooqi, S. A.; Jabeen, N.; Majeed, S.; Farooq, I., Advancements in nanoparticle fabrication by hazard free eco-friendly green routes. *Appl. Mater. Today* **2016**, *5*, 150-199.
187. Förster, H.; Wolfrum, C.; Peukert, W., Experimental study of metal nanoparticle synthesis by an arc evaporation/condensation process. *J. Nanopart. Res.* **2012**, *14*, 926.
188. Bae, C. H.; Nam, S. H.; Park, S. M., Formation of silver nanoparticles by laser ablation of a silver target in NaCl solution. *Appl. Surf. Sci.* **2002**, *197-198*, 628-634.
189. Wang, Y.; Xia, Y., Bottom-up and top-down approaches to the synthesis of monodispersed spherical colloids of low melting point metals. *Nano Lett.* **2004**, *4*, 2047-2050.
190. *Reducing agents in colloidal nanoparticle synthesis*. Royal Society of Chemistry: Cambridge, UK, 2021; p 465.
191. Varma, R. S., Greener and sustainable trends in synthesis of organics and nanomaterials. *ACS Sustainable Chem. Eng.* **2016**, *4*, 5866-5878.
192. Singh, J.; Dutta, T.; Kim, K. H.; Rawat, M.; Samddar, P.; Kumar, P., 'Green' synthesis of metals and their oxide nanoparticles: Applications for environmental remediation. *J. Nanobiotechnology* **2018**, *16*, 84.
193. Abdelbasir, S. M.; McCourt, K. M.; Lee, C. M.; Vanegas, D. C., Waste-derived nanoparticles: Synthesis approaches, environmental applications, and sustainability considerations. *Front. Chem.* **2020**, *8*, 782.
194. Huston, M.; DeBella, M.; DiBella, M.; Gupta, A., Green synthesis of nanomaterials. *Nanomaterials* **2021**, *11*, 2130.
195. Saratale, R. G.; Shin, H. S.; Kumar, G.; Benelli, G.; Ghodake, G. S.; Jiang, Y. Y.; Kim, D. S.; Saratale, G. D., Exploiting fruit byproducts for eco-friendly nanosynthesis: Citrus x clementina peel extract mediated fabrication of silver nanoparticles with high efficacy against microbial pathogens and rat glioma C6 cells. *Environ. Sci. Pollut. Res. Int.* **2018**, *25*, 10250-10263.
196. Ghosh, P. R.; Fawcett, D.; Sharma, S. B.; Poinern, G. E. J., Production of high-value nanoparticles via biogenic processes using aquacultural and horticultural food waste. *Materials* **2017**, *10*, 852.
197. Abboud, Y.; Saffaj, T.; Chagraoui, A.; El Bouari, A.; Brouzi, K.; Tanane, O.; Ihssane, B., Biosynthesis, characterization and antimicrobial activity of copper oxide nanoparticles (CONPs) produced using brown alga extract (*Bifurcaria bifurcata*). *Appl. Nanosci.* **2013**, *4*, 571-576.

198. Ibrahim, H. M. M., Green synthesis and characterization of silver nanoparticles using banana peel extract and their antimicrobial activity against representative microorganisms. *J. Radiat. Res. Appl. Sci.* **2019**, *8*, 265-275.
199. Kumar, K. M.; Mandal, B. K.; Kumar, K. S.; Reddy, P. S.; Sreedhar, B., Biobased green method to synthesise palladium and iron nanoparticles using Terminalia chebula aqueous extract. *Spectrochim. Acta A Mol. Biomol. Spectrosc.* **2013**, *102*, 128-133.
200. Rastogi, L.; Arunachalam, J., Green synthetic route for the size controlled synthesis of biocompatible gold nanoparticles using aqueous extract of garlic (*Allium Sativum*). *Adv. Mater. Lett.* **2013**, *4*, 548-555.
201. Devi, P. S.; Banerjee, S.; Chowdhury, S. R.; Kumar, G. S., Eggshell membrane: A natural biotemplate to synthesise fluorescent gold nanoparticles. *RSC Adv.* **2012**, *2*, 11578-11585.
202. Kumar, R.; Roopan, S. M.; Prabhakarn, A.; Khanna, V. G.; Chakroborty, S., Agricultural waste Annona squamosa peel extract: Biosynthesis of silver nanoparticles. *Spectrochim. Acta A Mol. Biomol. Spectrosc.* **2012**, *90*, 173-176.
203. Vivek, R.; Thangam, R.; Muthuchelian, K.; Gunasekaran, P.; Kaveri, K.; Kannan, S., Green biosynthesis of silver nanoparticles from Annona squamosa leaf extract and its in vitro cytotoxic effect on MCF-7 cells. *Process Biochem.* **2012**, *47*, 2405-2410.
204. Bastos-Arrieta, J.; Florido, A.; Perez-Rafols, C.; Serrano, N.; Fiol, N.; Poch, J.; Villaescusa, I., Green synthesis of Ag nanoparticles using grape stalk waste extract for the modification of screen-printed electrodes. *Nanomaterials* **2018**, *8*, 946.
205. Dubey, S. P.; Lahtinen, M.; Sillanpaa, M., Tansy fruit mediated greener synthesis of silver and gold nanoparticles. *Process Biochem.* **2010**, *45*, 1065-1071.
206. AboDalam, H.; Devra, V.; Ahmed, F. K.; Li, B.; Abd-Elsalam, K. A., Chapter 29 - Rice wastes for green production and sustainable nanomaterials: An overview. In *Agri-waste and microbes for production of sustainable nanomaterials*, Abd-Elsalam, K. A.; Periakaruppan, R.; Rajeshkumar, S., Eds. Elsevier: 2022; pp 707-728.
207. Fillaudeau, L.; Blanpain-Avet, P.; Daufin, G., Water, wastewater and waste management in brewing industries. *J. Clean. Prod.* **2006**, *14*, 463-471.
208. Thiel, P. G.; du Toit, P. J., The chemical composition of a brewery waste. *J. Inst. Brew.* **1965**, *71*, 509-514.
209. Moshtagh, B.; Hawboldt, K.; Zhang, B., Optimization of biosurfactant production by *Bacillus Subtilis* N3-1P using the brewery waste as the carbon source. *Environ. Technol.* **2019**, *40*, 3371-3380.
210. Barbosa-Pereira, L.; Pocheville, A.; Angulo, I.; Paseiro-Losada, P.; Cruz, J. M., Fractionation and purification of bioactive compounds obtained from a brewery waste stream. *Biomed. Res. Int.* **2013**, *2013*, 408491.
211. Stefanello, F. S.; Dos Santos, C. O.; Bochi, V. C.; Fruet, A. P. B.; Soquetta, M. B.; Dorr, A. C.; Nornberg, J. L., Analysis of polyphenols in brewer's spent grain and its comparison with corn silage and cereal brans commonly used for animal nutrition. *Food Chem.* **2018**, *239*, 385-401.
212. Brewing beer: The brewing process. <https://braeuamberg.at/en/brewing-process> (accessed 1 June 2020).
213. Fărcaș, A. C.; Socaci, S. A.; Mudura, E.; Dulf, F. V.; Vodnar, D. C.; Tofană, M.; Salanță, L. C., Exploitation of brewing industry wastes to produce functional ingredients. In *Brewing technology*, Kanauchi, M., Ed. IntechOpen: London, UK, 2017.
214. *Handbook of brewing*. 2nd ed.; CRC Press Taylor & Francis Group: Boca Raton, FL, USA, 2006.
215. Corbo, M. R.; Bevilacqua, A.; Petrucci, L.; Casanova, F. P.; Sinigaglia, M., Functional beverages: The emerging side of functional foods. *Compr. Rev. Food Sci. Food Saf.* **2014**, *13*, 1192-1206.

216. Hellborg, L.; Piskur, J., Yeast diversity in the brewing industry. In *Beer in health and disease prevention*, Preedy, V. R., Ed. Academic Press: London, UK, 2008.
217. Yantcheva, N. S.; Karashanova, D. B.; Georgieva, B. C.; Vasileva, I. N.; Stoyanova, A. S.; Denev, P. N.; Dinkova, R. H.; Ognyanov, M. H.; Slavov, A. M., Characterization and application of spent brewer's yeast for silver nanoparticles synthesis. *Bulg. Chem. Commun.* **2019**, *51*, 173-177.
218. Sharma, R. K.; Yadav, S.; Dutta, S.; Kale, H. B.; Warkad, I. R.; Zbořil, R.; Varma, R. S.; Gawande, M. B., Silver nanomaterials: Synthesis and (electro/photo) catalytic applications. *Chem. Soc. Rev.* **2021**, *50*, 11293-11380.
219. Xiong, W.; Dai, W.; Hu, X.; Yang, L.; Wang, T.; Qin, Y.; Luo, X.; Zou, J., Enhanced photocatalytic reduction of CO₂ into alcohols on Z-scheme Ag/Ag₃PO₄/CeO₂ driven by visible light. *Mater. Lett.* **2018**, *232*, 36-39.
220. Ge, J.; Long, J.; Sun, Z.; Feng, H.; Hu, J.; Koh, S. W.; Yu, Q.; Xiao, J.; Li, H., Vertical silver@silver chloride core-shell nanowire array for carbon dioxide electroreduction. *ACS Appl. Energy Mater.* **2019**, *2*, 6163-6169.
221. Kim, C.; Jeon, H. S.; Eom, T.; Jee, M. S.; Kim, H.; Friend, C. M.; Min, B. K.; Hwang, Y. J., Achieving selective and efficient electrocatalytic activity for CO₂ reduction using immobilized silver nanoparticles. *J. Am. Chem. Soc.* **2015**, *137*, 13844-50.
222. Alizadeh, T.; Nayeri, S., Graphite/Ag/AgCl nanocomposite as a new and highly efficient electrocatalyst for selective electrooxidation of oxalic acid and its assay in real samples. *Mater. Sci. Eng. C* **2019**, *100*, 826-836.
223. Khan, Z. U. H.; Khan, A.; Shah, A.; Wan, P.; Chen, Y.; Khan, G. M.; Khan, A. U.; Tahir, K.; Muhammad, N.; Khan, H. U., Enhanced photocatalytic and electrocatalytic applications of green synthesized silver nanoparticles. *J. Mol. Liq.* **2016**, *220*, 248-257.
224. Isse, A. A.; Gottardello, S.; Maccato, C.; Gennaro, A., Silver nanoparticles deposited on glassy carbon. Electrocatalytic activity for reduction of benzyl chloride. *Electrochem. Commun.* **2006**, *8*, 1707-1712.
225. Bansal, V.; Li, V.; O'Mullane, A. P.; Bhargava, S. K., Shape dependent electrocatalytic behaviour of silver nanoparticles. *CrystEngComm.* **2010**, *12*, 4280-4286.
226. Li, Z.; Fu, J.-Y.; Feng, Y.; Dong, C.-K.; Liu, H.; Du, X.-W., A silver catalyst activated by stacking faults for the hydrogen evolution reaction. *Nat. Catal.* **2019**, *2*, 1107-1114.
227. Zhan, F.; Wang, Q.; Li, Y.; Bo, X.; Wang, Q.; Gao, F.; Zhao, C., Low-temperature synthesis of cuboid silver tetrathiotungstate (Ag₂WS₄) as electrocatalyst for hydrogen evolution reaction. *Inorg. Chem.* **2018**, *57*, 5791-5800.
228. Wang, Z.; Xu, X.; Si, Z.; Liu, L.; Liu, Y.; He, Y.; Ran, R.; Weng, D., In situ synthesized MoS₂/Ag dots/Ag₃PO₄ Z-scheme photocatalysts with ultrahigh activity for oxygen evolution under visible light irradiation. *Appl. Surf. Sci.* **2018**, *450*, 441-450.
229. Si, H.-Y.; Mao, C.-J.; Zhou, J.-Y.; Rong, X.-F.; Deng, Q.-X.; Chen, S.-L.; Zhao, J.-J.; Sun, X.-G.; Shen, Y.-M.; Feng, W.-J.; Gao, P.; Zhang, J., Z-scheme Ag₃PO₄/graphdiyne/g-C₃N₄ composites: Enhanced photocatalytic O₂ generation benefiting from dual roles of graphdiyne. *Carbon* **2018**, *132*, 598-605.
230. Chen, X.; Yu, C.; Zhu, R.; Li, N.; Chen, J.; Li, S.; Xia, W.; Xu, S.; Wang, H.; Chen, X., Ag₃PO₄ deposited on CuBi₂O₄ to construct Z-scheme photocatalyst with excellent visible-light catalytic performance toward the degradation of diclofenac sodium. *Nanomaterials* **2019**, *9*, 959.
231. Liu, W.; Wang, M.; Xu, C.; Chen, S.; Fu, X., Ag₃PO₄/ZnO: An efficient visible-light-sensitized composite with its application in photocatalytic degradation of Rhodamine B. *Mater. Res. Bull.* **2013**, *48*, 106-113.

232. Liu, L.; Qi, Y.; Lu, J.; Lin, S.; An, W.; Liang, Y.; Cui, W., A stable $\text{Ag}_3\text{PO}_4@g\text{-C}_3\text{N}_4$ hybrid core@shell composite with enhanced visible light photocatalytic degradation. *Appl. Catal. B* **2016**, *183*, 133-141.
233. Tavker, N.; Gaur, U. K.; Sharma, M., Agro-waste extracted cellulose supported silver phosphate nanostructures as a green photocatalyst for improved photodegradation of RhB dye and industrial fertilizer effluents. *Nanoscale Adv.* **2020**, *2*, 2870-2884.
234. Katsumata, H.; Hayashia, T.; Taniguchia, M.; Suzukib, T.; Kaneco, S., AgI/Ag₃PO₄ hybrids with highly efficient visible-light driven photocatalytic activity. *Mater. Res. Bull.* **2015**, *63*, 116-122.
235. Liu, X.; Cai, L., Novel indirect Z-scheme photocatalyst of Ag nanoparticles and polymer polypyrrole co-modified BiOBr for photocatalytic decomposition of organic pollutants. *Appl. Surf. Sci.* **2018**, *445*, 242-254.
236. Qin, Y.; Li, F.; Tu, P.; Ma, Y.; Chen, W.; Shi, F.; Xiang, Q.; Shan, H.; Zhang, L.; Tao, P.; Song, C.; Shang, W.; Deng, T.; Zhu, H.; Wu, J., Ag₃PO₄ electrocatalyst for oxygen reduction reaction: enhancement from positive charge. *RSC Adv.* **2018**, *8*, 5382-5387.
237. Erikson, H.; Sarapuu, A.; Tammeveski, K., Oxygen reduction reaction on silver catalysts in alkaline media: A minireview. *ChemElectroChem.* **2019**, *6*, 73-86.
238. Pagliaro, M.; Della Pina, C.; Mauriello, F.; Ciriminna, R., Catalysis with silver: From complexes and nanoparticles to MORALs and single-atom catalysts. *Catalysts* **2020**, *10*, 1343.
239. Chouhan, N., Silver nanoparticles: Synthesis, characterization and applications. In *Silver nanoparticles- Fabrication, characterization and applications*, Maaz, K., Ed. IntechOpen: London, UK, 2018.
240. Dong, X.-Y.; Gao, Z.-W.; Yang, K.-F.; Zhang, W.-Q.; Xu, L.-W., Nanosilver as a new generation of silver catalysts in organic transformations for efficient synthesis of fine chemicals. *Catal. Sci. Technol.* **2015**, *5*, 2554-2574.
241. Zhang, K.; Suh, J. M.; Choi, J.-W.; Jang, H. W.; Shokouhimehr, M.; Varma, R. S., Recent advances in the nanocatalyst-assisted NaBH₄ reduction of nitroaromatics in water. *ACS Omega* **2019**, *4*, 483-495.
242. Mabey, T.; Cristaldi, D. A.; Oyston, P.; Lymer, K. P.; Stulz, E.; Wilks, S.; Keevil, C. W.; Zhang, X., Bacteria and nanosilver: The quest for optimal production. *Crit. Rev. Biotechnol.* **2019**, *39*, 272-287.
243. Fabbri, E.; Schmidt, T. J., Oxygen evolution reaction—The enigma in water electrolysis. *ACS Catal.* **2018**, *8*, 9765-9774.
244. Fabbri, E.; Haberer, A.; Waltar, K.; Kötz, R.; Schmidt, T. J., Developments and perspectives of oxide-based catalysts for the oxygen evolution reaction. *Catal. Sci. Technol.* **2014**, *4*, 3800-3821.
245. Doyle, R. L.; Lyons, M. E. G., The oxygen evolution reaction: Mechanistic concepts and catalyst design. In *Photoelectrochemical solar fuel production*, Giménez, S.; Bisquert, J., Eds. Springer, Cham.: 2016; pp 41-104.
246. Grätzel, M., Mesoscopic solar cells for electricity and hydrogen production from sunlight. *Chem. Lett.* **2005**, *34*, 8-13.
247. Turner, J. A., Sustainable hydrogen production. *Science* **2004**, *305*, 972-974.
248. McKone, J. R.; Lewis, N. S.; Gray, H. B., Will solar-driven water-splitting devices see the light of day? *Chem. Mater.* **2013**, *26*, 407-414.
249. Song, J.; Wei, C.; Huang, Z. F.; Liu, C.; Zeng, L.; Wang, X.; Xu, Z. J., A review on fundamentals for designing oxygen evolution electrocatalysts. *Chem. Soc. Rev.* **2020**, *49*, 2196-2214.
250. Greeley, J.; Markovic, N. M., The road from animal electricity to green energy: combining experiment and theory in electrocatalysis. *Energy Environ. Sci.* **2012**, *5*, 9246-9256.

251. Valdes, A.; Brillet, J.; Gratzel, M.; Gudmundsdottir, H.; Hansen, H. A.; Jonsson, H.; Klupfel, P.; Kroes, G. J.; Le Formal, F.; Man, I. C.; Martins, R. S.; Norskov, J. K.; Rossmeisl, J.; Sivula, K.; Vojvodic, A.; Zach, M., Solar hydrogen production with semiconductor metal oxides: New directions in experiment and theory. *Phys. Chem. Chem. Phys.* **2012**, *14*, 49-70.
252. Markovic, N. M.; Ross Jr, P. N., Surface science studies of model fuel cell electrocatalysts. *Surf. Sci. Rep.* **2002**, *45*, 117-229.
253. Conway, B. E., Electrochemical oxide film formation at noble metals as a surface-chemical process. *Prog. Surf. Sci.* **1995**, *49*, 331-452.
254. Wang, Y.; Zhang, J., Structural engineering of transition metal-based nanostructured electrocatalysts for efficient water splitting. *Front. Chem. Sci. Eng.* **2018**, *12*, 838-854.
255. Yu, M.; Budiayanto, E.; Tuysuz, H., Principles of water electrolysis and recent progress in cobalt-, nickel-, and iron-based oxides for the oxygen evolution reaction. *Angew. Chem. Int. Ed. Engl.* **2022**, *61*, e202103824.
256. Galán-Mascarós, J. R., Water oxidation at electrodes modified with earth-abundant transition-metal catalysts. *ChemElectroChem.* **2015**, *2*, 37-50.
257. Liu, J. J.; Fu, X. L.; Chen, S. F.; Zhu, Y. F., Electronic structure and optical properties of Ag_3PO_4 photocatalyst calculated by hybrid density functional method. *Appl. Phys. Lett.* **2011**, *99*, 191903.
258. Martin, D. J.; Liu, G.; Moniz, S. J.; Bi, Y.; Beale, A. M.; Ye, J.; Tang, J., Efficient visible driven photocatalyst, silver phosphate: Performance, understanding and perspective. *Chem. Soc. Rev.* **2015**, *44*, 7808-7828.
259. Hasiija, V.; Raizada, P.; Hosseini-Bandegharai, A.; Thakur, V. K.; Van Le, Q.; Nguyen, V. H.; Singh, P., A strategy to develop efficient Ag_3PO_4 -based photocatalytic materials toward water splitting: Perspectives and challenges. *ChemCatChem.* **2021**, *13*, 2965-2987.
260. Tao, R.; Yang, S.; Shao, C.; Li, X.; Li, X.; Liu, S.; Zhang, J.; Liu, Y., Reusable and flexible $\text{g-C}_3\text{N}_4/\text{Ag}_3\text{PO}_4$ /polyacrylonitrile heterojunction nanofibers for photocatalytic dye degradation and oxygen evolution. *ACS Appl. Nano Mater.* **2019**, *2*, 3081-3090.
261. Hou, Y.; Zuo, F.; Ma, Q.; Wang, C.; Bartels, L.; Feng, P., Ag_3PO_4 oxygen evolution photocatalyst employing synergistic action of Ag/AgBr nanoparticles and graphene sheets. *J. Phys. Chem. C* **2012**, *116*, 20132-20139.
262. Song, C.; Zhang, J., Electrocatalytic oxygen reduction reaction. In *PEM fuel cell electrocatalysts and catalyst layers: Fundamentals and applications*, Zhang, J., Ed. Springer: London, 2008; pp 89-134.
263. Khotseng, L., Oxygen reduction reaction. In *Electrocatalysts for fuel cells and hydrogen evolution - Theory to design*, Ray, A.; Mukhopadhyay, I.; Pati, R. K., Eds. IntechOpen: London, UK, 2018.
264. Maricle, D. L.; Hodgson, W. G., Reduction of oxygen to superoxide anion in aprotic solvents. *Anal. Chem.* **1965**, *37*, 1562-1565.
265. Dincer, I.; Siddiqui, O., Fundamentals. In *Ammonia fuel cells*, Dincer, I.; Siddiqui, O., Eds. Elsevier: 2020; pp 13-32.
266. Ma, R.; Lin, G.; Zhou, Y.; Liu, Q.; Zhang, T.; Shan, G.; Yang, M.; Wang, J., A review of oxygen reduction mechanisms for metal-free carbon-based electrocatalysts. *npj Comput. Mater.* **2019**, *5*, 78.
267. Wang, B., Recent development of non-platinum catalysts for oxygen reduction reaction. *J. Power Sources* **2005**, *152*, 1-15.
268. Ooka, H.; Huang, J.; Exner, K. S., The Sabatier principle in electrocatalysis: Basics, limitations, and extensions. *Front. Energy Res.* **2021**, *9*, 654460.
269. Senarathna, K. G. C.; Randiligama, H. M. S. P.; Rajapakse, R. M. G., Preparation, characterization and oxygen reduction catalytic activities of nanocomposites of Co(ii)/montmorillonite

- containing polypyrrole, polyaniline or poly(ethylenedioxythiophene). *RSC Adv.* **2016**, *6*, 112853-112863.
270. Wu, J.; Yang, H., Platinum-based oxygen reduction electrocatalysts. *Acc. Chem. Res.* **2013**, *46*, 1848–1857.
271. Mitsushima, S.; Kawahara, S.; Ota, K.-i.; Kamiya, N., Consumption rate of Pt under potential cycling. *J. Electrochem. Soc.* **2007**, *154*, B153-B158.
272. Qaseem, A.; Chen, F.; Wu, X.; Johnston, R. L., Pt-free silver nanoalloy electrocatalysts for oxygen reduction reaction in alkaline media. *Catal. Sci. Technol.* **2016**, *6*, 3317-3340.
273. Guo, R.; Lai, X.; Huang, J.; Du, X.; Yan, Y.; Sun, Y.; Zou, G.; Xiong, J., Phosphate-based electrocatalysts for water splitting: Recent progress. *ChemElectroChem.* **2018**, *5*, 3822-3834.
274. Choi, S.; Park, Y.; Choi, J.; Lee, C.; Cho, H.-S.; Kim, C.-H.; Koo, J.; Lee, H. M., Structural effectiveness of AgCl-decorated Ag nanowires enhancing oxygen reduction. *ACS Sustain. Chem. Eng.* **2021**, *9*, 7519-7528.
275. Calzaferri, G.; Brühwiler, D.; Glaus, S.; Schürch, D.; Currao, A.; Leiggenger, C., Quantum-sized silver, silver chloride and silver sulfide clusters. *J. Imaging Sci. Technol.* **2001**, *45*, 331-339.
276. Antony, J.; Sure, R.; Grimme, S., Using dispersion-corrected density functional theory to understand supramolecular binding thermodynamics. *Chem. Comm.* **2015**, *51*, 1764-1774.
277. Computational chemistry. https://en.wikipedia.org/w/index.php?title=Computational_chemistry&oldid=1092990660 (accessed 1 July 2022).
278. Foster, M. E.; Sohlberg, K., Empirically corrected DFT and semi-empirical methods for non-bonding interactions. *Phys. Chem. Chem. Phys.* **2010**, *12*, 307-322.
279. Young, D., *Computational chemistry: A practical guide for applying techniques to real world problems*. Wiley: 2004.
280. Morgante, P.; Peverati, R., The devil in the details: A tutorial review on some undervalued aspects of density functional theory calculations. *Int. J. Quantum Chem.* **2020**, *120*, e26332.
281. Tirado-Rives, J.; Jorgensen, W. L., Performance of B3LYP density functional methods for a large set of organic molecules. *J. Chem. Theory Comput.* **2008**, *4*, 297-306.
282. Izutsu, K., *Electrochemistry in nonaqueous solutions*. John Wiley & Sons, Inc.: Germany, 2002.
283. Kim, T.; Choi, W.; Shin, H.-C.; Choi, J.-Y.; Kim, J. M.; Park, M.-S.; Yoon, W.-S., Applications of voltammetry in lithium ion battery research. *J. Electrochem. Sci. Technol.* **2020**, *11*, 14-25.
284. Lee, J. *Electrochemical sensing of oxygen gas in ionic liquids on screen printed electrodes*. Curtin University, 2014.
285. *Electrochemical methods*. 2nd ed.; John Wiley & Sons, Inc.: USA, 2000.
286. Banks, C. E.; Compton, R. G., *Understanding voltammetry*. 3rd ed.; World Scientific: London, UK, 2018.
287. Pulse voltammetric techniques. https://www.basinc.com/manuals/EC_epsilon/Techniques/Pulse/pulse (accessed 10 February 2022).
288. Molina, Á.; Laborda, E.; Rogers, E. I.; Martínez-Ortiz, F.; Serna, C.; Limon-Petersen, J. G.; Rees, N. V.; Compton, R. G., Theoretical and experimental study of differential pulse voltammetry at spherical electrodes: Measuring diffusion coefficients and formal potentials. *J. Electroanal. Chem.* **2009**, *634*, 73-81.
289. *Handbook of electrochemistry*. Elsevier: 2007.

290. Rajeshwar, K., Photoelectrochemistry, fundamentals and applications. In *Encyclopedia of Applied Electrochemistry*, Kreysa, G.; Ota, K.-i.; Savinell, R. F., Eds. Springer New York: New York, NY, 2014; pp 1550-1556.
291. Strandwitz, N. C.; Good, J.; Lewis, N. S., Photoelectrochemistry of semiconductors. In *Electrochemistry encyclopedia*, Nagy, Z., Ed. The Electrochemical Society, Inc.: 2011.
292. *Rotating electrode methods and oxygen reduction electrocatalysts*. Elsevier: 2014; p 322.
293. Koutecký-Levich plot. The inverse measured current is plotted versus the inverse square root of rotation rate. Plot, K.-L., Ed. Wikipedia: 2017.
294. Atkins, P.; de Paula, J.; Keeler, J., *Atkin's physical chemistry*. 11th ed.; Oxford University Press: Oxford, UK, 2018.
295. Reusch, W. Nuclear magnetic resonance spectroscopy 2020. Spectroscopy. <https://chem.libretexts.org/@go/page/1240> (accessed 10 November 2021).
296. Aryal, S. Nuclear magnetic resonance (NMR) spectroscopy. <https://microbenotes.com/nuclear-magnetic-resonance-nmr-spectroscopy/> (accessed 21 October 2021).
297. *Magnetic resonance technology- hardware and system component design*. Royal Society of Chemistry: Cambridge, UK, 2016.
298. *Spectroscopic methods for nanomaterials characterization*. Elsevier: 2017; Vol. 2.
299. Harvey, D., *Modern analytical chemistry*. 2000.
300. UV/vis/IR spectroscopy analysis of nanoparticles 2012. (accessed 10 November 2021).
301. Evanoff, D. D., Jr.; Chumanov, G., Synthesis and optical properties of silver nanoparticles and arrays. *ChemPhyschem*. **2005**, *6*, 1221-1231.
302. Gable, K. FTIR instrumentation and theory. sites.science.oregonstate.edu/chemistry/courses/ch361-464/ch362/irinstrs.htm (accessed 15 November 2021).
303. *Fundamentals of Fourier transform infrared spectroscopy*. 2nd ed.; CRC Press: Florida, USA, 2011; p 198.
304. Gaillard, F.; Linossier, I.; Sweeney, M.; Reffner, J. A.; Romand, M., Grazing-angle micro-FTIR spectroscopy (GAM-FTIR): Applications to adhesion studies. *Surf. Interface Anal.* **1999**, *27*, 865-870.
305. *Fourier transform infrared spectrometry*. 2nd ed.; John Wiley & Sons, Inc.: New Jersey, USA, 2007.
306. Henkie, J. Infrared reflection-absorption spectroscopy of iron pentacarbonyl on gold, enhanced with xenon-induced peak shifts for surface sensitivity. The University of Guelph, Ontario, Canada, 2016.
307. Buffeteau, T.; Desbat, B.; Turlet, J. M., Polarization modulation FT-IR spectroscopy of surfaces and ultra-thin films: experimental procedure and quantitative analysis. *Appl. Spectrosc.* **1991**, *45*, 380-389.
308. Grundmeier, G.; von Keudell, A.; de los Arcos, T., Fundamentals and applications of reflection FTIR spectroscopy for the analysis of plasma processes at materials interfaces. *Plasma Process. Polym.* **2015**, *12*, 926-940.
309. Light scattering. In *Current protocols in protein science*, Coligan, J. E.; Dunn, B.; Ploegh, H. L.; Speicher, D. W.; Wingfield, P. T., Eds. John Wiley & Sons, Inc.: New York, USA, 1998.
310. Kholodenko, A. L.; Douglas, J. F., Generalized Stokes-Einstein equation for spherical particle suspensions. *Phys. Rev. E Stat. Phys. Plasmas Fluids Relat. Interdiscip. Topics* **1995**, *51*, 1081-1090.
311. *Springer handbook of nanotechnology*. Springer: Germany, 2004.

312. Ashby, M. F.; Ferreira, P. J.; Schodek, D. L., *Nanomaterials, nanotechnologies and design- An introduction for engineers and architects*. Elsevier: Oxford, UK, 2009.
313. Meyer, V. R., *Practical high-performance liquid chromatography*. 5th ed.; John Wiley & Sons, Inc.: UK, 2010.
314. *Liquid chromatography fundamentals and instrumentation*. Elsevier: 2017; p 417-429.
315. HPLC principle and instrumentation. https://noteshippo.com/hplc-high-performance-liquid-chromatography-principle-types-instrumentation-applications/#Instrumentation_of_HPLC (accessed 10 January 2022).
316. Klug, H. P.; Alexander, L. E.; Wiley, J.; Sons, *X-ray diffraction procedures: For polycrystalline and amorphous materials*. 2nd ed.; Wiley: 1974.
317. Waseda, Y.; Matsubara, E.; Shinoda, K., *X-ray diffraction crystallography: Introduction, examples and solved problems*. Springer: NY, USA, 2011; p 322.
318. Bragg law. In *Encyclopedia Britannica*, Encyclopaedia, T. E. o., Ed. 2022.
319. Epp, J., 4 - X-ray diffraction (XRD) techniques for materials characterization. In *Materials Characterization Using Nondestructive Evaluation (NDE) Methods*, Hübschen, G.; Altpeter, I.; Tschuncky, R.; Herrmann, H.-G., Eds. Woodhead Publishing: 2016; pp 81-124.
320. Langford, J. I.; Wilson, A. J. C., Scherrer after sixty years: A survey and some new results in the determination of crystallite size. *J. Appl. Crystallogr.* **1978**, *11*, 102-113.
321. Russ, J. C.; Frs, M. A.; Kiessling, R.; Charles, J., *Fundamentals of energy dispersive X-ray analysis: Butterworths monographs in materials*. Elsevier Science: 2013.
322. DIY X-ray fluorescence spectrometry. <https://physicsopenlab.org/2016/02/24/diy-xrf-spectrometry/> (accessed 9 November 2021).
323. Heyman, B. Science in translation part I: What is portable X-ray fluorescence spectroscopy? <https://shumla.org/scienceintranslationpart1/> (accessed 7 July 2022).
324. Sauer, M.; Hofkens, J.; Enderlein, J., Basic principles of fluorescence spectroscopy. In *Handbook of fluorescence spectroscopy and imaging*, Sauer, M.; Hofkens, J.; Enderlein, J., Eds. 2011; pp 1-30.
325. Suryanarayana, C., Microstructure: An introduction. In *Aerospace materials and material technologies*, Prasad, N.; Wanhill, R., Eds. Springer, Singapore: 2017; pp 105-123.
326. *Scanning microscopy for nanotechnology: Techniques and applications*. Springer: New York, NY, USA, 2007; p XIV, 522.
327. Chauhan, A. Deformation and damage mechanisms of ODS steels under high-temperature cyclic loading. Karlsruhe Institut für Technologie (KIT), Germany, 2018.
328. Johnson, R., Energy-dispersive X-ray microanalysis. Scientific, T., Ed. Thermo Fisher Scientific Inc.
329. Friel, J. J.; Lyman, C. E., X-ray mapping in electron-beam instruments. *Microsc. Microanal.* **2006**, *12*, 2-25.
330. Fagerlund, G., Determination of specific surface by the BET method. *Mater. Constr.* **1973**, *6*, 239-245.
331. Brunauer, S.; Deming, L. S.; Deming, W. E.; Teller, E., On a theory of the van der Waals adsorption of gases. *J. Am. Chem. Soc.* **1940**, *62*, 1723-1732.
332. BET Specific Surface Area. <https://www.particletechlabs.com/analytical-testing/gas-adsorption-and-porosimetry/bet-specific-surface-area> (accessed 18 November 2021).
333. Hwang, N.; Barron, A. R., BET surface area analysis of nanoparticles. OpenStax: 2011. <http://cnx.org/content/m38278/1.1>.

334. Donohue, M.; Aranovich, G. L., Classification of Gibbs adsorption isotherms. *Adv. Colloid Interface Sci.* **1998**, *76*, 137-152.
335. ben Mosbah, M.; Mechi, L.; Khiari, R.; Moussaoui, Y., Current state of porous carbon for wastewater treatment. *Processes* **2020**, *8*, 1651.
336. Akash, M. S. H.; Rehman, K., *Essentials of pharmaceutical analysis*. Springer Nature: Singapore, 2020.
337. Coate, A. W.; Redfern, J. P., Thermogravimetric analysis. *Analyst* **1963**, *88*, 906-924.
338. Kwon, J.-H.; Shahbaz, H.; Ahn, J.-J., Advanced electron paramagnetic resonance spectroscopy for the identification of irradiated food. *Am. Lab.* **2014**, *46*, 1-4.
339. Ahmad, R.; Kuppusamy, P., Theory, instrumentation, and applications of electron paramagnetic resonance oximetry. *Chem. Rev.* **2010**, *110*, 3212-3236.
340. *Biomolecular EPR spectroscopy*. CRC Press: Florida, USA, 2009.
341. *Electron paramagnetic resonance- Elementary theory and practical applications*. John Wiley & Sons, Inc.: New Jersey, USA, 2007.
342. Sannicolò, F.; Mussini, P. R.; Benincori, T.; Martinazzo, R.; Arnaboldi, S.; Appoloni, G.; Panigati, M.; Quartapelle Procopio, E.; Marino, V.; Cirilli, R.; Casolo, S.; Kutner, W.; Noworyta, K.; Pietrzyk-Le, A.; Iskierko, Z.; Bartold, K., Inherently chiral spider-like oligothiophenes. *Chem. Eur. J.* **2016**, *22*, 10685-10685.
343. Sannicolo, F.; Rizzo, S.; Benincori, T.; Kutner, W.; Noworyta, K.; Sobczak, J. W.; Bonometti, V.; Falciola, L.; Mussini, P. R.; Pierini, M., An effective multipurpose building block for 3D electropolymerisation: 2,2'-Bis(2,2'-bithiophene-5-yl)-3,3'-bithianaphthene. *Electrochim. Acta* **2010**, *55*, 8352-8364.
344. M.J. Frisch, G. W. T., H.B. Schlegel, G.E. Scuseria, M.A. Robb, J.R. Cheeseman, G. Scalmani, V. Barone, G. a. Petersson, H. Nakatsuji, X. Li, M. Caricato, A. V. Marenich, J. Bloino, B.G. Janesko, R. Gomperts, B. Mennucci, H.P. Hratchian, J. V. Ortiz, A.F. Izmaylov, J.L. Sonnenberg, Williams, F. Ding, F. Lipparini, F. Egidi, J. Goings, B. Peng, A. Petrone, T. Henderson, D. Ranasinghe, V.G. Zakrzewski, J. Gao, N. Rega, G. Zheng, W. Liang, M. Hada, M. Ehara, K. Toyota, R. Fukuda, J. Hasegawa, M. Ishida, T. Nakajima, Y. Honda, O. Kitao, H. Nakai, T. Vreven, K. Throssell, J. a. Montgomery Jr., J.E. Peralta, F. Ogliaro, M.J. Bearpark, J.J. Heyd, E.N. Brothers, K.N. Kudin, V.N. Staroverov, T. a. Keith, R. Kobayashi, J. Normand, K. Raghavachari, a. P. Rendell, J.C. Burant, S.S. Iyengar, J. Tomasi, M. Cossi, J.M. Millam, M. Klene, C. Adamo, R. Cammi, J.W. Ochterski, R.L. Martin, K. Morokuma, O. Farkas, J.B. Foresman, D.J. Fox *Gaussian 09*, Inc.: Wallingford CT, USA, 2009.
345. Hanwell, M. D.; Curtis, D. E.; Lonie, D. C.; Vandermeersch, T.; Zurek, E.; Hutchison, G. R., Avogadro: An advanced semantic chemical editor, visualization, and analysis platform. *J. Cheminformatics* **2012**, *4*, 17.
346. *Avogadro: An open-source molecular builder and visualization tool*, 1.2.0.
347. Dennington, R.; Keith, T. A.; Millam, J. M. *GaussView, Version 5*, 2009.
348. BIOVIA, D. S. *Discovery Studio Modeling Environment*, Dassault Systèmes: San Diego, CA, USA, 2020.
349. Frisch, M. J.; Trucks, G. W.; Schlegel, H. B.; Scuseria, G. E.; Robb, M. A.; Cheeseman, J. R.; Scalmani, G.; Barone, V.; Petersson, G. A.; Nakatsuji, H.; Li, X.; Caricato, M.; Marenich, A. V.; Bloino, J.; Janesko, B. G.; Gomperts, R.; Mennucci, B.; Hratchian, H. P.; Ortiz, J. V.; Izmaylov, A. F.; Sonnenberg, J. L.; Williams; Ding, F.; Lipparini, F.; Egidi, F.; Goings, J.; Peng, B.; Petrone, A.; Henderson, T.; Ranasinghe, D.; Zakrzewski, V. G.; Gao, J.; Rega, N.; Zheng, G.; Liang, W.; Hada, M.; Ehara, M.; Toyota, K.; Fukuda, R.; Hasegawa, J.; Ishida, M.; Nakajima, T.; Honda, Y.; Kitao, O.; Nakai, H.; Vreven, T.; Throssell, K.; Montgomery Jr., J. A.; Peralta, J. E.; Ogliaro, F.; Bearpark, M. J.; Heyd, J. J.; Brothers, E. N.; Kudin, K. N.; Staroverov, V. N.; Keith, T. A.; Kobayashi, R.; Normand, J.;

Raghavachari, K.; Rendell, A. P.; Burant, J. C.; Iyengar, S. S.; Tomasi, J.; Cossi, M.; Millam, J. M.; Klene, M.; Adamo, C.; Cammi, R.; Ochterski, J. W.; Martin, R. L.; Morokuma, K.; Farkas, O.; Foresman, J. B.; Fox, D. J. *Gaussian 16 Rev. C.01*, Wallingford CT, USA, 2016.

350. Bruice, P. Y., *Organic chemistry*. 5 ed.; Pearson Education: 2006; p 1319.

351. Breneman, C. M.; Wiberg, K. B., Determining atom-centered monopoles from molecular electrostatic potentials. The need for high sampling density in formamide conformational analysis. *J. Comput. Chem.* **1990**, *11*, 361-373.

352. Brooks, B. R.; Bruccoleri, R. E.; Olafson, B. D.; States, D. J.; Swaminathan, S.; Karplus, M., CHARMM: A program for macromolecular energy, minimization, and dynamics calculations. *J. Comput. Chem.* **1983**, *4*, 187-217.

353. Gajda, M.; Rybakiewicz, R.; Cieplak, M.; Żółek, T.; Maciejewska, D.; Gilant, E.; Rudzki, P. J.; Grab, K.; Kutner, A.; Borowicz, P.; Kutner, W.; Noworyta, K. R., Low-oxidation-potential thiophene-carbazole monomers for electro-oxidative molecular imprinting: Selective chemosensing of aripiprazole. *Biosens. Bioelectron.* **2020**, *169*, 112589.

354. Berendsen, H. J. C.; Postma, J. P. M.; van Gunsteren, W. F.; DiNola, A.; Haak, J. R., Molecular dynamics with coupling to an external bath. *J. Chem. Phys.* **1984**, *81*, 3684-3690.

355. Svensson, M.; Humbel, S.; Froese, R. D. J.; Matsubara, T.; Sieber, S.; Morokuma, K., ONIOM: A multilayered integrated MO + MM method for geometry optimizations and single point energy predictions. A test for Diels–Alder reactions and Pt(P(*t*-Bu)₃)₂ + H₂ oxidative addition. *J. Chem. Phys.* **1996**, *100*, 19357-19363.

356. Dapprich, S.; Komáromi, I.; Byun, K. S.; Morokuma, K.; Frisch, M. J., A new ONIOM implementation in Gaussian98. Part I. The calculation of energies, gradients, vibrational frequencies and electric field derivatives. *J. Mol. Struct.* **1999**, *461-462*, 1-21.

357. Becke, A. D., Density-functional thermochemistry. III. The role of exact exchange. *J. Chem. Phys.* **1993**, *98*, 5648-5652.

358. Lee, C.; Yang, W.; Parr, R. G., Development of the Colle-Salvetti correlation-energy formula into a functional of the electron density. *Phys. Rev. B* **1988**, *37*, 785-789.

359. Parr, R. G. In *Density functional theory of atoms and molecules*, Horizons of Quantum Chemistry, Dordrecht, 1980//; Fukui, K.; Pullman, B., Eds. Springer Netherlands: Dordrecht, 1980; pp 5-15.

360. Cornell, W. D.; Cieplak, P.; Bayly, C. I.; Gould, I. R.; Merz, K. M.; Ferguson, D. M.; Spellmeyer, D. C.; Fox, T.; Caldwell, J. W.; Kollman, P. A., A second generation force field for the simulation of proteins, nucleic acids, and organic molecules. *J. Am. Chem. Soc.* **1995**, *117*, 5179-5197.

361. Vreven, T.; Morokuma, K., Investigation of the S₀→S₁ excitation in bacteriorhodopsin with the ONIOM(MO:MM) hybrid method. *Theor. Chem. Acc.* **2003**, *109*, 125-132.

362. Gökcan, H.; Kratz, E.; Darden, T. A.; Piquemal, J.-P.; Cisneros, G. A., QM/MM simulations with the Gaussian electrostatic model: A density-based polarizable potential. *J. Phys. Chem. Lett.* **2018**, *9*, 3062-3067.

363. Derjaguin, B. V.; Muller, V. M.; Toporov, Y. P., Effect of contact deformations on the adhesion of particles. *J. Colloid Interface Sci.* **1975**, *53*, 314-326.

364. Canterbury, U. o., Determination of chloride ion concentration by titration (Volhard's method). College of Science: Christchurch, New Zealand.

365. Standardization, I. O. f., ISO 1871:2009. Food and feed products — General guidelines for the determination of nitrogen by the Kjeldahl method. 2009.

366. Grubestic, R. J.; Vukovic, J.; Kremer, D.; Vladimir-Knezevic, S., Spectrophotometric method for polyphenols analysis: Prevalidation and application on *Plantago L.* species. *J. Pharm. Biomed. Anal.* **2005**, *39*, 837-842.

367. Hewitt, B. R., Spectrophotometric determination of total carbohydrate. *Nature* **1958**, *182*, 246-247.
368. Jurkova, M.; Olsovska, J.; Cejka, P., Determination of sugars and saccharides in beer. *Kvasny Prum.* **2018**, *64*, 58-64.
369. Jacob, F., *Wort, beer and beer-based beverages, the mitteleuropäische brautechnische analysenkommision*. MEBAK: Germany, 2013; p 603.
370. Bisutti, I.; Hilke, I.; Raessler, M., Determination of total organic carbon-an overview of current methods. *TrAC - Trends Anal. Chem.* **2004**, *23*, 716-726.
371. Pillai, K. C.; Thangamuthu, R.; Ilangovan, G., Behavior of cathodically pretreated platinum on Fe(CN)₆³⁻ electroreduction in KNO₃: Dependence on pretreatment. *Electroanalysis* **1995**, *7*, 1182-1188.
372. Lounasvuori, M. M.; Rosillo-Lopez, M.; Salzmann, C. G.; Caruana, D. J.; Holt, K. B., Electrochemical characterisation of graphene nanoflakes with functionalised edges. *Faraday Discuss.* **2014**, *172*, 293-310.
373. Degen, T.; Sadki, M.; Bron, E.; König, U.; Nénert, G., The HighScore suite. *Powder Diffr.* **2014**, *29*, S13-S18.
374. Hubbard, C. R., RIR- measurement and use in quantitative XRD. *Powder Diffr.* **1988**, *3*, 74-77.
375. Standardization, I. O. f., ISO/ASTM 51607:2013 Practice for use of the alanine-EPR dosimetry system. 2013.
376. Tanaka, K.; Shichiri, T.; Wang, S.; Yamabe, T., A study of the electropolymerization of thiophene. *Synth. Met.* **1988**, *24*, 203-215.
377. Roncali, J., Conjugated poly(thiophenes): Synthesis, functionalization, and applications. *Chem. Rev.* **1992**, *92*, 711-738.
378. Bain, A. D., Chemical exchange in NMR. *Prog. Nucl. Magn. Reson. Spectrosc.* **2003**, *43*, 63-103.
379. IR spectrum table & chart. <https://www.sigmaaldrich.com/IN/en/technical-documents/technical-article/analytical-chemistry/photometry-and-reflectometry/ir-spectrum-table> (accessed 10 January 2022).
380. O'Connor, B.; Chan, E. P.; Chan, C.; Conrad, B. R.; Richter, L. J.; Kline, R. J.; Heeney, M.; McCulloch, I.; Soles, C. L.; DeLongchamp, D. M., Correlations between mechanical and electrical properties of polythiophenes. *ACS Nano* **2010**, *4*, 7538-7544.
381. Wang, X.-S.; Feng, X.-Q., Effects of thickness on mechanical properties of conducting polythiophene film. *J. Mater. Sci. Lett.* **2002**, *21*, 715-717.
382. *Organic electrochemistry: Revised and expanded*. 5th ed.; CRC Press: Boca Raton, FL, USA, 2015.
383. Malkowsky, I. M.; Griesbach, U.; Pütter, H.; Waldvogel, S. R., Unexpected highly chemoselective anodic ortho-coupling reaction of 2,4-dimethylphenol on boron-doped diamond electrodes. *Eur. J. Org. Chem.* **2006**, *2006*, 4569-4572.
384. Quell, T.; Hecken, N.; Dyballa, K. M.; Franke, R.; Waldvogel, S. R., Scalable and selective preparation of 3,3',5,5'-tetramethyl-2,2'-biphenol. *Org. Process Res. Dev.* **2017**, *21*, 79-84.
385. Georget, D. M. R.; Belton, P. S., Effects of temperature and water content on the secondary structure of wheat gluten studied by FTIR spectroscopy. *Biomacromolecules* **2006**, *7*, 469-475.
386. Farhat, I. A.; Orset, S.; Moreau, P.; Blanshard, J. M. V., FTIR study of hydration phenomena in protein-sugar systems. *J. Colloid Interface Sci.* **1998**, *207*, 200-208.

387. Zhabankov, R. G.; Firsov, S. P.; Buslov, D. K.; Nikonenko, N. A.; Marchewka, M. K.; Ratajczak, H., Structural physico-chemistry of cellulose macromolecules. Vibrational spectra and structure of cellulose. *J. Mol. Struct.* **2002**, *614*, 117-125.
388. Duarte, I. F.; Barros, A.; Almeida, C.; Spraul, M.; Gil, A. M., Multivariate analysis of NMR and FTIR data as a potential tool for the quality control of beer. *J. Agric. Food Chem.* **2004**, *52*, 1031-1038.
389. Talari, A. C. S.; Martinez, M. A. G.; Movasaghi, Z.; Rehman, S.; Rehman, I. U., Advances in Fourier transform infrared (FTIR) spectroscopy of biological tissues. *Appl. Spectrosc. Rev.* **2016**, *52*, 456-506.
390. Zhou, C.; Jiang, W.; Via, B. K.; Fasina, O.; Han, G., Prediction of mixed hardwood lignin and carbohydrate content using ATR-FTIR and FT-NIR. *Carbohydr. Polym.* **2015**, *121*, 336-341.
391. Edelmann, A.; Lendl, B., Toward the optical tongue: Flow-through sensing of tannin-protein interactions based on FTIR spectroscopy. *J. Am. Chem. Soc.* **2002**, *124*, 14741-14747.
392. Ma, J.; Niu, X.; Wang, J.; Wu, J., Facile synthesis of Ag₃PO₄ with the assistance of N, N-dimethylformamide and urea for high performance photocatalysis. *Catal. Commun.* **2016**, *77*, 55-59.
393. Link, S.; El-Sayed, M. A., Optical properties and ultrafast dynamics of metallic nanocrystals. *Annu. Rev. Phys. Chem.* **2003**, *54*, 331-366.
394. Natale, L. C.; Alania, Y.; Rodrigues, M. C.; Simões, A.; de Souza, D. N.; de Lima, E.; Arana-Chavez, V. E.; Hwer, T. L. R.; Hiers, R.; Esteban-Florez, F. L.; Brito, G. E. S.; Khajotia, S.; Braga, R. R., Synthesis and characterization of silver phosphate/calcium phosphate mixed particles capable of silver nanoparticle formation by photoreduction. *Mater. Sci. Eng. C* **2017**, *76*, 464-471.
395. Padmanabhan, S. K.; Pal, S.; Licciulli, A., Diatomite/silver phosphate composite for efficient degradation of organic dyes under solar radiation. *Bull. Mater. Sci.* **2020**, *43*.
396. Saud, P. S.; Pant, B.; Twari, A. P.; Ghouri, Z. K.; Park, M.; Kim, H. Y., Effective photocatalytic efficacy of hydrothermally synthesized silver phosphate decorated titanium dioxide nanocomposite fibers. *J. Colloid Interface Sci.* **2016**, *465*, 225-232.
397. Karg, E.; Ferron, G.; Schumann, G.; Schmid, O. In *Specific BET surface area measurement of low-mass-samples*, 12th ETH Conference on Combustion Generated Nanoparticles, Zurich, Switzerland, Zurich, Switzerland, 2008.
398. Liu, L.; Ding, L.; Liu, Y.; An, W.; Lin, S.; Liang, Y.; Cui, W., A stable Ag₃PO₄@PANI core@shell hybrid: Enrichment photocatalytic degradation with π - π conjugation. *Appl. Catal. B* **2017**, *201*, 92-104.
399. Martín-Gómez, A. N.; Navío, J. A.; Jaramillo-Páez, C.; Sánchez-Cid, P.; Hidalgo, M. C., Hybrid ZnO/Ag₃PO₄ photocatalysts, with low and high phosphate molar percentages. *J. Photochem. Photobiol. A: Chem.* **2020**, *388*, 112196.
400. Gu, S.; Li, B.; Zhao, C.; Xu, Y.; Qian, X.; Chen, G., Preparation and characterization of visible light-driven AgCl/PPy photocatalyst. *J. Alloys Compd.* **2011**, *509*, 5677-5682.
401. Murugesan, P.; Narayanan, S.; Manickam, M.; Murugesan, P. K.; Subbiah, R., A direct Z-scheme plasmonic AgCl@g-C₃N₄ heterojunction photocatalyst with superior visible light CO₂ reduction in aqueous medium. *Appl. Surf. Sci.* **2018**, *450*, 516-526.
402. Waterhouse, G. I. N.; Bowmaker, G. A.; Metson, J. B., The thermal decomposition of silver (I, III) oxide: A combined XRD, FT-IR and Raman spectroscopic study. *Phys. Chem. Chem. Phys.* **2001**, *3*, 3838-3845.
403. H. Siddiqui, M. R.; Adil, S. F.; Assal, M. E.; Ali, R.; A. Al-Warthan, A., Synthesis and characterization of silver oxide and silver chloride nanoparticles with high thermal stability. *Asian J. Chem.* **2013**, *25*, 3405-3409.

404. Stobinski, L.; Lesiak, B.; Zemek, J.; Jiricek, P., Time dependent thermal treatment of oxidized MWCNTs studied by the electron and mass spectroscopy methods. *Appl. Surf. Sci.* **2012**, *258*, 7912-7917.
405. Bracci, M.; Bruzzese, P. C.; Famulari, A.; Fioco, D.; Guidetti, A.; Liao, Y.-K.; Podvorica, L.; Rezayi, S. F.; Serra, I.; Thangavel, K.; Murphy, D. M., Paramagnetic species in catalysis research: A unified approach towards (the role of EPR in) heterogeneous, homogeneous and enzyme catalysis. In *Electron paramagnetic resonance*, The Royal Society of Chemistry: 2021; Vol. 27, pp 1-46.
406. Tikhonov, N. I.; Khutsishvili, S. S.; Vakul'skaya, T. I.; Kuznetsova, N. P.; Emel'yanov, A. I.; Pozdnyakov, A. S., Formation of silver-containing nanocomposites during thermolysis of polyacrylonitrile salt: EPR study. *Polym. Sci. Ser. B* **2021**, *63*, 175-181.
407. Khutsishvili, S. S.; Vakul'skaya, T. I.; Aleksandrova, G. P.; Sukhov, B. G., Stabilized silver nanoparticles and nanoclusters Ag_n in humic-based bioactive nanocomposites. *J. Clust. Sci.* **2017**, *28*, 3067-3074.
408. Xu, B.; Kevan, L., Formation of silver ionic clusters and silver metal particles in zeolite rho studied by electron spin resonance and far-infrared spectroscopies. *J. Phys. Chem.* **1991**, *95*, 1147-1151.
409. Châtelain, A.; Millet, J.-L.; Monot, R., Lineshapes of the electron paramagnetic resonance of small silver particles. *J. Appl. Phys.* **1976**, *47*, 3670-3672.
410. Olm, M. T.; Symons, M. C. R.; Eachus, R. S., An e.s.r. study of AgCl-NaCl binary mixtures. *Proc. R. Soc. Lond. A* **1984**, *392*, 227-245.
411. Allard, T.; Menguy, N.; Salomon, J.; Calligaro, T.; Weber, T.; Calas, G.; Benedetti, M. F., Revealing forms of iron in river-borne material from major tropical rivers of the Amazon Basin (Brazil). *Geochim. Cosmochim. Acta* **2004**, *68*, 3079-3094.
412. McBride, M.; Kung, K.-H., Complexation of glyphosate and related ligands with iron (III). *Soil Sci. Soc. Am. J.* **1989**, *53*, 1668-1673.
413. Gachard, E.; Belloni, J.; Subramanian, M. A., Optical and EPR spectroscopic studies of silver clusters in Ag,Na-Y zeolite by γ -irradiation. *J. Mater. Chem.* **1996**, *6*, 867-870.
414. Mitrikas, G.; Trapalis, C. C.; Boukos, N.; Psyharis, V.; Astrakas, L.; Kordas, G., Size distribution and EPR of silver nanoparticles in SiO₂ matrix. *J. Non-Cryst. Solids* **1998**, *224*, 17-22.
415. Greenslade, D. J., Electron spin resonance studies of irradiated silver halides. *Brit. J. Appl. Phys.* **1965**, *16*, 1921-1922.
416. Yang, X.; Qin, J.; Jiang, Y.; Li, R.; Li, Y.; Tang, H., Bifunctional TiO₂/Ag₃PO₄/graphene composites with superior visible light photocatalytic performance and synergistic inactivation of bacteria. *RSC Adv.* **2014**, *4*, 18627-18636.
417. Ma, X.; Lu, B.; Li, D.; Shi, R.; Pan, C.; Zhu, Y., Origin of photocatalytic activation of silver orthophosphate from first-principles. *J. Phys. Chem. C* **2011**, *115*, 4680-4687.
418. Yi, Z.; Ye, J.; Kikugawa, N.; Kako, T.; Ouyang, S.; Stuart-Williams, H.; Yang, H.; Cao, J.; Luo, W.; Li, Z.; Liu, Y.; Withers, R. L., An orthophosphate semiconductor with photooxidation properties under visible-light irradiation. *Nat. Mater.* **2010**, *9*, 559-564.
419. Shen, Z.; Liu, B.; Pareek, V.; Wang, S.; Li, X.; Liu, L.; Liu, S., Sustainable synthesis of highly efficient sunlight-driven Ag embedded AgCl photocatalysts. *RSC Adv.* **2015**, *5*, 80488-80495.
420. Cui, C.; Wang, Y.; Liang, D.; Cui, W.; Hu, H.; Lu, B.; Xu, S.; Li, X.; Wang, C.; Yang, Y., Photo-assisted synthesis of Ag₃PO₄/reduced graphene oxide/Ag heterostructure photocatalyst with enhanced photocatalytic activity and stability under visible light. *Appl. Catal. B* **2014**, *158-159*, 150-160.
421. Zhang, D.; Wang, J., In situ photoactivated plasmonic Ag₃PO₄@silver as a stable catalyst with enhanced photocatalytic activity under visible light. *Mater. Res.* **2017**, *20*, 702-711.

422. Liu, Q. Y.; Zheng, Y. F.; Wang, L.; Song, X. C., Synthesis of BiIO₄/Ag₃PO₄ nanocomposite with enhanced photocatalytic activity for degradation of phenol. *J. Nanoparticle Res.* **2019**, *21*, 32.
423. Song, C.; Shang, C.; Li, S.; Wang, W.; Qi, M.; Chen, J.; Liu, H., Efficient visible-light-responsive Ag₃PO₄/g-C₃N₄/hydroxyapatite photocatalyst (from Oyster shells) for the degradation of Methylene Blue: Preparation, properties and mechanism. *Catalysts* **2022**, *12*, 115.
424. Xie, L.; Yang, Z.; Xiong, W.; Zhou, Y.; Cao, J.; Peng, Y.; Li, X.; Zhou, C.; Xu, R.; Zhang, Y., Construction of MIL-53(Fe) metal-organic framework modified by silver phosphate nanoparticles as a novel Z-scheme photocatalyst: Visible-light photocatalytic performance and mechanism investigation. *Appl. Surf. Sci.* **2019**, *465*, 103-115.
425. Zhang, M.; Du, H.; Ji, J.; Li, F.; Lin, Y. C.; Qin, C.; Zhang, Z.; Shen, Y., Highly efficient Ag₃PO₄/g-C₃N₄ Z-scheme photocatalyst for Its enhanced photocatalytic performance in degradation of Rhodamine B and phenol. *Molecules* **2021**, *26*, 2062.
426. Strong, F. C., Faraday's laws in one equation. *J. Chem. Educ.* **1961**, *38*, 98.
427. Winkelmann, J., Diffusion of oxygen (1); water (2); potassium nitrate (3): Landolt-Börnstein - Group IV Physical Chemistry 15A. In *Gases in Gases, Liquids and their Mixtures*, Lechner, M. D., Ed. Springer-Verlag Berlin Heidelberg: 2007; Vol. 15A.
428. Xing, W.; Yin, M.; Lv, Q.; Hu, Y.; Liu, C.; Zhang, J., 1 - Oxygen solubility, diffusion coefficient, and solution viscosity. In *Rotating electrode methods and oxygen reduction electrocatalysts*, Xing, W.; Yin, G.; Zhang, J., Eds. Elsevier: Amsterdam, 2014; pp 1-31.
429. Lu, Y.; Chen, W., Size effect of silver nanoclusters on their catalytic activity for oxygen electro-reduction. *J. Power Sources* **2012**, *197*, 107-110.
430. Ohyama, J.; Okata, Y.; Watabe, N.; Katagiri, M.; Nakamura, A.; Arikawa, H.; Shimizu, K.-i.; Takeguchi, T.; Ueda, W.; Satsuma, A., Oxygen reduction reaction over silver particles with various morphologies and surface chemical states. *J. Power Sources* **2014**, *245*, 998-1004.
431. Kubasheva, Z.; Sprynskyy, M.; Railean-Plugaru, V.; Pomastowski, P.; Ospanova, A.; Buszewski, B., Synthesis and antibacterial activity of (AgCl, Ag)NPs/diatomite hybrid composite. *Materials* **2020**, *13*, 3409.
432. Iravani, S., Green synthesis of metal nanoparticles using plants. *Green Chem.* **2011**, *13*, 2638.
433. El-Seedi, H. R.; El-Shabasy, R. M.; Khalifa, S. A. M.; Saeed, A.; Shah, A.; Shah, R.; Iftikhar, F. J.; Abdel-Daim, M. M.; Omri, A.; Hajrahand, N. H.; Sabir, J. S. M.; Zou, X.; Halabi, M. F.; Sarhan, W.; Guo, W., Metal nanoparticles fabricated by green chemistry using natural extracts: Biosynthesis, mechanisms, and applications. *RSC Adv.* **2019**, *9*, 24539-24559.
434. Meshram, S. M.; Bonde, S. R.; Gupta, I. R.; Gade, A. K.; Rai, M. K., Green synthesis of silver nanoparticles using white sugar. *IET Nanobiotechnol.* **2013**, *7*, 28-32.
435. Dwivedi, A. D.; Gopal, K., Biosynthesis of silver and gold nanoparticles using Chenopodium album leaf extract. *Colloids Surf. A Physicochem. Eng. Asp.* **2010**, *369*, 27-33.
436. Lin, Z.; Wu, J.; Xue, R.; Yang, Y., Spectroscopic characterization of Au³⁺ biosorption by waste biomass of *Saccharomyces cerevisiae*. *Spectrochim. Acta A Mol. Biomol. Spectrosc.* **2005**, *61*, 761-765.
437. de Hoffmann, E.; Stroobant, V., *Mass spectrometry: Principles and applications*. Wiley: 2007.
438. What is mass spectrometry? <https://www.broadinstitute.org/technology-areas/what-mass-spectrometry#:~:text=Mass%20spectrometry%20is%20an%20analytical,the%20sample%20components%20as%20well.> (accessed 7 July 2022).
439. Mass spectrometry. http://www.premierbiosoft.com/tech_notes/mass-spectrometry.html (accessed 7 July 2022).
440. Flowers, P.; Neth, E. J.; Robinson, W. R.; Theopold, K.; Langley, R., Chemistry: Atoms first 2e. Openstax: 2019. <https://openstax.org/details/books/chemistry-atoms-first-2e>.



Everything has a reason
What comes will go
As the river flows, let life too
Stagnant places never grow